CABLE-IN-CONDUIT SUPERCONDUCTORS FOR FUSION MAGNETS

Electro-magnetic modelling for understanding and optimizing their transport properties

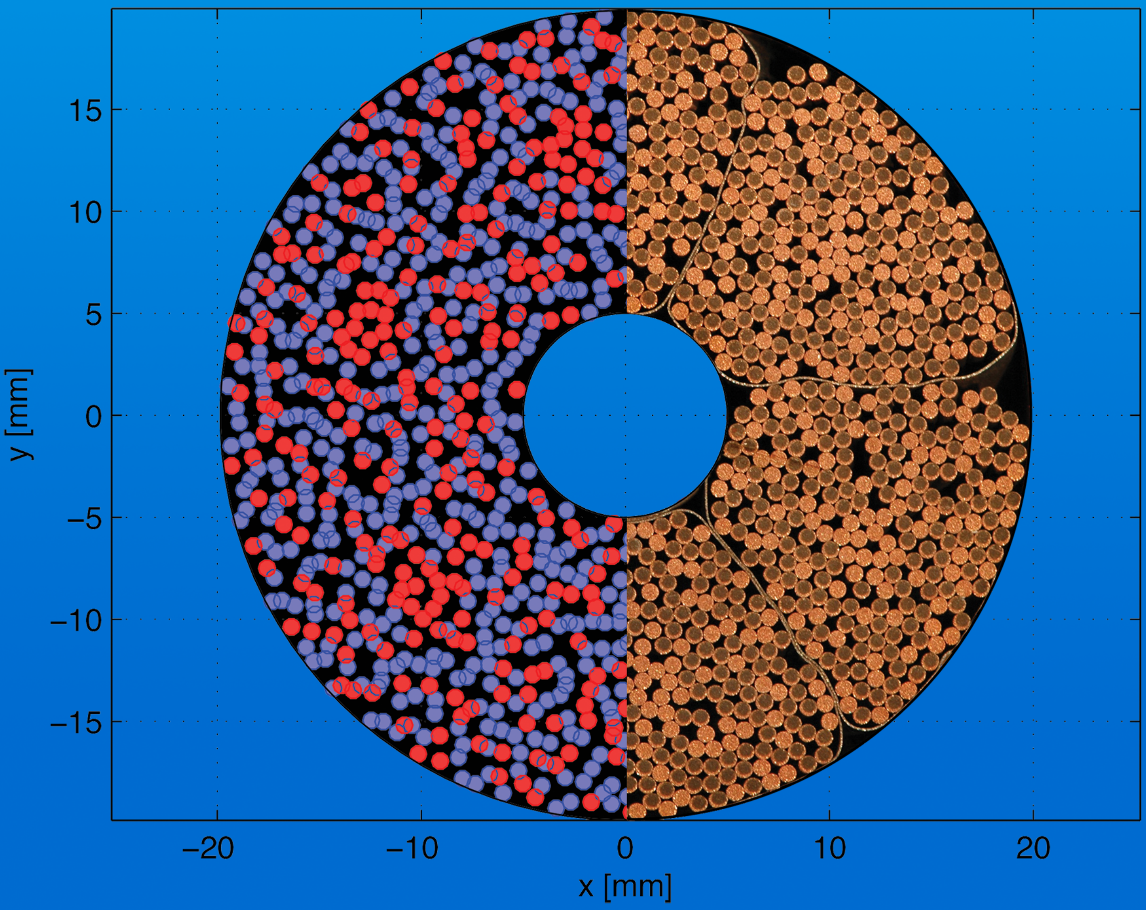

Gabriella Rolando

CABLE-IN-CONDUIT SUPERCONDUCTORS FOR FUSION MAGNETS

ELECTRO-MAGNETIC MODELLING FOR UNDERSTANDING AND OPTIMIZING THEIR TRANSPORT PROPERTIES

Dissertation graduation committee:

Chairman: Prof. dr. G. van der Steenhoven	University of Twente
Supervisor: Prof. dr. ir. H.H.J. ten Kate	University of Twente
Assistant-supervisor: Dr. M.M.J. Dhallé	University of Twente
Referees: Dr. A. Devred	ITER Organization, Cadarache, France
Dr. A. Verweij	CERN, Geneva, Switzerland
Members: Prof. dr. ir. R. Akkerman	University of Twente
Prof. dr. ir. H.J.M. ter Brake	University of Twente
Prof. dr. ing. B. van Eijk	NIKHEF, Amsterdam
Prof. dr. N.J. Lopes Cardozo	Eindhoven University of Technology

The research described in this thesis was carried out at the University of Twente and financially supported by the ITER Organization, Cadarache, France as well as Fusion For Energy, Barcelona, Spain.

Cover by S. C. Bukowiec. Cross-section of an ITER Toroidal Field CIC conductor formed by the assembly of a simulated conductor in JackPot-ACDC and a photograph of the real cable. Photo courtesy of K. Yagotintsev.

Cable-In-Conduit Superconductors for Fusion Magnets
G. Rolando
Ph.D. thesis, University of Twente, The Netherlands
ISBN 978-90-365-3563-2
Printed by Ipskamp Drukkers, Enschede, the Netherlands

CABLE-IN-CONDUIT SUPERCONDUCTORS FOR FUSION MAGNETS

Electro-magnetic modelling for understanding and optimizing their transport properties

PROEFSCHRIFT

ter verkrijging van
de graad van doctor aan de Universiteit Twente,
op gezag van de rector magnificus,
prof. dr. H. Brinksma,
volgens besluit van het College voor Promoties
in het openbaar te verdedigen
op vrijdag 8 november 2013 om 12.45 uur

door

Gabriella Rolando

geboren op 12 augustus 1985
te Avigliana, Italië

Dit proefschrift is goedgekeurd door de promotor:
Prof. dr. ir. H.H.J. ten Kate

Dla mojego męża Sebastiana

Table of contents

Chapter 1

Introduction

Among the many applications of superconductivity, nuclear fusion constitutes a relatively new and promising field. ITER, a fully superconducting tokamak, is the first device in fusion history designed to produce a net output power. For large current-carrying capacity and improved stability, the machine relies on the Cable-In-Conduit Condutor (CICC) concept, by which some 500 to 1500 normal conducting and superconducting strands are cabled in multiple stages. This thesis deals with the application of numerical tools for understanding and optimizing the transport properties performance of CIC conductors and their joints under various operating conditions.

In the first chapter an introduction to nuclear fusion and magnetic confinement, with particular emphasis on the ITER magnet system, is given.

The superconducting materials, conductor and joint layouts relevant for this thesis are presented.

The stability of superconductors and the main limitations of the performance of CIC conductors and their joints are introduced. Given the potentially extended operation interruption and high reparation cost implied by stability loss, the occurrence of such events should be carefully avoided.

1.1 Nuclear fusion

Nuclear fusion is a nuclear reaction by which two or more atomic nuclei join to form a heavier nucleus. In the process, matter is not conserved and part of the mass of the fusing nuclei is converted into energy. The energy release is due to the action of two opposing forces, the nuclear force drawing together protons and neutrons, and the Coulomb force causing protons to repel each other. However, at very short ranges nuclear force can overcome electric repulsion, hence building up nuclei up to iron and nickel from lighter ones by fusion causes net energy release from the net attraction of these particles.

Fusion is the process that powers active stars and produces virtually all elements through nucleosynthesis. In the core of the stars, gravitational forces create the extreme density and temperature necessary for fusion.

On Earth, *thermonuclear* fusion is the only process that appears to be useful for generating fusion energy. At temperatures in excess of 100 million degree, nuclei no longer form neutral atoms but exist in the plasma state, in which the ionized atoms are accelerated to high speed. Under such conditions, they can overcome the Coulomb barrier and approach each other close enough for the attractive nuclear force to achieve fusion.

The most promising fusion reaction, allowing for the highest energy gain at the lowest temperature, involves two H isotopes, deuterium (D) and tritium (T). In the fusion of deuterium and tritium, one helium nuclei, one neutron, and energy are produced, see Figure 1.1. The helium nucleus carries an electric charge which responds to the magnetic field of the fusion reactor and thus remains confined within the plasma. However, ∼80% of the energy produced is carried away from the plasma by the neutron, which has no electrical charge and is therefore unaffected by magnetic field. In fusion power plants, the neutrons will be absorbed by the walls of the machine, transferring their energy as heat that will be used to produce steam and, by way of conventional turbines and alternators, electricity.

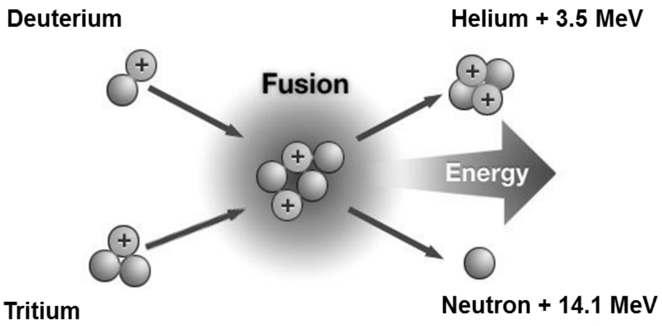

Figure 1.1: Two atoms of deuterium (D) and tritium (T) fuse forming a helium nucleus (He), a neutron and releasing energy.

Fusion is an attractive energy source because the necessary fuels are abundantly available and only limited amounts (∼250 kg per year for a 1 GW fusion power plant) are needed in the reaction. In addition, fusion emits no pollution or greenhouse gases. Its major by-product is helium: an inert, non-toxic gas. Moreover, it is inherently safe, because any variation in the required conditions will cause the plasma to cool down within seconds, stopping the reaction.

Among the drawbacks of fusion is the radioactivity acquired by the reactor. Although, the half-life of the radio isotopes produced in the reaction is less than those from nuclear fission, fusion waste is considerably more radioactive. Concerns also exist about the possible release of tritium that can be easily incorporated into water. With a half-life of ∼12.3 years, tritium can remain in the environment for more than 100 years after its creation.

Since its start in the 1920s, research on fusion energy has largely progressed and several fusion machines, mainly of the tokamak type (see section 1.2), have been constructed, which can generate and maintain plasmas for several minutes. At present, the largest operating fusion experiment in the world is the Joint European Torus (JET). JET has been the first tokamak to use deuterium and tritium as fusion fuel. The machine also holds the record for the generation of fusion energy with 16 MW during 1 second, and a continuous fusion capacity of 4 MW during 4 seconds. ITER, see section 1.2.1, presently under construction, represents the next step towards the exploitation of fusion energy, being the first *pulsed* device designed to produce a net output power. In spite of the substantial progress, several technological challenges remain on the road leading to commercial fusion power plants [1]:

- To achieve the conditions enabling a net energy production, plasmas must be maintained at high density and temperature for a few hours or even in steady-state. This requires the minimization of energy loss due to small-scale turbulences and plasma instabilities. At the same time, a large fraction of the heating power must be radiated by the confined plasma to avoid excessive heat load on localised components of the machine. Operating plasma regimes simultaneously ensuring high plasma confinement and radiation have yet to be qualified.

- The power necessary to maintain plasmas at high temperatures is ultimately exhausted in a narrow region of the reaction chamber called the divertor. Although, exhaust systems able to withstand heat fluxes up to 20 MW/m^2 (which is of the same order of the heat load on the sun's surface) have been produced for ITER, solutions for the larger power load on the divertor expected in future fusion machines still needs to be developed.

- Neutron resistant materials able to withstand 14 MeV neutron flux and maintain their structural and thermal conduction properties for long operation times need to be developed. Although some candidates materials already exist (EUROFER for the breeding blanket, tungsten for plasma facing component armour and copper alloys for the divertor coolant interface) much more R&D is needed to find new ones. Also the completion of their characterisation under relevant conditions requires the creation of dedicated irradiation facilities.

- Tritium self-sufficiency is mandatory for future fusion power plants. Tritium self-sufficiency requires the research of efficient breeding and extraction systems as well as tritium loss minimization.

In order to address the above issues, the DEMO project [1] is currently envisaged as an intermediate step between ITER and prototype fusion power plants. On a longer time scale, alternative magnetic confinement fusion devices may also reach sufficient technological maturity. In this respect, the stellarator is the most promising configuration offering advantages over tokamaks, such as capability for steady-state operation and lower occurrence rate of plasma instabilities [1]. Currently, the stellarator machine W7X using a superconducting magnet system as well is in its final stage of construction [2].

Finally, to be economically successful fusion will need to demonstrate its potential for competitive cost of electricity. Extended operation times and high efficiency of the power conversion cycle will have to be ensured for commercial fusion power plants. To reduce construction costs, materials allowing extended operational time and simple fabrication routes should be identified. Plasma regimes of operation with improved confinement will also contribute to reduce plant size and cost. In the far future high temperature superconductors may eventually replace the actual NbTi and Nb_3Sn superconductors in the magnets, avoiding the use of helium and increasing the reliability of the machine by higher stability margin. This, however, will only materialize when high temperature superconductors will be produced on a large scale and cost per current-meter is largely reduced.

1.2 Magnet systems for fusion

In order for fusion to occur, high plasma densities must be achieved. With increasing density, the plasma temperature rises to such extreme values that no material withstands contact with. A common approach to generating fusion power uses magnetic field to confine the plasma. Consisting of charged particles, plasmas can be shaped and confined by magnetic forces so that a suitable magnetic field may act as a recipient that is not affected by heat.

The simplest magnetic configuration is a long solenoid, where the magnetic field lines run parallel to the axis of the cylinder. Such a magnetic field prevents charged particles being lost radially, but does not confine them at the ends of the solenoid. To solve the problem two approaches can be used. One consists in blocking the ends with magnetic mirrors; the other in trapping the plasma particles by bending the magnetic field lines around so that they close on themselves in a doughnut-shape.

The latter solution has resulted in the development of the tokamak reactor, which is today's most used design in magnetic confinement fusion experiments, see Figure 1.2. Magnets around the walls of the toroid shaped tokamak produce the toroidal field. However, a toroidal magnetic field alone would provide poor confinement because its strength decreases from the centre to the edge, so that the particles tend to drift outwards. For complete confinement, an additional poloidal field is required, causing the plasma particles to spin in a helix pattern and thus keeping them constantly moving toward the center of the torus and away from the walls. Most of the poloidal field in tokamaks is provided by a solenoid positioned in the open bore of the toroid. Acting as the primary windings of a transformer, the central solenoid induces a current through the plasma, which acts as the secondary windings, that also contributes to heating the plasma through ohmic heating. Depending on the specific design of the reactor, additional sets of control coils (like the Poloidal Field coils in Figure 1.2) may be added to the tokamak magnet system that, generating a vertical magnetic field, contribute to the plasma confinement.

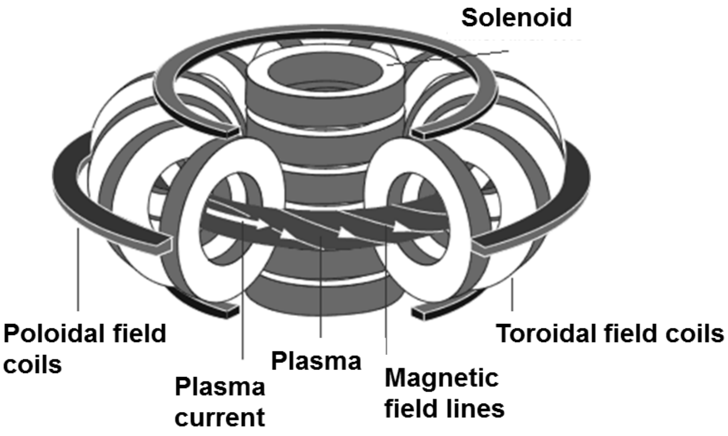

Figure 1.2: Magnetic confinement in a tokamak fusion reactor.

1.2.1 ITER

The ITER project comprises building the world's largest (830 m^3 of plasma volume) and most advanced experimental tokamak fusion reactor at the Cadarache site in southern France. The organization of the project is described elsewhere [3]. The machine is expected to demonstrate the feasibility of producing more power from fusion than is used to sustain it, a challenge not yet been achieved by previous fusion reactors. The project goal is an energy gain factor Q of 10, corresponding to an output of 500 MW for 50 MW of input power.

To generate the powerful magnetic field required to confine the plasma while avoid ohmic heating that would limit the efficiency of the machine, the use of superconducting magnets is essential. This allows a significant limitation of the energy consumption, and thus operation cost, during the long plasma pulses envisaged for the reactor. The ITER magnet system comprises 48 superconducting coils, see Figure 1.3:

- 18 Toroidal Field (TF) coils;
- 1 Central Solenoid (CS), composed of 6 coil modules;
- 6 Poloidal Field (PF) coils;
- 9 pairs of Correction Coils (CC).

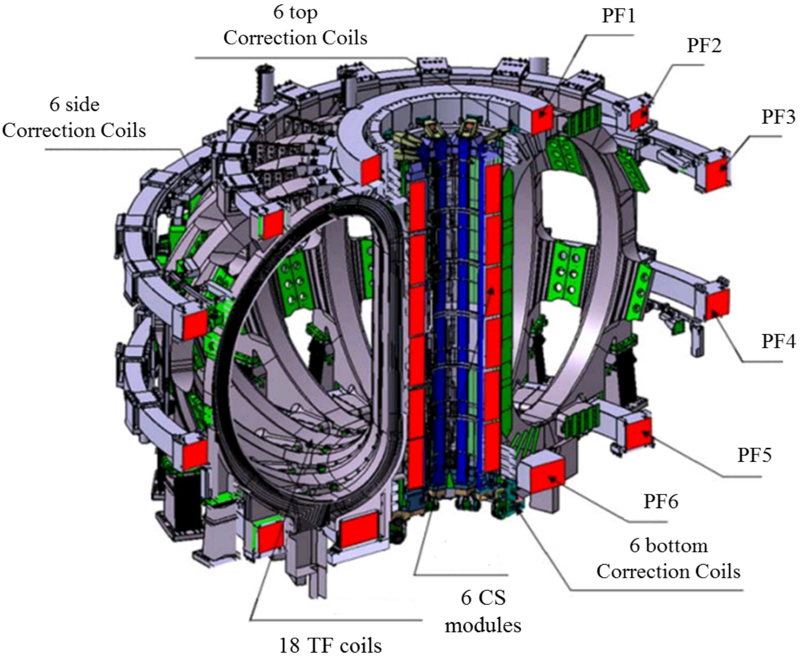

Figure 1.3: The magnet system of ITER [4].

The 18 Torodial Field coils are designed to carry a 68 kA steady-state current, generating a maximum magnetic field of 11.8 T. Their dimensions (each coil is 14 m high and 9 m wide) and total toroid weight exceeding 6000 tons make them one of the biggest components of the ITER machine.

The backbone of the magnet system is the Central Solenoid, featuring an inner radius of 1.3 m and outer radius of 2.08 m for a total height of more than 12 m. The Central Solenoid is composed of six stacked modules, whose currents (up to 40-45 kA) can be independently driven to enable the testing of different operating scenarios. The Central Solenoid design is such as to provide a peak magnetic field of 13 T and a magnetic field ramp rate of 1.3 T/s [5].

The Poloidal Field system consists of six horizontal solenoidal magnets placed outside the toroidal magnet structure, with diameters in the range 8 to 24 m. The coils are designed to allow a maximum current of 48 to 55 kA and to provide a peak magnetic field exceeding 6 T [6].

Correction coils inserted between the Toroidal and Poloidal Field coils and distributed around the tokamak complete the ITER magnet system, correcting the error field modes. Although lighter than the other coils and carrying a smaller current (10 kA), the Correction Coils are large in size (up to 8 m wide) and can feature a non-planar shape.

ITER plasma scenarios

Details of the scenarios envisaged for ITER operation can be found in [7]. Figure 1.4 shows the current in the Poloidal Field coils and in the six modules of the Central Solenoid during a 15 MA plasma pulse, which represents the reference operating scenario adopted throughout this thesis.

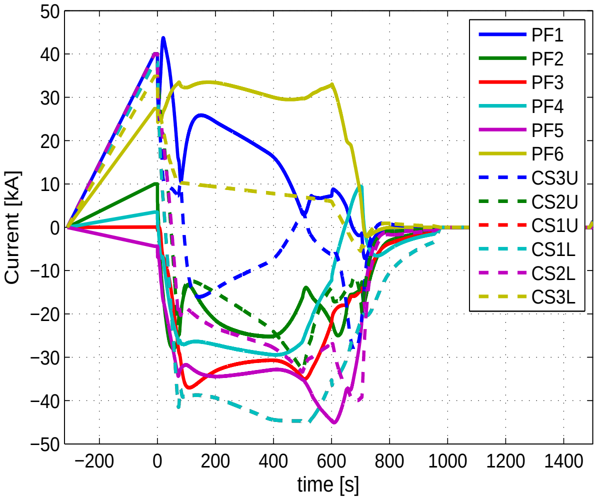

Figure 1.4: Nominal operating currents in the 6 modules of the ITER Central Solenoid and 6 Poloidal Field coils during the 15 MA plasma scenario [7]. For t<0 s currents in the coils are ramped to the nominal values. The discharge starts at t = 0 s.

Four main phases can be recognized from the coil currents point of view:

- in the interval -310<t<0 s the currents in the coils are ramped up to their nominal values. The current charge process lasts for 300 s and it is followed by a plateau of 10 s;
- at t = 0 s the Start of Discharge (SOD) occurs, when the the currents in the coils are rapidly varied to induce and shape the plasma. Very fast magnetic field variations take place especially in the first ~1.5 s, but a significant ramp rate is observed up to ~80 s;
- the successive phase between 80<t<700 s, when a burning plasma is first achieved and then slowly cooled down, is characterized by lower current, and hence lower magnetic field variations;

- finally between 700<t<950 s all coil currents are ramped down to zero. A long 0 kA current plateau is then maintained for ~900 s, after which the successive plasma pulse is initiated by ramping up the currents again.

Being characterized by the highest field change rates, the Start of Discharge represents the most critical operating phase for the stability of the superconducting magnets, as further discussed in section 1.4.

A second operating scenario, corresponding to a 17 MA plasma pulse, is used in chapter 5 for analysing the Toroidal Field coil joint stability and it is shown in Figure 1.5.

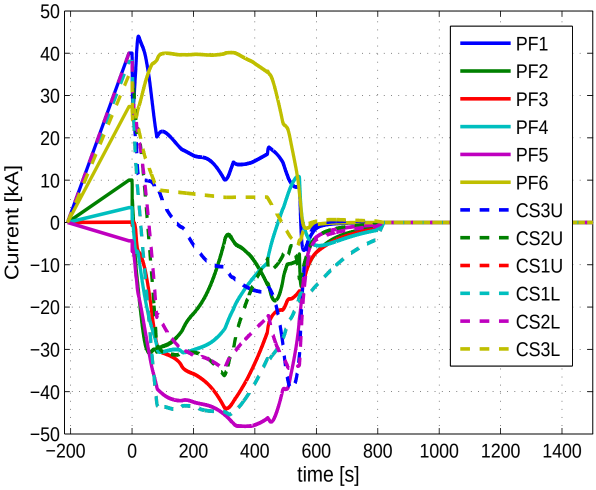

Figure 1.5: Nominal operating currents in the 6 modules of the ITER Central Solenoid and 6 Poloidal Field coils during the 17 MA plasma scenario [7]. For t<0 s currents in the coils are ramped to the nominal values. The discharge starts at t = 0 s.

1.3 Superconductivity in practical conductors

Superconductivity is a phenomenon whereby certain materials, when cooled to low temperature, can conduct steady-state currents without electrical resistance. The transition from the normal conducting to the superconducting state occurs at a critical temperature T_c characteristic of the material, see Figure 1.6.

The superconducting state is also bounded to a magnetic field lower than the upper critical magnetic field B_{c2} and to current densities below a critical value J_c. The critical temperature, field and engineering current density, i.e. the critical current density normalized to the wire/tape cross-section, of the most common practical superconducting materials are summarized in Table 1.1.

In crystal-like superconductors, like Nb_3Sn, the critical behaviour is significantly affected by the strain ϵ as well. In these materials, lattice deformation alters B_{c2}

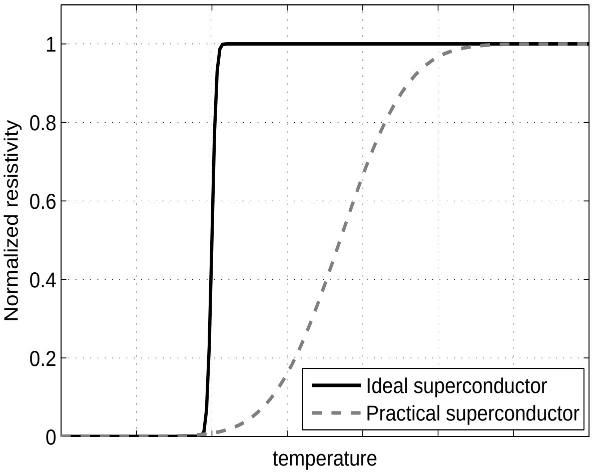

Figure 1.6: Resistance versus temperature in ideal and practical superconductors around the critical temperature T_c.

Table 1.1: Critical temperature, upper critical field and engineering critical current density for practical superconductors [8].

Material	T_c **at 0 T [K]**	B_{c2} **at 0 K [T]**	$J_e(B, 4.2\,K)$ **[A/mm²]**
NbTi	9.2	14.6	1800 (5 T)
Nb_3Sn	18.3	24-28	1900 (12 T)
YBaCuO	92	>100	400 (20 T)
$Bi_2Sr_2CaCu_2O_x$	94	>100	600 (20 T)

and T_c, while micro-structural cracks limit the transport current.

Given the above limits, the performance of a superconductor is generally described by means of a critical surface in the J-B-T space, see Figure 1.7. For combinations of the three parameters corresponding to points below the critical surface, the material is in the superconducting state. The material is instead normal conducting for points above the critical surface.

In practical applications of superconductivity, the operating temperature is set around 4.2 K (liquid helium temperature at one atmosphere). Therefore the relevant parameter to characterize the performance of the different superconducting materials is their critical current density variation with the applied magnetic field. Figure 1.8 illustrates the engineering critical current density dependence on the applied magnetic field at 4.2 K for a number of practical superconductors.

For the most used materials, i.e. NbTi and Nb_3Sn, Eqs. 1.1 [10] and 1.5 [11], respectively, are commonly adopted to describe the J_c change with temperature,

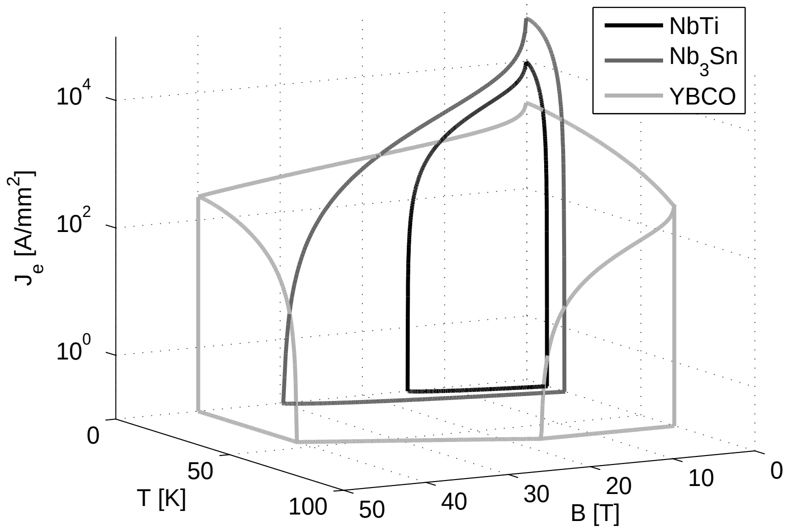

Figure 1.7: The critical surface of NbTi, Nb3Sn and YBCO [9].

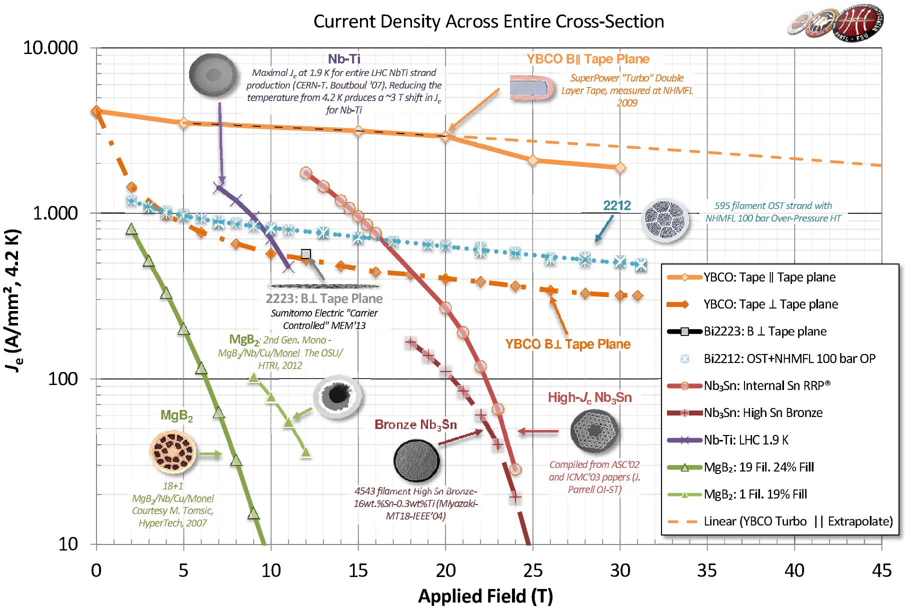

Figure 1.8: Engineering critical current density versus applied magnetic field for several practical superconductors [8].

magnetic field and, eventually, strain.

$$\textbf{NbTi:}\quad J_c = \frac{C_0}{B}(1-t^{1.7})^{\gamma} b^{\alpha}(1-b)^{\beta} \quad [\text{A}\cdot\text{mm}^{-2}], \tag{1.1}$$

with t reduced temperature, b reduced magnetic field and B applied magnetic field. C_0, γ, α and β are fitting parameters for the specific wire. The reduced temperature is defined in Eq. 1.2

$$t = \frac{T}{T_{C0}}, \tag{1.2}$$

where T is the operating temperature and T_{C0} is the critical temperature at 0 T. The reduced magnetic field is given in Eq. 1.3

$$b = \frac{B}{B_{c2}(T)}, \tag{1.3}$$

where $B_{c2}(T)$ is the upper critical magnetic field at the operating temperature T. This is expressed in Eq. 1.4

$$B_{c2}(T) = B_{c20} \cdot (1 - t^{1.7}) \quad [\mathrm{T}], \tag{1.4}$$

where B_{c20} is the upper critical magnetic field at 0 K.

$$\mathbf{Nb_3Sn:} \quad J_c = \frac{C_1}{B} \cdot S \cdot (1 - t^{1.52})(1 - t^2) b^p (1 - b)^q \quad [\mathrm{A{\cdot}mm^{-2}}], \tag{1.5}$$

with t reduced temperature, b reduced magnetic field, S strain dependent term and B applied magnetic field. C_1, p and q are fitting parameters for the specific wire. The reduced temperature is defined according to Eq. 1.6

$$t = \frac{T}{T_C^*(\epsilon)}, \tag{1.6}$$

where

$$T_c^*(\epsilon) = T_{cm}^* \cdot S^{\frac{1}{3}} \quad [\mathrm{K}], \tag{1.7}$$

with T_{cm}^* the inhomogeneity averaged critical temperature. The reduced magnetic field is given in Eq. 1.8

$$b = \frac{B}{B_{c2}^*(\epsilon, T)}, \tag{1.8}$$

where

$$B_{c2}^*(\epsilon, T) = B_{c2m}^*(0) \cdot S \cdot (1 - t^{1.52}) \quad [\mathrm{T}], \tag{1.9}$$

with $B_{c2m}^*(0)$ the inhomogeneity averaged upper critical magnetic field at 0 K. The strain dependent term S is defined in Eq. 1.10

$$S = \frac{C_{a,1} \cdot [\sqrt{\epsilon_{shift}^2 + \epsilon_{0,a}^2} - \sqrt{(\epsilon_{axial} - \epsilon_{shift})^2 + \epsilon_{0,a}^2}] - C_{a,2} \cdot \epsilon_{axial}}{1 - C_{a,1} \cdot \epsilon_{0,a}} + 1, \tag{1.10}$$

where $C_{a,1}$ and $C_{a,2}$ are the second an third invariant of the axial strain sensitivity, ϵ_{axial} is the axial strain (sum of applied and pre-compression strains), $\epsilon_{0,a}$ is the remaining strain component when $\epsilon_{axial} = 0$, and ϵ_{shift} is the measurement related strain given by Eq. 1.11

$$\epsilon_{shift} = \frac{C_{a,2} \cdot \epsilon_{0,a}}{\sqrt{C_{a,1}^2 - C_{a,2}^2}}. \tag{1.11}$$

NbTi is the principle material used in practical applications of superconductivity and it allows operation in magnetic field up to ∼8 T. In the ITER project, NbTi is used in the Poloidal Field coils and in the Correction Coils. The Nb_3Sn compound is adopted instead when magnetic fields up to ∼16 T are required. However, due to its brittle nature that makes it difficult to process, the usage of Nb_3Sn has been so far relatively limited. Indeed the ITER Central Solenoid and Toroidal Field coils are its first large-scale applications.

Both NbTi and Nb_3Sn are low-temperature superconductors requiring cooling with liquid helium in the 1.9-5 K range. As illustrated in Figure 1.9 for NbTi and Nb_3Sn, the specific heat of the materials at cryogenic temperatures is significantly reduced compared to room temperature (∼2000 times lower). It follows that even a small energy release could produce a large temperature rise, and thus lead to a quench, i.e a sudden and irreversible transition from the superconducting to the normal state. Following a quench, re-cooling of the magnets down to their operation temperature is necessary, which, apart from being costly, causes an interruption of the normal operation. Therefore, to avoid the occurrence of quenches, magnets must be built with a temperature margin ΔT such as to ensure reliable operation against the most critical scenarios (i.e. plasma disruption

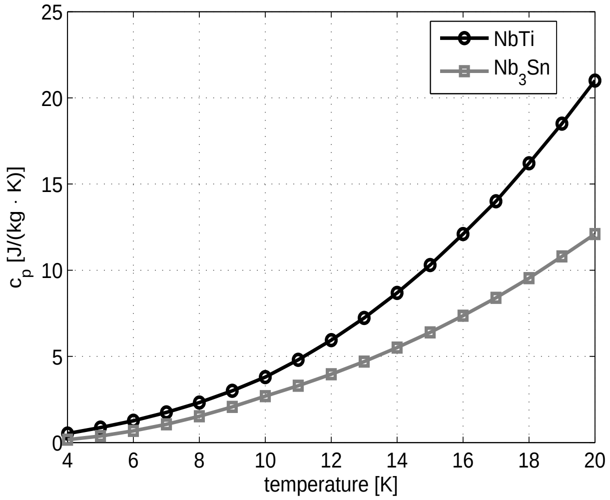

Figure 1.9: Specific heat at constant pressure versus temperature for NbTi and Nb_3Sn at cryogenic temperatures.

in tokamaks machine) and in the entire windings, including sensitive areas like the high-magnetic field region and joints. The temperature margin ΔT is defined according to Eq. 1.12 [12]

$$\Delta T = T_{cs} - T_{op} = (T_c(B) - T_{op}) \cdot (1 - \frac{I_{op}}{I_c}) \quad [\mathrm{K}] \tag{1.12}$$

where T_{cs}, T_{op} and $T_c(B)$ are the current sharing temperature, operating temperature and critical temperature at the applied magnetic field B, respectively; whereas I_{op} and I_c the operating and critical currents. As shown in Figure 1.6, in practical superconductors the transition from the normal to the superconducting state is not sharp, but occurs over an extended temperature range. As a consequence, a criterion needs to be set to establish the boundary between superconducting and resistive conditions. For low temperature superconductors, the current sharing temperature T_{cs} is commonly defined as the value at which an electric field of 10 μV/m is detected along the sample while ramping the temperature at fixed current. In analogy to the critical temperature T_c of ideal superconductors, the T_{cs} is thus determined by current, magnetic field and, eventually, strain. The current sharing, i.e. the possibility to re-distribute over-currents among wires, also plays a role on the T_{cs}. The operating temperature T_{op} is the local temperature of the superconductor determined by the cooling conditions and energy loss within the windings.

1.3.1 Strands

For stability and AC loss reasons [13], practical superconductors are shaped into wires (diameter 0.7-1.3 mm), or when used in cables called strands, comprising a large number of thin superconducting filaments (diameter 1-100 μm) twisted and embedded in a low-resistivity matrix of normal metal. The main specifications for the ITER NbTi and Nb_3Sn strands are detailed in Tables 1.2 and 1.3, while a few characteristic strand cross-sections are shown in Figures 1.10 and 1.11.

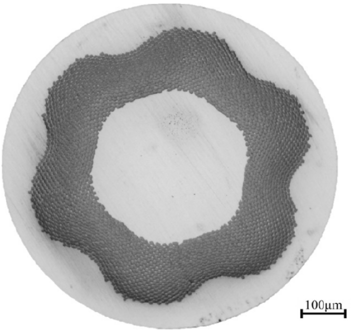

Figure 1.10: Transverse cross-section of the WST NbTi-type 2 strand for ITER Poloidal Field conductors [14].

Table 1.2: Specifications of ITER NbTi strands [15].

	Type 1	**Type 2**
Ni plated strand diameter [mm]	0.730 ± 0.005	0.730 ± 0.005
Twist pitch [mm]	15 ± 2	15 ± 2
Twist direction	right hand	right hand
Ni plating thickness [μm]	2.0 + 0 - 1	2.0 + 0 - 1
Cu-to-non-Cu volume ratio	1.6 - 0.05/+ 0.15	2.3 - 0.05/+ 0.15
Filament diameter [μm]	$\leqslant$ 8	$\leqslant$ 8
Inter-filament spacing [μm]	$\geqslant$ 1	$\geqslant$ 1
RRR of Ni-plated strand	>100	>100
Minimum critical current [A] at 4.22 K and B_{ref}	306 (B_{ref} = 6.4 T)	339 (B_{ref} = 5 T)
Resistive transition index in the 0.1-to-1 μV/cm range at 4.22 K and B_{ref}	>20 (B_{ref} = 6.4 T)	>20 (B_{ref} = 5 T)
Max hysteresis loss [mJ/cm^3] per strand unit volume at 4.22 K over a ± 1.5 T cycle	55	45

Table 1.3: Specifications of ITER Nb_3Sn strands [15].

	TF	**CS**
Un-reacted Cr strand diameter [mm]	0.820 ± 0.005	0.830 ± 0.005
Twist pitch [mm]	15 ± 2	15 ± 2
Twist direction	right hand	right hand
Cr plating thickness [μm]	2.0 + 0 - 1	2.0 + 0 - 1
Cu-to-non-Cu volume ratio	1.0 ± 0.1	1.0 ± 0.1
Filament diameter [μm]	$\leqslant$ 5	$\leqslant$ 5
RRR of Cr-plated strand	>100	>100
Minimum critical current [A] at 4.22 K and 12 T	190	228
Resistive transition index in the 0.1-to-1 μV/cm range at 4.22 K and 12 T	>20	>20
Max hysteresis loss [mJ/cm^3] per strand unit volume at 4.22 K over a ± 3 T cycle	500	500

Since the resistivity of superconductors above their critical temperature T_c is relatively high, a low resistive path for the current is necessary in the case of transition to the normal state to avoid excessive ohmic heating and, in the worst case scenario, even melting as further discussed in 1.4. Cu for NbTi, CuSn/Cu for Nb_3Sn, Ag for BSCCO-2212 and steel/Cu for YBCO wires are typically used as matrix materials, exhibiting an electrical resistivity that is several orders of magnitude lower than the one of the filaments in the normal state.

Filament diameters well below 10 μm are required for the ITER strands to reduce AC hysteresis loss, as detailed in Tables 1.2 and 1.3. The subdivision into

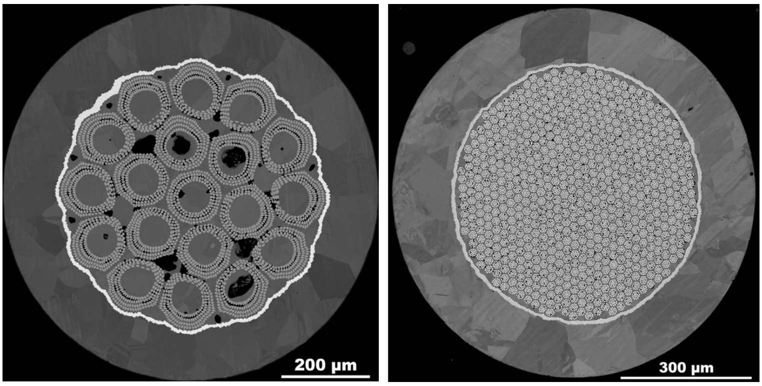

Figure 1.11: Transverse cross-sections of the internal tin-Kiswire (left) and bronze-JASTEC (right) strands for ITER Toroidal Field conductors [16].

small filaments also improves the stability of the strands against local thermal disturbances, allowing fast heat and current transfer to the surrounding matrix. Filament twisting is introduced to reduce inter-filament coupling currents induced by time-varying magnetic field. In twisted wires, the magnetic flux linked to the current loops changes sign every half-twist pitch. For sufficiently short twist pitches, not enough space is available for large transverse currents to build up.

Relatively hard and highly-resistive coatings are applied to the strands, typically Ni for NbTi and Cr for Nb_3Sn, to reduce their coupling in the final cable.

1.3.2 Cable-In-Conduit Conductors

To achieve the large currents needed to generate high magnetic fields, many strands are cabled, as illustrated in Figure 1.12. The ITER magnets rely on the Cable-In-Conduit Conductor (CICC) concept, by which up to ∼1500 strands are twisted in multiple cabling stages around a central spiral and then inserted in a

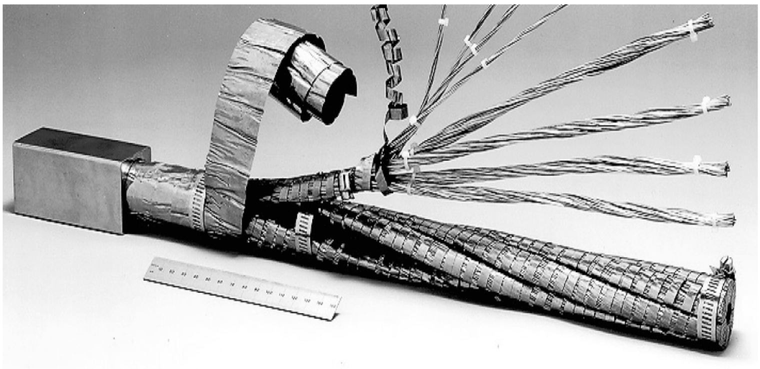

Figure 1.12: View of an ITER Poloidal Field conductor showing the underlying multi-stage structure.

metal jacket. The He leak-tight jacket surrounding the cable primarily provides mechanical reinforcement by taking up practically all of the Lorentz force in the coil windings during operation. The difference between the jackets of the ITER Toroidal Field and Central Solenoid CIC conductors is due to the expected difference in electro-magnetic forces on the conductors and is shown in Figure 1.13.

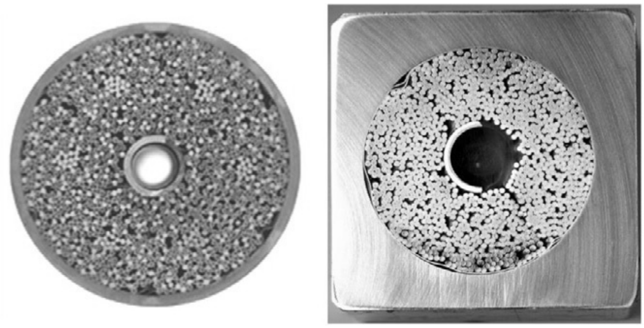

Figure 1.13: Cross-sections of the Toroidal Field (left) and Central Solenoid (right) conductors [17].

For cooling, supercritical He flows through the interstices between the strands (typical void fraction $\sim$30 %) and the central channel. The combination of forced He flow and large strand-coolant contact (wetted perimeter) results in optimal cooling and thus stability against significant power dissipation. A central channel delimited by a metal spiral is usually added to reduce the He pressure drop, while facilitating He circulation between the strand bundles.

Copper strands can be included in the cable to offer a low resistivity current path in the case of transition of the superconductor to the normal state, and hence improve the stability. Metal barriers (wraps) are added around the last stage sub-cables (petals) to reduce inter-strand coupling in pulsed operation. The main specifications of the ITER CIC conductors are detailed in Tables 1.4 to 1.6.

Table 1.4: Specification of ITER Correction Coils and Main Busbar CIC conductors [15].

	CC	**MB**
Cable pattern	3 x 4 x 5 x 5	(2SC+1Cu) x 3 x 5 x (5+C0) x (6+C1)
Core	-	C0: 3 x 4 Cu C1: 1 + 6 + 12 + 18 + 24
Cable wrap	0.08 mm thick 40% overlap	0.08 mm thick 40% overlap
Nr. of SC strands	300	900
Void fraction	35.4%	35% (bundle) 20% (C1)
Cable size [mm]	14.8 (side)	40 (diameter
Jacket [mm]	Square 19.2 x 19.2 316LN	Circular Ø46 JK2LB

Table 1.5: Specification of ITER Toroidal Field and Central Solenoid CIC conductors [15].

	TF	**CS**
Cable pattern	((2SC+1Cu) x 3 x 5 x 5 + C) x 6	(2SC+1Cu) x 3 x 4 x 4 x 6
Core C	3Cu x 4	-
Centr. spiral [mm]	8 x 10	7 x 9
Petal wrap	0.10 mm thick 50% coverage	0.05mm thick 70% coverage
Cable wrap	0.10 mm thick 40% overlap	0.08 mm thick 40% overlap
Nr. of SC strands	900	576
Void fraction	29.7%	33.5%
Cable diameter [mm]	39.7	32.6
Jacket [mm]	Circular Ø43.7 316LN	Circle in square 49 x 49 JK2LB

Table 1.6: Specification of ITER Poloidal Field CIC conductors [15].

	PF 1,6	**PF 5**	**PF 2,3,4**
Cable pattern	3SC x 4 x 4 x 5 x 6	(3SC x 4 x 4 x 4 +C) x 6	(((2SC + 1Cu) x 3 x 4 + C1) x 5 +C2) x 6
Core diam. [mm]	-	2.85	1.20(C1) / 2.70(C2)
Centr. spiral [mm]	10 x 12	10 x 12	10 x 12
Petal wrap	0.05 mm thick 50% coverage	0.05 mm thick 50% coverage	0.05 mm thick 50% coverage
Cable wrap	0.10 mm thick 40% overlap	0.10 mm thick 40% overlap	0.10 mm thick 40% overlap
Nr. of SC strands	1440	1152	720
Void fraction	34.3%	34.1%	34.2%
Cable diam. [mm]	37.7	35.3	35.3
Circle in square 316L Jacket [mm]	53.8 x 53.8	51.9 x 51.9	51.9 x 51.9

1.3.3 Joints between CIC conductors

Given the extreme dimensions of the ITER coils, several unit lengths of conductor need to be joined to wind the coils. In addition to the joints between cable units also terminal joints are necessary to interface the coils with the bus bars connecting the power supplies. Several types of joint layouts between CIC conductors exist, as illustrated in Figures 1.14 and 1.15.

In lap-type joints, the CIC conductors have stripped off their jackets, cable wraps and outer petal wraps over a length slightly longer than the cable pitch. The conductors are then pressed against a saddle-shaped Cu sole by stainless steel covers, reducing the void fraction to ~20-25%, see Figure 1.14c. For better electrical contact with the sole, a solder filling the cable voids and strand coating can be added. The central spiral in the CIC conductor is replaced by

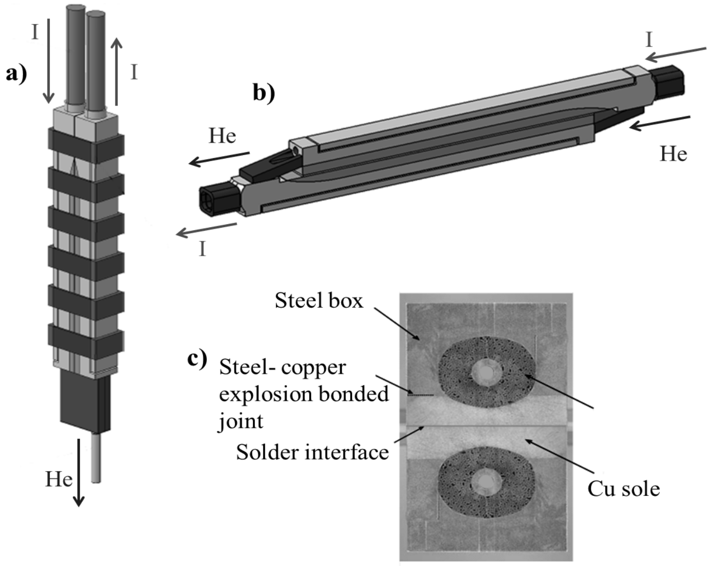

Figure 1.14: Lap-type joints: (a) praying hands configuration, (b) shaking hands configuration and (c) cross-section.

a stainless steel tube to preserve the shape of the conductor cross-section during compression. Lap-type joints exist in two configurations, praying hands and shaking hands, corresponding to the relative positions of the joined cables, as illustrated in Figures 1.14a and 1.14b respectively.

Butt joints, as in Figure 1.15a, are made by diffusion bonding of two cables, highly compacted in a copper sleeve and heat treated in a vacuum chamber under high contact pressure (∼25-30 MPa) and temperature (∼700-750 ^{o}C). The joining parts are cut square, polished, and aligned before joining. Void fractions as low as 5-8% are required to ensure a large contact area. To provide cooling for the cable and the joint interface, a conical flow distributor is inserted into the central spiral, while a steel spacer provides channels and holes to the outer diameter of the cable [18, 20].

To avoid the complex bonding procedure of the butt joints and the relatively large size of lap-type joints, a novel joint concept has been recently developed and patented by ENEA (Italy) [19], see Figure 1.15b. The design is based on the interpenetration of two CIC conductors, which allows joint dimensions only slightly larger than the original conductor. After jacket removal over a length of at least one cable pitch, all the last-but-one cabling stage bundles are pried apart and cut at different complementary lengths. One single cable is then re-constituted by matching the two trimmed conductors head-to-head and re-twisting them. A copper tube is pulled over the joint area and compacted in order to lower interstrand contact resistance and supply additional thermo-electrical stabilization. Finally, a new jacket is welded to the ends of the original ones.

The sintered joint design envisaged for the ITER Central Solenoid is a vari-

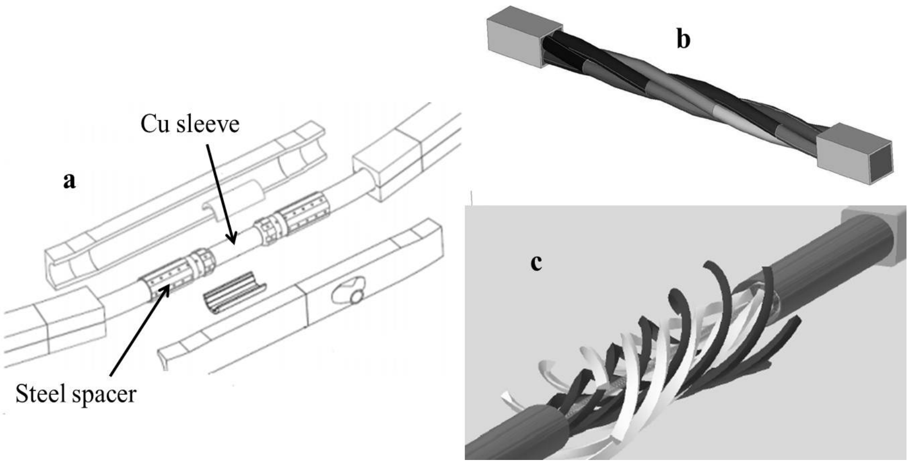

Figure 1.15: Other joints between CIC conductors: (a) butt joint [18], (b) ENEA joint [19] and (c) sintered joint [20].

ation of the ENEA concept [20]. In Figure 1.15c the so-called ’6x6’ configuration is shown where half of the sub-cables of the last-but-one stage are cut and reassembled so that the finished joint is not thicker than the original cable. In contrast to the butt joint initially considered for the ITER Central Solenoid, the sintered joint is less tightly compacted and features helium in the cable space and the central channel all the way through.

1.4 Stability of CIC conductors

To achieve the envisaged repetition rates of plasma cycles in ITER, and hence proper operation of the machine, it is important to build magnets with a well-proven stability margin. Loss of stability implies significant costs both in terms of operation time and money. Following a quench event re-cooling of the magnets down to their operation temperature is required, which causes the interruption of the experiment. In the worst case, quench may result in a damage of the conductor if the temperature of the hot spot and stress on the system are not properly restrained. Considering that the ITER magnet system cost amounts to more than 1 billion €(28% of the total machine cost) and that spare pieces may not be readily available, the occurrence of such events must be absolutely avoided.

Different phenomena can occur in superconducting cables and joints that limit their performance. Current unbalance among the strands originates in the natural spread in the contact resistances between strands and joints. When, as a result of the current non-uniformity, the current in a given strand exceeds the critical current determined by the local magnetic field and temperature, a transition to the normal state occurs. The successive evolution of one initial normal zone into a quench or into recovery of the conductor depends on the possibility for the saturated strand to expel excess current into the surrounding strands, thereby limiting ohmic heating and temperature rise.

The exposure to time-varying magnetic field induces currents in multi-strand cables, both within the individual strands and between them. The flow of coupling currents through the resistive parts of the strands and cable produces ohmic heating, and thus a temperature increase. Such loss can therefore potentially lead to a quench. Moreover, the addition of induced coupling currents can cause the strand total current to become higher than the critical current, leading to local normal zones in strands and eventually quench of the entire conductor.

Stability issues are even more critical in the joints due to the unavoidable ohmic heating in the joint resistance. Low-resistive joints allow a reduction of ohmic heating and, possibly, improved current uniformity by facilitating current sharing among strands. On the other hand, highly resistive barriers around strands and petals are required to limit eddy, inter-strand and inter-cable coupling currents in pulsed operation. As in most superconductivity applications, these two opposing requirements necessitate a carefully balanced design of strands, cables and joints.

1.5 Scope of the thesis

The objective of this thesis is to study, understand and optimize the performance of full-size CIC conductors and their joints under various working scenarios. Realistic cases from the operation of the ITER magnet system are used throughout the work. The ultimate goal is to control and warrant sufficient stability margin ($\Delta T = T_{cs} - T_{op}$) of conductors and joints anywhere inside the magnet system and under the most demanding operating conditions. The relevance of the analysis lies in the negative consequences of stability loss with respect to operation shutdown time and reparation cost.

Full-size short conductor sample and model coils tests are an essential part of the ITER magnet R&D program. Nevertheless, the assembly of samples and their test is time consuming and expensive, which makes it practically impossible to perform systematic studies on real conductors to cover all cases. Moreover, practical test conditions may differ significantly from real operating ones due to the limitations imposed by the experimental facility. Therefore, in order to assess the relevance of the specific test configuration as well as to systematically study and optimize the conductors under real operating conditions, numerical simulations are mandatory. The code JackPot-ACDC, featuring the description of CIC conductors with strand-level details, is used throughout this thesis to analyse the performance of cables and joints.

Figure 1.16 shows the general structure of the thesis.

- In chapter 2, an overview of existing models that describe Alternating Current losses and stability of CIC conductors and joints to a certain extent is presented. The new numerical code JackPot-ACDC is introduced and the main features of the pulsed, steady-state and joint models used in the analysis are described. A validation of the code is presented as well.

- In chapter 3 the steady-state stability of full-size NbTi short sample conductors and model coils is dealt with. Local in-cable power dissipation and current non-uniformity at quench are quantified and their relation is explored. The performance of ITER conductor samples with respect to their joint layout and test configuration is discussed.
- In chapter 4 the stability of CIC conductors in pulsed mode is analysed. The effect of the twist pitch sequence on the inter-strand coupling loss is investigated. The ratio between the successive pitches is identified as a key parameter in determining the loss. Following an identified flaw in the cable design, an alternative twist sequence is proposed for the ITER Central Solenoid conductor. The performance of various twist schemes proposed for the ITER CS are analysed under the most severe load case, a plasma scenario.
- In chapter 5 the stability of lap-type joints is discussed. The characteristic and critical behaviour of ITER Toroidal Field and Poloidal Field coil joints are investigated under different operating scenarios. A modification is proposed to reduce the excessive steady-state dissipation in Toroidal Field coil joints and for the large coupling currents in Poloidal Field coil joints.
- In chapter 6 general conclusions and recommendations are presented concerning the performance and limitations of CIC conductors and lap-type joints and their impact on the operational margin of the superconducting magnets in ITER.

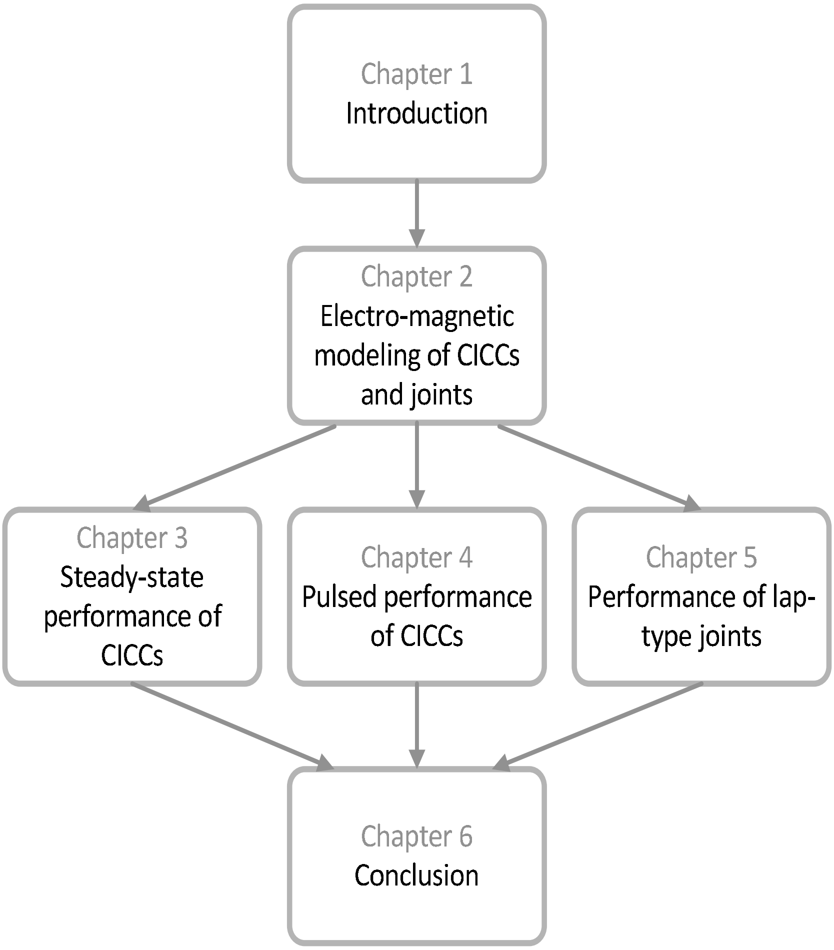

Figure 1.16: Outline of the thesis. The arrows show the main flow of information and the connections among the chapters.

Chapter 2

Electro-magnetic modelling of CIC conductors and their joints

Since the introduction of the Cable-In-Conduit Conductor concept, several analytical and numerical models have been developed to understand and optimize their electro-magnetic performance. However, current non-uniformity and coupling loss in CIC conductors strongly depend on the complex network of contacts resulting from the assembly of hundreds to about a thousand strands in multiple cabling stages. It follows that models detailing the cable down to the strand level are required to properly describe such phenomena, which imposes significant challenges due to the resulting size of the numerical problem to be solved.

In this chapter an overview of the existing analytical and numerical models for CIC conductors and lap-type joints is presented and their main limitations discussed.

The latest numerical network model JackPot-ACDC is described, which is so far the only available code capable to simulate meters of CIC conductors and full-size lap-type joints with strand-level detail. Apart from the axial strain state of Nb_3Sn *strands, no free parameters exist in the code. All the required information is derived directly from the trajectories of the strands or from measurements of specific cable internal properties. A benchmark study of the model against three test cases is presented.*

2.1 Introduction

Due to the high cost involved in testing of conductor samples and model coils, simulation is an essential tool for studying and improving the performance of ITER conductors.

CIC conductors consist of several hundreds of strands twisted and compacted in multiple cabling stages. The cabling procedure results in strands following entangled trajectories, and thus forming a complex network of electrical and thermal contacts. Therefore, a strand-level detail model is needed to address correctly phenomena such as transport current distribution and inter-strand coupling currents, which are determined by the paths of the strands within the conductor.

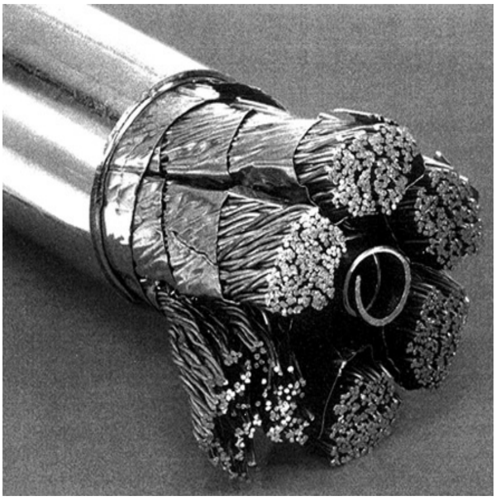

Figure 2.1: View of an ITER Toroidal Field prototype conductor showing the complexity of the internal network of strands [21].

In practice the proper description of CIC conductors is complicated by the short bending wave-length of the strands, requiring the definition of dense networks of nodes along the cables. Considering the high number of strands and the long unit lengths of conductor in coils and even in short samples, this results in a cumbersome system of equations. As a consequence, the numerical electro-magnetic (EM) modelling of CIC conductors is a time-consuming process, requiring significant computing resources.

Several, mainly analytical, models were developed in the past to study the stability of CIC conductors and joints. In an attempt to drastically reduce the complexity and size of the analysed system, often rather crude approximations were introduced that limited the interpretative and predictive potential severely.

Here, the existing electro-magnetic models are classified according to the specific operating scenario they attempt to address. While some models are specifically developed to describe the performance under steady-state (section 2.2) or varying magnetic field and current conditions (section 2.3); others can be applied to every operation mode (section 2.4). It is noticed that a relatively large amount of studies on stability issues in CIC conductors exists. On the contrary, only a few references were found on the electro-magnetic simulation of conductor joints.

The core of this chapter is concerned with the detailed description of the JackPot-ACDC model as well as its validation (section 2.5).

2.2 EM models for steady-state conditions

The simplest way to predict the steady-state performance of a CIC conductor consists in estimating its critical current from the one of a single strand at peak magnetic field. Such an approach implicitly assumes all strands to carry identical currents and subjected to the same magnetic field.

Already in [22] the limits of such assumptions were recognized. A first attempt to calculate strand trajectories within CIC conductors was undertaken allowing the definition of a varying magnetic field on the strands depending on their positions in the cable. An electrical network taking into account the uneven distribution of contact resistances within the joints as well as the inter-strand resistances was also used to describe current non-uniformity.

However, to achieve a realistic distribution, the strand positions were adjusted independently at every cable cross-section, which resulted in discontinuous trajectories. Moreover, the CIC conductor was represented through a limited number of macro-strands carrying uniform current.

Following this work, several other models were developed within the ITER R&D effort aiming at the prediction of the steady-state performance of the full-size short conductor samples tested in the SULTAN facility [23] starting with the measured strand properties. Table 2.1 shows a survey of the main features of each model.

In their original implementation these codes adopted several simplifications. A uniform current distribution was generally assumed and in all cases strands were supposed to be 'insulated', meaning that no current re-distribution is possible.
To achieve a better correspondence with experimental results, strand and petal overload factors were successively introduced in models [25, 26, 27], while current re-distribution was also added in [27] .

Despite the above improvements, the descriptive ability of the models of Table 2.1 was limited by several factors such as:

- Description of the joints was not included in the system;
- Current over-load was arbitrarily set to fit the experimental data;
- Basic cabling routine was used to calculate the trajectories of the strands;
- Strands were grouped in bundles to reduce the complexity and size of the problem;
- Insulated strands or a fixed value were assumed for the inter-strand contact resistance.

Table 2.1: Survey of the main features of numerical models for simulating the steady-state stability of SULTAN samples [24] (+ adopted aspect, - non-adopted aspect).

	Ref.[25]	**Ref.[26]**	**Ref.[27]**	**Ref.[28]**	**Ref.[29]**	**Ref.[30]**
Magnetic field (self+background)						
Vectorial sum	+	+	+	-	-	+
Approximate sum	-	-	-	+	+	-
$\boldsymbol{T_{He}}$						
Constant over length equal to $T_{measured}$	-	+	+	-	+	-
Variable over length (average in cable cross-section)	+	-	-	+	-	+
$\boldsymbol{T_{strand}}$						
Equal to T_{He} (not for stability)	-	-	+	-	-	-
From heat balance with He	+	+	-	+	+	+
Electric field						
Average in cable cross-section	-	+	-	-	+	+
Average along strand and in cross-section	+	-	+	+	-	-
$\boldsymbol{n}$**-value**						
Individual for each strand	+	+	+	+	+	-
$\boldsymbol{I_c}$ **anisotropy**	+	-	+	-	-	-
Stability						
Heat balance of strand at B_{peak}	-	+	+	+	+	-
Overall conductor stability	+	-	-	-	-	+

2.3 EM models for pulsed conditions

Three main mechanisms can be distinguished in superconducting cables that contribute to the overall loss under time-dependent current and magnetic field conditions.

Hysteresis loss is intrinsic to the superconducting filaments and is the main dissipation mechanism at low magnetic field sweep rates. It is caused by the movement of flux lines within the superconducting material due to changes in the magnetic field. Since flux lines enclose normal cores, a resistive loss occurs when they move. The resulting loss mechanism has a hysteretic behaviour because the energy dissipated depends only on the energy stored in the line tension of the flux lines.

Under time-dependent conditions, inter-filament currents are induced that commutate across the resistive matrix material to another filament, travel in the reverse direction and 'jump back' across the matrix, each time causing ohmic loss.

Inter-strand coupling occurs in cables in a similar way to inter-filament coupling in strands. When the inter-strand contact resistance is low enough, the induced currents may pass across the strand interfaces, causing dissipation. As the coupling increases with reducing void fraction, inter-strand currents are the dominant loss source in tightly compacted, high current carrying CIC conductors subjected to rapid magnetic field sweeps.

In lap-type joints, additional loss terms are present that depend on the joint orientation with respect to the direction of the changing magnetic field. Apart from eddy currents in the Cu sole, inter-cable coupling currents may arise linking the cables on the two sides of the joint.

Several analytical models have been developed, which allow reasonable predictions of the losses within single multi-filamentary strands for specific magnetic field variations. However, the determination of inter-strand coupling loss in CIC conductors and joints is a challenging problem due to their direct dependence on the cable geometry and to the variability of the inter-strand and strand-to-joint contact resistances. The main ideas are briefly sketched below. For hysteresis and intra-strand coupling losses the description in [13] is followed; for the inter-strand coupling loss the method in [31] is adopted instead.

2.3.1 Hysteresis loss

When exposed to a changing magnetic field, shielding currents of density $\pm J_c$ build up in the outer layer of superconducting filaments, which screen the interior from the changing magnetic field. Figure 2.2 illustrates the case for a round filament without transport current in a transverse magnetic field.

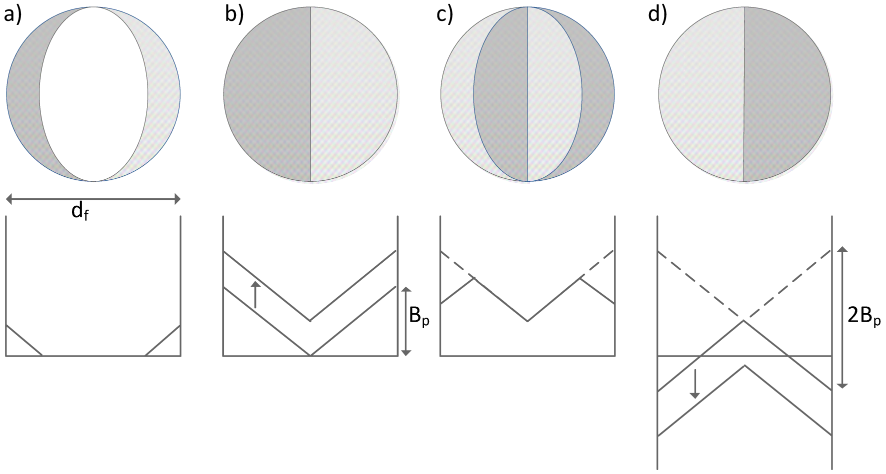

Figure 2.2: Current and magnetic field profiles in a superconducting filament (without transport current) in a transverse time-varying external magnetic field $B_{a,i}$. (a) $B_{a,a} < B_p$, (b) $B_{a,b} = B_p$ and larger, (c) $B_{a,b} - 2B_p < B_{a,c} < B_{a,b}$, (d) $B_{a,d}$=$B_{a,b} - 2B_p$ and smaller.

As the magnetic field increases, the boundary between the screening current region and the current-free region shifts towards the centre of the filament because the critical current density is limited. The full penetration of the filament with screening currents is reached at the so-called full-penetration magnetic field B_p, which for transverse magnetic field and cylindrical filaments can be expressed as

$$B_p = \frac{\mu_0\, J_c\, d_f}{\pi} \quad [\mathrm{T}], \tag{2.1}$$

with J_c the critical current density and d_f the filament diameter.
The magnetisation, defined as the magnetic moment per unit volume, produced by the screening currents caused by transverse and parallel magnetic fields is given by Eqs. 2.2 and 2.3, respectively

$$M = \frac{2}{3\pi} J_c\, d_f \quad [\mathrm{A{\cdot}m^{-3}}], \tag{2.2}$$

$$M = \frac{1}{6} J_c\, d_f \quad [\mathrm{A{\cdot}m^{-3}}]. \tag{2.3}$$

A typical magnetization loop is shown in Figure 2.3. The energy dissipation per cycle in a unit volume is equal to the area enclosed by the hysteresis loop, which may be written as

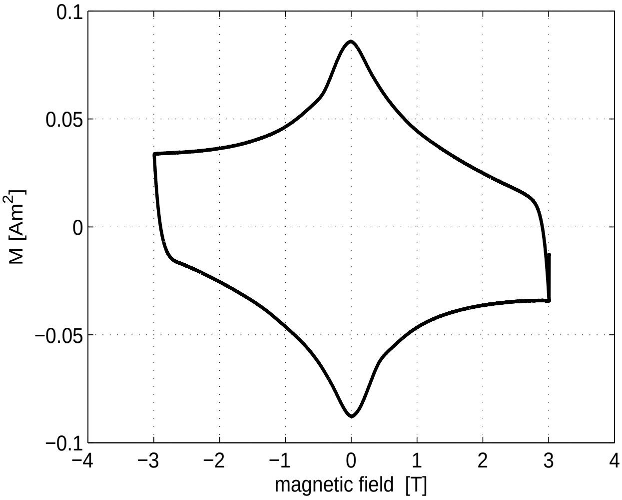

Figure 2.3: Magnetization loop of a Nb_3Sn OST-1 strand for the ITER Toroidal Field conductors at T = 4.2 K, B = 3 T and f = 10 mHz. Data courtesy of C. Zhou.

$$Q_{hyst} = \oint M dB \quad [\mathrm{J/m^3{\cdot}cycle}]. \tag{2.4}$$

The result can be equivalently expressed in terms of a power loss per unit volume

$$P_{hyst} = M\dot{B} = \frac{2}{3\pi} J_c\, d_f \left|\frac{dB}{dt}\right| \quad [\mathrm{W{\cdot}m^{-3}}]. \tag{2.5}$$

When the filaments carry a transport current I_t, as in operational cables, the magnetization is reduced. However, since the work done by the power supply to keep I_t constant adds to the work needed to generate the external magnetic field, the overall loss is increased by a factor $1 + [I_t/I_c]^2$

$$P_{hyst} = \frac{2}{3\pi} J_c\, d_f \cdot [1 + \frac{{I_t}^2}{{I_c}^2}] \cdot \left|\frac{dB}{dt}\right| \quad [\mathrm{W{\cdot}m^{-3}}]. \tag{2.6}$$

For closely packed filaments, proximity effects may exist in the strands due to Cooper pairs tunnelling through the normal barrier between adjacent filaments. In this case, an effective diameter d_{eff} corresponding to the size of the bundle of coupled filaments must be used in Eq. 2.6 instead of the pure filament diameter d_f.

2.3.2 Inter-filament coupling loss

Figure 2.4 shows a multi-filamentary wire subjected to a uniform external magnetic field B_e, changing with a rate $\dot{B}_e$. The arrows indicate the path followed by inter-filament coupling currents. Coupling currents flow along the filaments and cross over through the resistive matrix every half twist pitch. The matrix crossing currents follow a vertical path, parallel to the changing magnetic field. At each end of the wire, the currents cross over horizontally and return along the other side of the strand.

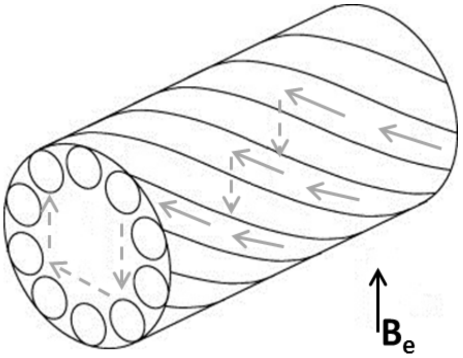

Figure 2.4: Twisted filamentary composite in a changing transverse magnetic field showing the path used to calculated the flux linkages.

The coupling currents thus give rise to an axial $cos\theta$-like current distribution around the wire, which generates a perfect dipole field in its interior. Therefore, a uniform internal magnetic field B_i is generated by the coupling currents

$$B_i = B_e - \dot{B}_i\, \tau \quad [\mathrm{T}], \tag{2.7}$$

where

$$\tau = \frac{\mu_0}{2\rho_t} (\frac{L}{2\pi})^2 \quad [\mathrm{s}], \tag{2.8}$$

with L the twist pitch and ρ_t the transverse inter-filamentary resistivity.

The constant of proportionality τ is called the time constant of the system and it represents the time needed by the coupling currents to decay after the external magnetic field has stopped changing. The power per unit volume dissipated by the induced currents is obtained integrating $J^2\,\rho$ along the current path, which results in

$$P = \frac{\dot{B_i}^2}{\rho_t}\left(\frac{L}{2\pi}\right)^2 = \frac{2\dot{B_i}^2}{\mu_0}\tau \quad [\mathrm{W{\cdot}m^{-3}}]. \tag{2.9}$$

The loss per cycle due to a sinusoidal magnetic field of amplitude B_a is given by

$$Q = \frac{B_a^2}{\mu_0}\frac{2\pi\,\omega\,\tau}{(1+\omega^2\tau^2)} \quad [\mathrm{J/m^3{\cdot}cycle}]. \tag{2.10}$$

The equations above have been derived for a wire with circular cross-section. In order to generalize the formulas, the coefficient 2 has to be replaced by the shape factor n of the wire (which is 2 for a circular strand). Detailed treatments of the inter-filament coupling loss for different cross-sectional shapes, types of magnetic field variation and frequencies can be found in [13, 32, 33, 34, 35, 36].

Apart from a factor related to the shape, the inter-filament coupling loss depends on a single parameter, the time constant τ, determined by the twist pitch and the effective transverse resistivity, which is a function of the filament-to-matrix contact resistance, effective matrix resistivity and cross-sectional layout of the filaments. The behaviour can be compared to the characteristic of an LR circuit by which the resistance is the transverse resistivity per unit length, the self-inductance is determined by the twist pitch and the driving voltage is caused by the changing magnetic field.

The coupling currents occupy a distinct volume at the outer radius of the strands called the 'saturation' region, where the filaments are forced to carry the critical current density. As coupling currents increase, the volume of the saturated region grows towards the centre of the wire. From a loss computation point of view, the change of position of the boundary can be generally ignored, but the extra loss due to the penetration of the flux through the saturated region should be added. In [37] this is approximated by the hysteresis loss of a solid wire having the strand diameter.

2.3.3 Inter-strand coupling loss

Inter-strand coupling loss is generally treated analogously to inter-filament coupling loss. Therefore, the expressions given in section 2.3.2 for the coupling loss in a strand, Eqs. 2.9 and 2.10, are also used for a cable but adopting an appropriate effective time constant τ_{eff}.

The method offers the advantage of enabling an easy treatment of any number of cabling stages theoretically. Consequently, this is the mostly used model for the calculation of inter-strand coupling loss in CIC conductors.

In multi-stage cables a high number of current loops, and hence time constants, exist. Therefore, the effective time constant of a CIC conductor can be defined as the sum over the N stages composing the cable of multiple time constants n_i, each corresponding to a subsequent cabling stage

$$n\tau_{eff} = \sum_{i=1}^{N} n_i \tau_i \quad [\mathrm{s}]. \tag{2.11}$$

Each $n_i\tau_i$ accounts for the increase of the loss at each new cabling stage i. The above formulation is based on the assumption that the coupling currents in a given stage do not interfere with the coupling currents of the other stages. Therefore, it implies that losses in each stage can be evaluated independently from the others. In practice the coupling between the various cabling stages cannot be neglected; however such a problem cannot be easily treated analytically.

In general for $i > 1$, it can be written

$$n_i\tau_i = \frac{\mu_0}{2\rho_i}\left(\frac{p_i^*}{2\pi}\right)^2 \frac{1}{1 - v_{i-1}} \quad [\mathrm{s}], \tag{2.12}$$

with p_i^*, ρ_i and v_i the effective twist pitch length, the effective resistivity and the average void fraction of cabling stage i. The effective twist pitch length p_i^* and resistivity ρ_i can be expressed respectively as

$$p_i^* = p_i - \frac{r_{i-1}}{R_{i-1}} p_{i-1} \quad [\mathrm{m}], \tag{2.13}$$

and

$$\rho_i = \frac{\rho_b\, e_b}{\epsilon_i\, R_{i-1}} \quad [\Omega\cdot\mathrm{m}], \tag{2.14}$$

where p_i, R_i, r_i and ϵ_i are the twist pitch length, the outer radius, the twist radius and the contact area ratio of cabling stage i. $\rho_b\, e_b$ is the resistivity-thickness product of the contact resistive barrier [31].

This model of inter-strand coupling loss presents several limitations. Although now an analytic expression exists for the time constant of CIC conductors, large uncertainties in the required parameters cause their estimates to be not very accurate. Therefore, it is preferred to measure and derive the time constant from the slope α of the initial linear section of the loss versus frequency curve

$$n\tau_{eff} = \alpha \frac{\mu_0}{2\pi^2 B_a^2} \quad [\mathrm{s}]. \tag{2.15}$$

If simple formulas involving a single time constant can be used to estimate the loss at low ramp rates of the applied magnetic field; more complex relations are required for higher frequencies or faster ramp rates. Moreover, the analysis of a conductor subjected to a magnetic field variation of any orientation (neither purely transverse nor parallel) and shape cannot be conveniently treated.

Although useful to understand the phenomenon, the predictive potential of the model is limited and the study of the precise influence of cabling patterns on the coupling currents and associated loss is therefore hardly possible.

2.3.4 Eddy and inter-cable coupling losses in lap-type joints

Design of joints between superconductors is commonly simplified to controlling the overall cable-to-cable resistance and arriving at a level below 1 nΩ. However, when connecting two large size CIC conductors the matter becomes far more complex. Variations in local heat dissipation within the joint and current sharing among the strands have to be controlled carefully to warrant sufficient temperature margin in the superconductor everywhere and make sure the joint does not become the performance limiting element of the magnet.

The problem has received much less attention from the modelling point of view than AC loss in cables. A model for the loss calculation in lap-type joints, the most common configuration developed for fusion magnets, is presented in [38] and applied to the ITER Poloidal Field coil joints. The proposed approach takes into account:

- inter-strand coupling loss in the CIC conductors and eddy current loss in the sole due to both axial and radial magnetic fields;
- inter-cable coupling loss due to the radial magnetic field;
- ohmic dissipation in the sole due to transport current.

The first three components of the joint loss are estimated using the time-constant formulation presented in section 2.3.3 for CIC conductors, but choosing appropriate values for the shape factor and current decay time for the joint layout. The ohmic heating is then added given by $W_{Joule} = R_{joint}\, I_{coil}^2$, where R_{joint} is the joint DC resistance and I_{coil} the coil current.

A more refined computation of the inter-cable loss is also described, where the coupling currents are obtained by solving the diffusion equation

$$\frac{\partial i}{\partial t} = -\frac{h}{\mu_0}\frac{dB_r}{dt} + L\,h\frac{R_{joint}}{d\,\mu_0}\frac{\partial^2 i}{\partial x^2} \quad [\mathrm{A{\cdot}s^{-1}}], \tag{2.16}$$

with i the loop current flowing in a cable at the coordinate x along the joint, h the effective joint width, L the joint length and d the distance between the cables axes in the joint. The diffusion equation is applied to the inter-cable current only, since the transport current is assumed to be equally shared among the main sub-cables (petals). As a consequence, the current density produced by the transport current crossing the joint plane can be considered uniform along the sole. By integrating over the joint length the product of joint resistance and sum of the transport and inter-cable current densities, a better estimation of the Joule and inter-cable losses is obtained.

2.4 Multi-purpose EM models

More recently the development of models that address both steady-state and pulsed performance of CIC conductors has received increasing attention. The adopted approach is typically numerical, allowing for the treatment of a wider number of cases than analytic methods that can be applied only to strongly simplified layouts. Given the discrete nature of the contacts among strands and with the joint parts, network models appear particularly suited to describe CIC conductors. The conductor is thus represented by an electric network, which is coupled to the changing magnetic field and obeying Kirchoff's laws.

The CUDI-CICC code developed at the University of Twente [39] is based on the numerical network model CUDI for Rutherford-type cables [40]. CUDI-CICC is able to simulate inter-strand coupling currents due to different scenarios of time-varying magnetic fields in cables of infinite and finite lengths carrying transport current. In the model the cable elements are represented by resistances and inductances in series. The series resistances represent conductor defects or current sharing from superconducting filaments to the stabiliser due to current saturation. Transverse resistances, whose values are correlated to experimentally obtained data, connect the cable elements and allow current re-distribution in the case of saturation. The magnetic field on the current carrying elements is the sum of the background and self- fields, as produced by both transport and coupling currents. The network model is flexible, enabling the simulation of conductors of different size and shape, twist pitch and strand properties. However, the main limitation is the maximum number of cable elements that can be handled in an acceptable CPU time and without exceeding the available computing resources. This results in a description of the CIC conductor limited to the last stage sub-cables, thus ignoring all details of lower stages.

The THELMA model, a joint effort between the Universities of Bologna, Udine and the Polytechnic of Torino, is a more sophisticated model specifically developed to describe the performance of CIC conductor samples and coils [41, 42, 43, 44]. It uses a distributed parameter circuit approach, where the values of resistances and conductances are based on contact areas computed from the trajectories of the strands and a resistivity parameter obtained from experimental data. Various geometries of joints and terminations can be modelled in THELMA, allowing to study the effect of current imbalance. The electro-magnetic code can also be coupled to a two-fluids (He flowing in the annular cable region and He flowing in the central channel) thermal-hydraulic routine. The thermal-hydraulic model computes the temperatures of strands, helium and jacket along the conductor consistently with the evolution and distribution of heat sources calculated by the electro-magnetic part of the code. The thermodynamic state of the Helium in each channel is described by its temperature, pressure and flow speed. Although it is able to handle a higher number of cable elements than CUDI-CICC, the main limitation of THELMA is again the maximum size of the problem that can be solved.

2.5 JackPot-ACDC

JackPot-ACDC is a numerical network model developed at the University of Twente for the analysis and optimization of CIC conductors and their joints.

The code was originally meant to study the jacket potential distribution (hence the name JackPot) of CIC conductors resulting from the steady-state tests of ITER full-size short conductor samples in the SULTAN facility (CRPP, Switzerland) [45]. This initial steady-state model was then extended with the inclusion of self- and mutual inductances as well as coupling with a changing background magnetic field, in order to cope with pulsed operation [46]. More recently, a lap-type joint module has been added, which, in combination with a geometrical model of the ITER magnet system and its magnetic field distribution, allows the study of the performance of ITER lap-type joints under relevant operating conditions [47, 48].

The key advantage of JackPot-ACDC over other models is that it can handle considerably larger systems thanks to the use of the Matlab [49] programming environment in combination with advanced computing techniques like the Multi-Level Fast Multiple Method (MLFMM). This makes of JackPot-ACDC the only available code at present enabling steady-state and pulsed analysis of up to tens of meters of ITER-like CIC conductors and full-size lap-type joints with strand-level details included.

Furthermore, the network model of the conductor can be conveniently coupled with joints, whether these are described through a Finite Element Model (FEM) or with the Partial Element Equivalent Circuit (PEEC) technique.

At present the main limitation of JackPot-ACDC, though faster and more advanced than other models mentioned before, still is the computing time, that increases significantly with the size of the analysed system and the refinement of the adopted discretization. As an example, the simulation of a 1 m long section of ITER Central Solenoid conductor with strand-level detail (total number of unknowns = 102816) during the initial phase of an ITER 15 MA plasma scenario (current ramp up in the coils and first 100 s of discharge) can take up to 30 hours of CPU time on a PC with 64 Gb of RAM, Intel(R) Core(TM) i7-3930K CPU @ 3.20 GHz and NVIDIA GeForce GTX 680 Graphic Processing Unit. The modelling of a full-size ITER Poloidal Field coil joint (including 0.3 m long conductor sections outside the copper sole) for an overall number of 472988 unknowns can require up to 5 days of CPU time in the case of rapid magnetic field variations and low joint resistance. However, the same problems would be impossible to solve with other existing codes since the computation of the full mutual inductance matrix would already require several hours, and likely result in exceeding the available memory capacity.

In the following sections the main features of JackPot-ACDC that are relevant for this thesis are described. In sections 2.5.1 and 2.5.2 the modelling of cables and joint are presented, respectively. In section 2.5.3 intra- and inter-petal resistances are described, as well as strand-to-joint resistances and the way the parameters are extracted from measured data. Section 2.5.4 deals with self- and mutual inductances, which are used in sections 2.5.5 and 2.5.6 to establish the coupling with a time-dependent magnetic field. The system of equations in the core of JackPot-ACDC is briefly discussed in section 2.5.7, while in sections 2.5.8 and 2.5.9 the strand scaling laws and jacket network model are described. In section 2.5.10 the thermal routine is reviewed. Finally, in section 2.5.11 the validation of the model with the aid of three ITER relevant test cases is demonstrated.

2.5.1 Cable model

The first step taken by the code is determining the trajectories of the strands, which are then used for quantifying various components of the electrical model.

Several efforts have been made in the past to simulate the complicated trajectories of strands in CIC conductors [22, 50]. The reshaping phase, in which the sub-cables are twisted and compacted into the next cabling stage, makes the modelling of the strand trajectories particularly difficult. To achieve a cable geometry similar to that of an ITER CIC conductor, the cabling routine of JackPot-ACDC uses a mapping function that changes the coordinates of the strands from a circular to a petal-like cross-section, which is part of the next cabling stage. The main steps of the reshaping function are illustrated in Figure 2.5

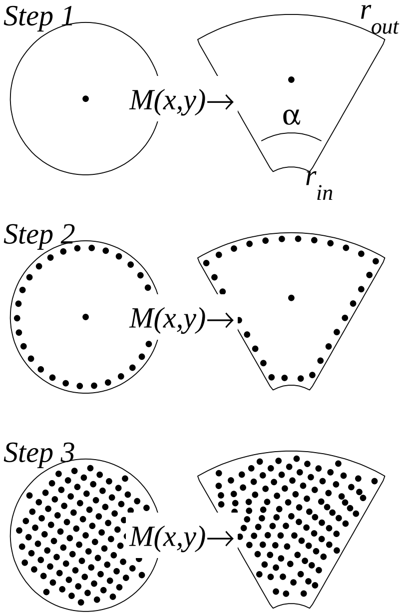

Figure 2.5: The three steps composing the reshaping of the sub-cables to compact them into the successive cabling stages [45].

First, the dimensions of the reshaped petal in terms of inner radius r_{in}, outer radius r_{out} and subtended angle α are determined. The angle α depends on the number of sub-cables that form the successive cabling stage. The inner radius accounts for the central helium channel in the last cabling stage or the eventual presence of copper cores. The outer radius is then determined from the imposed requirement that the cross-sectional area of the sub-cables must not change during the reshaping operation. In the successive steps, to ensure a homogeneous distribution in the next cabling stage, the strands are uniformly distributed along the periphery of the petal and then along straight lines connecting the barycentre with the periphery.

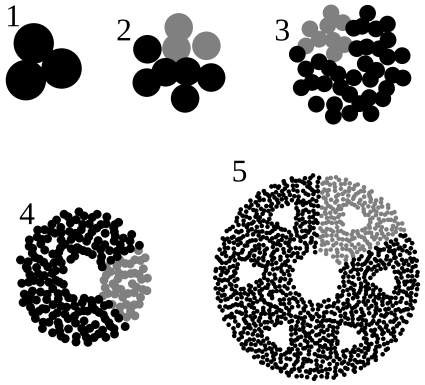

Figure 2.6: Cross-sectional view of the successive cabling stages for an ITER Toroidal Field conductor. In each stage, the grey strands represent a sub-cable shaped and defined in the previous step [45].

Figure 2.6 shows the cabling process for an ITER Toroidal Field cable. Three strands from the first cabling stage are twisted into a bundle. Next, three bundles are reshaped as explained in Figure 2.5 and twisted into a new sub-cable. The procedure is repeated for each stage following the principles of a cabling machine, until the final cable layout is reached.

The angle of each sub-cable is given by the sum of three contributions, namely:

- the angle due to the twisting of the strands, which depends only on the axial position along the cable and the twist pitch of the considered cabling stage;
- the angle due to the even distribution of N sub-cables over 360^o, where N is the number of sub-cables compacted in the considered cabling stage;
- a random angular offset.

As shown in Figure 2.7, the final geometrical model shows occasional overlap areas of the strands. In JackPot-ACDC this information is used to decide that strands are in contact and to calculate the inter-strand contact resistances.

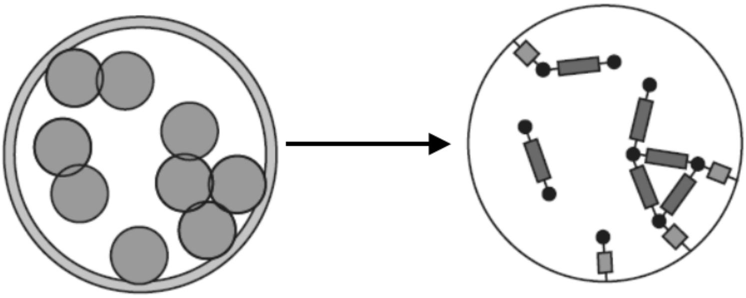

Figure 2.7: The cabling function of JackPot-ACDC produces overlap areas between strands, which are used in a successive phase to build the network of resistances.

2.5.2 Joint model

Different techniques are used in JackPot-ACDC to model cable-to-cable joints and cable-to-socket terminations depending on the analysed operating mode. A COMSOL finite element model [51] is used when focusing on the steady-state performance of the sample [52], see Figure 2.8. The approach allows fast and precise evaluation of the joint resistance even for complex geometries involving different materials. The dependence of the resistivity of constituent materials on parameters such as magnetic field and RRR can also be easily incorporated.

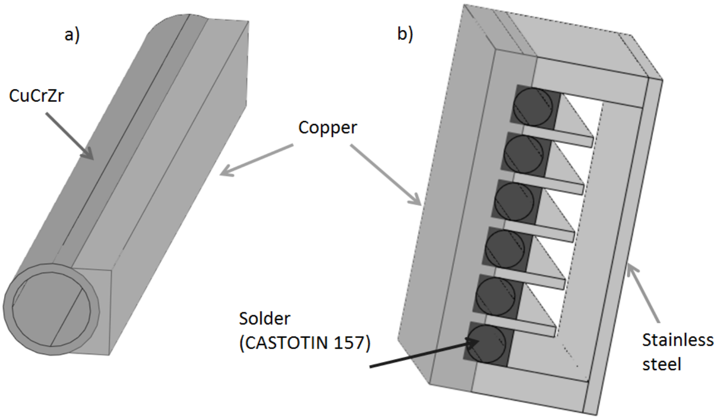

Figure 2.8: Finite element model of the (left) Poloidal Field Insert Sample [53] and (right) CNPF1 [54] bottom joints [52]. In the PFIS joint the conductor is swaged into a CuCrZr sleeve connected to the power supply/adjacent conductor through a copper saddle. The CNPF1 sample, instead, features a 'Combo-box' type of joint where the 6 sub-cables of the last stage are separately soldered to the copper block.

The main drawback of the finite element model method is the difficulty of including mutual inductances between strands and joint elements. Therefore, when ramped operation is concerned, the so-called PEEC technique is used [55]. This method is effective for rectilinear objects and is easy to implement. Figure 2.9a shows a 2D object modelled with the PEEC technique. The expansion to a 3D model is straightforward. An orthogonal grid of voltage nodes is created across the object, which are connected through resistors. Mutual inductive couplings can be evaluated analytically and take place only between parallel current paths, which saves a considerable amount of computation time and memory. In the spatial discretization of a copper sole, the nodes located in the cable area as well as the current paths to and from such nodes are removed from the model, as shown in Figure 2.9b.

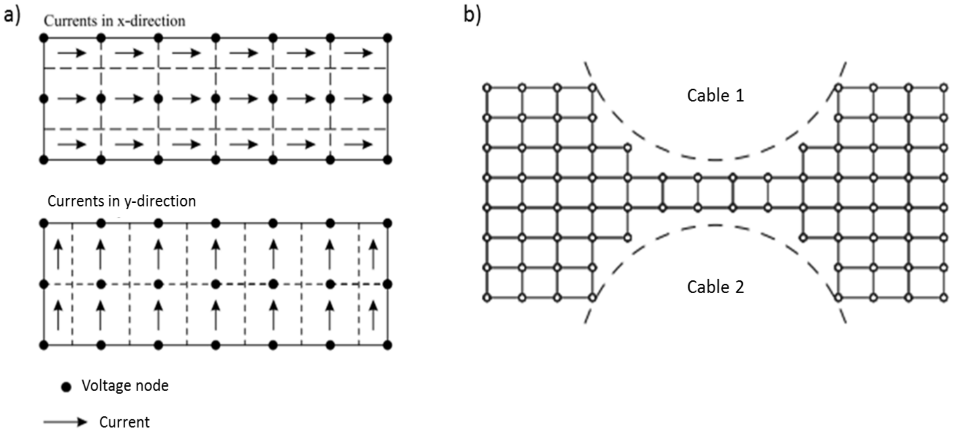

Figure 2.9: (Left) a 2D rectangular object modelled with the PEEC technique. (Right) The voltage nodes (circles) and current paths (straight lines) in the cross-section of the copper sole as represented through the PEEC method [48].

2.5.3 Resistances

JackPot-ACDC assigns values to the resistances based on the geometry of the physical contact area between couples of strands or strands and joint, as determined by the cabling routine. In general, the resistance is given by the ratio of a resistivity parameter ρ' expressed in $[\mu\Omega \cdot m^2]$, and a contact area A $[m^2]$.

$$R = \frac{\rho'}{A} \quad [\mu\Omega\ ]. \tag{2.17}$$

Inter-strand resistances

The inter-strand contact area is obtained from the computed trajectories of the strands according to the following procedure:

- the cable is divided into a number of sections along its axis. The length of each section dz is typically chosen to be smaller than the shortest twist pitch in order to minimise the probability of missing contacts between strands;

- at the end of each section, the distance d_{ss} between the couples of strands is calculated;
- the width w_{ss} of the contact is defined by

$$w_{ss} = d_{str} \cdot \sqrt{1 - min[1, (\frac{d_{ss}}{d_{str}})^2]}, \tag{2.18}$$

  where d_{str} is the strand diameter, see Figure 2.10;
- the contact area is obtained by multiplying the contact width w_{ss} by the distance dz between successive intersections.

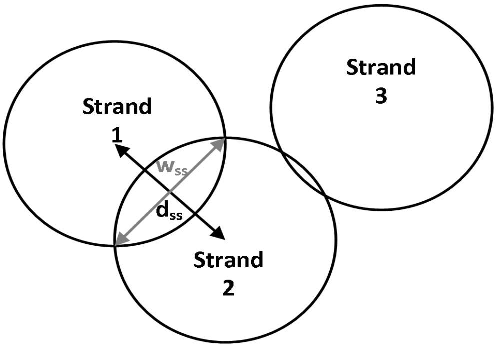

Figure 2.10: Schematic view of the inter-strand distance and width between strands for the evaluation of the contact area.

Eq. 2.18 not only ensures that strands are disconnected when their distance is larger than their diameter, but also that in the unlikely event that two strands completely intersect, the contact width, and hence the inter-strand resistance, still has a finite value.

The resistivity parameter ρ' of Eq. 2.17, instead, is obtained from experimental data as detailed below. If petal wraps are present, the resulting increase of inter-strand resistance can be represented by using different resistivity parameters for the inter and intra-petal contacts. Since wraps strongly hinder current transfer, their presence can also be accounted for as simply an absence of contact between strands located in different petals.

Strand-to-sole resistances

The resistance between strands and the copper sole of the joint is calculated similarly to the inter-strand contact resistance, as illustrated in Figure 2.11:

- since the radius of curvature of the cable circumference is much larger than the one of the strand, it is possible to approximate the outer edge of the cable locally as a flat plane;

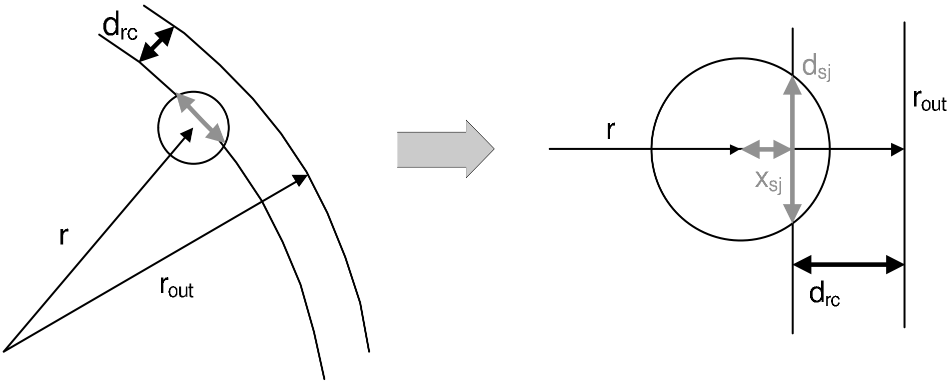

Figure 2.11: Schematic view of the strand-to-sole distance $r_{out} - d_{rc} - r$ and the contact width d_{sj} used for the evaluation of the contact area.

- the distance between the centre of the strand and the inner edge of the cable is then defined as $x_{sj} = r_{out} - d_{rc} - r$, where r_{out} and r are the outer radius of the cable and the radial position of the strand within the cable, respectively. The parameter d_{rc} allows to vary the inner radius of the cable inside the joint in order to adjust the number of strands in direct contact with the sole. The correction is important to reproduce the current non-uniformity caused by the joints and its physical justification lays in the compaction of the cable within the joint, causing a priori unknown reduction of the cable outer diameter. The value of d_{rc} is determined by counting the actual number of contacts in both the simulation and in a photograph of the cross-section of the real conductor, and adjusting the parameter to match the results;
- the contact width d_{sj} is then given by $d_{sj} = 2 \cdot \sqrt{(\frac{d_{str}}{2})^2 - x_{sj}^2}$, where d_{str} is the strand diameter;
- the contact area is obtained multiplying the contact width d_{sj} by the distance between successive axial subdivisions dz.

In practice, the expression of x_{sj} needs to be corrected according to Eq. 2.19 to avoid errors in the case of no $(r - d_{rc} < r_{out})$ or full $(r > r_{out} - d_{rc})$ strand-sole contact

$$x_{sj} = min(\frac{d_{str}}{2}, max(0, r_{out} - d_{rc} - r)) \quad [\mathrm{m}]. \tag{2.19}$$

As for the inter-strand contact, an experimentally derived resistivity parameter is required to get the final strand-to-sole resistance.

To improve the contact between the cable and the sole, solder can be added to the joints either by adding solder at the cable edges or by a complete filling of all cable voids. Several soldering methods exist that result in solder layers with different, and difficult to estimate, thickness. In the model the presence of solder is accounted for by multiplying the diameter of the strands within the solder layer by a factor k, arbitrarily set to 1.5. In such a way the strands are more likely to contact with other strands and the width of the contact becomes larger. Both effects make current re-distribution among the strands easier.

As the resistivity parameter, the solder penetration depth is also obtained from experimental measurements. The solder layer can be homogeneously distributed around the perimeter of the cable as well as limited to a defined angular range.

Joint element resistance

When using a finite element model of the joint, the values of the resistances between joint elements and between joint elements and the current source can be directly calculated with COMSOL by applying a reference DC voltage at the joint-source connection plate and a current flow through the inner surface of the joint.

In the PEEC model the value of the resistors connecting couples of voltage nodes is determined by the length and the cross section of the current path between two voltage nodes.

Determination of the resistivity parameters

The values of the resistivity parameters required to define the inter-strand and strand-to-sole resistances as well as the thickness of an eventual solder layer are derived from experimental data.

In the Twente Press Experiment for testing full-size ITER CIC conductors [56] the inter-strand resistances are measured at cryogenic temperatures. Since the strands are in the superconducting state, all nodes within a strand are at the same potential. Therefore the contact resistances between a couple of strands are in parallel with each other. A couple of strands is chosen and fed with a known current, while all the other strands are left disconnected. From the measured voltage drop across the two strands, the effective value of the inter-strand resistance is obtained. The measurement is typically performed with couples of strands selected in different sub-cables, to get a complete mapping of the inter-strand resistance values.

The conductor sample in the Twente Press Experiment is then simulated with JackPot-ACDC and the value of the inter-strand resistivity parameter is obtained from the best fit to the experimentally observed distribution of effective inter-strand resistances. Figure 2.12 shows the measured and fitted inter-strand resistance distributions for virgin conditions of two ITER Toroidal Field conductor samples [57]. The values of the fitted intra-petal ρ_{ss} and inter-petal ρ_{ip} resistivity parameters are reported in the insets.

The experimentally measured inter-strand resistance values span a relatively large interval of more than two decades (see Figure 2.12). This is related to the choice of the couples of strands, which are selected both inside the same petal

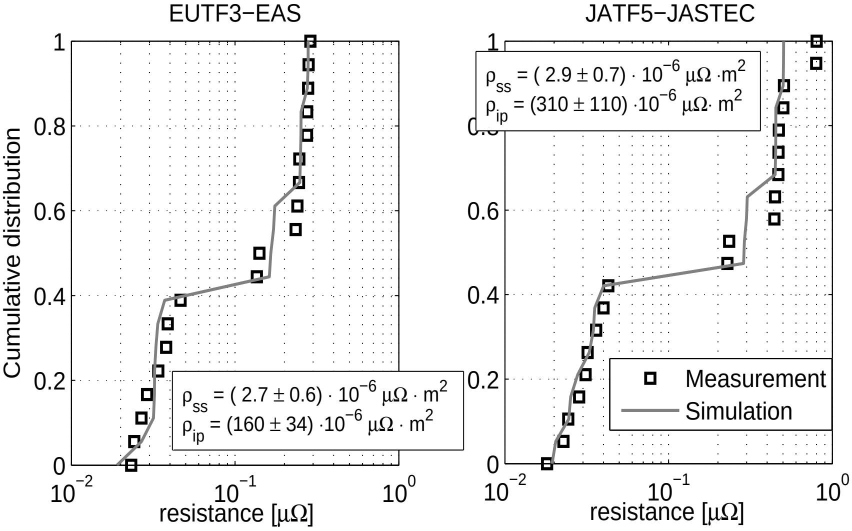

Figure 2.12: Measured and simulated cumulative distribution of the inter-strand resistances of the EUTF3-EAS (left) and JATF5-JASTEC (right) samples in virgin condition. The insets report the values of the intra-petal and inter-petal resistivities as obtained from the fit with JackPot-ACDC.

and in different petals. Since a wrap is present around the last stage sub-cables, a two-parameter fit accounting for the different magnitudes of the intra-petal and inter-petal resistances has been adopted.

The error on the measured inter-strand resistance distribution is very small and not relevant for the analysis of the results. However, an error bar can be defined for the intra-petal and inter-petal resistivity parameters based on the scatter in the intra-petal and inter-petal resistance measurements resulting from the selected combinations of contacts. Therefore, the errors reported in the insets of Figure 2.12 are obtained assuming the same relative standard deviation for the resistivity parameters and the corresponding intra-petal or inter-petal resistance distribution.

Analogously, fitting measured inter-strand resistance values from joint sections, the values of both inter-strand and strand-to-sole resistivity parameters and of the thickness of the eventual solder layer can be determined.

When no inter-strand resistance measurements are available, the value of the resistivity parameters can also be estimated from the measured AC losses. In an AC loss experiment, a section of conductor is exposed to a uniform sinusoidally varying magnetic field. A DC magnetic field larger than the filament penetration field may be added to evaluate the effect on the hysteresis loss; while generally no transport current is applied. The time-varying magnetic field induces coupling currents between the strands, which result in ohmic dissipation in the inter-strand contacts. The variation of the loss with frequency of the applied magnetic field is mapped, from which the value of the coupling loss time constant can be estimated. The experiment can then be simulated with JackPot-ACDC to obtain the inter-strand resistivity parameter. Figure 2.13 shows the measured and simulated coupling loss for a conductor sample for the ITER Central Solenoid [58]. The loss measurements were carried out at the SULTAN facility before and after the cyclic application of electro-magnetic load to the conductor.

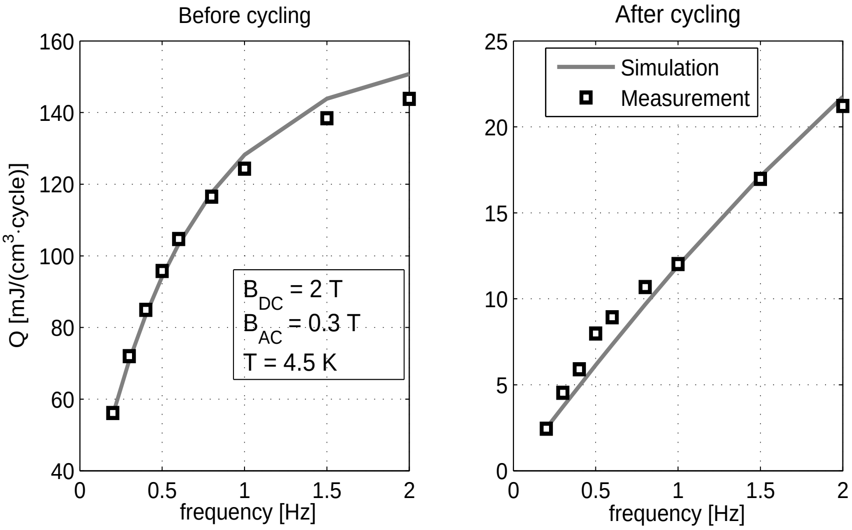

Figure 2.13: Measured [59] and simulated coupling loss density per cycle versus frequency for the the ITER Central Solenoid Baseline conductor design (see chapter 4) before and after electro-magnetic cycling.

For the fit, a conductor section of length 0.39 m is simulated, corresponding to the length covered by the AC coils in the experiment. A sinusoidal magnetic field of amplitude 0.3 T is applied with frequencies in the range 0.2 to 2 Hz in a 2 T background magnetic field. The hysteresis loss, estimated at 8 mJ/cm^3 for the conductor of Figure 2.13, is subtracted from the measured total loss in order to compare only the coupling loss contributions.

2.5.4 Self- and mutual inductances

Given two circuits c_i and c_j carrying time varying currents, the induced flux can be written as

$$\Phi_j = M_{ij} \cdot i_i = \int_{S_j} \vec{B}_i \cdot \vec{n} dS \quad [\mathrm{T}], \tag{2.20}$$

where S_j is a generic surface with border the circuit c_j and B_i is the magnetic field generated by circuit c_i.
Defining a magnetic vector potential $\vec{A}$, the magnetic field $\vec{B}$ can be written as

$$\vec{B} = \vec{\nabla} \times \vec{A} \quad [\mathrm{T}]. \tag{2.21}$$

Substituting in the flux expression and using Stokes'theorem, Eq. 2.20 becomes

$$\Phi_j = \int_{S_j} (\vec{\nabla} \times \vec{A}) \cdot \vec{n} dS = \oint_{c_j} \vec{A} \cdot d\vec{L_j} \quad [\mathrm{T}]. \tag{2.22}$$

The expression of the magnetic field in terms of vector potential can also be substituted in the fourth Maxwell's equations (in the electrostatic limit)

$$\vec{\nabla} \times \vec{B} = \mu_0 \vec{J} \rightarrow \vec{\nabla} \times (\vec{\nabla} \times \vec{A}) = \mu_0 \vec{J} = \vec{\nabla}(\vec{\nabla} \cdot \vec{A}) - \nabla^2 \vec{A}. \tag{2.23}$$

It is always possible to find a new vector potential $\vec{A'} = \vec{A} + \vec{\nabla} f$, with f scalar potential, which still satisfies Eq. 2.21. Therefore it is possible to choose the vector potential such that $\vec{\nabla} \cdot \vec{A} = 0$ (Coulomb gauge). In Coulomb gauge the fourth Maxwell's equation becomes

$$\nabla^2 \vec{A} = -\mu_0 \vec{J}. \tag{2.24}$$

The solution of this Poisson's equation is

$$\vec{A} = \frac{\mu_0 i_j}{4\pi} \oint_{c_i} \frac{d\vec{L_j}}{|\vec{r_{i,j}}|} \quad [\mathrm{V{\cdot}s/m}], \tag{2.25}$$

with $|\vec{r_{ij}}|$ the distance between a point x_j on the source line L_j and x_i target point, and i_j the current in the L_j line.
Substituting Eq. 2.25 back in Eq. 2.22 for the flux leads to

$$\Phi_j = \frac{\mu_0 i_j}{4\pi} \oint_{c_i} \oint_{c_j} \frac{d\vec{L_i} \cdot d\vec{L_j}}{|\vec{r_{i,j}}|} \quad [\mathrm{T}]. \tag{2.26}$$

With Eq. 2.26 the mutual inductance becomes

$$M_{ij} = \frac{\mu_0}{4\pi} \oint_{c_i} \oint_{c_j} \frac{d\vec{L_i} \cdot d\vec{L_j}}{|\vec{r_{i,j}}|} \quad [\mathrm{H}]. \tag{2.27}$$

The mutual inductance can thus be re-written in terms of a current-normalized vector potential $\vec{A'_{ij}} = \vec{A_{ij}}/i_j$ as

$$M_{ij} = \oint_{c_i} \vec{A'_{ij}} \cdot d\vec{L_i} \quad [\mathrm{H}], \tag{2.28}$$

where

$$\vec{A'_{ij}} = \frac{\mu_0}{4\pi} \oint_{c_j} \frac{d\vec{L_j}}{|\vec{r_{ij}}|} \quad [\mathrm{V{\cdot}s/(A{\cdot}m)}]. \tag{2.29}$$

Since the inter-strand current density is much lower than the one in the strands and, moreover, its path length is shorter, the coupling with inter-strand currents is not taken into account in JackPot-ACDC. Taking this into consideration, the

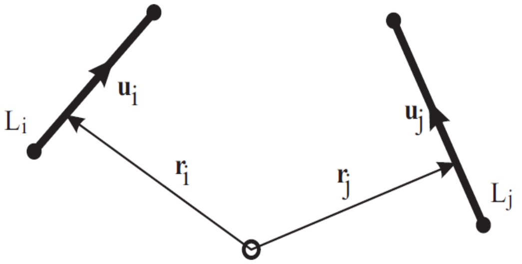

Figure 2.14: Configuration for the calculation of the mutual inductances between current carrying elements $\vec{L_i}$ and $\vec{L_j}$ [47].

integration paths in the previous integrals reduce to the length of the strand segments described earlier.

Equation 2.29 can be evaluated analytically as described in appendix 6.4. Therefore, the mutual coupling between lines i and j, see Figure 2.14, involves only one integration, which is solved numerically with Gaussian quadrature.

If the two line elements are far enough from each other, i.e. the ratio between their distance and their length is large, Eq. 2.28 can be approximated as

$$M_{ij} \approx \vec{A'_{ij}}(\vec{r_j} - \vec{r_{i,c}}) \cdot \vec{L_i} \quad [\mathrm{H}], \tag{2.30}$$

where the vector $\vec{r_{i,c}}$ points to the centre of line element i. This way also the remaining integral is eliminated.

For even larger distances between the lines, Eq. 2.29 may also be simplified to

$$\vec{A'_{ij}}(\vec{r_{j,c}} - \vec{r_{i,c}}) = \frac{\mu_0}{4\pi} \frac{\vec{L_j}}{|\vec{r_{j,c}} - \vec{r_{i,c}}|} \quad [\mathrm{V{\cdot}s/(A{\cdot}m)}], \tag{2.31}$$

with $\vec{r_{j,c}}$ pointing to the centre of line element j.

JackPot-ACDC makes use of both simplifications; the full expressions Eqs. 2.28 and 2.29 for strand sections that are in close proximity (i.e. strands located in the same box or in adjacent boxes in the spatial grid used for the system subdivision); and approximations of Eqs. 2.30 and 2.31 for strands at a larger distance.

The self-inductances of the strand segments are calculated following [60], which yields

$$L = 0.2 \cdot l \cdot [\ln(\frac{l}{GMD} + \sqrt{1 + \frac{l^2}{GMD^2}}) - \sqrt{1 + \frac{GMD^2}{l^2}} + \frac{GMD}{l}] \quad [\mathrm{H}], \tag{2.32}$$

where l is the length of the strand segment and GMD the Geometric Mean Distance of the filaments, corresponding to the radius of the filament bundle. In Eq. 2.32, the coefficient 0.2 has the unit of $[\frac{H}{m}]$.

Following a procedure similar to the one illustrated for the mutual couplings between the strands, the inductances for the PEEC model can be derived. However, the line integration is now substituted by the integration over the volume of the elements. In the PEEC model of the joint box, mutual inductive coupling takes place only between parallel current paths. Given two rectilinear blocks i and j carrying parallel currents as in Figure 2.15, their mutual inductance is calculated as

$$M_{ij} = \frac{\mu_0 \vec{u_i} \cdot \vec{u_j}}{4\pi S_i S_j} \int_{V_i} \int_{V_j} \frac{1}{|\vec{r_i} - \vec{r_j}|} dV_i dV_j \quad [\mathrm{H}], \tag{2.33}$$

where V_i and V_j are the volumes of the blocks, $\vec{r_i}$ and $\vec{r_j}$ the vectors pointing to locations inside the blocks, $\vec{u_i}$ and $\vec{u_j}$ unit vectors pointing in the direction of the current flow, and S_i and S_j the areas perpendicular to this current flow. Also Eq. 2.33 can be rewritten in terms of a current-normalized vector potential

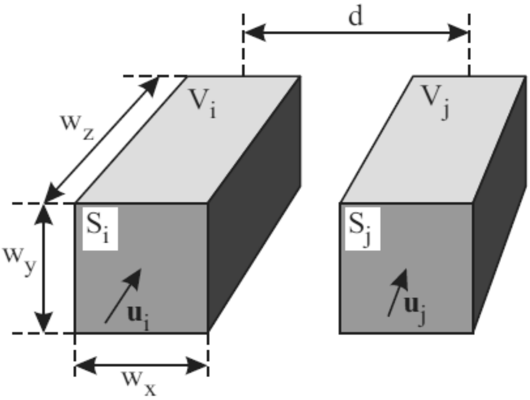

Figure 2.15: Configuration for the calculation of the mutual inductances between current joint box elements [48].

$$M_{ij} = \frac{1}{S_i} \int_{V_i} \vec{A'_{ij}} \cdot \vec{u_i} dV_i \quad [\mathrm{H}], \tag{2.34}$$

with

$$\vec{A'_{ij}} = \frac{\mu_0}{4\pi S_j} \int_{V_j} \frac{\vec{u_j}}{\vec{r_{ij}}} dV_j \quad [\mathrm{V{\cdot}s/(A{\cdot}m)}]. \tag{2.35}$$

As for the mutual couplings between the strands, Eq. 2.35 can be solved analytically [61], reducing the number of volume integrals to one. The solution of this integral can be found numerically by using, for instance, a Gaussian quadrature or the Simpson rule in three dimensions. Eqs. 2.34 and 2.35 can also be used to calculate the self-inductance of a block, since the analytical solution of $\vec{A_{ij}}$ does not contain singularities.

Although the calculation of the mutual inductance is already reduced to one volume integral, the PEEC approach still requires the inclusion of a large number of couplings. To save computation time, some simplifications can be made if the distance between blocks is large enough (i.e. strands located further than one box in the spatial grid used for the system subdivision). For instance, Eq. 2.34 can be reduce to

$$M_{ij} = \frac{V_i}{S_i} \vec{u_i} \cdot \vec{A'_{ij}}(\vec{r_{i,c}}, \vec{r_j}) \quad [\mathrm{H}], \tag{2.36}$$

where $\vec{r_{i,c}}$ is the position of the centre of volume i.
For blocks separated even further, equation 2.35 can be approximated by

$$\vec{A'_{ij}}(\vec{r_{i,c}}, \vec{r_j}) \approx \frac{\mu_0}{4\pi S_j} \frac{V_j \vec{u_j}}{|\vec{r_i} - \vec{r_j}|} \quad [\mathrm{V} \cdot \mathrm{s} \ /(\mathrm{A} \cdot \mathrm{m})]. \tag{2.37}$$

JackPot-ACDC uses Eq. 2.34 for the calculation of the self-inductances and Eqs. 2.36 and 2.37 for the mutual inductances between the PEEC blocks.

The main problem encountered when dealing with the inductance calculation in CIC conductors and joints is the computation time. If N is the number of strand sections in the cable, the total time required to calculate all mutual inductances scales as $O(N^2)$.

The calculation can be made significantly faster by using Graphics Processing Units (GPUs) that allow parallel computation. However, a far greater improvement is achieved by adopting the Multi-Level Fast Multipole Method (MLFMM) [62, 63]. MLFMM is normally used to calculate the electric potential of a configuration of point charges, but it can be expanded to line sources, as accomplished in JackPot-ACDC. Instead of calculating the elements of a matrix, it computes the interactions between the elements directly. Thus, in the model, it returns a vector with coupling voltages at the strand and joint element locations.

The method distinguishes between interactions of elements that are close to each other (near-field interactions) and elements that are farther away (far-field interactions). The near field interactions are evaluated directly, whereas the far-field interactions are evaluated by making use of series expansions.

Sources in the far-field interaction list can be grouped and re-used for other target locations, which effectively fastens the calculations. Since there are many more far-field interactions than near-field interactions, the overall gain in computation speed can be considerable.

Since the line sources in JackPot-ACDC (currents) generate a vector field, for the evaluation of the mutual inductances the three components of the magnetic field need to be evaluated separately. For the far-field interactions, Eqs. 2.30 and 2.31 for the strands and Eqs. 2.36 and 2.37 for the joint elements are used.

Eqs. 2.31 and 2.37 can be implemented directly in MLFMM, provided that the distance between the elements is large enough. This is controlled by the number of levels in the MLFMM grid. Since the direct interaction between particles inside one box, and in adjacent boxes, still has an $O(N^2)$ complexity, it would be advantageous to make the grid fine enough so that each box contains only one particle. However, this would place the strand sections too close to each other for allowing the approximation of Eqs. 2.31 and 2.37. To solve this problem, JackPot-ACDC makes use of the ability of GPUs to perform the calculation of a large number of direct interactions in parallel. This allows the boxes to be larger, such that they contain several hundreds of elements, while in addition creating the required distance between boxes in the far-field list. The distances between the strands required for the implementation of MLFMM and the consequent computational speed gain are quantified in [47].

2.5.5 Coupling with magnetic field

Two main configurations of time-varying external magnetic fields are considered throughout this thesis:

- a solenoidally varying magnetic field, as applied in AC loss experiments;
- the time and space dependent ITER magnetic field, used to evaluate the performance of conductors and joints in the magnet windings during operating plasma scenarios.

Coupling with a solenoidal magnetic field

In order to determine the coupling with a solenoidal magnetic field, the magnetic field is expressed in terms of magnetic vector potential (Eq. 2.21). Assuming the magnetic field to be directed along the $-y$ direction, it can be written as

$$B_y = \partial_x A_z - \partial_z A_x \quad [\mathrm{T}]. \tag{2.38}$$

Since the vector potential is not unique, it can be chosen such that A_x is the only non-zero component and may be re-written separating the variables, i.e. as the product of two terms: one depending on the magnetic field amplitude and one on the position

$$\vec{A} = A_x \vec{u_x} = -B_y z \vec{u_x} = f(B) f(\vec{r}) = |B| \vec{A'} \quad [\mathrm{V{\cdot}s/m}], \tag{2.39}$$

where $\vec{A'}$ is the vector potential normalized to the magnetic field magnitude.
The voltage drop induced by the changing external magnetic field is given by Faraday's law

$$\epsilon = -\frac{\partial \Phi}{\partial t} \quad [\mathrm{V}]. \tag{2.40}$$

As shown in the previous section, the magnetic flux can be formulated in terms of the magnetic vector potential

$$\Phi = \oint_{L_j} \vec{A} \cdot \vec{L_j} \quad [\mathrm{T}]. \tag{2.41}$$

Combining Eqs. 2.40 and 2.41 and considering that $f(B)$ does not depend on the position while $f(\vec{r})$ does not vary with time, the induced voltage becomes

$$\epsilon = -\oint_{L_j} \vec{A} \cdot \vec{L_j} = -(\oint_{L_j} \vec{A'} \cdot \vec{L_j}) \frac{d|B|}{dt} \quad [\mathrm{V}]. \tag{2.42}$$

The term between the brackets is the coupling coefficient with the time-varying external magnetic field and depends on the vector potential, normalised to the magnetic field magnitude. From Eq. 2.39, it is clear that the magnetic vector potential (and thus also the coupling coefficient) is a function of the axial coordinate z. However, given a certain area, the change in flux produced by the time varying magnetic field must be the same, wherever the area is located in space, because the magnetic field is assumed uniform (solenoidal magnetic field). Since this conditions holds only for closed paths, it follows that unlike the mutual inductances, the coupling of a time-varying external magnetic field with the inter-strand currents cannot be neglected.

Coupling with the ITER magnetic field

JackPot-ACDC computes the coupling of strands and joints inside the ITER magnet windings taking into account the magnetic field generated by the Central Solenoid, the Poloidal Field coils and the plasma. Coupling with the Toroidal Field coils is nil during plasma scenarios, since they are constant current magnets. The field of the Correction Coils is small and can thus be neglected.

For the coupling calculation, the Central Solenoid, the Poloidal Field coils and the plasma are approximated as planar current lines. Substituting Eq. 2.26 in Eq. 2.40, the voltage induced in the strand segment l by variations of the current i in the loop L is

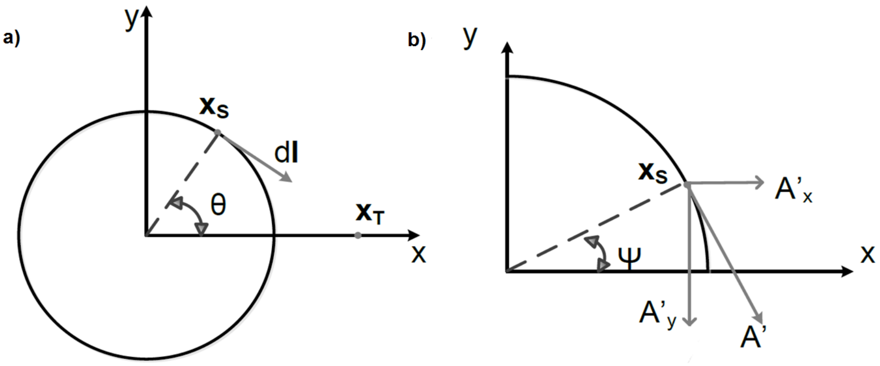

Figure 2.16: (Left) Configuration for the calculation of the current-normalized vector potential on a target point $\vec{x_T}$ on the x-axis. (Right) Decomposition on a generic point.

$$|\epsilon| = \frac{\mu_0}{4\pi}\frac{\partial i}{\partial t}\oint_L \int_l \frac{d\vec{L}\cdot d\vec{l}}{|\vec{r_{Ll}}|} \quad [\mathrm{V}]. \tag{2.43}$$

Using the current-normalized vector potential $\vec{A'}$ of Eq. 2.29, this can be rewritten as

$$|\epsilon| = \frac{\partial i}{\partial t}\int_l \vec{A'}\cdot d\vec{l} \quad [\mathrm{V}]. \tag{2.44}$$

In order to calculate the current-normalized vector potential in the configuration of Figure 2.16a, let us consider the point $\vec{x_S} = (r_S cos\theta, r_S \sin\theta, h_S)$ of the current source, where the current is oriented along the direction $d\vec{I} = (sin\theta, -cos\theta, 0)$. For simplicity, the vector potential can be initially evaluated at the point $\vec{x_T} = (r_T, 0, h_T)$ located on the x-axis of the system of reference. Therefore, the distance between source and target $\vec{r} = (r_T - r_S cos\theta, -r_S sin\theta, h_T - h_S)$ is

$$|\vec{r}| = \sqrt{r_S^2 + x_T^2 - 2\, r_T\, r_S cos\theta + (h_T - h_S)^2} \quad \text{[m]}. \tag{2.45}$$

It can be verified that in this configuration $\vec{A'}$ is directed along the y-axis

$$A'_y = -\frac{\mu_0}{4\pi}\int_0^{2\pi} \frac{r_S cos\theta}{|\vec{r}|} d\theta \quad \text{[V·s/(A·m)]}. \tag{2.46}$$

The components of the current-normalized vector potential in a generic point $\vec{x}$, see Figure 2.16b, can then be obtained by decomposing the vector found at $\vec{x_T}$ as follows

$$\vec{A'} = \begin{cases} A'_x = |\vec{A'}_{\vec{x_T}}| sin\psi \\ \\ A'_y = -|\vec{A'}_{\vec{x_T}}| cos\psi \quad \text{[V·s/(A·m)]}. \\ \\ A'_z = 0 \end{cases} \tag{2.47}$$

2.5.6 Magnetic field calculation

JackPot-ACDC calculates the magnetic field as the sum of the background magnetic field and the self-field of the conductor sample.

Background magnetic field

The background magnetic field experienced by a conductor sample in a test facility can be expressed in terms of an analytic function or as a set of data points describing its spatial variation. As an example, Figure 2.17 shows the axial magnetic field profile in the SULTAN facility.

A model of the ITER Poloidal Field coil, Central Solenoid and plasma system is implemented in JackPot-ACDC, where the Poloidal Field and Central Solenoid coils and the plasma are represented by their current centre lines. For the plasma, this corresponds to the average current position during a plasma scenario. A schematic view of the model can be found in Figure 2.18a.

The same procedure described for the calculation of the coupling coefficients with the time-varying magnetic field is followed for mapping the ITER magnetic field. The field is first evaluated on a target point $\vec{x_T}$ located on the x-axis

$$B_x = B_r = -\frac{\mu_0 i}{4\pi}\int_0^{2\pi} \frac{(h_T - h_S) r_S cos\theta}{|\vec{r}|^3} d\theta \quad \text{[T]}, \tag{2.48}$$

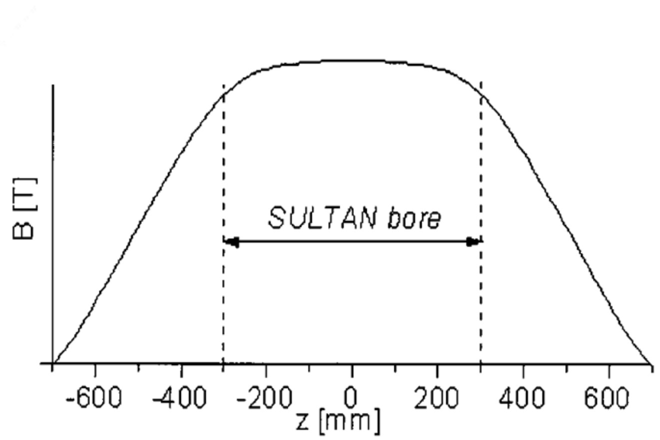

Figure 2.17: Magnetic field profile along the SULTAN facility. Courtesy of P.Bruzzone.

$$B_z = -\frac{\mu_0 i}{4\pi}\int_0^{2\pi}\frac{(h_T - h_S) r_S sin\theta}{|\vec{r}|^3} d\theta \quad [\mathrm{T}], \tag{2.49}$$

and successively interpolated on a generic point $\vec{x}$ in space

$$\vec{B} = \begin{cases} B_x = |\vec{B}_{r_{x_{\vec{T}}}}| cos\psi \\ \\ B_y = |\vec{B}_{r_{x_{\vec{T}}}}| sin\psi \quad [\mathrm{T}]. \\ \\ B_z = B_z \end{cases} \tag{2.50}$$

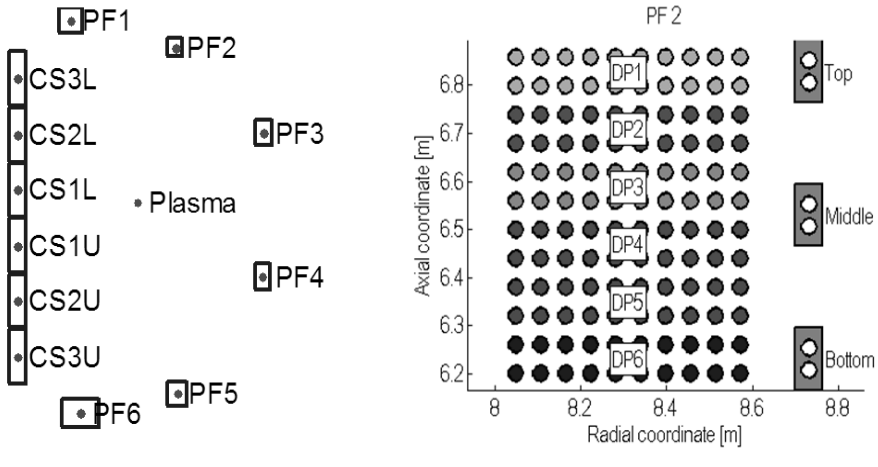

Figure 2.18: (Left) Cross-sections and current centre lines of the ITER Poloidal Field and Central Solenoid coil system and plasma. (Right) Each turn is taken into account for the coil to which the simulated conductor or joint belongs to.

Simulations with COMSOL finite element models using the current centre line approximation of the coils demonstrated that the approach is accurate enough, and significantly faster compared to the 2D or 3D representation of the full-size coil systems. The error is always less than 10%, except for the coil to which the simulated conductor or joint belongs to. For this reason, the latter coil is simulated in more detail by applying Eqs. 2.48 and 2.49 to each turn, see Figure 2.18b.

Since, for simplicity, this approach does not take into account the various joggles and connections in and between the double pancakes, the current in the coils is corrected by a factor

$$I_{coil} = \frac{N_{tot}}{N_r \cdot N_z} I_{scen} \quad [\mathrm{A}], \tag{2.51}$$

where N_{tot} is the effective number of turns in each coil, N_r and N_z the number of turns in radial and axial directions respectively and I_{scen} the nominal plasma scenario current.

Self-magnetic field

The Biot-Savart law is used for the magnetic self-field evaluation

$$\vec{B} = \frac{\mu_0}{4\pi} \int I \frac{d\vec{I} \times \vec{r}}{|\vec{r}|^3} \quad [\mathrm{T}], \tag{2.52}$$

with I the element current, $\vec{r}$ the distance between the current element and the point where the magnetic field is calculated and $d\vec{I}$ the current direction vector.

For steady-state analysis, a simple approach is used where at each cross-section, the magnetic field generated by a current in the centre of the conductor is calculated at eight positions on the outer edge of the cable. In a second step, the magnetic field is then interpolated over the exact locations of the strands.

For analysing pulsed operation, where the coupling currents can be potentially large (and therefore may generate high self-magnetic field values) the more refined MLFMM-based approach described in [64] is adopted.

2.5.7 System of equations

The electro-magnetic model of the superconducting cables and joints in JackPot-ACDC is based on a discrete parameter circuit approach. The equations are derived applying Kirchoff's laws to the voltage nodes and current branches defined along the strand and joints.

The system of equations solved by the code can generically be written as

$$\begin{cases} 0 = G \cdot V + G \cdot C^T \cdot \dot{B}_{ext} + D_i \cdot I \\ \\ M \frac{\partial I}{\partial t} = D_v \cdot V + C^L \cdot \dot{B}_{ext} + \Delta V. \end{cases} \tag{2.53}$$

The first equation describes the current balance at each voltage node, with

- $G \cdot V$ inter-strand currents through the transverse conductance matrix G;
- $G \cdot C^T \cdot \dot{B}_{ext}$ induced transverse currents due to the coupling C^T with the time-varying magnetic field $\dot{B}_{ext}$;
- $D_i \cdot I$ current balance along the axial direction.

The second equation describes the voltages across the current elements, with

- $M\frac{\partial I}{\partial t}$ self- and mutually induced voltages;
- $D_v \cdot V$ voltage difference between the nodes delimiting the current element;
- $C^L \cdot \dot{B}_{ext}$ induced voltage due to the coupling C^L with the time-varying magnetic field $\dot{B}_{ext}$;
- ΔV voltage drop across the strand or joint box resistance.

The voltage drop along the superconducting strands is a non-linear function of the strand current, temperature and magnetic field (and strain in the case of Nb3Sn), which is generally expressed by the power law

$$\Delta V_{SC} = V_c \cdot (\frac{I_{strand}}{I_c})^n \quad [\mathrm{V}]. \tag{2.54}$$

V_c is typically set to 10 $\mu V/m$, whereas I_{strand} and I_c are the strand current and critical current, respectively.

The system of equations is solved with the Sundials IDA solver [65] that addresses systems of differential-algebraic equations (DAEs) using Backward Differentiation Formula methods. When far from saturation, the non-linear voltage drop along the superconducting strands can be neglected leading to a simplified linear system of equations. This is solved with the Matlab built-in biconjugate gradient stabilized method (BiCGSTAB). In the case of purely harmonic magnetic field and current variations, the solution of the system can be further accelerated by making use of Fast Fourier Transform (FFT) analysis.

Finally, a significant simplification of Eq. 2.53 occurs in steady-state conditions. The built-in Matlab solver *fsolve* for non-linear equations is then used. In steady-state analysis, the connection of the sample with a current source may be taken into account, which adds a further unknown represented by the source voltage. In order for the system of equations to have a unique solution, Eq. 2.55 is included

$$\sum_{m=1}^{N_{str}} I_m = I_s, \tag{2.55}$$

with I_m a strand current and I_s the total cable current.

2.5.8 Strand scaling law

Different scaling formulas can be implemented in JackPot-ACDC to parametrize the critical current of the superconducting strands.

For Nb_3Sn conductors the Twente-ITER scaling law of Eq. 1.5 [11] is used to describe the dependence of the critical current I_c on strain, temperature and magnetic field. The scaling factors are generally obtained from strand characterization measurements performed at the University of Twente. The axial compressive strain is the only free parameter in the model. The classic scaling law of Eq. 1.1 [10] or the more recent 2-pinning components model (developed at ENEA) [66] are adopted for NbTi strands.

The n-value is determined from a double-logarithmic fit of the experimental V-I slopes measured during the I_c characterization.

The dependence of I_c on the strand-magnetic field angle is also taken into account in the code. The model proposed in [67] is used for Nb_3Sn. The derivation in [68] is adopted instead for NbTi strands. Since the latter formula allows the strand critical current to diverge to infinity for angles approaching zero, a minimum strand-magnetic field angle can be set to avoid unrealistic results when getting near to this limit.

2.5.9 Jacket model

The original implementation of JackPot-ACDC aimed at explaining the voltage traces measured on the jacket of the ITER full-size short conductor samples tested in the SULTAN facility. As such, the code also includes a simplified model of the jacket of CIC conductors, see Figure 2.19.

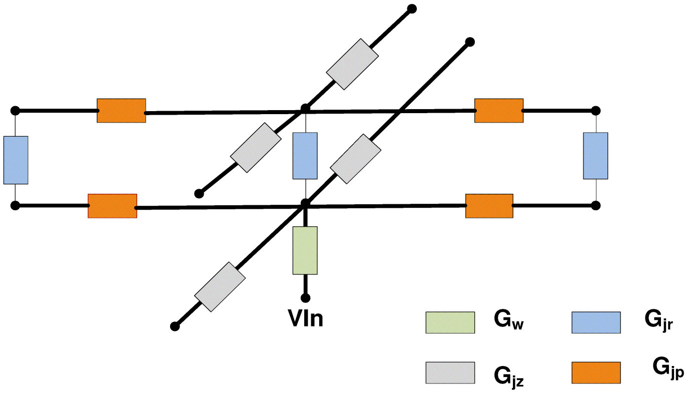

Figure 2.19: Conductances network implemented in the finite element model of the CIC conductor jacket, with G_w warp conductance, G_{jr} joint element conductance in the radial direction, G_{jz} joint element conductance in the axial direction and G_{jp} joint element conductance in the azimuthal direction.

By interpolating the voltages of the strands in direct contact with the outer edge of the cable, a voltage distribution on the inner surface of the jacket is computed. The potential on the outer surface of the jacket is then obtained by solving the equivalent circuit of resistors in Figure 2.19. In the model, the eventual presence of wraps around the conductor can be accounted for through the resistance G_w.

This simplified representation of the jacket voltage is able to qualitatively explain the features of the V-T traces observed during test [69]. However, the achievement of quantitative agreement with the experimental values is very difficult, since it depends on the ability to reproduce the precise trajectories of the strands inside the cable. Therefore, a calorimetric method based on the power dissipated inside the CIC conductor is used in the analysis when quantitative comparison with voltage traces is required.

2.5.10 Thermal model

A thermal model of the CIC conductor and joint box is implemented in the transient analysis for the evaluation of the temperature and current margins resulting from pulsed current and magnetic field operation. The thermal model is based on [70] and enables the calculation of the temperatures of helium, cable and copper sole along the axis of the joint. For a higher level of detail, an individual temperature is calculated for each petal. The copper sole is divided into two halves, allowing the analysis of thermal gradients in the case of junctions between conductors under different cooling conditions.

Figure 2.20 shows the arrangement of the thermal model in the cross-section of the joint. The temperature in the central helium channel is not taken into account, because inside the joint, the central spiral is replaced by a pipe through which heat exchange is minimal. However, in the feeder CIC conductor of the Toroidal Field coils the central channel is substituted by a copper rope, which results in two additional temperature distributions (copper strand bundle and helium).

Heat exchange between individual bundles is only possible through the helium. The corresponding heat transfer coefficients are derived from experiments on transverse heat transfer in CIC conductors [71, 72] and thus account for both heat conduction and convection. Heat exchange between each petal and the sole halves is proportional to the area contact, which varies along the cable axes due to their twist.

The temperature distributions are obtained solving Eqs. 2.56 - 2.58 for the two sole halves (subscript $sole$), the n strand bundles (subscript cbl, n) and n helium

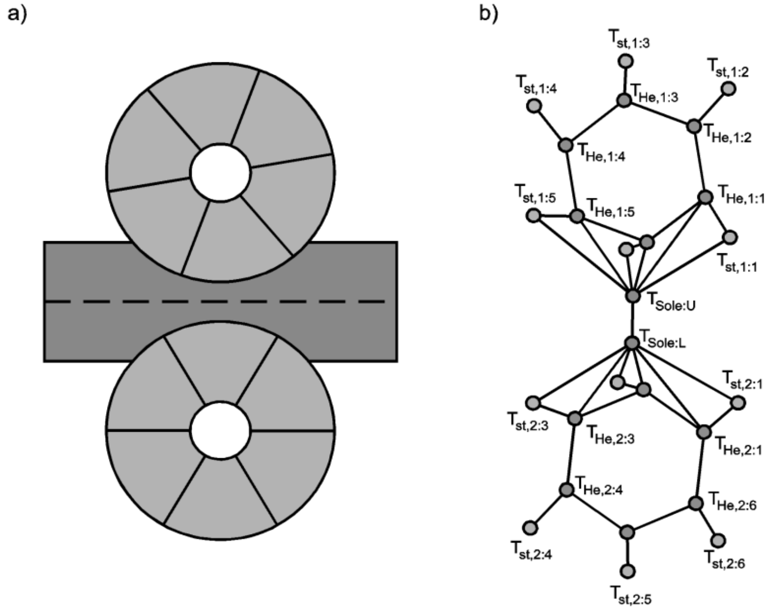

Figure 2.20: (Left) Schematic of a joint cross-section (see Figure 1.14c for comparison with a real joint). (Right) Corresponding thermal network.

channels (subscript He, n):

$$\begin{aligned} A_{sole}\rho_{Cu}c_{p,Cu}\frac{\partial T_{sole}}{\partial t} =& A_{sole}k_{sole}\frac{\partial^2 T_{sole}}{\partial z^2} + \frac{dP_{sole}}{dz} \\ & - \sum_{i=1}^{6} C_{cbl-sole}h_{cbl-sole}(T_{sole} - T_{cbl,i}) \\ & - \sum_{i=1}^{6} C_{sole-He}h_{sole-He}(T_{sole} - T_{He,i}) \\ & - C_{sole-sole}h_{sole-sole}(T_{sole} - T'_{sole}) \end{aligned} \tag{2.56}$$

$$\begin{aligned} A_{cbl}\rho_{cbl}c_{p,cbl}\frac{\partial T_{cbl,n}}{\partial t} =& A_{cbl}k_{cbl}\frac{\partial^2 T_{cbl,n}}{\partial z^2} - C_{cbl-He}h_{cbl-He}(T_{cbl,n} - T_{He,n}) \\ & - C_{cbl-sole}h_{cbl-sole}(T_{cbl,n} - T_{sole}) + \frac{dP_{cbl,n}}{dz} \end{aligned} \tag{2.57}$$

$$\begin{aligned} A_{He}\rho_{He}c_{p,He}\frac{\partial T_{He,n}}{\partial t} =& A_{He}k_{He}\frac{\partial^2 T_{He,n}}{\partial z^2} - \dot{m}\cdot c_{p,He}\frac{\partial T_{He,n}}{\partial z} \\ & - C_{cbl-He}h_{cbl-He}(T_{He,n} - T_{cbl,n}) \\ & - C_{sole-He}h_{sole-He}(T_{He,n} - T_{sole}) \\ & - \sum_{i=1}^{6} C_{He-He}h_{He-He}(T_{He,n} - T_{He,i}) \end{aligned} \tag{2.58}$$

with A the cross-sectional area, ρ the density, c_p the specific heat at constant pressure, k the heat conductivity, h the heat transfer coefficient, C the contact perimeter, $\dot{m}$ the He mass flow and P the power dissipation.

Constant temperature and constant temperature gradient boundary conditions are used at the extremes of the simulated portion of conductor.

A second order polynomial fit is used for the product of the temperature dependent heat capacities and densities of the sole and the cable bundle with the values of the coefficients a, b and c for the different materials listed in Table 2.2:

$$\rho(T)c_p(T) = aT^2 + bT + c \quad [\mathrm{J/(m^3{\cdot}K)}]. \tag{2.59}$$

Table 2.2: Coefficients of the second order polynomial fit used for the temperature dependent specific heat and densities [73].

Material	**a** **[J/m^3·K^3]**	**b** **[J/m^3·K^2]**	**c** **[J/m^3·K]**
NbTi	450	-2300	5500
Nb_3Sn	315	-908	400
Cu	150	-1060	2850

For the cable bundles, the volume average of the specific heat of superconductor and copper is used

$$c_{p,cbl} = \frac{A_{SC} \cdot c_{p,SC} + A_{Cu} \cdot c_{p,Cu}}{A_{SC} + A_{Cu}} \quad [\mathrm{J/(kg{\cdot}K)}], \tag{2.60}$$

with A the cross-sectional area of each material. The copper volume includes not only the fraction of copper in the superconducting strands, but also the copper strands. In a similar way the density of the strand bundles is calculated.

For simplicity and because the joint has a relatively short length, it is assumed that the helium pressure is constant everywhere in the model. This implies that the helium density and specific heat are only dependent on temperature. The reference He data are extracted from the 'Thermophysical properties of fluid systems' database of NIST [74].

The general assumption that the helium mass flow in the annulus of a CIC conductor is 1/3 of the total mass flow is also adopted in the thermal model. As such, the mass flow in each petal corresponds to $1/(3 \cdot N_p)$ of the total mass flow, where N_p is the number of petals. In the case of a copper core replacing the central He channel, as in the feeder conductor of the Toroidal Field coils, the helium flow repartition between bundle area and central core is determined on the base of the local void fraction.

In addition to the steady-state current and ramped current power dissipation in CIC conductors, joint box and strand-to-sole contacts, the temperature profile computed by the thermal model takes also into account the hysteresis loss in each petal through Eq. 2.6.

The thermal model for a single CIC conductor is obtained in a straightforward way from the one previously described. An additional He variable is included in this case that accounts for the central He channel.

In its current implementation, the thermal model is solved at the end of the electro-magnetic module. As such, temperature variations that may occur during the simulated scenario are not considered in the critical current, and thus the voltage drop, of the superconducting strands. Therefore, a second simulation, taking the computed temperature profile as input, is run when the presence of saturated strands is observed in the analysed system.

Although theoretically feasible, an upgrade of the thermal routine to a fully coupled electro-magnetic and thermal model with strand-level detail, is not considered at present. The main reason for this is the questionable accuracy and therefore the limited gain in physics insight of such models considering the large uncertainties affecting the knowledge of the local heat exchange in CIC conductors.

2.5.11 Model validation

The validation of the JackPot-ACDC model is presented considering three test-cases:

- ITER full-size short conductor samples in steady-state operation;
- a CIC conductor in an AC magnetic field;
- a lap-type joint in an AC magnetic field.

Case 1: Steady-state simulation of ITER full-size conductor samples

In order to qualify the conductors envisaged for the ITER magnets, full-size short conductor samples are tested in the SULTAN facility [23]. The steady-state performance of the conductors is assessed in terms of current-sharing temperature T_{cs} and critical current I_c. These parameters correspond to the temperature and current values, respectively, at which the averaged measured electric field reaches 10 μV/m. In T_{cs} experiments, the temperature of the coolant is gradually increased until the quench point, while the current in the sample is kept constant. Similarly, in I_c tests the transport current is augmented in steps at a constant temperature until the sample quenches beyond the critical current defined at the electric field level of 10 μV/m.

A complete description of the Poloidal Field Insert Sample (PFIS) [53] and CNPF1 sample [54] used in the validation and the simulation details can be found in sections 3.2.1 and 3.2.3. Here the comparison between the simulation and the experimental results is presented for validation purpose only. The inter-strand and strand-to-sole resistivity parameters used in the code are obtained by fit of inter-strand resistance distributions measured on cable [75] and joint [76] samples, see section 3.3.2.

Figure 2.21 shows a summary of the measured and calculated critical currents and current sharing temperatures for different values of the SULTAN facility background magnetic field for the two legs of PFIS. The agreement between simulation and experiment is found to be very good at all considered points, within 0.12 K and few kA for T_{cs} and I_c runs, respectively.

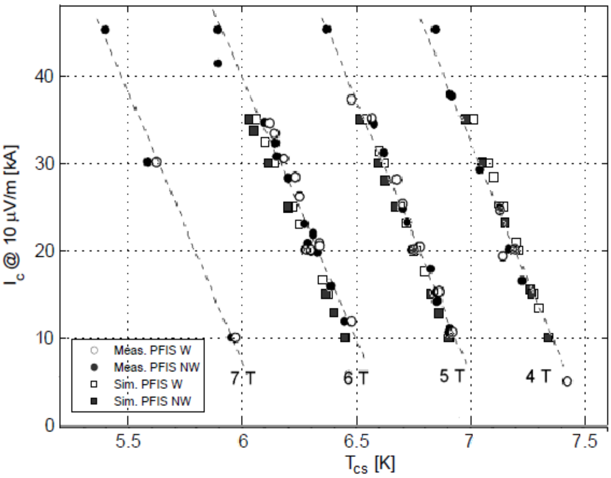

Figure 2.21: Critical currents versus current sharing temperature of the PFIS samples. Squares represent calculated data, circles correspond to measurements. The applied magnetic field is in the range 4 to 7 T. Data points from [53].

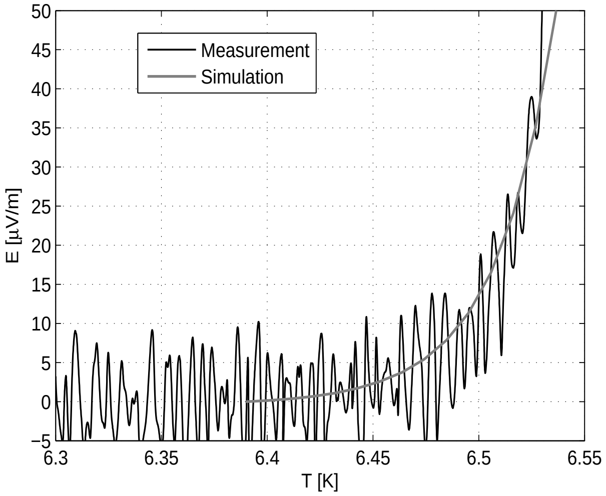

Figure 2.22: Electric field versus temperature for the CNPF1 conductor sample, T_{cs} run #SSPF2D180510 with transport current 20 kA and SULTAN background magnetic field of 5 T. Data courtesy of P.Bruzzone.

Due to the observed tendency of the CNPF1 sample to quench even at relatively low currents without appreciable transition, critical current and current sharing temperature could be measured only for few experimental runs. Therefore it is not possible to draw up an analogous graph for this conductor. However, also for the CNPF1 sample JackPot-ACDC is able to properly describe the voltage rise in the sample when a smooth transition is observed. This is illustrated in Figure 2.22 where the simulated and measured evolutions of the electric field during a T_{cs} run are compared.

In Figures 2.21 and 2.22 the similarity between the slopes of the simulated and experimental curves should be noticed. Similar slopes indicate that the current unbalance of the sample could be realistically reproduced by the finite element models of the joints and their interface with the conductor.

Case 2: AC simulation of a Cable-In-Conduit conductor

The accuracy of the JackPot-ACDC model in the case of harmonic magnetic field sweeps is illustrated in Figure 2.23. In this example, two ITER Toroidal Field conductors, namely the EUTF3-EAS [77] and the JATF5-JASTEC [78] samples, are exposed to a pure AC magnetic field with amplitude 0.15 T and frequencies in the 10 to 120 mHz range. The coupling losses of the two 0.4 m long sections are simulated using the inter-strand resistivity parameters obtained from the fit of the resistance distributions in virgin condition, see Figure 2.12. Both total coupling loss and cable inter-strand resistance measurements were carried out at the University of Twente.

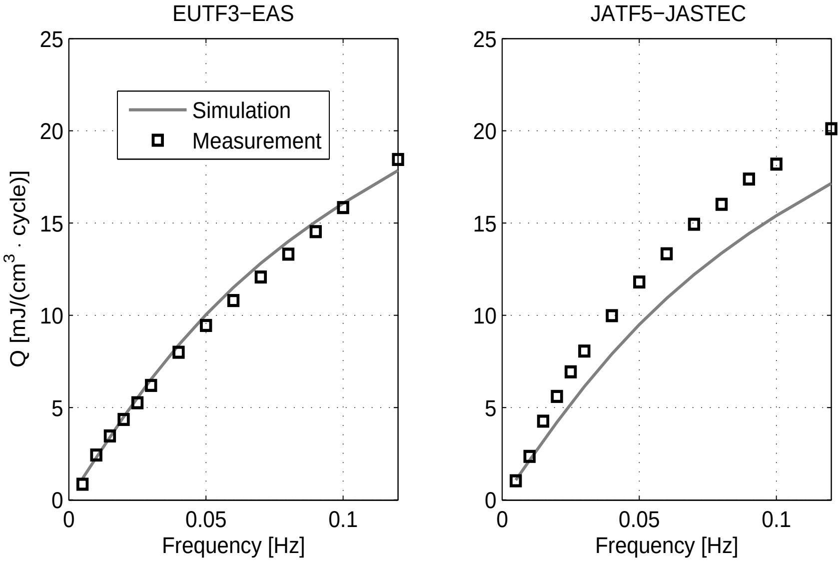

Figure 2.23: Measured and simulated coupling loss density per cycle versus frequency for the virgin EUTF3-EAS (left) and JATF5-JASTEC (right) Toroidal Field samples.

For the comparison to coupling loss only, the hysteresis loss is subtracted from the total loss measured. The simulations are in good agreement with the measured data. The maximum difference between simulated and experimental loss is of ±16% at 0.1 Hz in the case of the JATF5-JASTEC sample. The most likely cause of this discrepancy is a deviation of the twist pitch sequence of this sample from the reference value for ITER Toroidal Field conductors, i.e. 80-140-190-300-420 mm [15], which is instead used in the simulation. The observed difference is compatible with the magnitude of the deviations from the nominal twist pitch sequence (up to about 10%) that can be expected inside a CIC conductor.

Case 3: AC simulation of a lap-type joint

A validation of JackPot-ACDC with an ITER mock-up joint is described in [48]. Here a second validation is presented for a full-size terminal joint of the ITER Correction Coils. In the framework of the design and development of the ITER Correction Coils, two terminal joint samples were manufactured at the Institute of Plasma Physics Chinese Academy of Sciences (ASIPP, Hefei - China) and tested for AC loss at the University of Twente. The joint design and dimensions are described in [79, 80, 81].

The loss was assessed at 4.2 K in an AC magnetic field with amplitude 0.4 T in the 10 to 85 mHz frequency range both in absence and in presence of a 1 T DC background magnetic field. Measurements were performed by gas flow calorimetry for Edge On and Face On orientations illustrated in Figure 2.24.

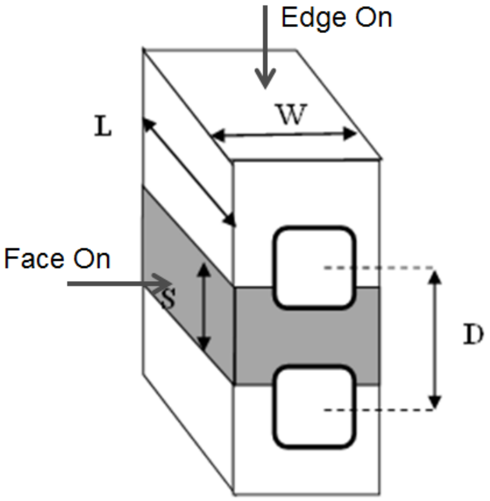

Figure 2.24: Face On and Edge On magnetic field orientations for a lap-type joint.

In order to determine the magnitude of the different loss terms and the loss contributions enhanced by coupling in a full joint, additional tests were carried out on the following components:

- half joint, i.e cable and copper sole, for inter-cable loss enhancement in full joint configuration;
- half sole, i.e. copper only after cable removal, for eddy current loss assessment;
- stack of four round insulated Correction Coil conductors for inter-strand coupling loss determination. The conductor sections are compacted to 25% void fraction to match the value in the joint (normal void fraction is 36%).

To perform the measurements, one of the joints was disassembled, revealing weak connections between the sole halves. Therefore, the second joint sample was opened and re-soldered prior to test. The observed poor bonding between the joint halves is in agreement with the large DC resistance reported for the two joint samples [82]. The effect can also be observed in Fig 2.25 summarizing the experimental results for the two full joint samples and the half joint. The low contact resistance between the sole halves largely reduces the inter-cable coupling in the Face On configuration of the initial joint, where it approaches the half joint value. Interestingly, even after re-soldering, the Edge On loss appears to be still slightly higher than the one in Face On configuration. Assuming a good contact between the joint halves after re-soldering, the result seems to point towards weak strand-to-sole connections.

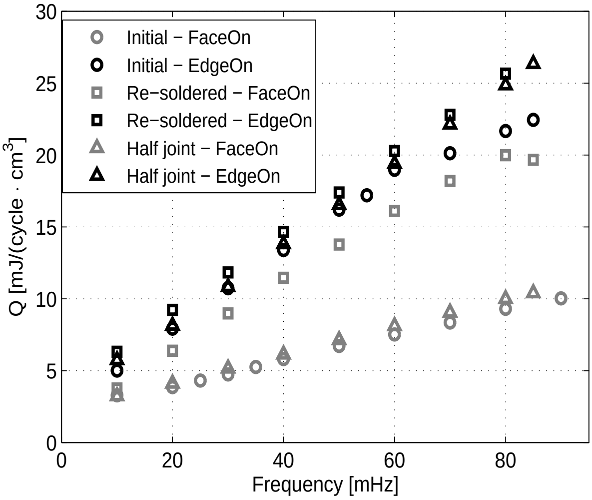

Figure 2.25: Measured Face On and Edge On total AC loss density per cycle versus frequency of the applied AC magnetic field at B_{DC}=0 T and 4.2 K for initial joint, half joint and re-soldered joint. The loss is normalized to the joint or half joint volumes.

The test data found are used to validate the JackPot-ACDC model of an ITER-type lap-type joint. As a first step, eddy current losses are calculated in a copper bar of rectangular cross-section having the same dimensions of the copper sole in the Correction Coil joints. This analysis allows the validation of the PEEC model of the joint box against both analytic formulas and finite element software. From [83], the energy dissipation per cycle in a rectangular conductor without current and exposed to a magnetic field with amplitude B and low angular frequency ω is

$$Q = \frac{l_c}{12\rho}\pi\omega B^2 a^3 b \quad [\text{J/cycle}], \tag{2.61}$$

where l_c is the conductor length, a and b the conductor dimensions parallel and perpendicular to the applied magnetic field and ρ the material resistivity.

The finite element simulation of the eddy current loss is performed with COMSOL. Figure 2.26 shows the eddy current loss in the copper bar calculated with the three methods, assuming an AC magnetic field amplitude of 0.15 T and RRR of 100. The loss estimated by JackPot-ACDC is in very good agreement with both the predictions of the analytic formula and the finite element model. A maximum spread in the results of 6% is observed at the highest simulated frequency for a magnetic field directed along the wide edge of the bar.

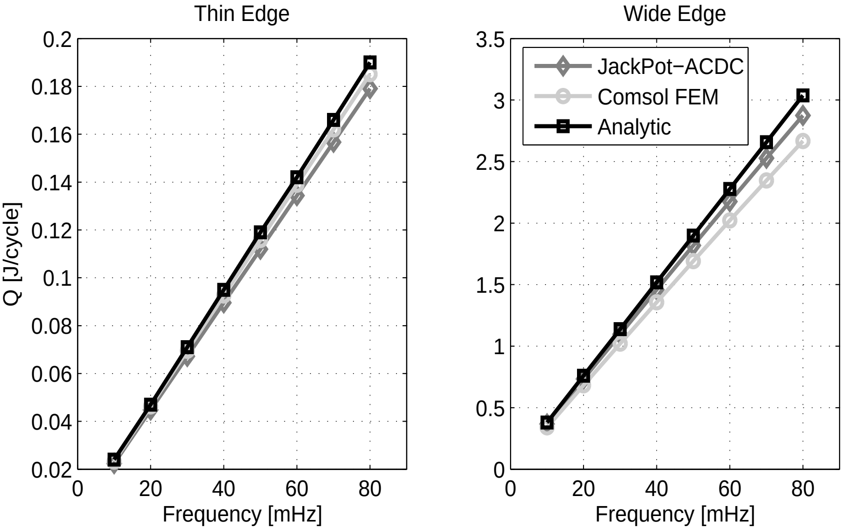

Figure 2.26: Eddy current loss per cycle versus frequency in a copper bar (RRR=100) of rectangular cross-section as computed by JackPot-ACDC, COMSOL FE model and analytic formula. The magnetic field is directed along the thin (left) and the wide (right) edge of the conductor.

Having verified the correctness of the joint box model of JackPot-ACDC, this can be used to fit the measured eddy current loss in a half sole of a Correction Coil joint, for which the copper RRR value is not known a priori. The simulation is found to match well the experimental data, in both Face On and Edge On configurations, for a Cu RRR of 50.

Since no inter-strand resistance measurements exist for the conductor and joint sections of the Correction Coils, the values of the resistivity parameters required by JackPot-ACDC are estimated on the base of the available measurements on NbTi strands [46]. As in [48], the resistivity for NbTi strands with Ni plating can be used for the inter-strand contacts. However, a correction accounting for the compaction in the joints is required. Considering that in the Correction Coil joints the void fraction is one third lower than in the conductor of [48] and that the diameter of the strands in the Correction Coil cable is also 10% smaller, a reduction of the inter-strand resistance of at least 40% can be expected. As illustrated in Figure 2.27 a good match between simulation and measurement is obtained for a resistivity parameter that is 65% lower than the value for Ni coated strand in [46] ($\rho'_{ss} = 10.5 \cdot 10^{-6} \mu\Omega{\cdot}\mathrm{m}^2$). The difference is likely to be related to the compaction process that can modify the strand pitches and contacts in a way that is difficult to predict and possibly to variations in material properties.

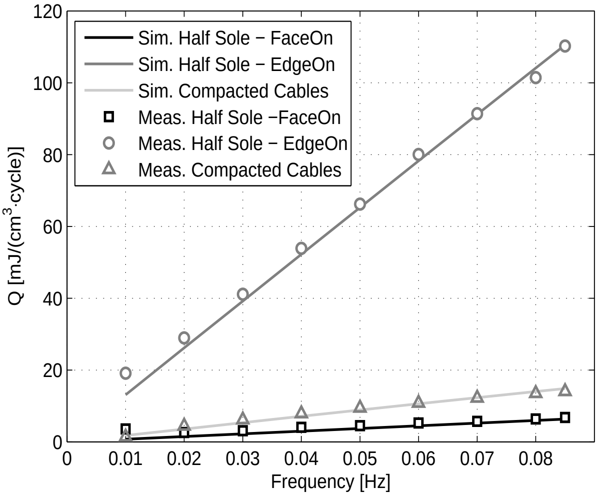

Figure 2.27: Simulated and measured coupling and eddy current loss densities per cycle versus frequency in the copper sole of the Correction Coil joint after cable removal and in a stack of four compacted Correction Coil conductors subjected to an AC magnetic field with amplitude 0.4 T at 4.2 K.

In accordance with [48], the resistivity parameter for NbTi strands without plating (bare copper) is used instead for the strand-sole resistances. Also in this case a correction is applied for the weak contact pointed out in the experimental measurements of Figure 2.25, which results in an increase of the resistivity parameter of one order of magnitude ($\rho'_{sj} = 31.5 \cdot 10^{-6} \mu\Omega{\cdot}\mathrm{m}^2$). The comparison between the measured and simulated loss in a half joint and in the re-soldered joint is plotted in Figure 2.28.

For the half joint, the match simulation-measurement is very good for both magnetic field orientations. However, for the re-soldered joint a good comparison is achieved only in Edge On configuration where the loss per unit volume is the same as for the half joint. In Face On configuration the simulation overestimates

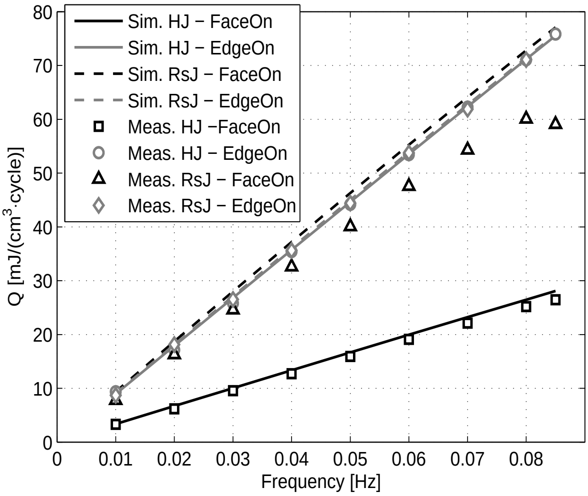

Figure 2.28: Simulated and measured coupling and eddy current loss densities per cycle versus frequency in a half (HJ) and in the re-soldered (RsJ) Correction Coil joint subjected to an AC magnetic field of amplitude 0.4 T at 4.2 K.

the inter-cable coupling. It has been verified that the difference is not due to strand saturation. The most probable explanation is an asymmetry in the strand-to-sole resistance on the two sides of the copper sole. A worse contact of the cable with the joint box cannot be excluded, although cannot be confirmed through measurements either since both joint samples are not any more available for test.

2.6 Conclusion

The electro-magnetic models for simulating CIC conductors performance can be categorized according to the operating conditions they address.

Numerical steady-state codes aim at explaining the voltage-temperature (or voltage-current) performance of conductors and the current non-uniformity. In general, their predictive power is limited by their poor level of including cable details and inaccurate description of joints and current transfer among the strands.

AC analytic models describe well hysteresis and inter-filament losses in strands. By analogy with the inter-filament coupling, inter-strand loss, the main dissipation mechanism in high current carrying CIC conductors subjected to rapid magnetic field changes, can also be modelled in terms of an effective time constant nτ. However, the predictive potential of this approach is strongly limited by the uncertainties affecting the model parameters and the necessity to resort to complex relations at high sweep rates combined with the applicability to pure AC magnetic fields only.

Numerical network models instead, that can be applied to any realistic operating condition, have been recognized as most suitable to represent the complex pattern of discrete contacts in a CIC conductor. To this category belongs the novel code JackPot-ACDC that allows the simulation of CIC conductors and lap-type joints to strand-level detail.

JackPot-ACDC calculates the trajectories of the strands following the cabling steps of a real conductor. The information is used to compute the inter-strand and strand-to-sole contacts, self- and mutual inductances as well as the coupling with time-varying magnetic fields. Apart from the input of the axial strain value of Nb_3Sn strands, the only required parameter is the inter-strand resistivity, that is obtained from the fit to measured performance data. Therefore, no free parameters exist in the code that can be tuned to match the experiment. The model calculates the current in each strand and joint element and, for time-transient cases, it also estimates the temperature increase produced by the resulting power dissipation.

The high potential of the code is proven through its application to three test-cases corresponding to the most common configurations encountered during the experimental assessment of the performance of conductors and joints. The comparison with the measured results shows JackPot-ACDC to be a very powerful tool for the investigation and optimization of the electro-magnetic performance of CIC conductors and lap-type joints.

Chapter 3

Steady-state performance of CIC conductors

High-current CIC conductors are characterized by large cable diameters, leading to significant magnetic field gradients over their cross-section. This results in elevated electric field, dissipation and reduced stability margin in localized sections of the transposed strands. Moreover, the current in CIC conductors is not uniformly distributed among strands due to the spread in the strand-to-sole contact resistances in the conductor joints. The combination of self-magnetic field and current imbalance can lead to premature quenches in the worst case. The issue is particularly relevant for NbTi-type CIC conductors because of the steep dependence of the critical current density of the material on the magnetic field.

In this chapter the influence of the cable internal magnetic field profile in combination with cable and joint layouts on the steady-state performance of both ITER NbTi full-size short conductor samples and model coils is presented.

Power dissipation and strand current imbalances are visualized and quantified and their relation is explored.

The importance of the analysis lays in specifying quantitatively the boundaries for the design of the ITER Poloidal Field coils given the coil configurations, joint properties and applied magnetic field conditions.

3.1 Introduction

A high current-carrying capacity is related to a large cable diameter and inherently to a significant magnetic self-field that, combined with the applied magnetic field, determines the magnetic field distribution over the CIC conductor cross-section. Following their trajectories from one side of the conductor to the opposite one, the twisted strands experience large variations of magnetic field leading to locally elevated electric field levels. As a result, the power dissipation over the cross section is not homogeneous.

In addition, the currents in the strands of CIC conductors are not all the same. Sources of imbalance are the joints at the extremities of a conductor. The spread in the electrical resistances between superconducting strands and the normal conducting parts in the terminals of the current leads causes a corresponding spread in the strand currents under stead-state conditions. The final current distribution in the high-field region of a magnet results from the inter-play of this initial non-uniformity and the re-distribution along the cable between the joints and the high magnetic field region. Therefore, the conductor design has to feature a compromise between low transverse resistance to allow inter-strand current sharing and high transverse resistance to limit coupling loss.

The combination of self-magnetic field and current imbalance can result in local hot spots leading, in the worst case, to premature quenches. The issue is particularly critical for NbTi CIC conductors due to their large n-values and much steeper dependence of J_c on magnetic field compared to Nb_3Sn [25, 84].

A significant effort has been spent in recent years to understand the steady-state performance of cables and to relate it to strand properties.

The effect of current non-uniformity and re-distribution on the quench performance of triplex and sub-size CIC conductors was extensively investigated in [85, 86, 87, 88, 89, 90]. From the measurements of magnetic field variations with Hall sensors, quantitative information on the current imbalance among strands or sub-cables could be obtained, which was then related to the overall stability of the conductors. However, the analysis was limited to relatively small cables for which the self-magnetic field was irrelevant.

The self-magnetic field was recognized to have a primary importance in limiting the current carrying capacity of medium size and large NbTi CIC conductors in [91]. In this work, the steady-state performance of the conductors was described in terms of an 'effective' field with a value between the background and peak magnetic fields. However, the observation that the effective magnetic field needed to explain the experimental quench conditions under the assumption of a uniform current distribution can exceed the peak magnetic field, was an evidence of current imbalance within the cable. The effect of strand coating, copper fraction in the cross-section and petal wraps on current non-uniformity were analysed. The occurrence of sudden quenches was also related to the self-magnetic field, rather than being caused by sudden disturbances.

Although offering qualitative interpretation of the main issues related to the steady-state performance of NbTi CIC conductors, the work in [91] did not provide quantitative insight in the level of current imbalance and in the dissipation at quench. Indeed the experimental assessment of these parameters is extremely difficult, if not impossible. Direct measurement of the strand currents requires special samples. Moreover, the installation of sensors inevitably modifies the structure of the cable and becomes infeasible with more than a couple of dozen strands [92]. Indirect methods, measuring local magnetic field variations, can be applied to conductors with any number of strands and do not disturb the cable structure. However, they need careful calibration and reconstruction methods [93] and strand-level details are very hard to extract. Therefore, the only way to obtain quantitative information with a strand-level detail about current non-uniformity and power dissipation in full-size CIC conductors in steady-state conditions is through numerical simulation.

The aim of this chapter is to explore the quench limitations of ITER-type NbTi CIC conductors in relation to the joint layout causing the current imbalance and magnetic field map quantitatively. The current imbalance of the analysed conductors is assessed and its quantitative relation with quench probability investigated. The main parameters affecting the current imbalance inside a CIC conductor are identified and their relative importance in view of the possible optimisation of joint design for magnets is discussed.

The analysis is performed with the code JackPot-ACDC, taking into account the precise trajectories of all individual strands, joint design, cabling configuration, spatial distribution of the magnetic field, sample geometry and experimentally determined inter-strand resistance distributions. Although unable to actually simulate quenches in CIC conductors, JackPot-ACDC does accurately calculate the voltages and currents in a cable, and thus allows to determine the power dissipation, either locally or globally, at the instant at which the sample quenched during the experiment. As such, the model enables the calculation of the minimum quench power of the CIC conductors under test. The analysis shows the effect of various conductor parameters on the steady-state quench stability of both short conductor samples and coils. Note that, helium temperature, pressure and flow rate, cable design and void fraction as well as strand properties also play a role in the CIC conductor steady-state performance. This analysis focuses exclusively on conductors operating under ITER-relevant conditions or in the experimental set-ups employed for their characterization.

The electro-magnetic code shows an excellent quantitative descriptive potential for CIC conductor transport properties. Therefore, the influence of local thermal gradients over the cross-section of the cable appears to be negligible for the purpose of the present study, justifying the adopted approximations.

3.2 Conductors and samples layout

To assess the performance of full-size ITER Poloidal Field conductors, both short conductor samples and a demonstration insert coil were manufactured in the past years. The Poloidal Field Insert Sample (PFIS) was tested in the SULTAN facility at CRPP (Switzerland) in 2004. The steady-state tests of the sample revealed poor performance compared to design expectations due to early quenches of the conductor [53]. This result was attributed to current imbalance introduced by the joints that could not be solved before entering the high magnetic field region of the sample. The overloaded strands reached saturation, which eventually led to a quench of the entire conductor [94, 95]. Of high importance was the self-magnetic field of the cable, which caused a considerable magnetic field gradient over the conductor cross-section [96, 97].

In order to get a better understanding of the behaviour of high current NbTi CIC conductors and joints under relevant ITER operational conditions, the Poloidal Field Conductor Insert (PFCI) was built in Europe and tested at JAERI Naka (Japan) in 2008. Although it was constructed using the same conductor as the PFIS, the PFCI steady-state performance met the ITER operation requirements without premature quenches. The improved performance was attributed to the longer conductor length and increased distance between the joints and the high magnetic field region [98].

More recently, the first Chinese Poloidal Field conductor sample (CNPF1) was tested successfully at the SULTAN facility. The sample featured a new layout for the upper terminations together with a 'U' bend bottom section to avoid current imbalance as produced by conventional joints [54].

3.2.1 Poloidal Field Insert Sample details

The preparation and instrumentation details of the PFIS may be found in [99]. The hairpin sample comprises two conductor sections called 'legs' connected at one end by a joint, see Figure 3.1. One leg consists of the regular CIC conductor

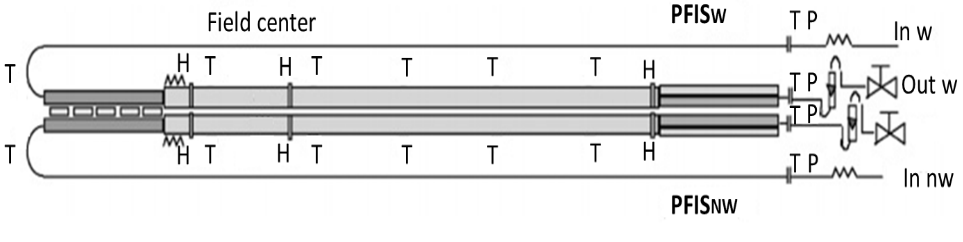

Figure 3.1: PFIS hairpin sample layout, with bottom joint on the left and upper terminal joints on the right [53]. The positions of temperature 'T', pressure 'P' and Hall sensors 'H' are also indicated. For test, the sample was vertically positioned with the coolant flowing from the bottom to the top. Different He inlet temperature and applied magnetic field values were used for the conductor characterization.

of the Poloidal Field Conductor Insert (W), while the second has the steel wraps around the final stage sub-cables completely removed (NW). The PFIS size is the standard one for SULTAN samples, about 3.5 m long, including the bottom joint and the upper connections. The main parameters for the two legs are summarized in Tables 1.2 and 3.1.

Table 3.1: PFIS conductors and sample parameters [99, 100].

	PFIS W	**PFIS NW**
Petal wraps	yes	no
Twist pitches sequence [mm]	42-86-122-158-489	42-86-122-158-530
	Bottom Joint	**Upper Termination**
Termination length [mm]	450	420
Cu plate RRR	41	86
CuCrZr sleeve RRR	2.5	
Sleeve-plate contact angle	135^o	

3.2.2 Poloidal Field Conductor Insert test coil details

The design and manufacture of the PFCI test coil is described in [101, 102, 103]. The PFCI is a single-layer solenoid wound with 50 m of the same NbTi CIC conductor used for the PFIS W leg, see Figure 3.2 right and Tables 1.2 and 3.2. The upper turn is connected to an intermediate joint to test the joint behaviour under ITER-relevant magnetic field conditions.

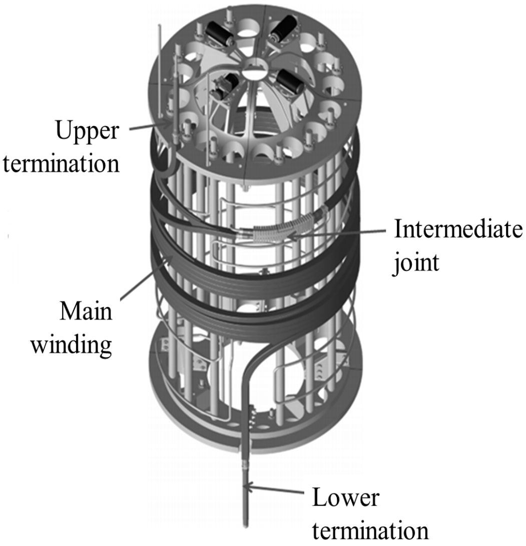

Figure 3.2: PFCI sample layout [102], showing the intermediate joint located between the main winding and the upper turn to test the joint behaviour in the magnetic field range expected on joints during operation in the ITER magnets.

Table 3.2: PFCI conductor and sample parameters.

	PFCI
Twist pitches sequence [mm]	45-85-125-160-410
Cu plate RRR	300
CuCrZr sleeve RRR	6
Strand-sleeve soldering	SnPb paste coating

3.2.3 First Chinese Poloidal Field conductor sample details

While the PFIS conductor and PFCI coil samples are assembled with the conductor envisaged for the ITER Poloidal Field coils 1 and 6, the CNPF1 conductor sample relies on the conductor for the ITER Poloidal Field coils 2, 3 and 4, see Table 1.6. Details about its assembly are reported in [54], while the main parameters of the conductor can be found in Tables 1.2 and 1.6. The strands have a diameter of 0.76 mm and are cabled with a 45-85-145-250-450 mm twist pitches sequence.

The CPFN1 was tested in the SULTAN facility and features the same overall geometry as the PFIS sample. However, major differences exist in the layout of their terminations and bottom joint.

The terminations of the PFIS are prepared by swaging the cable into tubular CuCrZr sleeves, see Figure 3.3. The electrical connection between cable and sleeve is improved, after having the jacket removed, by replacing the Ni coating from the strands at the cable surface with Ag coating. In addition, the inner surface of the sleeve is tinned. At the bottom joint the sleeves are joined by copper saddles. Copper plates connect the upper terminations to the secondary winding of the SULTAN transformer. The contact between sleeve and copper is obtained through indium wires squeezed by the joint clamp to a 0.2 mm thick layer. The main parameters of the joints are summarized in Table 3.1.

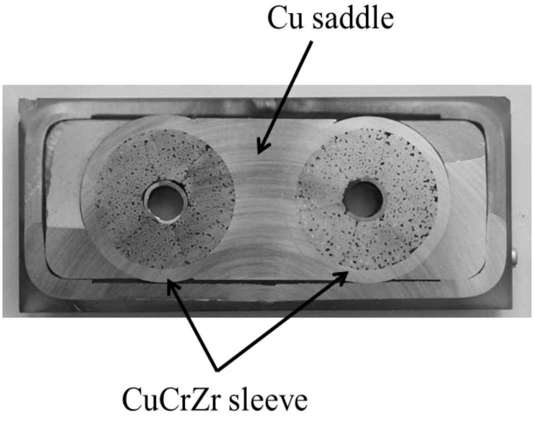

Figure 3.3: PFIS hairpin sample, bottom joint cross-section [102].

The PFCI sample features the same joint and terminations design as the PFIS. However, improvements are implemented regarding a higher RRR of the materials and the strand-sleeve soldering technique, as detailed in Table 3.2.

The most important modifications of the CNPF1 sample are the new layouts of both upper terminations and bottom joint. For the connections to the SULTAN transformer, a combo box solution developed at CEA is adopted, see Figure 3.4. Petal wraps are removed at the extremities of the cable, so that the last stage sub-cables can be individually soldered into grooves machined in a bi-metallic plate. The bottom joint is replaced by a 'U' bend inserted into a hairpin bending box, as shown in Figure 3.5.

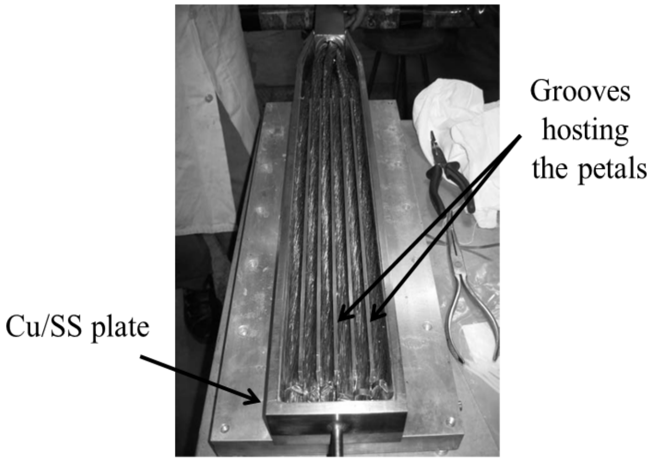

Figure 3.4: CNPF1 sample upper termination featuring the combo box design [104].

Figure 3.5: CNPF1 sample bottom 'U' bend in the hairpin box [104].

3.3 Modelling of the samples

In this section the modelling details that are relevant for the simulation of the steady-state performance of the analysed samples are discussed.

3.3.1 Finite Element model of joint and terminations

To reproduce the current imbalance inside the sample, a finite element model of the joints and terminations is implemented in COMSOL, see Figure 2.8.

For the CNPF1 sample, the copper sole of the upper termination is accurately modelled in order to mimic its assembly procedure. The strand bundles from the last cabling stage (petals) are unwound and individually connected to one of the available slots in the sole, which is then filled with solder. A series of simulations was carried out with the petals placed in different slots, to cover the uncertainty of how the petals are exactly connected in the real SULTAN sample. The simulation reveals negligible influence of the exact petal-slot combination on the computed steady-state performance.

3.3.2 Contact resistances

Table 3.3 summarises the parameters used for the definition of the contact resistances in the PFIS simulation.

Table 3.3: PFIS simulation parameters.

	PFIS W	**PFIS NW**
ρ'_{ss} - cable region [$\cdot 10^{-12}\Omega\cdot\mathrm{m}^2$]	159	101
ρ'_{ss} - joint region [$\cdot 10^{-12}\Omega\cdot\mathrm{m}^2$]	122	42
ρ'_{sj} [$\cdot 10^{-12}\Omega\cdot\mathrm{m}^2$]	2100	97
Solder layer thickness [mm]	0	0

The inter-strand ρ'_{ss} and strand-to-sole ρ'_{sj} resistivity parameters are fixed by matching the results from simulations with inter-strand [75] and joint [76] resistance measurements. Since no data are available for the leg without wraps, the PFIS NW strand-to-sole resistivity parameter is obtained by rescaling the corresponding value for the leg with wraps (PFIS W) using the experimentally determined ratio between the inter-petal resistance of the two conductors in the virgin state. The partial wraps removal from the outer surface of the cable in the terminations of PFIS W is also taken into account in the rescaling operation. The presence of wraps around the last stage sub-cables, which highly limits current re-distribution, is modelled as the absence of contacts between strands located in different petals in the PFIS W leg. Finally, although the use of solder is reported for the PFIS, its thickness is neglected in the simulation which is justified by the experimentally observed poor electrical contact [101].

The parameter set of PFIS W is also used in the simulations of the PFCI and CNPF1 samples, since no specific inter-strand resistance measurements exist for the latter two conductors. Similar resistivity values are expected though, since the strands feature similar material composition.

Following the adoption of a different soldering technique in the PFCI, it is likely that a solder layer with finite thickness is present in the joints of this sample. However, no information is available regarding the thickness. Therefore, the solder layer is assumed negligible in the calculations, after having verified that it would not produce significant effects on the result. As an example, Figure 3.6 shows the simulated strand current distributions at the quench instant for the PFCI critical current test run #027-02 in the case of non-soldered and soldered joints. The 1.5 mm solder layer corresponding to two strand diameters can be regarded as a realistic maximum average thickness based on the estimations in [45]. The background magnetic field and the conductor temperature of the run are 6 T and 5.8 K, respectively. In Figure 3.6, the intermediate and bottom joints of the PFCI test coil are located at 0 m and 42 m along the cable axis, respectively. Proceeding from the joints to the centre of the coil, the presence of both a magnetic field and a thermal gradient forces current re-distribution from the most overloaded strands. As a consequence, the spread in the strand current distribution is maximum at the extremes of the simulated length and it decreases towards its centre. The effect of the solder is such as to cause a small reduction of the spread in the strand current distribution. At the joint locations, the addition of the 1.5 mm solder layer causes a variation of 6% in the standard deviation of the strand current distribution. However, the change of the standard deviation is only ∼1.5% in the centre of the coil compared to the case without solder in the joints. Therefore, the addition of solder has no significant effect on the strand current distribution of the PFCI sample, which is mainly driven by the joint geometry combined with the magnetic field and temperature profiles along

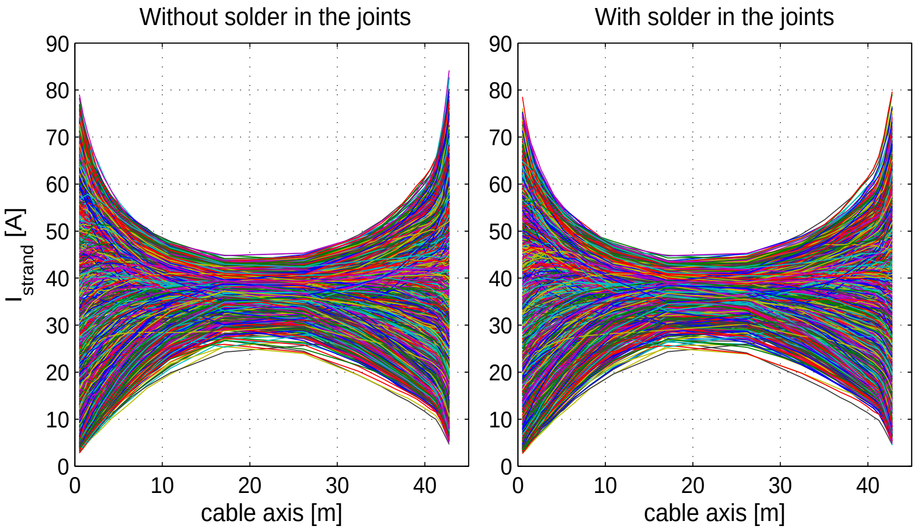

Figure 3.6: Strand current distribution along the PFCI sample for run #027-02 without (left) and with (right) soldered joints. The solder effect is negligible, causing a small reduction of the peak strand currents at the joints (i.e. at the extremes of the cable). The magnetic field and temperature profiles along the coil are the main forces driving the strand current distribution.

the coil.

3.3.3 Effect of temperature profile

A general assumption for steady-state analysis is that the temperature is uniform everywhere in the CIC conductor, both in the cross-section and along the axial length. Although this is a reasonable assumption for the short conductor samples tested in SULTAN, where the high magnetic field region has a length of about 0.5 m, this approximation is not adequate for long conductor samples in coils like the PFCI. The issue is of particular relevance for NbTi conductors due to the steep dependence of their critical current on temperature. Moreover, the PFCI test configuration featured a double cooling circuit as illustrated in Figure 3.7. This resulted in a slightly lower temperature in the conductor section close to the intermediate joint compared to the centre of the main winding.

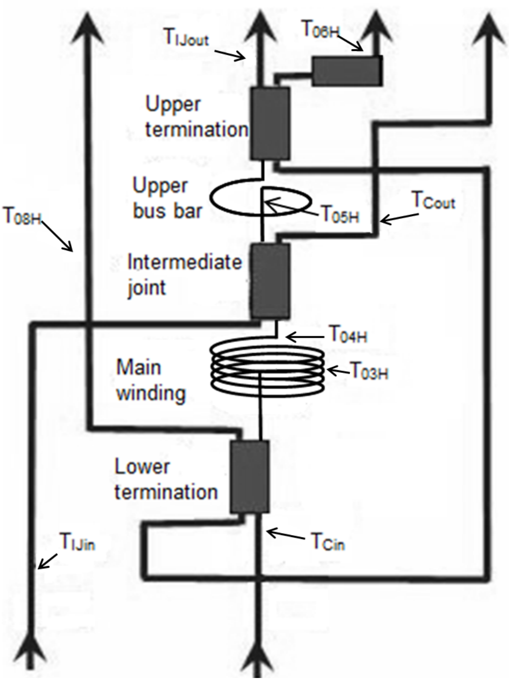

Figure 3.7: PFCI coil sample cooling scheme and temperature sensor locations [98].

Therefore, a longitudinal temperature profile is implemented in the PFCI simulation through a linear interpolation of the temperature measurements at inlet (T_{Cin}), outlet (T_{H04}) and middle (T_{H03}) of the main winding. As an example, the top plot in Figure 3.8 shows the power dissipation profile along the coil for the test run #035-01 (a current sharing temperature test with a transport current of 55 kA and background magnetic field of 6 T) assuming a uniform temperature along the sample. Under these conditions JackPot-ACDC wrongly locates the peak power dissipation, and thus the origin of the quench, at the intermediate

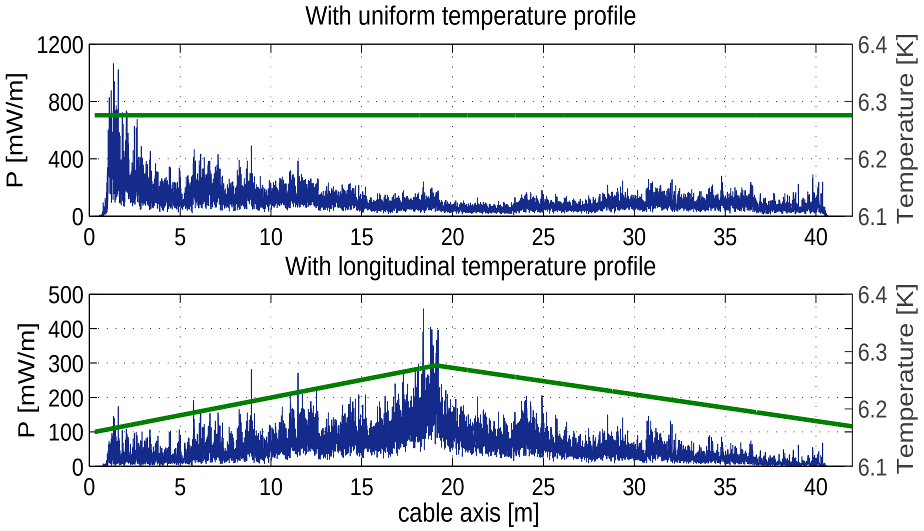

Figure 3.8: Calculated power dissipation distribution at quench for PFCI run #035-01 without (top) and with (bottom) the coil axial temperature profile (y-secondary axis).

joint (i.e. 0 m). Although the magnetic field over the intermediate joint is lower compared to the centre of the coil, the current imbalance in this region is high, as illustrated in Figure 3.6. The combination of elevated current non-uniformity and magnetic field causes, in the simulation with uniform temperature along the winding, the peak dissipation to be located at the intermediate joint. However, the measured quench position is correctly located by JackPot-ACDC in the centre of the coil (i.e. ~20 m), when the temperature gradient along the winding is taken into account, as shown in Figure 3.8 bottom. The temperature profile is defined according to the available measured temperature data, i.e. the readings of sensors T_{Cin}, T_{H04} and T_{H03} in Figure 3.7. The case shows the large impact that the combination of high magnetic field and current non-uniformity has on the power dissipation of a conductor. In the presence of significant current imbalance, a detailed knowledge of both magnetic and temperature profiles are essential to correctly describe the quench performance of a sample.

3.4 Simulation accuracy

The accuracy of the steady-state simulations of the PFIS and CNPF1 samples is discussed in section 2.5.11 concerning the validation of JackPot-ACDC. Figures 2.21 and 2.22 show examples of the good agreement between computations and measurements. In particular, the ability of the code to reproduce the experimentally determined slopes of both V-T and V-I curves is relevant. These slopes are related to the current distribution among the strands and can be correctly reproduced due to the appropriately detailed modelling of the joint and terminations. Therefore, the quantitative study of the current imbalance at strand-level is considered validated for the simulated samples.

The comparison between simulation and measurement appears to be somewhat less precise for the PFCI. In this case, the simulation is generally found to shift the instant of the quench. In T_{cs} runs, the temperature at which the coil reaches the quench electric field is on average some 80 mK higher in the simulations than in the measurements. In spite of this, the PFCI simulation results are significantly better than the predictions presented in [105, 106] using the THELMA model, where the deviation between calculation and experiment amounts up to 0.4 K or more.

The shift appears to be somehow higher for critical current runs, where on average the measured quench current is 12 kA lower than the value expected based on the model. It could be argued that the reason for the increased mismatch with critical current runs may be attributed to the presence of hysteresis loss during current ramps produced by the variation of the self-magnetic field of the coil. However, a typical current ramp from 0 to 26 kA causes a self-magnetic field change of about 0.5 T. Assuming a background magnetic field of 8.5 T and 10 μm for the diameter of the superconducting filaments, the loss according to Eq. 2.6 would be 5 J/m^3, resulting in a maximum temperature increase of a few mK only. Therefore, the most likely explanation is related to the coupling currents during a current ramp (which are not present during temperature ramps with constant current) that are not considered in the simulations.

The precise origin of the larger simulation-measurement discrepancy in the case of the PFCI coil sample is not understood at present for both T_{cs} and I_c runs. Given the relevance of the temperature profile on the performance of the conductor discussed in the previous section, measuring a more accurate temperature profile along the 45 m length of the coil could help in understanding the problem.

For the analysis discussed here, the simulated electric field values are obtained from the computed power dissipation inside the cable and not from the jacket voltage. This choice is made because the jacket potential is likely to be less accurate due to the non-uniform potential distribution in the cable. Moreover, the model of the jacket is such that it only 'senses' the potential of the outermost layer of strands in the conductor cross-section. As such, the jacket potential in the simulation strongly depends on the computed trajectories of the strands that obviously cannot correspond exactly to the geometry inside the real sample.

3.5 Effective heated spot length

The heat generation inside a CIC conductor at the start of a quench is concentrated in local spots along the strands. The effective length of a heated spot depends on the properties of the strand (n-value, $I_c(B)$ steepness) and cable layout (twist pitch, void fraction, diameter). It can be determined by plotting the strand peak heating power density versus cable quench current for different normalization volumes (i.e. heated spot lengths), see Figure 3.9.

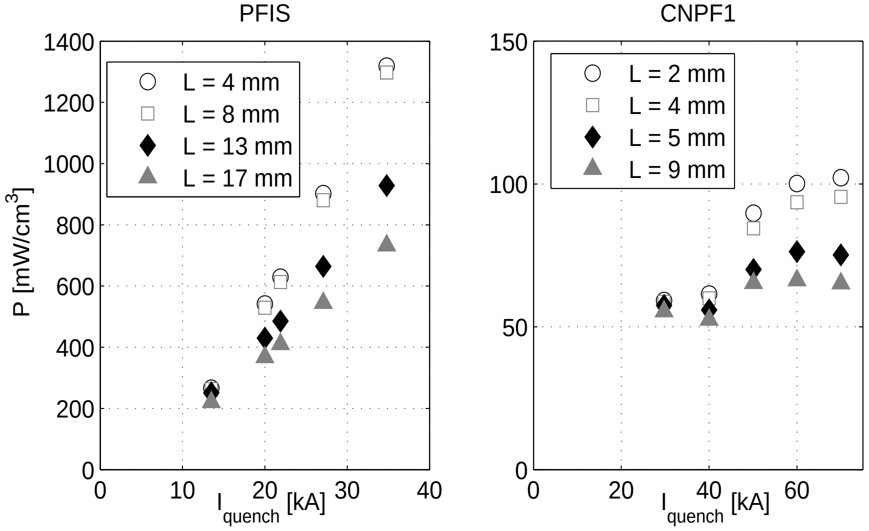

Figure 3.9: Strand heating power versus quench current for different lengths of the heated spot in the PFIS (left) and CNPF1 (right) samples.

To compare the performance of samples made with different strands, the heating power is normalized to a certain strand volume. The strand is cut into sections along its length and for each section the local heating power density is calculated. The power density computation is repeated for strand sections of increasing lengths, indicated as L in the legends of the plots in Figure 3.9. For section lengths shorter than or equal to the length of the heated spot, the power density will have a constant value. When the strand section length exceeds the length of the heated spot, the power density will drastically drop since the ohmic heating outside the quench spot is several orders of magnitude lower. Using the PFIS case as an example, when the strands are 'cut' into sections of 4 and 8 mm, the same heating power density is obtained. However, when the section length is further increased to 13 mm, the heating power density significantly reduces.

Since they are made out of the same cable, the heated spot lengths of PFIS and PFCI are found, not surprisingly, to coincide (8 mm). The heated spot length of the CNPF1 is lower (4 mm), which is likely related to the sharper V-I transition of its strands [66] and the different conductor geometry.

As an exercise, it is instructive to compare the heated spot length at quench with the length of the Minimum Propagation Zone (MPZ) derived from an analytic formula. Following [13], the length of the MPZ under adiabatic conditions can be expressed as

$$l_{MPZ} = \sqrt{\frac{2\lambda \cdot (T_c - T_{op})}{\rho J^2}} \quad \text{[mm]}, \tag{3.1}$$

with λ thermal conductivity, T_c and T_{op} the critical and operating temperatures of the conductor respectively, ρ the axial strand resistivity in the normal state and J the mean current density.

Table 3.4 summarizes the l_{MPZ} values estimated for the PFIS and CNPF1. They are obtained assuming a RRR = 100 for the copper in the strands, T_c equal to the experimental quench temperature and T_{op} as the temperature measured by sensors far from the high field region of the samples.

Table 3.4: l_{MPZ} and effective heated spot length for the PFIS and CNPF1 samples.

Sample	**Run**	$\mathbf{I_{op}}$ **[kA]**	$\mathbf{T_q}$ **[K]**	$\mathbf{T_{op}}$ **[K]**	$\mathbf{l_{MPZ}}$ **[mm]**	**Effective heated spot length [mm]**
PFIS	#070418	20	6.4	6.1	14	8
	#070402	45	5.5	4.9	9	
CNPF1	#120503	40	6.9	5.9	12	4
	#140506	55	6.0	5.5	5	

Table 3.4 shows how the agreement between the analytic l_{MPZ} prediction and effective heated spot length improves with the operating current. A good agreement is indeed expected at high current since only then current re-distribution among neighbouring strands can be disregarded.

3.6 Heating power at quench

When accurately taking into account the network of contacts in the conductor and the detailed geometry of joints and magnetic field, JackPot-ACDC allows to compute the instantaneous power dissipation just prior to a quench. However, since the code cannot identify the quench point itself, this needs to be determined from the experimental data in terms of quench current, temperature or electric field.

The power densities generated in the three samples, in the entire cable as well as locally in the strand are illustrated in Figures 3.10 and 3.11.

In the analysis, the quench point is defined in terms of the experimentally measured temperature or electric field at 'take-off'. An error estimate is also included corresponding to the uncertainty in the precise temperature or electric field value at the 'take-off'.

The points in Figures 3.10 and 3.11 are obtained from simulations at various magnetic fields and temperatures, chosen within the current range explored during the tests. Though not very accurately, from the data points trends for each sample can be observed, which are marked by lines.

In the PFIS conductor sample, both cable and strand peak heating power densities evolve in a similar way, dropping at about 35 kA for the leg with wraps, while a stable behaviour is maintained in the leg without wraps up to higher currents (∼45 kA). These current levels remarkably correspond to the experimentally observed thresholds for sudden quenches in the samples [53]. The 'knee' in the strand heating power at quench of the PFIS can be interpreted in terms of

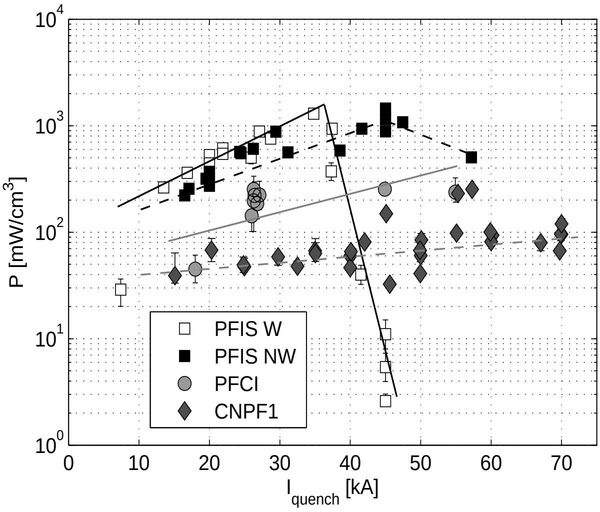

Figure 3.10: Peak heating power density in the strands versus quench current. Lines are guides to the eye showing the trend.

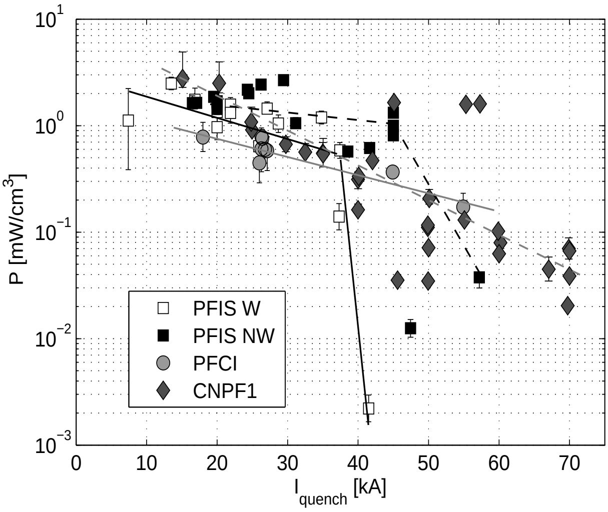

Figure 3.11: Heating power density in the cable versus quench quench. Lines are guides to the eye showing the trend.

different quench regimes (cable and single strand stability) at low and high currents, as previously reported for Rutherford and triplex cables, as well as sub-size CIC conductors [107, 89, 90]. In triplex cables, increasing current non-uniformity has been associated also to a reduced current threshold determining the quench regime transition. The same behaviour is also seen in the PFIS conductor sample where, in the left leg, the presence of wraps highly impedes current redistribution, therefore causing an earlier transition to the single strand quench behaviour. The scarcity of measurements above the knee, combined with changing test conditions (ramp rate and He flow rate) for a significant number of test points make drawing further conclusions from the available data not justified.

The possibility that the knee may result from an underestimation of the average cable and strand temperatures at quench, increasing with cable current, seems implausible. There are no arguments to support the sudden appearance of such a strong temperature deviation. Only a change in quench regime, a transition from cable to strand quench regime, may produce a sharper increase of the temperature of the quenching strand, but this would also be associated to a reduced quench power. Moreover, it can not explain the knee in the cable heating power density, for which the measured average strand temperature is the only available practical and valid value.

The cable and strand peak heating power of the PFCI coil sample follow trends analogous to those observed for the PFIS conductor sample in the cable quench regime. The order of magnitude lower strand peak power density of this sample indicates a better current uniformity. No clear sign of a quench regime transition can be found for the PFCI coil sample, possibly because it lies beyond the tested experimental range.

For the SULTAN samples, the cable heating power is normalized to the conductor volume exposed to the high magnetic field region of the facility, as defined in Figure 2.17. In the case of the PFCI coil sample, the adoption of a similar criteria would result in an artificially low dissipation. Due to the combination of the magnetic field gradient and the axial temperature profile along the windings, the power dissipation in the high magnetic field region of the coil is not uniform. Therefore, the normalization volume is chosen as the portion of conductor subtended by the heat generation peak. With such a choice, the cable heating power density of the PFCI coil sample appears to be in line with the other analysed samples in the cable quench regime, see Figure 3.11.

In the CNPF1 conductor sample, the strand peak heating power at quench is much lower than in the other conductors, due to a better current distribution among the strands, see Figure 3.12. Furthermore, unlike the PFIS conductor and PFCI coil samples, it remains relatively constant in the whole tested range.

An interesting observation is that the PFIS conductor sample could actually reach a higher local peak power density than the CNPF1 conductor sample and to a lesser extent than the PFCI coil sample. A correlation with the level of current non-uniformity seems plausible and is discussed in the next section.

3.7 Current non-uniformity

The claim that current imbalance among strand is the main driver for the early quenches in the PFIS conductor sample is further justified with Figure 3.12. The plot shows the ratio between the current in the strand with the peak power dissipation and the average strand current at the instant of quench.

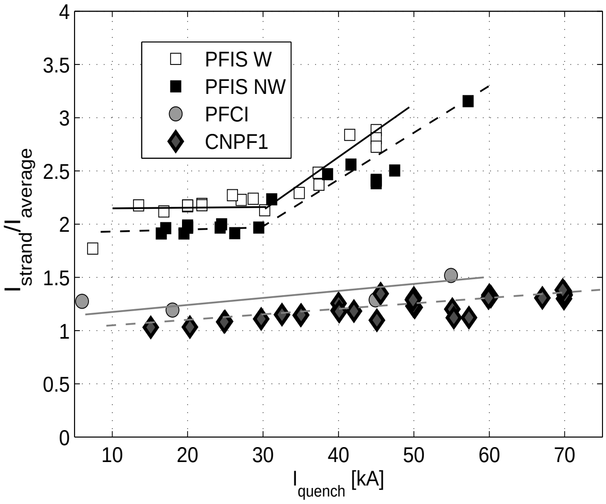

Figure 3.12: Overload of the strand with peak heating power at quench versus quench current. Lines are guides to the eye showing the trend.

Although it remains stable up to 30 kA, around a value of 2.2 and 2.0 for PFIS W and PFIS NW, respectively, the strand overload increases for higher quench currents which leads at the end to a premature quench. The increase of the current imbalance in this sample was already predicted indirectly in [97, 108] based on the growing difference observed between experimental quench current and the peak magnetic field critical current estimate. Since the threshold for the overload rise does not coincide with the transition between cable and single strand quench regimes previously identified, at present no clear quantitative correlation can be determined between strand overload and premature quench of the conductor. Therefore the analysis suggests that no comprehensive conclusion can be drawn focusing exclusively on the current imbalance, but other factors seem to play a role as well.

Regarding the PFCI coil sample, Figure 3.12 shows remarkably that the strand overload at quench is significantly lower (~1.3-1.4) and hardly varies with quench current. Since the coil features the same strand, cable and joint design as the PFIS conductor sample, the much better current imbalance is likely caused by the greater distance between joints and high magnetic field region, allowing for a better re-distribution of the currents.

The CNPF1 conductor sample shows the lowest and most stable current imbalance of all analysed conductors. Since CNPF1 is a short conductor sample like PFIS, no significant current re-distribution is expected between joint and high magnetic field region due to the short intermediate distance. The improved current uniformity therefore must originate from the new layout applied in the upper terminations and from the exclusion of the bottom joint.

As already observed, the simulation results show that the PFIS conductor sample can operate at a higher local peak heating power than the CPFN1 conductor sample and, to a less extent, than the PFCI coil sample. Although speculative and not derived from the analysis presented here, the most likely explanation is that the higher local peak heating power tolerable in the PFIS conductor sample is related to a higher temperature gradient and thus better cooling of the hot spots by their immediate surroundings. In the case of large current non-uniformity, the heat in the cable volume is concentrated in relatively small spots with much higher temperature than most of the surrounding strands, which is characterized by a much lower dissipation. This surrounding cable volume with lower temperature provides better cooling conditions than in cables with more homogeneously distributed heating power. This thermal effect, however, cannot be clearly separated from arguments following the so-called cable and single strand quench regimes as observed for the PFIS conductor sample. In addition it should be noted that the CNPF1 conductor sample has different strands, and the cable has a different configuration.

3.8 Effect of field profile and joint layout on stability

Following the precise trajectories of all strands inside a CIC conductor, JackPot-ACDC allows the visualization and quantification of the heat generation spots inside a sample. Figures 3.13 and 3.14 show the heating power at quench for all strands of the PFIS W sample in the cross-section where the strand peak power density is located for a low and high current test run, respectively. In the plots, each dot corresponds to a single strand. The color and elevation of the dots

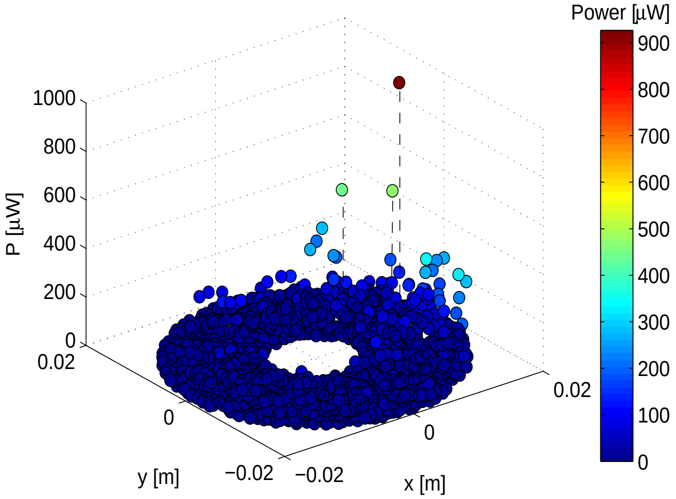

Figure 3.13: Strand heating power distribution at quench in the cross section of the PFIS W sample where the strand peak power generation is located at 13.5 kA and 6 T background magnetic field (run #020404).

represent their heating power. It can be observed that while only few strands show significant heating power at high cable current, i.e at 41.5 kA in Figure 3.14, the heat generation is spread over a wider part of the cross section at low current, i.e. at 13.5 kA in Figure 3.13 . An analogous behaviour is observed for the other analysed samples.

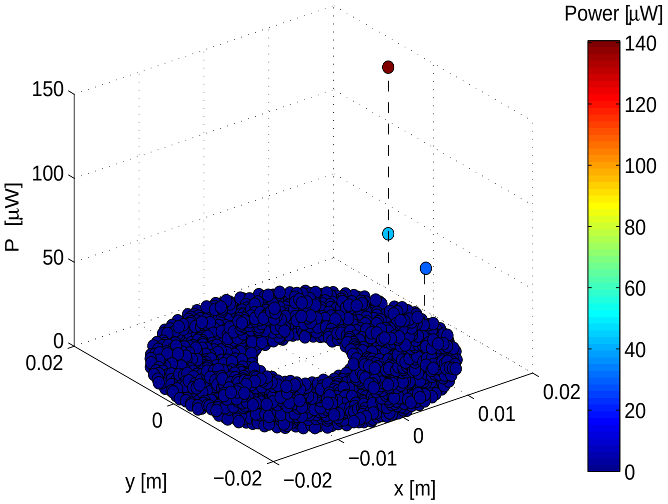

Figure 3.14: Strand heating power distribution at quench in the cross section of the PFIS W sample where the strand peak power generation is located at 41.5 kA and 6 T background magnetic field (run #050402).

Since, as shown in the previous section, there is no significant variation of the current imbalance with quench current for the PFCI and CNPF1 samples, an increased current non-uniformity cannot be the cause for the different heating power distributions. Therefore, the difference is mainly related to the steeper magnetic field gradient at high currents, due to the increasing 'weight' of the self-magnetic field of the conductor. The importance of the self-magnetic field in determining the location of quench can also be deduced from the fact that in both cases the highest power dissipation takes place at the inner edge of the conductor (i.e. $x < 0$ m) where the distance from the twin leg in a SULTAN sample (see Figure 3.1) is minimum. At this position the peak magnetic field resulting from the sum of background and self-field is located.

The strand heating power distribution along the cable axis for the same runs of the PFIS W sample is illustrated in Figure 3.15. Also in this direction, the number of strands taking part in the power generation at quench reduces with increasing transport current. Similar behaviour is observed for the other analysed samples. In the figure, the effect of the joint layout on the current distribution among the strands and therefore on the heating power distribution can also be observed. The high magnetic field region of SULTAN extends approximately between -0.2 m and +0.2 m along the cable axis and features an almost uniform magnetic field (Figure

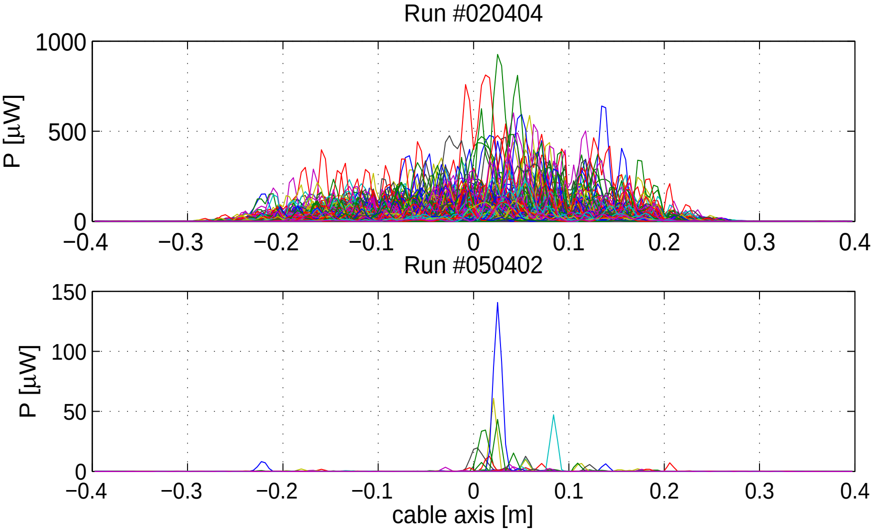

Figure 3.15: Strand heating power distribution along the cable axis of the PFIS W sample at (top) 13.5 kA and 6 T background magnetic field and (bottom) 41.5 kA and 6 T background magnetic field. Each line corresponds to the heating power of a single strand in the sample.

2.17). However, the resulting strand heating power distribution along the cable axis is not symmetric with respect to the centre of the high magnetic field region, as expected in the case of uniform current distribution. The observed asymmetry is a consequence of the combination of joint design, wraps, self-magnetic field and twist pitches.

The total strand heating power distribution along the PFIS conductor is illustrated for both legs of the sample in the same operating conditions in Figure 3.16. The power distribution resulting from a hypothetical rotation of 180^o of the copper plates in both terminations of the PFIS W sample, as illustrated in Figure 3.17, is also included to show the effect of the joint layout on the heating power distribution. In the PFIS W conductor sample the contact angle sleeve-Cu plate, its length and position with respect to peak magnetic field of the sample combined with the twist pitch sequence produce a current imbalance that can be hardly redistributed due to the presence of wraps. The configuration is such that the overloaded strands enter the high magnetic field region between 0 to 0.1 m along the cable axis causing an asymmetric power distribution. Removing the wraps in the joint proves to be effective in reducing the current imbalance. Indeed, the power distribution of PFIS NW sample is more symmetric than that of PFIS W sample. The rotation of the connection plates at the extremities of the sample leg is also found to help in achieving a more uniform power spread. This emphasizes the importance of the joint design on the conductor performance, especially for short conductor samples as the ones tested in SULTAN.

In order to study the effect of the terminals on the V-T performance of short

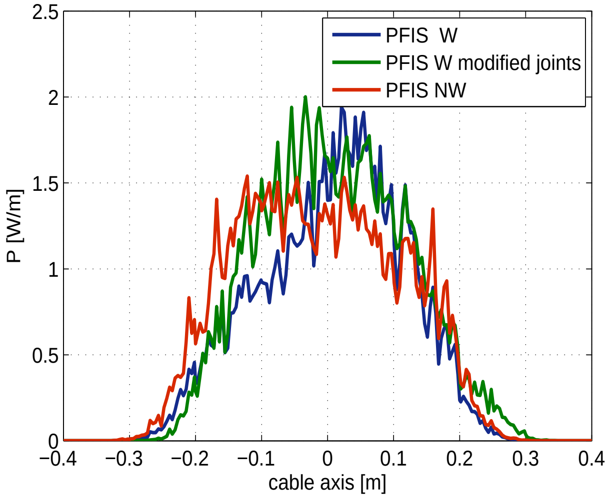

Figure 3.16: Strand heating power distribution along the cable axis for the two legs of the PFIS sample at 20 kA and 6 T background magnetic field. The effect of an hypothetical rotation of the copper plate in the terminals is also illustrated.

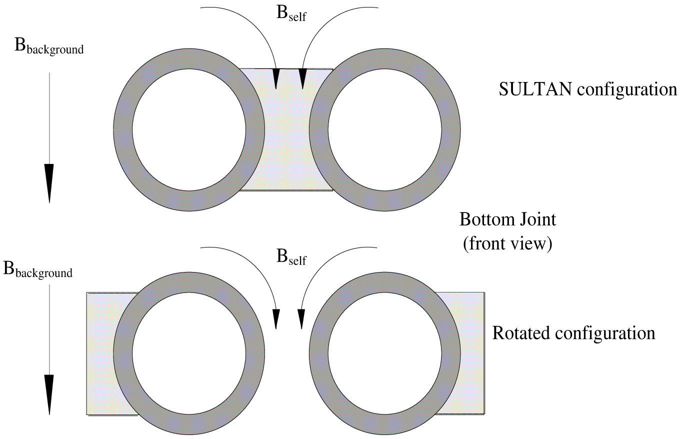

Figure 3.17: Position of the copper blocks connecting the conductors and to the copper bus terminals in the SULTAN facility, and in the hypothetical rotated configuration tested for simulation purposes.

conductor samples further, parametric variations of specific joint characteristics are simulated with JackPot-ACDC. In the analysis, the sample and joint layouts of the PFIS sample leg with petal wraps are adopted as reference. The V-T curve evolution is computed for the conditions of experimental run #070418, which are 20 kA of transport current in a 6 T background magnetic field. Since JackPot-ACDC cannot compute the quench instant of the conductor, the performances of the modified designs are compared at the reference temperature $T_r = 6.37$ K.

This corresponds to the experimentally determined quench temperature of the sample with nominal layout. The aim is to identify the joint parameters affecting the V-T evolution of short conductor samples, specifically in the SULTAN configuration, and their relative importance. In the analysis the following aspects are investigated: joint length, last stage twist pitch, cable-to-sole contact angle, copper RRR and solder layer thickness.

3.8.1 Joint length

The lengths of both bottom joint and upper termination are varied in the range 244-734 mm, corresponding to ratios $r = \frac{\text{joint length}}{\text{last stage pitch}}$ varying from 0.5 to 1.5. Although values of the ratio $r < 1$ are considered for parametric study purposes, they are not realistic from an application point of view for which $r > 1$ is considered as minimum. The resulting evolution of the electric field versus temperature is illustrated in Figure 3.18. When the joint length reduces below the last stage twist pitch, a sharp drop of the current sharing temperature T_{cs} occurs. For $r = 0.5$, the current sharing temperature of the short sample is reduced of about 150 mK compared to $r = 1$. The result is in qualitative agreement with experimental values on Nb_3Sn samples [109].

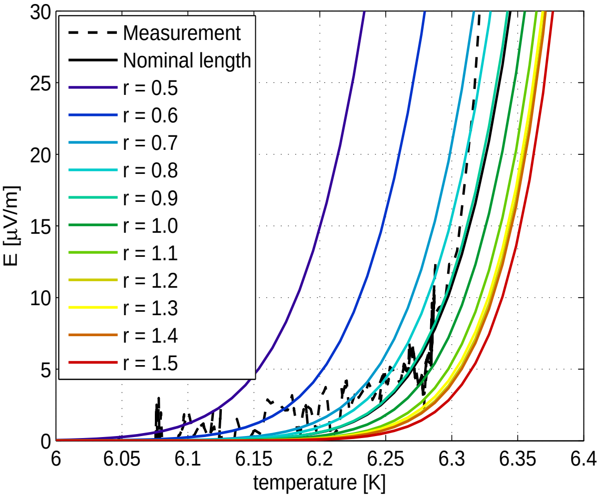

Figure 3.18: Electric field versus temperature for the PFIS W sample for different lengths of the bottom joint and upper termination at 20 kA and 6 T. The legend indicates the ratio r between the length of the joints and the last stage twist pitch.

On the contrary, increasing the length of the joint has a less distinct effect, with an improvement of the T_{cs} of less than 50 mK for the longest joint tested ($r = 1.5$). The corresponding increase of current overload of the strand with peak dissipation at the reference temperature T_r is shown in Figure 3.19. In the figure, the oscillations of the strand overload observed around $r = 1$ are caused by the

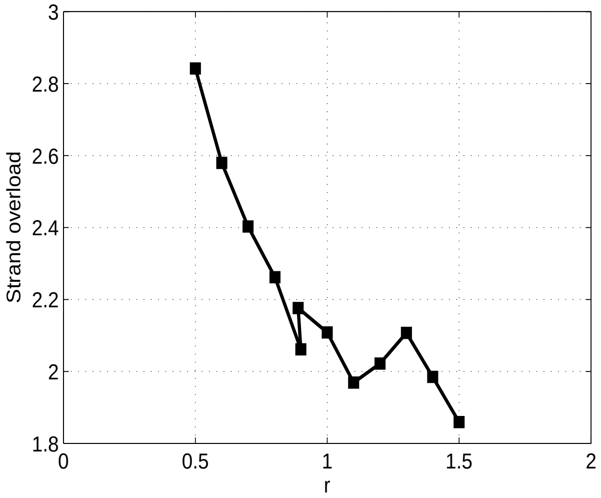

Figure 3.19: Overload ($\frac{I_{strand}}{I_{average}}$) of the strand with peak heating power at the reference temperature $T_r = 6.37$ K plotted against the ratio r between the length of the joints and the last stage twist pitch. The results refer to the for the PFIS W sample at 20 kA and 6 T.

progressive reduction of the contact with the sole for some of the last stage subcables, up to their complete disconnection. This changes the strand current paths and hence the strand with peak heating power and its overload. This behaviour is related to the assumed initial orientation of the petals with respect to the position of the copper sole.

3.8.2 Last stage twist pitch

The length of the twist pitch of the last cabling stage (nominal value = 489 mm) is varied in the range 244 to 734 mm, like in 3.8.1, keeping the joint length to its nominal value. As illustrated in Figure 3.20, the simulations show that a maximum increase of T_{cs} of less than 20 mK compared to the value with nominal pitches is obtained in the tested configuration for an increase of the twist pitch to 1.1 times its reference length. On the contrary, further increments or reductions of the last stage twist pitch produce a shift of the E-T plot towards lower temperatures.

These results may seem to be in contrast with the findings reported in the previous section, where the T_{cs} increased with larger $r = \frac{\text{joint length}}{\text{last stage pitch}}$. However, it should be noticed that unlike the joint length, variations of the twist pitch not only affect the number of strand-to-sole contacts, but also the network of resistances within the cable. Moreover, in short samples a change in the trajectories of the strands may have a large impact on the overall performance modifying the positions of the overloaded strands in the high magnetic field region.

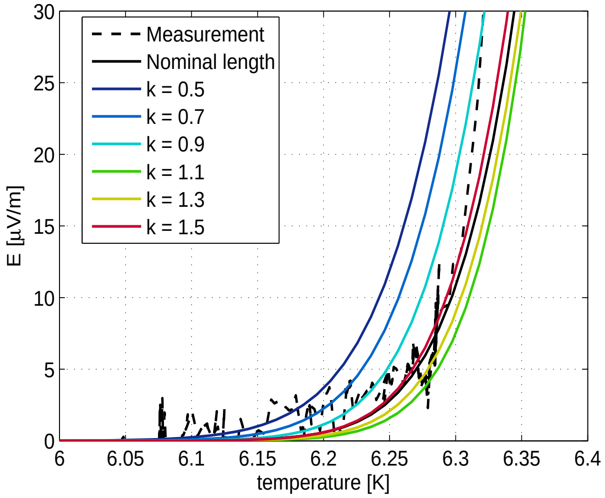

Figure 3.20: Electric field versus temperature for the PFIS W sample for different lengths of the last stage twist pitch at 20 kA and 6 T. The legend indicates the ratio k between the modified and nominal last stage pitches.

3.8.3 Contact angle

As shown in Figure 3.3, the nominal PFIS terminal layout is such that the cable is swaged into a sleeve, which is then connected to the copper sole. For the parametric analysis, the contact angle with the copper part of the joint is varied in the range 0.5 to 1.5 times its nominal value of 135^o.

The E-T curve of the tested sample is observed to shift to higher temperatures as the angle is increased towards 180^o because the contact areas for the last stage sub-cables touching the sole are augmented. However, for a contact angle of 180^o at maximum three petals can be connected to the sole. Therefore, although increasing the contact angle towards 180^o improves the current distribution within the last stage sub-cables, it affects little the current imbalance between the petals, which is the parameter determining the E-T characteristic of the sample. As a consequence, the maximum variation of T_{cs} observed in the analysis is rather small ($<$ 10 mK).

Contact angles larger than 180^o are considered in the parametric variation. Although in this configuration more petals are connected to the sole, no further improvements of the T_{cs} are observed compared to a contact angle of 180^o. This is related to longer, and thus more resistive, paths to connect these strands to the current inlet surface of the sole.

3.8.4 Copper RRR

The RRR values of the copper sole and of the CuCrZr sleeve are increased to assess their relevance on the E-T performance of the sample. In both cases it is found that the RRR has only a marginal influence on the current sharing temperature ($\Delta T_{cs} < 10$ mK), although it certainly affects the steady-state power dissipation, and thus the required cooling power, in the joints.

3.8.5 Solder layer thickness

Solder layers of increasing thickness (ranging between 1 to 10 mm) are applied to the joints of the sample. For the present study, the assumption is that more solder will cause a higher number of contacts and wider contact areas between the strands. However, in reality the addition of solder would also change the strand-to-sole resistivity parameter. In the simulations, the solder is uniformly distributed around the entire perimeter of the cable.

As shown in Figure 3.21, the E-T performance of the conductor steadily improves with the solder layer thickness. A corresponding decrease from 2.2 to 1.9 is observed in the current overload of the strand with peak heating power.

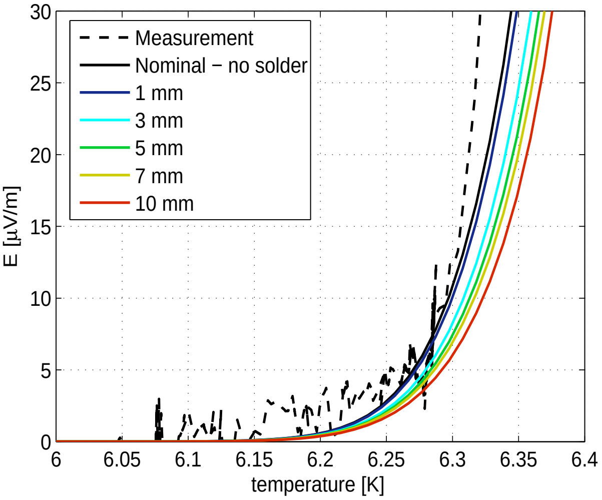

Figure 3.21: Electric field versus temperature for the PFIS W sample for different values of the thickness of the solder layer at 20 kA and 6 T. The legend indicates the thickness of the solder layer.

3.9 Conclusion

The influence of the sample and joint layouts on the current distribution in CIC conductors under steady-state conditions is quantitatively determined and its relation with strand and cable heating power at quench is assessed for both NbTi short conductor samples and coils. The importance of the analysis lies in specifying the maximum heating power, and hence current non-uniformity limit, for the design of the ITER Poloidal Field coils within the coil configuration, joint properties and applied magnetic field conditions.

For the first time the detailed heating power distribution and current non-uniformity are quantified and visualized. According to the model, a quench in large NbTi CIC conductors is initiated in local hot spots, often composed of single wires, with peak dissipation along sections of less than 10 mm. The hot spots are located in the high magnetic self-field zone of the cable cross-section.

In one short sample, different quench regimes are observed at low currents (cable quench regime) and high currents (single strand quench regime). The other two investigated samples instead show more homogeneous current distributions and hence no transition to the single strand quench regime. The more uniform current distributions are caused by either a longer distance between the joints and the high magnetic field region, or by improved joint design. No clear quantitative correlation is established between current imbalance and quench regime transition. However, the constantly increasing strand current overload can be regarded as the origin of the observed premature quenches.

Table 3.5 summarizes quench heating power and current imbalance at the operating conditions for the analysed samples (I ~50-52 kA and B ~5.0-5.7 T). From these data, threshold values for the maximum allowable current non-uniformity and power dissipation can be deduced that can be used for future conductor design and optimization. Due to their transition to the single strand quench regime below the operating current and magnetic field, the two legs of the PFIS sample must be excluded from this analysis. This would otherwise lead to unrealistically stringent and relaxed conditions for the tolerable dissipation and current imbalance, respectively. Therefore, based on the PFCI and CNP1 conductor test and simulation, a maximum current imbalance of 1.5 at operating conditions is allowed in ITER Poloidal Field cables to avoid the transition to the quench strand regime, and to prevent the risk of sudden quenches. Under these conditions the

Table 3.5: Quench power and current non-uniformity of the conductor samples at operating conditions of the ITER Poloidal Field coils.

	PFIS W	**PFIS NW**	**PFCI**	**CNPF1**
Type of conductor	PF1	PF1	PF1	PF2
Nominal operating current [kA]	52	52	52	50
Nominal effective peak field [T]	5.7	5.7	5.7	5.0
Strand peak power density at quench [mW/cm^3]	0.02	800	250	65
Cable power density at quench [mW/cm^3]	$8{\cdot}10^{-7}$	0.15	0.2	0.2
Current non-uniformity factor at quench	3.05	2.8	1.45	1.25

expected cable heating power at quench is in the range of 0.15 to 0.20 mW/cm^3. The strand peak heating power varies, depending on the strand characteristics and cable configuration, between 65 and 250 mW/cm^3.

The current imbalance is determined by the joint layout in relation to the cable design. Parametric analysis carried out on a short NbTi sample shows that particularly rapid performance degradation takes place when the joints are shorter than the last cabling pitch. The effect of variations of the last stage cabling pitch (for fixed joint length) is instead more complex to assess since it modifies the internal network of contacts and the trajectories of the strands with respect to the high magnetic field region. Possibly due to the presence of a sleeve around the cable in the reference joint layout, the contact angle between conductor and sole has only a marginal effect on the V-T curve.

From the analysis, the main driving force causing a re-distribution of the initial current non-uniformity is a magnetic (and eventually thermal) gradient along and in the cross-section of the CIC conductor. However, current re-distribution requires a significant length (several meters) of conductor, which makes it ineffective in the case of short conductor samples or joints placed in relatively high magnetic field regions. Removal of the petal wraps can help to reduce current imbalance. The addition of solder between strands and copper sole in the joints, however, appears more effective in tackling the problem.

All the above mentioned improvements for constant current operation have impact on the eddy and coupling losses to critical levels. Therefore their compatibility with pulsed operation has to be assessed as well and a convenient compromise decided upon.

Chapter 4

Pulsed performance of CIC conductors

Inter-strand coupling loss has a direct impact on the stability of Cable-In-Conduit conductors exposed to time-varying magnetic field. Not only cause the induced currents ohmic heating as they cross the resistive parts of the cable, but they may also rise the strand current above its critical value. As such, inter-strand coupling currents have to be tightly controlled to avoid the occurrence of quench.

The relation between twist pitches and coupling loss in ITER-type CIC conductors is investigated numerically with JackPot-ACDC. The analysis predicts a noticeable reduction of the loss for a ratio between successive cabling pitch lengths close to 1.

It is shown that by careful selection of the twist pitch ratios, CIC conductors cabled following long twist schemes can exhibit lower coupling loss than conductors with shorter pitches. The prediction is validated with measurements on four prototype conductors for the ITER Central Solenoid featuring different twist patterns.

To qualify their performance under relevant ITER conditions, the pulsed operation of the four Central Solenoid conductors is further assessed when exposed to a 15 MA plasma scenario beyond the available experimental results.

4.1 Introduction

In order to induce the plasma current, the Central Solenoid and the Poloidal Field coils of tokamak reactors need to operate in pulsed mode. As a consequence, the design of the CIC conductors for fusion application must ensure the stability of the conductors in the magnets during the rapid magnetic field transients that are required for plasma initiation. Magnetic field change rates up to 1.3 T/s are expected in the windings of the ITER Central Solenoid. This value is much higher than, for example, the magnetic field ramp rate of the dipoles for the Large Hadron Collider (LHC) at CERN, which is 6.5 mT/s and 80 mT/s in normal operation and at dump, respectively. Even higher magnetic field change rates, exceeding 5 T/s over the CSU1 and CSL1 modules of the Central Solenoid [110], have to be withstood by the conductors in the case of plasma disruption, when plasma instabilities may cause an abrupt temperature drop and the termination of the confined plasma.

The exposure to a time-varying magnetic field produces hysteresis loss in the superconducting filaments and coupling currents between filaments and strands. Inter-strand coupling constitutes the main loss term in large CIC conductors. The flow of coupling currents through the resistive parts of strands and cable causes ohmic dissipation and thus temperature increase, reducing the temperature margin. Moreover, the addition of coupling currents can increase the strand total current up to the point where the critical current is exceeded. Therefore, limitation of inter-strand coupling is an important issue for fusion magnets as these currents can potentially lead to a quench.

To reduce coupling loss, the inter-strand contact resistance can be increased. This is achieved both by surface plating of the strands [111, 112, 113] (for example with a 2 μm thick Cr layer) and by adding metal wraps around the sub-cables (coverage varying between 50% for the Toroidal Field coil conductor to 70% for the Central Solenoid conductor). High void fractions also result in lower coupling due to the reduction of the number of inter-strand contacts. On the contrary, the electro-magnetic load experienced by cables during operation causes an increase of the inter-strand conductance and thus the loss [114]. Finally, the cyclic history of the conductor influences coupling loss as well. The general observed trend in this case is a rise of the inter-strand contact resistance with cycling, although a subsequent reduction to values below the initial virgin state resistance is observed in NbTi conductors subjected to a very large number of cycles.

Apart from the magnitude of the inter-strand contact resistance, coupling losses in multi-stage CIC conductors are also determined by the twist pitch sequence of the successive cabling stages. The twist scheme also has major mechanical implications, determining the stiffness of the cable and hence its response to electro-magnetic and thermal loads. The issue is particularly relevant for Nb_3Sn conductors, due to the strain sensitivity of this material that results in the degradation of the steady-state performance of both coils and full-size short conductor samples with the cyclic application of loads [115, 116, 117, 118]. As a consequence, reduction of coupling loss and optimization of the mechanical performance cannot be done independently, in particular for Nb_3Sn conductors.

In this chapter, inter-strand coupling loss in multi-stage ITER-type CIC conductors is investigated numerically with the code JackPot-ACDC. The model allows fast and inexpensive parametric studies of the relationship between twist pitch sequence and coupling loss. Of particular interest is the option of combining a low coupling loss with a sequence of long twist pitches, since a scheme of long twist pitches has the potential of mitigating the current sharing temperature degradation issue of Nb_3Sn conductors [119].

The relevance of the topic is demonstrated by the campaign launched by the ITER Organization in 2011 to improve the coupling loss and mechanical performance of the conductor for the ITER Central Solenoid. This has resulted in the proposal of four cable designs addressing degradation and loss minimization through different twist schemes. To help assessing the most suitable design for the Central Solenoid conductor, the pulsed performance of the four cables during an operational plasma scenario is established with JackPot-ACDC.

4.2 Earlier studies on the relation between twist pitch sequence and coupling loss

Early investigations of the influence of the twist pitch sequence on the coupling loss is found in [120] and [121].

In [120], an analytical formula for the dependence of coupling loss on the ratio between the twist pitch of the wires and the twist pitch of the cable was derived. The calculations were developed for a single-stage conductor composed of superconducting wires arranged in a regular hexagonal pattern and embedded in a material with different conductivity. The minimum coupling loss was predicted for a ratio of 1 between wire and cable pitch in the hypothetical case that the cable has the same transverse conductivity as the wire. However, in practical conductors the transverse conductivity of the cable is dominated by the inter-strand contact surfaces and is significantly less than the wire conductivity, so that the minimum is shifted to lower pitch ratios. As an example, in the case of a 20% void fraction and a wire conductivity one order of magnitude higher than the cable one, the minimum coupling loss according to the relation in [120] is predicted for a wire to cable pitch ratio of 0.53.

An experimental approach to the problem was adopted in [121]. The coupling loss of a single-stage CIC conductor composed of nine superconducting wires soldered around a copper core was measured for different values and directions of the wire pitch. The minimum loss was again obtained for a wire pitch approximately half the cable one and for the same twist directions.

The cables used in the studies above featured relatively simple configurations compared to the layout of the conductors envisaged for ITER. ITER-type CIC conductors are composed of about thousand strands twisted in several stages. As a result of the multi-stage cabling, strands do not follow regular spatial distributions in the cross-section of the conductors. Furthermore, strands are not embedded in conducting matrices or soldered to copper cores. Obviously, the conclusions of [120, 121] cannot be straightforwardly translated to ITER-type conductors. Instead, a dedicated analysis taking into account all strands and cabling stages is required to investigate the relation between twist scheme and coupling loss.

Several publications address the evaluation of coupling losses in multi-stage CIC conductors [42, 43, 122, 123, 124, 125, 126, 127, 128]. Given the complex trajectories of strands in the cables and the relatively high cost of samples an relevant test facilities, analytic and experimental approaches to the problem have been troublesome. For these reasons, numerical simulation is the most suitable way for parametric studies and to investigate the twist pitches-inter-strand coupling loss relation. To treat the problem correctly, a numerical model like JackPot-ACDC is required that can reproduce the trajectories of all strands inside the cable.

4.3 Numerical analysis of the relation between twist pitch sequence and coupling loss

In order to investigate the relation between twist pitches and coupling loss in multi-stage CIC conductors, several tens of twist pitch sequences are systematically simulated for an ITER Toroidal Field-type conductor of two meter length. The only applied constraints are:

- a minimum length of 20 mm for the first stage twist pitch;
- $L_{p,i+1}$ at least 1 mm longer than $L_{p,i}$, with L_p twist pitch length of stage i;
- a maximum length of 500 mm for the last stage twist pitch.

A maximum twist pitch length of 500 mm is set in view of the limited length of a joint between conductors in ITER magnets. The minimum length is arbitrarily chosen to limit the number of cases.[1]

For each sequence, the coupling losses are computed for an applied AC magnetic field of amplitude 0.15 T and frequency in the range 0.05 to 2 Hz. The contact resistivity ρ'_{ss} is set to $5 \cdot 10^{-7} \mu\Omega{\cdot}\mathrm{m}^2$.

Figure 4.1 shows the coupling loss obtained for two of the generated twist pitch sequences. In the legend the length of the twist pitches of the five cabling stages are given in mm. The twist sequences in Figure 4.1 are selected among all the simulated cases since they invalidate the intuitive assumption that coupling loss increases with the length of the twist pitches. Indeed, the conductor with longer pitches at every cabling stage features a *lower* coupling loss than the one with a shorter twist sequence. This observation suggests that the twist pitch length

---

[1] Combinations with $L_{p,i+1}$ shorter than $L_{p,i}$ have also been investigated, but are considered irrelevant for Nb_3Sn conductors since they are unattractive from a mechanical point of view.

alone is surely not the only parameter determining the magnitude of the coupling loss in multi-stage CIC conductors.

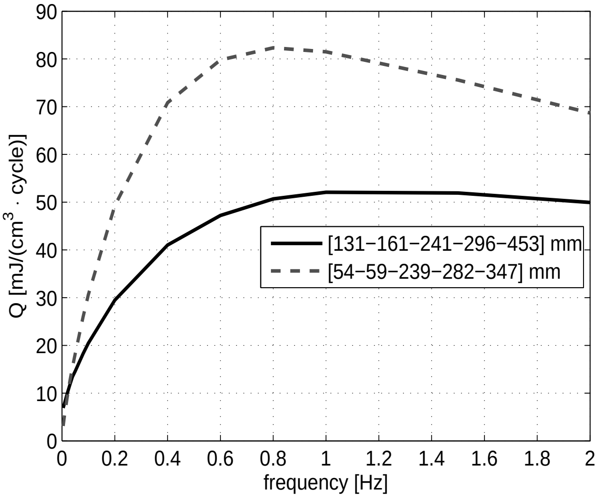

Figure 4.1: Coupling loss density per cycle versus frequency for two ITER Toroidal Field-type conductors with randomly generated twist pitch sequences. The legend displays the length in mm of the successive twist pitches of the five cabling stages.

To improve the understanding of the effect of the different cabling stages on the loss, the twist pitch of each individual stage of the sequences is varied separately (while all other stages have nominal values). The results of this analysis for the five stages of the sequence 131-161-241-296-453 mm of Figure 4.1 are illustrated in Figures 4.2 to 4.6. The coloured bar shows the applied elongation with respect to its nominal value.

It is generally observed that a reduction of the coupling loss can be achieved by increasing the length of the twist pitch of the first stage, which amounts to about 20% of the original loss for the 131-161-241-296-453 mm sequence in Figure 4.2. On the contrary, a shorter initial stage, keeping the other stages unvaried, results in an increase of the loss that reaches up to about 80% of the initial value for the 131-161-241-296-453 mm sequence in Figure 4.2. Therefore, depending on the exact twist sequence, the effect of the twist pitch of the first cabling stage on the final coupling loss can be substantial, especially when compared to the loss variation produced by similar changes in the twist pitches of the other cabling stages. The trend reverses for stage 4, see Figure 4.5, showing the intuitively expected reduction of the coupling loss for shorter pitch lengths. The relevance of the twist pitch length of the last cabling stage seems less pronounced, with minimum variations of the loss for both extension and reduction of the nominal value. This is likely related to the presence of metal wraps around the last stage sub-cables and possibly to the slightly different cabling structure of the last stage, featuring a channel for the helium in its centre. Finally, the influence of

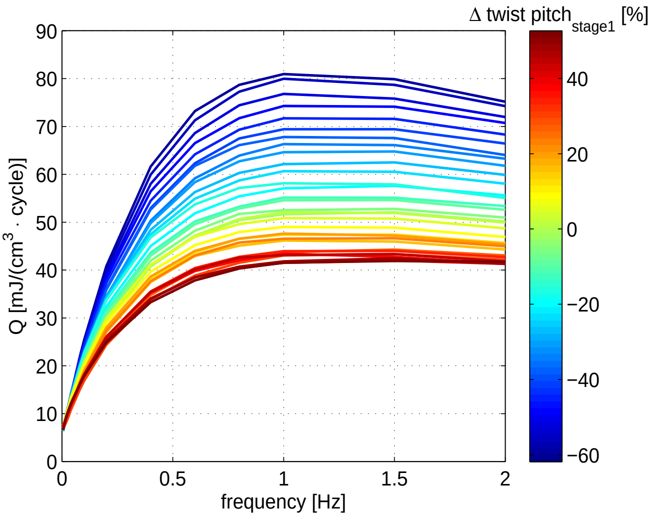

Figure 4.2: Coupling loss density per cycle versus frequency for systematic variations of the twist pitch of stage 1 of the 131-161-241-296-453 mm sequence.

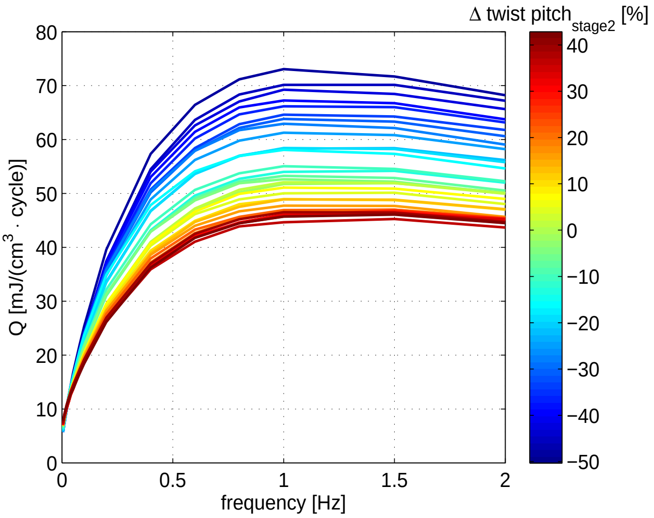

Figure 4.3: Coupling loss density per cycle versus frequency for variations of the twist pitch of stage 2 of the 131-161-241-296-453 mm sequence.

stages 2 and 3 is less regular and depends strongly on the starting twist sequence considered for the analysis.

The outcome of this study can be summarized as follows: elongating the pitch of the earlier (shorter) stages and shortening the later (longer) ones tends to reduce the coupling loss. In other words, when the twist pitches of stages 1 to 5 approach the values of the following and previous stages, there is a reduction of the coupling loss. Therefore, the use of similar twist pitches in the successive cabling stages,

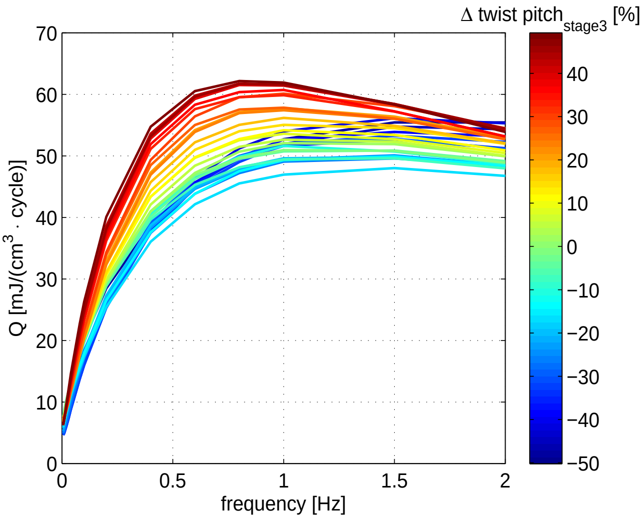

Figure 4.4: Coupling loss density per cycle versus frequency for variations of the twist pitch of stage 3 of the 131-161-241-296-453 mm sequence.

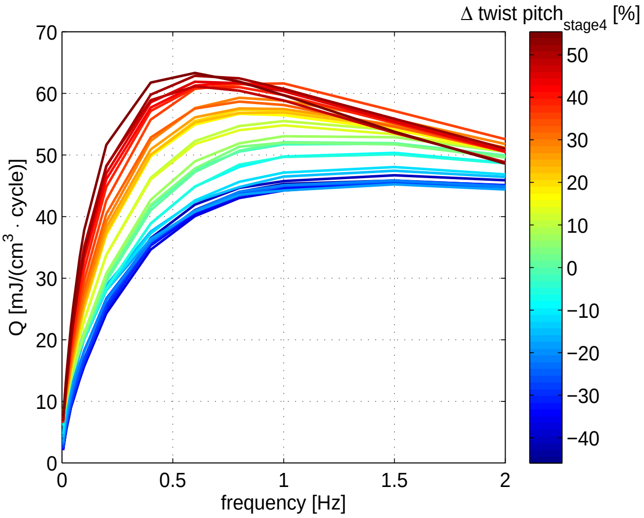

Figure 4.5: Coupling loss density per cycle versus frequency for variations of the twist pitch of stage 4 of the 131-161-241-296-453 mm sequence.

i.e. a stage-to-stage twist pitch ratio of 1, shows to be a suitable route to loss decrease.

The average stage-to-stage twist pitch ratio (r_{avg}) is calculated according to Eq. 4.1

$$r_{avg} = \frac{\sum_{i=1}^{N-1} \frac{L_{p,i+1}}{L_{p,i}}}{N-1} \tag{4.1}$$

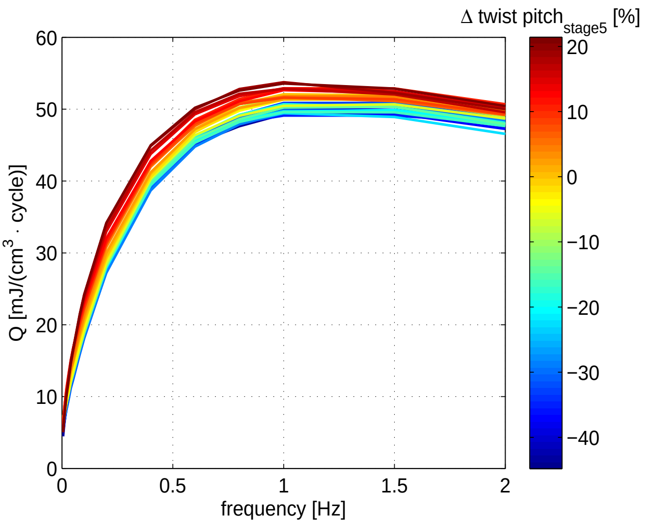

Figure 4.6: Coupling loss density per cycle versus frequency for variations of the twist pitch of stage 5 of the 131-161-241-296-453 mm sequence.

where $L_{p,i}$ is the twist pitch of stage i and N is the number of cabling stages. If the average stage-to-stage twist pitch ratio is calculated for the two sequences of Figure 4.1, it is found that the 131-161-241-296-453 mm sequence has a lower value ($r_{avg} \sim 1.5$) than the cable with 54-59-239-282-347 mm ($r_{avg} \sim 1.9$), which explains the lower loss in spite of the longer pitches.

In Figure 4.7 the coupling loss for an ITER CS-type conductor is shown for different ratios between the successive stages. The first stage twist pitch is set to 80 and 120 mm in the left and right plots, respectively. In both cases the last stage twist pitch is fixed at 450 mm due to its limited influence, see Figure 4.6. The same magnetic field amplitude and frequencies as in the analysis above are applied to these samples; while the inter-strand contact resistivity is set to $30 \cdot 10^{-6} \mu\Omega \cdot \mathrm{m}^2$. This value corresponds to the average inter-strand resistance after several thousands of load cycles of three ITER Toroidal Field conductors tested in the Twente Press Experiment [129, 78]. Figure 4.7 clearly shows the increase of coupling loss with increasing stage-to-stage twist pitch ratio. Given a fixed ratio, the use of a longer twist pitch in the first stage results in higher loss.

For completeness, Figure 4.8 reports the coupling loss obtained for an ITER Toroidal Field-type conductor, experimenting with different stage-to-stage twist pitch ratio sequences as detailed in Table 4.1. All simulations are performed with the same conditions as the calculations leading to Figures 4.2-4.6. In sequences I and II, the use of alternating ratios between the stages is explored. It is observed that the highest loss is achieved for the highest average ratio, and not for the longest initial pitch. On the contrary sequences III to V have constant ratios. In particular sequences IV and V employ the same twist pitch lengths in the five stages but in reversed orders. It can be noticed that the 1.1 sequence shows

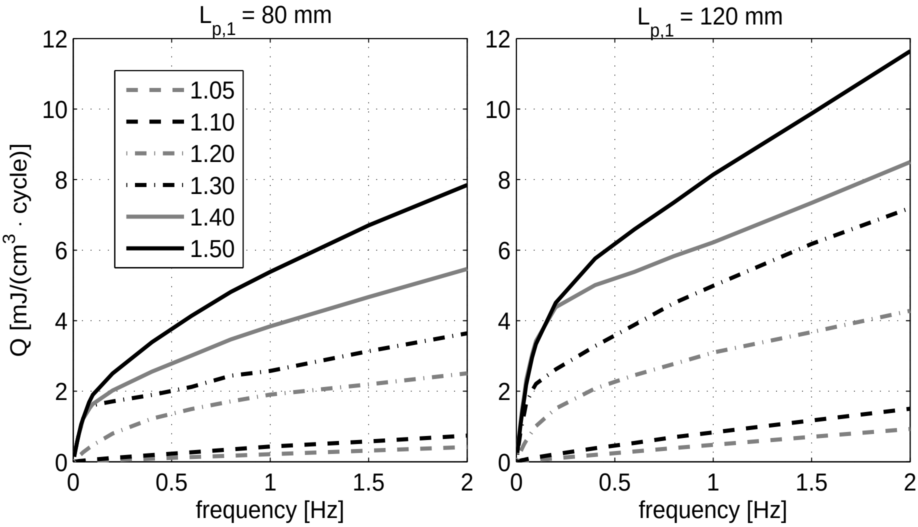

Figure 4.7: Coupling loss density per cycle versus frequency for two ITER Central Solenoid-type conductors with fixed ratios between the twist pitch lengths of successive cabling stages. The initial twist pitch is set to 80 and 120 mm for the left and right cases, respectively. The last stage twist pitch is fixed at 450.

Table 4.1: Additional twist pitch sequences explored in the analysis.

	I	**II**	**III**	**IV**	**V**
$L_{p,1}$ [mm]	120	188	40	341	500
$L_{p,2}$ [mm]	148	213	80	375	454
$L_{p,3}$ [mm]	222	278	160	413	413
$L_{p,4}$ [mm]	274	315	320	454	375
$L_{p,5}$ [mm]	420	420	640	500	341
Twist pitch ratio	1.23 - 1.5 alt.	1.13 - 1.3 alt.	2	1.1	0.9

lower loss than the one with fixed ratio 2, despite having an initial twist pitch $L_{p,1}$ that is more than eight times longer. No relevant difference is found between the sequences with twist pitches in reversed orders. Comparing constant and alternating ratios, it is clear that the first strategy gives the highest reduction of the loss.

The conclusions on the relation between twist pitch sequence and coupling loss discussed in this section hold for any CIC conductors featuring a multi-stage structure as the one assumed in the analysis, i.e. last stage sub-cables surrounded by metal wraps and arranged around a hollow channel for the helium. Such a configuration corresponds to the layout of the Toroidal Field, Central Solenoid and Poloidal Field conductors in ITER. In the case of conductors without petal wraps and central He channel, the effect of the last stage twist pitch on the coupling loss should be re-assessed, while the above conclusions remain valid for all the previous cabling stages. Conductors featuring special internal arrangements of

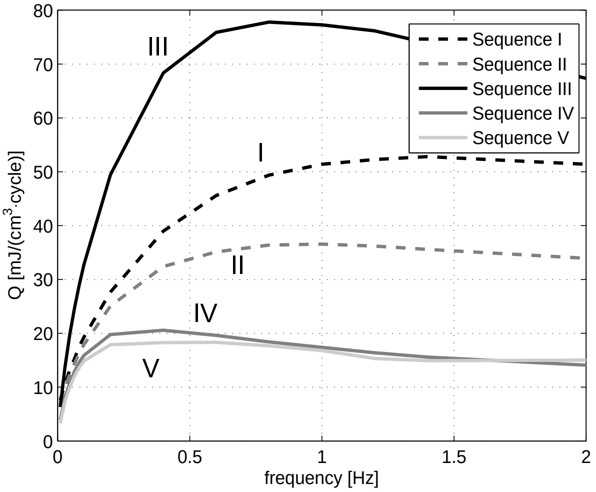

Figure 4.8: Coupling loss density per cycle versus frequency for the twist pitch sequences of Tab. 4.1 in the frequency range 0.01-2 Hz and $B_{AC} = 0.15$ T.

the strands (for example regular strand distributions according to geometrical patterns) should also be considered separately.

Finally, being related to the geometry of the trajectories of the strands, the relation between twist pitches sequence and coupling loss is independent of the strand material, i.e. NbTi or Nb_3Sn.

4.3.1 Loss reduction mechanism

The reduction of the coupling loss with a stage-to-stage twist pitch ratio close to 1 can be understood from the trajectories of the strands. With a traditional twist pitch sequence, the radial distance between pairs of strands varies considerably along the cable, creating wide loops and thus large flux variations. When the ratio between successive stages is kept close to 1, the relative distance between strands varies to a lesser extent along the cable axis, resulting in narrower loops, and hence lower coupling with the changing magnetic flux. This can be visualized in Figure 4.9 showing the trajectories of the superconducting strands in two triplets of an ITER Central Solenoid-type conductor along a length of 0.1 m. The left conductor features the original ITER Central Solenoid nominal twist pitch sequence [15]; while the right conductor has a fixed stage-to-stage twist pitch ratio of 1.1 and initial pitch length of 100 mm.

4.3.2 Verification of the current loop size

In the simulation results presented so far, the coupling losses are computed for relatively short conductor sections (up to 2 m). To verify that the loss reduction observed for stage-to-stage twist pitch ratios close to one is not an artefact of

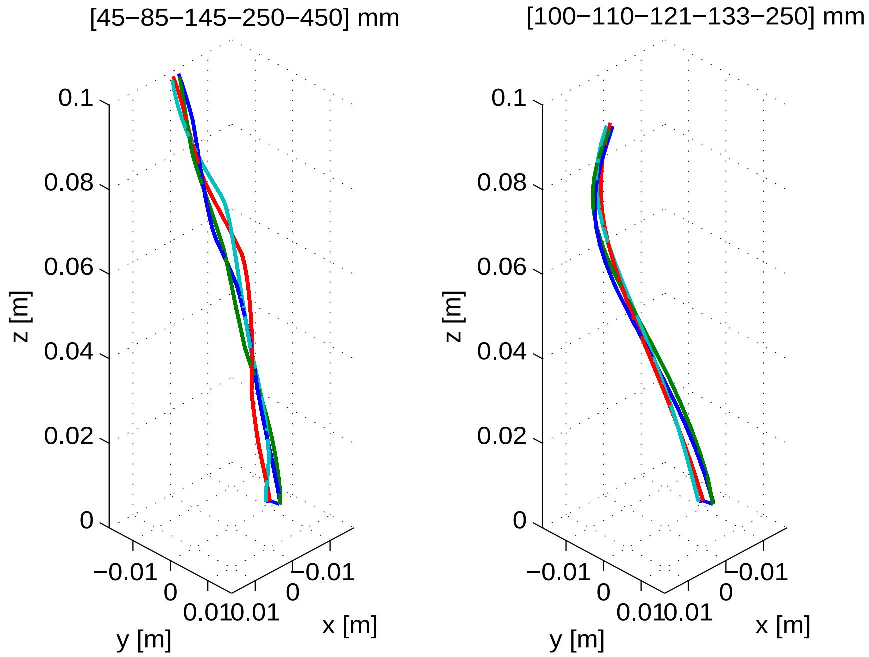

Figure 4.9: Trajectories of four superconducting strands in two triplets of an ITER Central Solenoid-type conductor. (Left) the conductor has the original nominal ITER Central Solenoid twist sequence. (Right) the conductor has a fixed stage-to-stage twist pitch ratio of 1.1 and initial twist pitch length of 100 mm. The values of the twist pitches of the five cabling stages are reported above the plots.

the limited simulation length (e.g. by not allowing the formation of large current loops extending over more than 2 m) coupling losses are also calculated for 10 m long conductor sections. The result is illustrated in the left panel of Figure 4.10 for three Central Solenoid-type conductors with original ITER Central Solenoid nominal twist pitches [15] 'Baseline', ShortŹ (20-45-80-150-450 mm) and LongŹ (110-118-125-139-352 mm) twist pitch sequences. The losses obtained for both, 2 m and 10 m, simulated lengths are practically the same. It can be concluded that in the case of long conductors featuring long pitches and subjected to magnetic field uniformly varying along their length, the formation of large loops carrying significant current is not observed.

As an additional verification, the bottom panel of Figure 4.10 plots the cumulative frequency distribution of the strand currents for the same cases. The peak currents calculated in the 10 m long samples are comparable to the values obtained for the 2 m long conductor. Moreover, the LongŹ twist pitch sequence features a narrower current distribution than the 'Baseline', disproving the occurrence of large current loops for long cabling pitches.

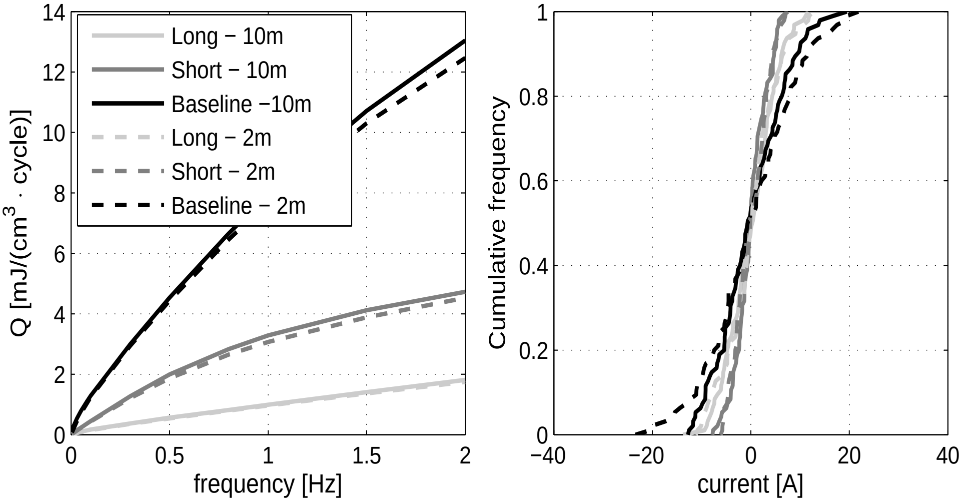

Figure 4.10: (Left) Coupling loss density per cycle versus frequency for an ITER Central Solenoid-type conductor with 'Baseline', 'Short and 'Long' twist pitch sequences for two different simulated lengths (2 m and 10 m). (Right) Cumulative distribution of the strand currents for the same cases.

4.4 Optimization of the twist pitch sequence for the ITER Central Solenoid conductor

4.4.1 Degradation of Nb_3Sn Cable-In-Conduit Conductors

The conductor of the ITER Central Solenoid is designed to carry currents up to 45 kA in a peak magnetic field of 13 T. Due to the Lorentz force produced by the current, the Nb_3Sn strands will experience distributed loads along their length, as well as cumulated loads from other strands transferred at the strand-to-strand contacts. On top of that, the differential thermal contraction between jacket and strands from heat treatment-to-operating temperature produces axial and bending strains.

It is known for a long time that strain in Nb_3Sn strands affects the critical current [130]. This can lead to a significant loss of performance when the conductors are subjected to electro-magnetic and thermal load cycling, as experimentally observed both in coils [115, 117] and in full-size short conductor samples [116, 118]. Figure 4.11 illustrates a worst-case evolution of the current sharing temperature T_{cs} with electro-magnetic loading of the conductor, showing severe progressive degradation. A relatively large drop of the T_{cs} may take place during the first load cycles. After this, the degradation with cycling continues (no saturation is generally observed) although at a lower rate. Further jumps in the T_{cs} can be observed in correspondence with thermal cycles, when the sample is warmed up and cooled down again.

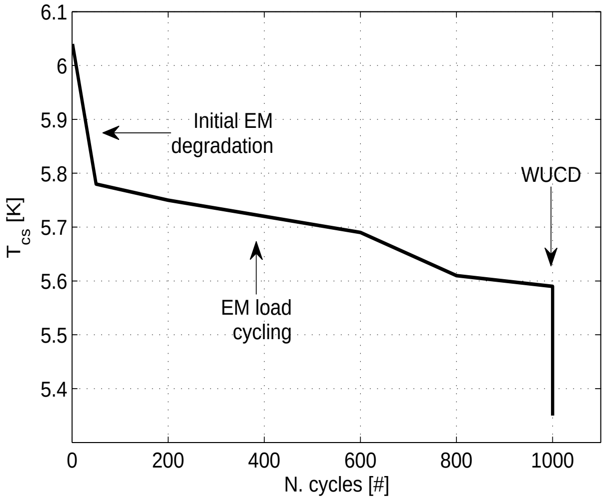

Figure 4.11: Current sharing temperature T_{cs} versus electro-magnetic and thermal (Warm Up Cool Down) cycling for the JASTEC leg of the ITER Toroidal Field conductor sample JATF-6. Data courtesy of P. Bruzzone.

It has to be noticed that such a degradation is not acceptable for practical conductors that need to retain a sufficient temperature margin during all the load cycles envisaged during their operation. As an example, the ITER requirement for the Central Solenoid conductor is a minimum current sharing temperature of 5.2 K after 60000 load cycles and 100 warm-up/cool-down cycles at operating conditions.

It is clear that to avoid a too high performance degradation, the strain in Nb_3Sn conductors, and hence the mechanical response need to be carefully controlled. Since the first tests of the Central Solenoid Model Coils (CSMC) [131], several improvements have been applied to the layout of the Central Solenoid conductor. Steel has substituted the initial Incoloy as jacket material in order to provide thermal pre-compression and thus to reduce the tensile strain associated with strand bending [132, 133]. The void fraction has been lowered from 36% to 33%, whereas the Cu:nonCu ratio increased by 25%. New high-J_c Nb_3Sn strands have been developed and accepted for conductor production as well.

Strain degradation can be controlled as well by proper design of the twist pitches sequence of the strands in the different cabling stages. In this context, two opposing approaches have emerged from the modelling work conducted since the Central Solenoid Model Coil test. A first way to reduce degradation relies on applying long twist pitches in the initial cabling stages. The solution is based on the TEMLOP model developed at the University of Twente to describe the mechanical response of strands within a cable bundle subjected to bending, strand crossing and line contacts under the influence of an electro-magnetic load [134]. The input data of the model are obtained from measurements performed in the

Twente Press Experiment and in the Test ARrangement for Strain Influence on the Strands (TARSIS) [135]. According to TEMLOP, the degradation can be mitigated using long twist pitches, resulting in a more homogeneous transverse load distribution and hence lowering the local peak strain at the strand-to-strand contact points. Alternatively, very short twist pitches have been proposed to solve the degradation issue based on [132, 136]. A reduction of the peak strain due to the shortening of the bending strand section is also predicted by TEMLOP in the case of short twist pitches. Note that, short pitches imply a larger fraction of superconductor required per meter conductor to wind a coil.

The long twist pitch solution was successfully verified in two experimental campaigns [119, 137, 138, 139] and led to the improvement of the ITER Toroidal Field conductor layout. A pseudo-short twist pitch sequence was also tested in the US ITER Toroidal Field 'Alternate' conductor [140, 141] exhibiting a short pitch in the first stage where 6 superconducting strands were cabled around a Cu core and showing no load degradation.

Since long twist pitches are generally associated with large current loops between the strands and therefore a high coupling loss, their application to the ITER Central Solenoid has always been regarded infeasible. However, the trends illustrated in section 4.3 concerning the relation between coupling loss and twist pitches scheme make it possible to combine long twist pitches with low coupling loss for improved degradation performance.

4.4.2 Proposal of a new twist pitch sequence

In 2011, a campaign was launched by the ITER Organization to improve the degradation performance of the conductors for the Central Solenoid, which resulted in the proposal of four cable designs [142]. The main parameters of the four proposed solutions are summarized in Table 4.2.

Table 4.2: Summary of the main parameters of the 4 designs for the ITER Central Solenoid conductor.

	Baseline	**3SC**	**LTP**	**STP**
Cable pattern	(2SC+1)x3x4 x4x6	3x3x4 x4x6	(2SC+1)x3x4 x4x6	(2SC+1)x3x4 x4x6
N. of SC strands	576	864	576	576
Cu:nonCu ratio	1.0	1.5	1.0	1.0
$L_{p,1}$ [mm]	45	45	110	20
$L_{p,2}$ [mm]	85	85	118	44
$L_{p,3}$ [mm]	145	145	126	78
$L_{p,4}$ [mm]	250	250	140	156
$L_{p,5}$ [mm]	450	450	352	423
Twist pitch ratio	1.8	1.8	1.1	2.0
Void fraction [%]	33	33	29	32

The Baseline, Long Twist Pitch (LTP) and Short Twist Pitch (STP) designs all feature the same cabling pattern, but different twist pitch sequences. While the first sample has the original nominal ITER twist scheme, the other two conductors rely on opposite solutions in the attempt to counteract T_{cs} degradation by cyclic loading. Short pitches are used in the STP cable, resulting in a very stiff structure. In contrast, the LTP conductor adopts long twist pitches in the initial cabling stages as suggested in [134]. In order to combine long pitch lengths with limited coupling loss, the outcome of the previous analysis on the interaction between coupling loss and twist pitches sequence is implemented in the design, resulting in a fixed stage-to-stage twist pitch ratio of 1.1 [17]. A fourth sample (3SC) with nominal twist scheme, but higher content of superconductor (3 superconducting strands in the first triplet instead of 2) is also proposed. This last sample also differs from the others in the sense that it has a higher Cu:nonCu ratio of the strands. The void fractions reported in Table 4.2 correspond to the values analysed after jacketing [142].

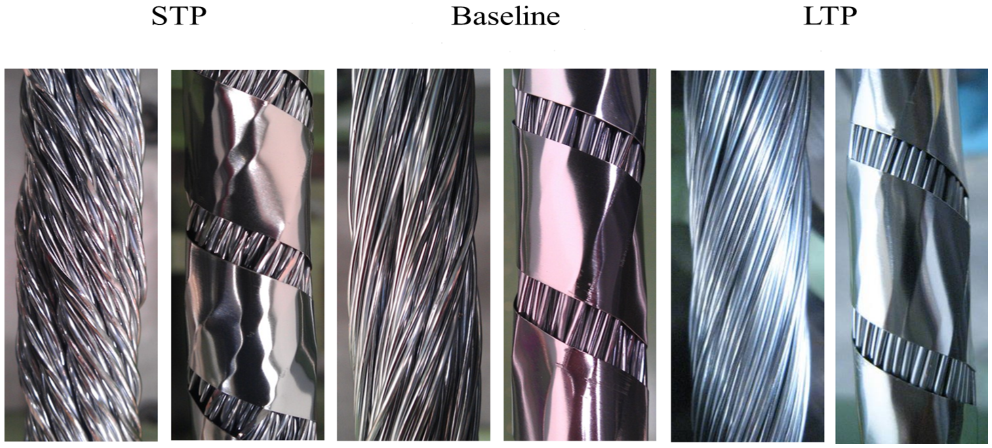

Figure 4.12: The STP (left), Baseline (centre) and LTP (right) petals manufactured at ICAS (Frascati, Italy).

With three out of four designs differing only in terms of twist pitches, they give opportunity to benchmark the coupling loss analysis carried out with JackPot-ACDC in section 4.3, and in particular to test the possibility of reducing the loss by choosing the stage-to-stage twist pitch ratio close to 1. In the next section, the experimental results of the four samples are presented and compared to the coupling loss prediction from JackPot-ACDC.

4.4.3 AC loss and T_{cs} measurements of the four CS conductors

AC loss characterization

The coupling losses a-priori predicted by JackPot-ACDC for the four conductors are illustrated in Figure 4.13 [134]. Since the real parameters were unavailable at the time of the prediction, identical void fraction and inter-strand resistivity

($1 \cdot 10^{-6} \mu\Omega \cdot \mathrm{m}^2$, corresponding to average before cycling conditions) were assumed in the simulation for all samples. The AC magnetic field amplitude was set to 0.4 T. Following the simulation results, the LTP conductor is expected to have the lowest coupling loss, exceeding in this respect also the performance of the STP design due to its stage-to-stage twist pitch ratio close to 1.

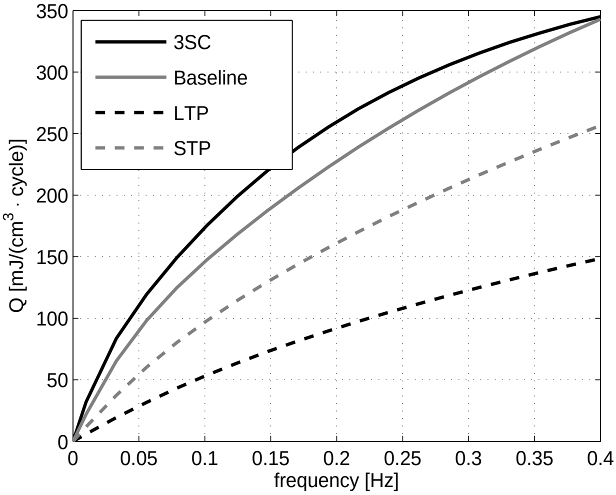

Figure 4.13: Simulated coupling loss density per cycle versus frequency for the four conductor designs proposed for the ITER Central Solenoid with identical void fraction and inter-strand resistivity.

From each of the four proposed designs, two full-size short conductor samples were assembled and tested in the SULTAN facility at CRPP (Switzerland). Two additional 1 m long sections of the LTP and STP conductors, cut from the same unit lengths used for the SULTAN samples, were delivered to the University of Twente for further characterization.

In the SULTAN facility, AC loss measurements were performed before and after the application of load cycles ($\sim$ 11,000 cycles for the Baseline and 3SC samples and $\sim$ 6,000 cycles for the LTP and STP samples). An AC magnetic field of amplitude 0.3 T was applied to the cables with frequency in the range 0.2 to 2 Hz and in the presence of a 2 T background magnetic field. AC loss measurements were carried out at the University of Twente on the conductors in virgin condition with $B_{AC} = 0.4$ T and frequency between 0.05 and 0.85 Hz. The characterization was performed both in 0 T and 1 T background magnetic fields.

Figure 4.14 left, displays the AC loss results obtained in the virgin state at SULTAN and at the University of Twente [143]. In order to properly compare the measurements performed in the different laboratories and with the results of JackPot-ACDC, the experimental values are corrected to take into account the specific experimental and simulation conditions. A first correction is related to the different magnetic field amplitudes employed at SULTAN (0.3 T) and at

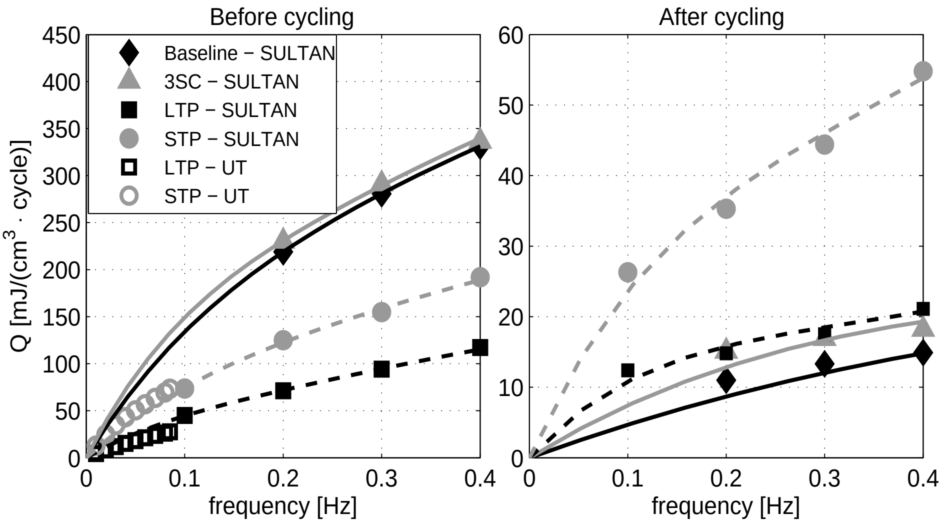

Figure 4.14: Coupling density per cycle loss versus frequency as measured at SULTAN and University of Twente before (left) and after load cycling (right). SULTAN data before cycling are scaled to 30% void fraction and $B_{AC} = 0.4$ T in order to compare them with University of Twente and simulation results.

the University of Twente as well as in the code (0.4 T). Since coupling losses are proportional to the squared value of the AC magnetic field amplitude, the SULTAN data are multiplied by a factor $(\frac{4}{3})^2$ after subtraction of the hysteresis loss. Moreover, since the simulation assumes identical void fractions (30%) for all samples, a second correction is applied to account for the different experimental values. The correction is based on the variation of the coupling loss time constant $n\tau$ with void fraction presented in [144]. Since the loss is expected to be proportional to the $n\tau$ value, a correction factor $\frac{n\tau_{30\%}}{n\tau_{exp\,vf}}$ is applied to the experimental data, where the subscript *exp vf* indicates the void fraction of the sample. Finally, intra-strand coupling loss also contribute to the overall measured loss, while they are not included in the power dissipation computed by JackPo-ACDC. In the present comparison, intra-strand coupling loss is not subtracted from the experimental data, but it is verified to be negligible in the frequency range used in the measurements.

Generally, good agreement is observed between the SULTAN and UT data, once they are normalized to common conditions. The comparison between the experimental data of Figure 4.14 left and the a-priori prediction of the code in Figure 4.13 is remarkably good as well. The code has correctly predicted the scaling of the coupling loss with the different twist pitches sequences. Moreover, the experiment has confirmed the possibility to reduce the loss in long twist pitch sequences by choosing the stage-to-stage twist pitch ratio close to 1, like in the LTP design.

For completeness, the coupling loss measured in the SULTAN facility after cycling is also shown in Figure 4.14 right, without correction applied. After cycling, a direct comparison of the data is only possible between the two legs of each SULTAN sample, i.e. Baseline-3SC and LTP-STP. This is related to the fact that the two samples were subjected to different numbers of load cycles. A significant reduction of the coupling loss is obtained after cycling for the Baseline, LTP and 3SC CIC conductors, in accordance with [144, 77, 145]. On the contrary, a much smaller decrease is observed for the STP due to the stiff structure of the cable resulting from the short pitches.

Steady-state performance characterization

The stiff structure featured by the STP conductor is also confirmed by the evolution of the T_{cs} with load cycling, shown in Figure 4.15.

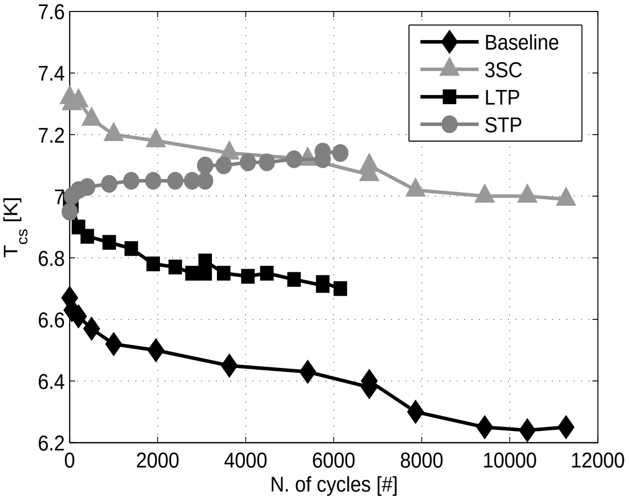

Figure 4.15: Measured T_{cs} with the number of cycles for the four CS conductors. Data courtesy of P. Bruzzone.

Using only the lowest T_{cs} degradation as performance assessment criteria (for steady-state conditions), the STP design appears to be mechanically the most stable conductor. While the T_{cs} of the Baseline, LTP and 3SC designs reduce with the number of cycles, an increase is observed for the STP sample. The result is related to the structure of the cable that presumably leads to a high initial strain state in the strands. The successive application of loads, causing small changes in the positions of the strands, could help alleviating the initial stress, resulting in a T_{cs} increase as argued in [142]. Note that this is the first time that a substantial and stable increase of the T_{cs} with load cycling is experimentally observed.

The higher initial current sharing temperature of the 3SC design is instead due to to the higher number of superconducting strands (Table 4.2) in this conductor.

4.5 Analysis of the EM performance of four ITER Central Solenoid conductor designs exposed to a 15 MA plasma scenario

Although useful to compare the relative performance of the conductors, the conditions applied during the qualification tests in the SULTAN may differ significantly from real ITER operating conditions. Therefore, in order to thoroughly qualify the different conductor designs, it is important to analyse their performance in ITER relevant conditions, i.e. with realistic values for the changing magnetic field and transport current. At present, such conditions cannot be fully reproduced in any of the existing experimental facilities. However, the conductor performance during a 15 MA plasma scenario, see Figure 1.4, taking into account the precise magnetic field and magnetic field change rate on the windings as well as the transport current and its variation in time, can be effectively assessed numerically with JackPot-ACDC.

4.5.1 Simulation conditions

Magnetic field

As mentioned in section 1.2.1, the ITER Central Solenoid comprises six modules whose currents can be independently driven to achieve better shaping of the plasma [5, 146]. Figure 4.16 illustrates how each module consists of a stack of 6 hexa-pancakes plus one central quad-pancake, yielding a total number of 40 and 14 turns in the axial and radial directions, respectively.

Due to their different transport currents and positions inside the ITER magnet system, the six Central Solenoid modules experience different magnetic field conditions during operation. Moreover, the magnetic field is not uniform over the cross-section of the modules, decreasing from the inner to the outer radius. The magnetic field profile along the axial direction depends on the considered module. From a coupling loss and stability point of view, the turns experiencing the highest magnetic field and magnetic field rate should be identified as they are subjected to the severest conditions. Therefore, the magnetic field and its ramp rate until t = 100 s during the 15 MA plasma scenario are calculated with the model described in section 2.5.6. To simplify the magnetic field computation, the coils and plasma are approximated by their current centre lines, as illustrated in Figure 2.18a. However, the magnetic field produced by the analysed module is calculated with a higher accuracy, taking the position of all its turns into account, see Figure 2.18b. The Toroidal Field contribution is neglected, amounting to only a few hundreds mT over the Central Solenoid volume.

The computations show that the worst conditions in pulsed operation are experienced by the turns at the inner radius of the quad pancake of the CSU2 and CSL2 modules.

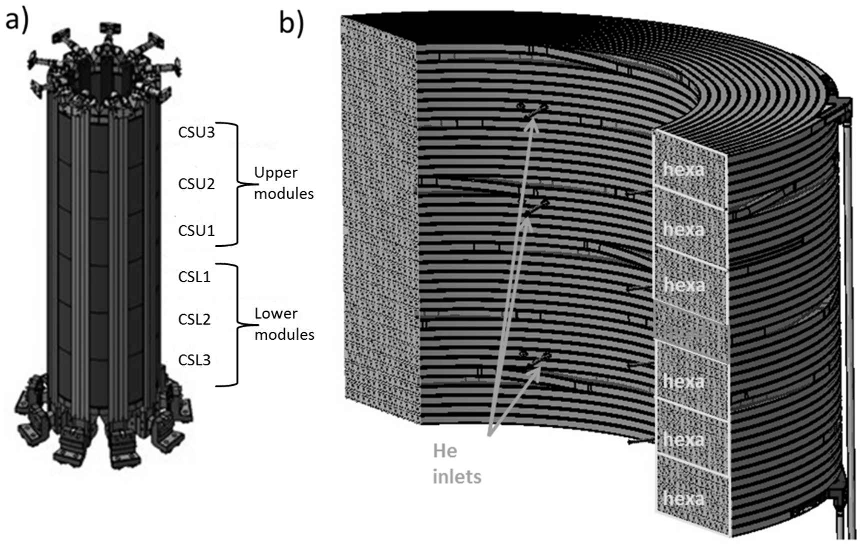

Figure 4.16: (Left) The ITER Central Solenoid comprises 6 modules. (Right) Each Central Solenoid module is a stack of 6 hexa- plus 1 quad-pancakes giving a total of 40 and 14 turns in the vertical and radial directions, respectively. Helium inlets are located at the inner radius of the modules, while outlets are at the outer radius (not shown here).

Temperature boundary conditions and coefficients

A 1 m long section of conductor belonging to the bottom inner turn of the quad pancake of the CSU2 module is selected for the analysis. The sample spans an angle of 40^o, between 80^o and 120^o with respect to the ITER system of reference. The choice of this location is because a helium inlet is located at 80^o of the inner radius of axial turn 22 of each module. This allows to set the temperature boundary condition accurately, which is 4.5 K at the inlet.

The thermal routine described in section 2.5.10 is used to estimate the temperature increase produced by the sum of coupling and hysteresis losses. It computes thirteen temperature variables at each cross-section, corresponding to the temperature of the strands and helium in the six petals and the temperature of the helium in the central channel. Table 4.3 summarizes the values of the main parameters of the thermal model [72].

Table 4.3: Main parameters of the thermal model of the Central Solenoid conductor under operating conditions.

Parameter	**Unit**	**Value**
Total He mass flow	g/s	8.33
Petal-Petal heat transfer coefficient	$W/(m^2{\cdot}K)$	330
Petal-Central channel heat transfer coefficient	$W/(m^2{\cdot}K)$	393
Petal-He in petal heat transfer coefficient	$W/(m^2{\cdot}K)$	1000

Inter-strand resistance

The inter-strand resistivity parameters used in the simulations are estimated, as described in section 2.5.3, by fitting the AC loss measurements performed at the SULTAN facility before and after load cycling of the conductors. Table 4.4 summarizes the resistivity parameters obtained from the fits by minimizing the difference between the measured and simulated coupling losses. To account for the presence of wraps around the last stage sub-cables that strongly decrease the inter-petal conductance, a two parameters fit (accounting for different intra-petal ρ'_{ss} and inter-petal ρ'_{ip} resistivities) is used to reproduce the measurements.

Table 4.4: Summary of the resistivity parameters used in the analysis.

Sample	**Before cycling**		**After cycling**	
	ρ'_{ss} [$\mu\Omega{\cdot}\mathrm{m}^2$]	ρ'_{ip} [$\mu\Omega{\cdot}\mathrm{m}^2$]	ρ'_{ss} [$\mu\Omega{\cdot}\mathrm{m}^2$]	ρ'_{ip} [$\mu\Omega{\cdot}\mathrm{m}^2$]
Baseline	$1.7{\cdot}10^{-6}$	$4.0{\cdot}10^{-3}$	$8.4{\cdot}10^{-5}$	$2.0{\cdot}10^{-1}$
3SC	$2.0{\cdot}10^{-6}$	$5.0{\cdot}10^{-3}$	$9.5{\cdot}10^{-5}$	$8.5{\cdot}10^{-2}$
LTP	$6.7{\cdot}10^{-7}$	$8.0{\cdot}10^{-5}$	$5.0{\cdot}10^{-6}$	$1.0{\cdot}10^{-2}$
STP	$7.0{\cdot}10^{-7}$	$7.0{\cdot}10^{-5}$	$2.0{\cdot}10^{-6}$	$8.0{\cdot}10^{-4}$

The parameters in Table 4.4 are derived from measurements carried out in a 2 T background magnetic field. During a plasma scenario, the magnetic field on the Central Solenoid windings varies in the 0 to 13 T range, resulting in a non-negligible change of the inter-strand resistance due to magneto-resistance. The effect is taken into account in the simulation and it is quantified based on the available AC loss measurements of the ITER CSJA3 sample, which have been performed at both 2 and 9 T background magnetic field. The assumption made here is that the influence of the magneto-resistance is representative for the different strand types. The measured losses at different background magnetic field are fitted with JackPot-ACDC. Because of the magneto-resistance, the resistivity increases at higher background magnetic fields. By linearly interpolating/extrapolating the resistivity change between 2 and 9 T, the inter-strand resistance can be corrected for the magneto-resistance during the plasma scenario simulation.

Note that the AC loss measurements used for the resistivity parameter estimates are performed without transport current in a relatively low transverse background magnetic field (2 T). In these conditions, no Lorentz force acts on the conductor. However, during an operating plasma scenario a Lorentz force will be present that, pressing the strands against each other, will cause a reduction of the inter-strand resistance [144, 147]. As a result the actual coupling loss under applied electromagnetic load in operating conditions will be higher than the values computed by JackPot-ACDC.

Current boundary conditions and scaling law

Given the limited length of conductor that can be handled by the code within an acceptable CPU time, the current distribution produced by the joints is not included in the model. Therefore, a uniform transport current distribution among the superconducting strands is imposed at the boundaries of the simulated section. Since the Central Solenoid modules are operated in pulsed mode, the current boundary conditions are expected to have only a minor influence on the coupling loss.

The Nb_3Sn strain scaling law, n-value and critical current dependence on the strand-field angle are discussed in sections 1.3 and 2.5.8. Since the specific strands used in the analysed samples have not been tested for the purpose of strain scaling, the parameters of the OST10098 strand [143], measured at University of Twente, are used. To adapt these data to the simulated strands, it is assumed that a correction of only the parameter C in the scaling law is necessary. The argumentation for this correction and for the chosen axial compressive strain, set to $\epsilon = -0.6\%$, are given in [143].

4.5.2 Simulation results

The results are presented for the four Central Solenoid conductors designs during a 15 MA plasma scenario up to t = 100 s, which is the most severe time interval with respect to the magnetic field and magnetic field ramp rates experienced by the coils, see Figure 1.4. Simulations are carried out both with inter-strand resistance values corresponding to before and after load cycling conditions, as listed in Table 4.4. Note, when comparing the results after cycling that while the Baseline and 3SC conductors have undergone more than 11,000 cycles, the LTP and STP ones have only been cycled 6,000 times. Some caution is also necessary when extrapolating to larger number of load cycles since no relevant conductor test data are yet available, nor foreseen, up to the 60000 cycles specified for the Central Solenoid operation.

Coupling and hysteresis losses

Figure 4.17 illustrates the coupling loss per meter of simulated conductor for each Central Solenoid design variant, both before (top) and after (bottom) load cycling. The simulation shows that before cycling the LTP conductor displays a significantly lower power dissipation than the other three cables, especially at the Start of Discharge, i.e. t ∼0 s. The result is in line with the simulations and measurements carried out in AC magnetic field. The other three designs exhibit roughly twice the LTP loss during the entire simulated time range. After cycling, the STP conductor dissipates significantly more than the other conductors. The higher dissipation is related to the limited increase of the inter-strand resistance with cycling in this design. In the plot after cycling, it can be noticed that the LTP conductor has not anymore the lowest power loss. This is caused by its lower void fraction in combination with the higher number of load cycles experienced by the Baseline and 3SC conductors.

The hysteresis loss in the centre of the four cables sections is shown in Figure

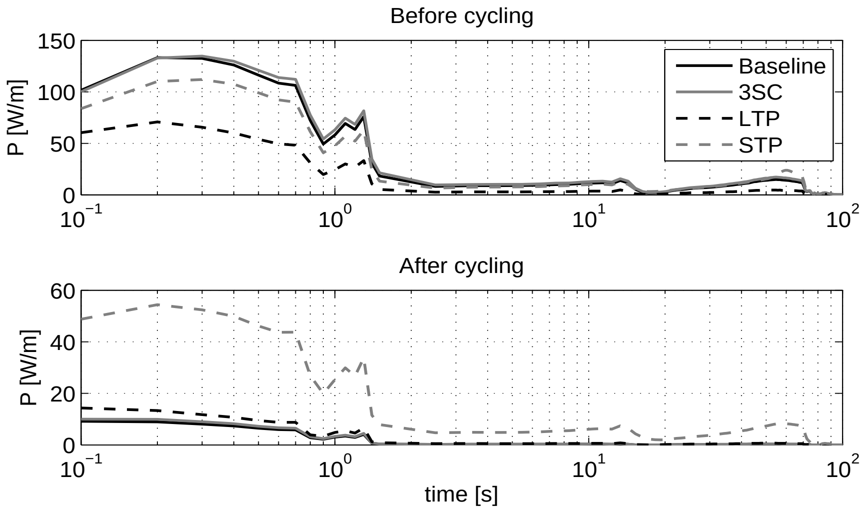

Figure 4.17: Coupling loss per meter versus time for the four designs for 0<t<100 s during a 15 MA plasma scenario before (top) and after (bottom) cycling.

4.18. As expected, the 3SC design features the highest hysteresis loss due to the

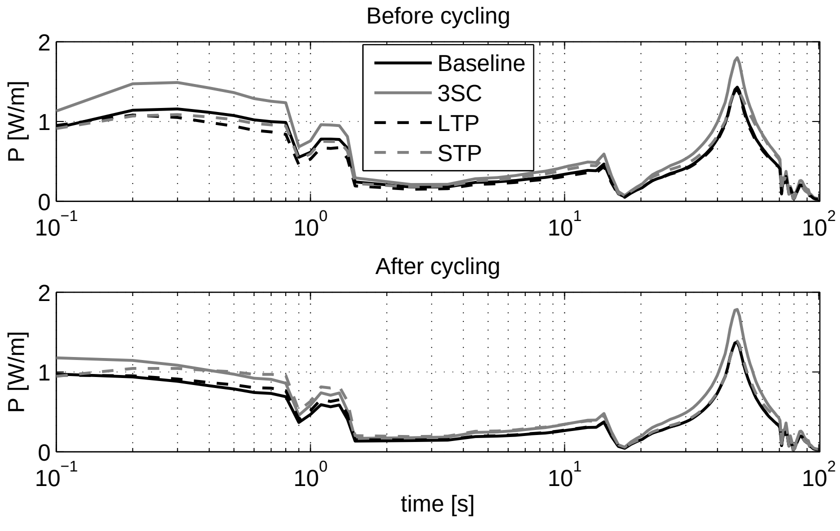

Figure 4.18: Hysteresis loss per meter versus time for the four designs for 0<t<100 s during a 15 MA plasma scenario before (top) and after (bottom) cycling.

higher content of superconductor; while the other three samples have practically similar values. As foreseeable, no relevant variation of the hysteresis loss is observed with cycling. The plots of the hysteresis loss versus time show two main peaks. The first one, located at t ∼0 s is due to the strong magnetic field change rate characterizing the Start of Discharge. The second peak at t ∼50 s is caused by a decrease of the absolute value of the magnetic field combined with a reduction of the average strand-magnetic field angle, both causing a large increase of the critical current density. However, when comparing Figures 4.17 and 4.18, it is concluded that the magnitude of the hysteresis loss in all conductors is negligible when compared with the coupling loss.

Strand current distribution

Figures 4.19 and 4.20 show the strand currents, sum of the transport and coupling currents, at the centre of the conductor sections before and after cycling.

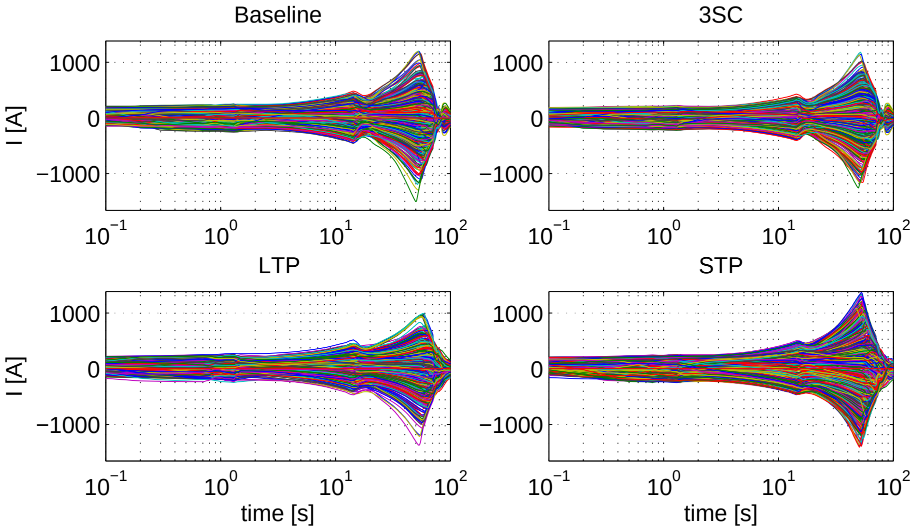

Figure 4.19: All strand currents versus time for 0<t<100 s during a 15 MA plasma scenario at the center of the four CIC conductors before cycling. Different colours represent different strands.

During the simulated portion of scenario, the largest spread in the strand current distributions is achieved around t ∼50 s, and not at the Start of Discharge when the conductors experience the largest magnetic field variations. This is likely related to the very fast nature of the initial transient, which does not allow the development of large coupling currents.

Before cycling, the STP conductor shows slightly higher peak strand currents at t ∼50 s compared to the other three design variants, while the difference is more contained at the Start of Discharge. On the contrary, after several thousands of load cycles the currents in the strands of the STP conductor are significantly higher along the entire simulated scenario. This is a consequence of the stiff structure of the STP conductor, resulting in a lower increase of the inter-strand contact resistance with load cycling than in the other tested cables. A larger spread in the strand current distribution is associated to a reduced stability margin especially at the Start of Discharge when the conductors experience a relatively large

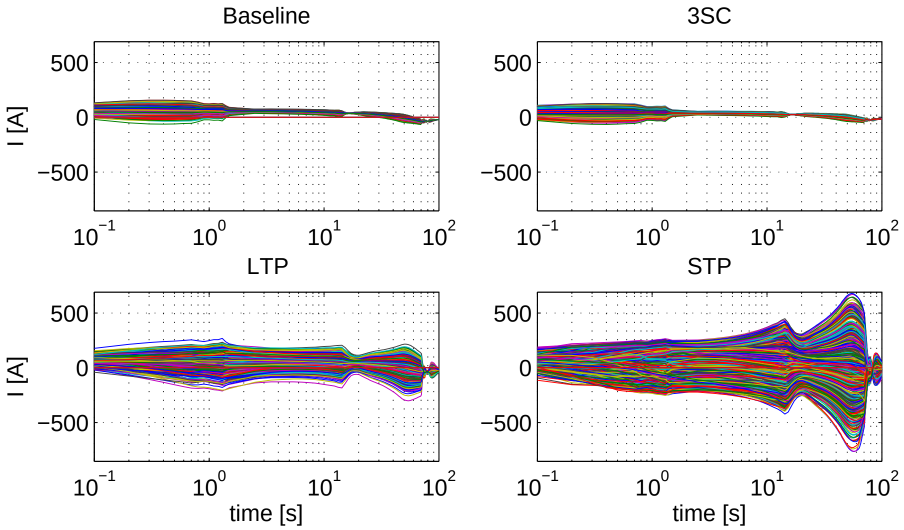

Figure 4.20: All strand currents versus time for 0<t<100 s during a 15 MA plasma scenario at the center of the four conductors after cycling. Different colours represent different strands.

magnetic field, which lowers the critical current of the strands.

The strand current cumulative distribution functions of the four conductors are shown in Figure 4.21. They are determined considering the strand currents

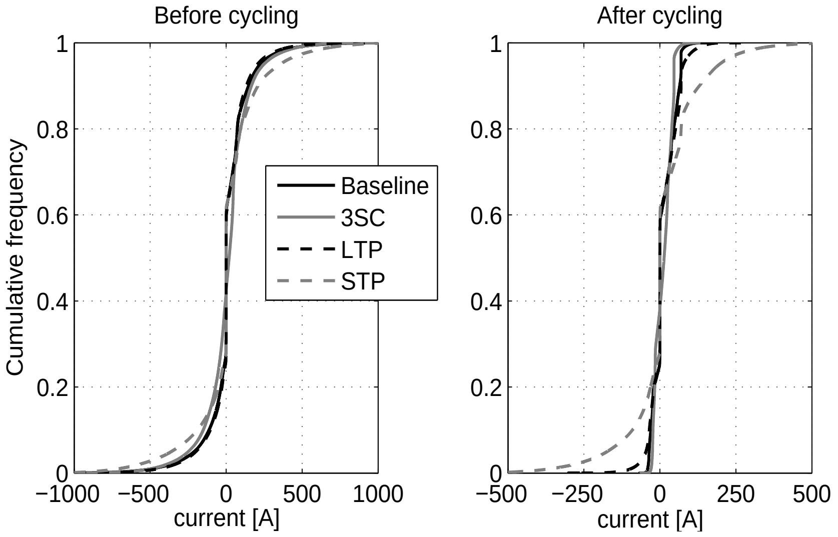

Figure 4.21: All strand current cumulative distribution functions for the four conductor designs before and after cycling.

over all the strand positions within the cable and at all simulated times. Also here, it can be noticed that the Baseline, 3SC and LTP conductors have similar distributions, with the LTP characterized by slightly higher peak values. The STP distribution on the other hand is significantly different, showing clearly a more frequent occurrence of large currents especially after cycling.

Effective temperature margin

From the overall power dissipation, the average temperature increase of the six petals of each conductor is calculated with the model described in section 2.5.10. The average petal temperature evolution during the simulated scenario is depicted in Figure 4.22. Since it has the highest dissipation among the conductors, the STP design variant features also the largest temperature increase after cycling, with a maximum of 4.97 K for the average petal temperature at the Start of Discharge, which is remarkably higher than the 4.60 K of the other three design variants.

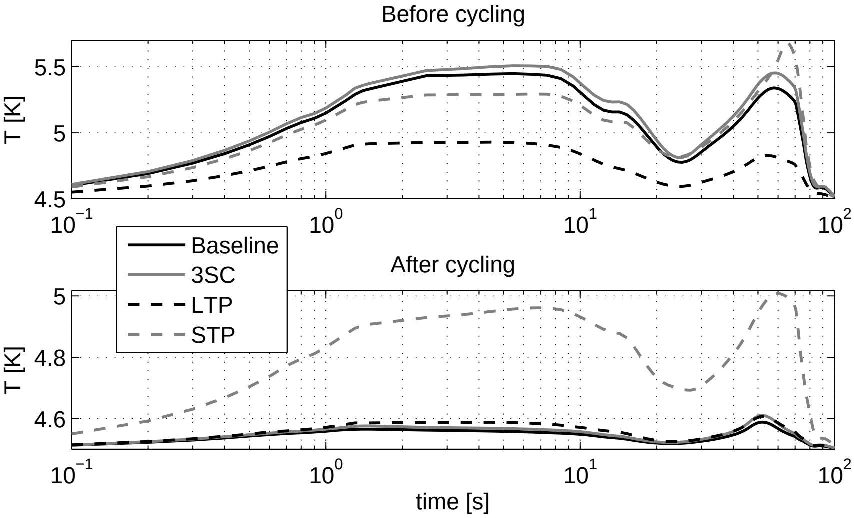

Figure 4.22: Average petal temperature versus time in the four conductor designs for 0<t<100 s during a 15 MA plasma scenario.

The general acceptance criteria to qualify the performance of ITER conductors consists in assessing the evolution of the T_{cs} of full-size short conductor samples under steady-state conditions with electro-magnetic and thermal load cycles. Based on this procedure, the STP conductor can be regarded as the best performing solution since it shows no decrease (even an increase) of its T_{cs} with cycling, see section 4.4.3. However, since the Central Solenoid is a pulsed coil, as shown in Figure 4.22, the four design variants will result in different temperature increases in the superconducting strands during a plasma scenario. Consequently, to use the measured current sharing temperature T_{cs} under steady-state conditions as a criterion alone is not enough to qualify the best performing solution. It is more relevant to take into account the difference between the maximum temperature during operation and the experimentally determined T_{cs}, called the effective temperature margin, as a selection criterion as well.

The effective temperature margin based on the computed peak petal temperature at the Start of Discharge is summarized in Figure 4.23. A correction accounting for the higher superconducting Nb_3Sn content is applied to the temperature difference of the 3SC sample for a fair comparison with the other cable patterns [143]. It is observed that before cycling, i.e. in virgin state, the LTP design features the highest effective temperature margin. On the contrary, after cycling, the STP conductor holds the peak ΔT of the four design variants, with a value of almost 2.2 K. However, the effective temperature margins of the LTP and STP conductors are practically the same, differing by 70 mK in spite of their large difference in T_{cs}. This issue is a direct consequence of the locked structure of the strands in the STP sample, causing only a small reduction of the coupling loss with cycling. Therefore, in this conductor the apparent advantage of a higher T_{cs} under steady-state conditions is in reality partially cancelled by a significantly higher strand temperature increase during operation in pulsed mode. Note that the increase in T_{cs} with number of load cycles as observed in the short sample test of the STP has yet to be confirmed for a long STP-like conductor in a relevant test coil.

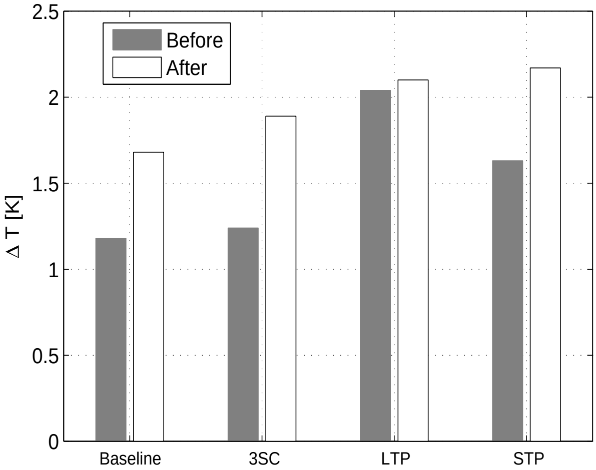

Figure 4.23: Effective temperature margin, defined as the difference between the predicted peak petal temperature at the Start of Discharge during a 15 MA plasma scenario and the experimentally determined T_{cs} for the four conductors before and after cycling.

Figure 4.23 shows an effective temperature margin for all four conductors variants exceeding 1 K and 1.5 K before and after cycling, respectively. Therefore, based on the analysis of the petal temperature and assuming that the T_{cs} degradation rate will not increase compared to the value at the highest number of load cycles reached in the experiment, successful operation of all four designs can be expected during the entire 60000 cycles life-time of the Central Solenoid coils

[143].

Although useful to compare the relative performance of the four designs, the effective temperature margin as defined in this section may not be the relevant parameter to judge the stability of a conductor in pulsed operation. On the contrary, the appearance of zones inside the conductor locally exceeding the critical current, and as a consequence the local temperature margin, should be taken into consideration when assessing the stability of the four conductor designs during a plasma scenario, as also recently advocated in [148].

Strand current margin

The current margin ΔI of a strand is defined as the difference between its critical current and actual current. Figure 4.24 shows the evolution of the minimum strand current margin up to t = 80 s during a 15 MA plasma scenario before and after cycling. For the minimum strand current margin, the lowest value of the strand current margin among all the strands at every position inside the conductor is taken.

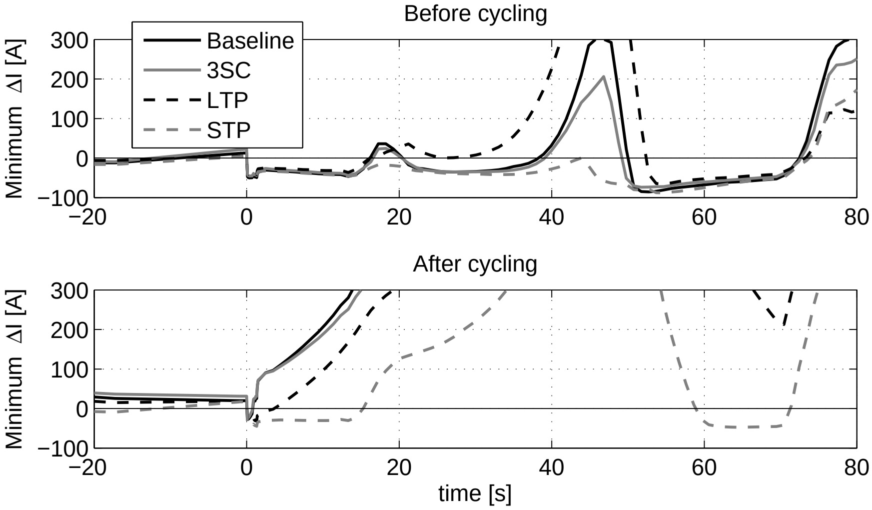

Figure 4.24: Minimum strand current margin among all strands in the four conductor variants versus time for -20<t<80 s during a 15 MA plasma scenario before (top) and after (bottom) cycling.

Before cycling, in all four conductors, strands are found that exceed their current margin by a few amperes already before the start of the plasma. The excess current increases with a maximum of about 50 A at the Start of Discharge. The evolution in the following phase depends on the cabling pattern. While the Baseline, 3SC and LTP conductors show a temporary recovery of the current margin, followed by a second dip, some of the STP conductor strands exceed their current margin up to about 70 s. After cycling, only the STP conductor shows a negative current margin prior to the Start of Discharge. At the Start of Discharge, all four conductors have strands with negative margins although for different time spans. While the Baseline and 3SC designs recover within 1 s; it takes 4 s and 15 s for the LTP and STP, respectively, to arrive at a positive current margin again. The minimum strand current margin is an extreme criterion and obviously it is important also to look at the number of strands exceeding their critical currents and their distribution over the cross section of the conductor.

The negative current margin shown in Figure 4.24 may seem to disagree with the large temperature margin estimated in the previous section. However, it should be noted that:

- the temperature margin is computed using the peak value at the Start of Discharge of the average petal temperature. However, strands can locally reach higher temperature values at the locations where the critical current is exceeded;
- the operation in pulsed mode is characterized by very different conditions compared to the steady-state conductor tests. Coupling currents can locally cause a considerable increase of the strand currents on top of the transport current, giving rise to large and more or less uniformly distributed dissipation areas in the cross-section of the cable depending on the position of the strands carrying excess-current. The spatial heat generation pattern not only affects the current re-distribution, but also the heat exchange with the helium coolant. Considering this, the conditions determining the stability of a conductor in pulsed mode can be significantly different from the ones during steady-state tests.

As a consequence, the qualification of the performance in pulsed mode through the T_{cs} alone or in terms of an effective temperature margin ΔT defined as in the previous section may not be sufficient to secure the stability of the conductor under the most severe operating conditions.

The question that arises from Figure 4.24 obviously is whether the presence of strands locally exceeding their critical current, and hence also stability, margin would result in a quench of the entire conductor. This question cannot be indisputably answered at present due to the limitations of the thermal model that computes only the average temperature of the petals. In reality, higher temperature values in individual strands or clusters of strands can be reached at the locations where the strands are driven far into saturation. As a consequence, considerable voltage drops could accumulate along strand sections exceeding their current margin, leading to a local normal zone and forcing a re-distribution of the excess current. The current re-distribution process is less efficient in the simulation using the lower average petal temperature, which can be considered as conservative. Even with a thermal model computing the local temperature of the strands, it still remains questionable whether a quench of the entire conductor can be reliably predicted since such a detailed model involves several parameters of which the accuracy is difficult to assess, making the overall precision of the prediction controversial.

Although the occurrence of a full conductor quench cannot be confirmed, the fraction and concentration of strands exceeding their critical current allow a cautious qualitative assessment of the probability of local quenches in strands and sub-cables. Figure 4.25 illustrates the distribution of excess-currents for the strands in the four conductors after cycling at the centre of the simulated lengths at t = 0.5 s. The red dots correspond to strands exceeding their critical current, whereas blue dots represent strands carrying a sub-critical current.

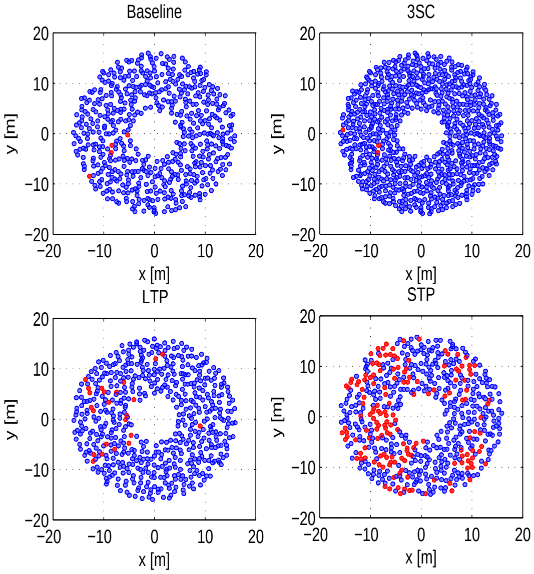

Figure 4.25: Distribution of excess-currents of the four conductor designs at the center of the simulated lengths at t = 0.5 s, after cycling. Red and blue dots correspond to strands having negative and positive current margins respectively.

After cycling only few strands exceed their critical current in the Baseline, 3SC and LTP designs, by which also sufficient current carrying capacity exists in their immediate surroundings. On the contrary, significantly more and closely packed red dots emerge from the STP plot, which is a clear indication that current redistribution is more problematic in this conductor.

Electric field

More insight in the stability of the four conductors may bring the comparison of the simulated peak electric field during the plasma scenario and the electric field at quench measured during steady-state T_{cs} tests. In Figures 4.26 and 4.27, the upper plots show the calculated average electric field along the strands before and after cycling. The bottom plots show the evolution of the electric field along the strands versus temperature measured during the steady-state T_{cs} test for the same cycling conditions.

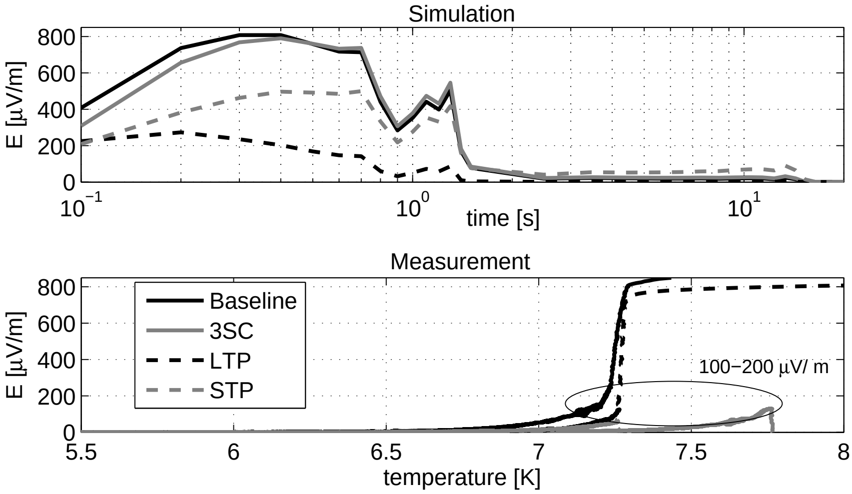

Figure 4.26: (Top) Calculated average electric field along the strands versus time for 0<t<20 s during a 15 MA scenario before cycling of the conductors. (Bottom) Measured electric field along the strands versus temperature during T_{cs} tests before cycling. Data courtesy of P. Bruzzone.

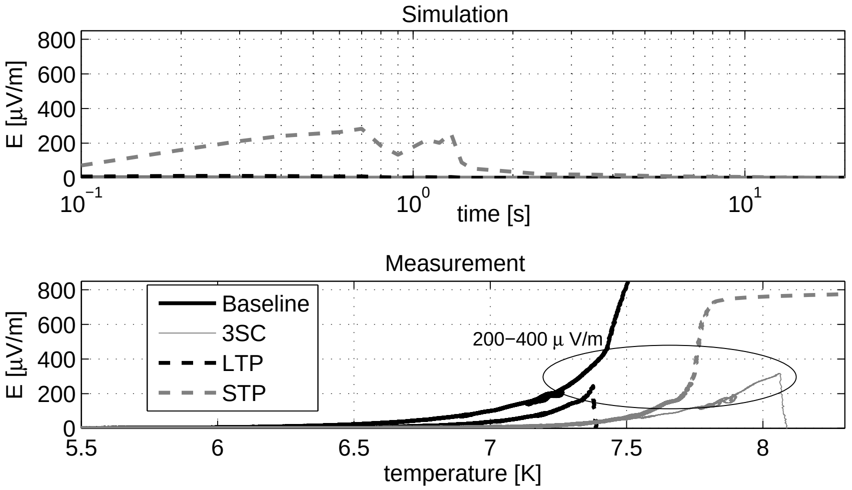

Figure 4.27: (Top) Calculated average electric field along the strands versus time for 0<t<20 s during a 15 MA scenario after cycling of the conductors. (Bottom) Measured electric field along the strands versus temperature during T_{cs} tests after cycling. Data courtesy of P. Bruzzone.

The measured electric field at quench in steady-state conductor tests varies in the range 100-200 $\mu V/m$ before and 200-400 $\mu V/m$ after cycling, respectively. The comparison with the calculated values reveals that all samples are exposed to electric field levels far above the steady-state quench level at the Start of Discharge before cycling. However, after cycling the maximum computed electric fields for the Baseline, 3SC and LTP conductors are far below the experimentally observed steady-state quench values. On the other hand, under the same conditions the STP design reaches a critical electric field value of 280μV/m, which may imply a significant risk for a quench.

The analysis of the maximum local electric field across the strand segments points in the same direction. As illustrated in Figure 4.28, after cycling the STP conductor features both the highest local maximum electric field and, most importantly, the highest probability density of high local electric field values.

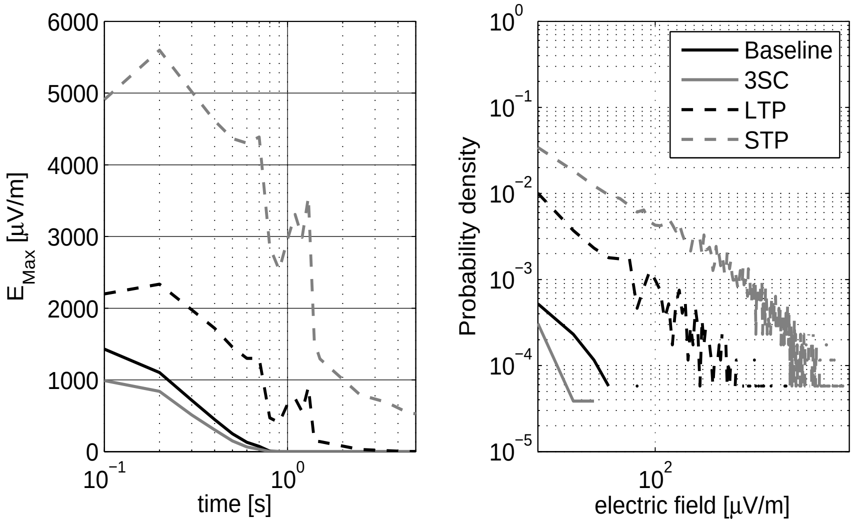

Figure 4.28: (Left) Maximum local electric field versus time for 0<t<5 s during a 15 MA plasma scenario. (Right) Probability density of the local electric field in the four conductor designs after cycling at t = 0.7 s.

Transient stability

The main issue of comparing electric field levels as presented above is that quasi steady-state quench conditions may differ significantly from pulsed ones. It is well-known that the transient stability margin of superconductors is also determined by the time duration and spatial distribution of the disturbance [149]. As discussed in Chapter 3, a quench in steady-state is tightly related to the existence of a magnetic field gradient over the cross-section of the conductor, which leads to a very localized power dissipation. On the other hand, the flow of coupling currents in pulsed mode involves practically the entire cross-section, giving rise to a more uniform heat generation. Moreover, during strong thermal transients the heat transfer coefficient h at the strand surface is different because of thermal diffusion in the boundary layer, and the induced flow in the heated compressible helium associated with increased turbulence and thus again an increase in h [150, 151, 152]. As a consequence, the strand-to-helium heat transfer coefficient may increase significantly during fast transients, allowing the conductor to survive larger heat depositions. A better quench risk assessment of the four Central Solenoid conductor designs would, therefore, require a correlation with quench data under pulsed conditions.

Although plasma scenario conditions cannot be reproduced in the present facilities, transient stability tests have been carried out in the past on few Nb_3Sn conductors to study their quench performance under fast magnetic field pulses [109, 153, 154]. The conductor, carrying a current of typically few tens of kA, is placed in a relatively high steady-state background magnetic field. A single full-wave or half-wave sinusoidal magnetic field pulse is then applied, and its amplitude increased until the sample quenches. The test is performed at constant temperature margin, defined as the difference between steady-state T_{cs} and operating temperature.

No transient stability measurements have been carried out in the framework of the Central Solenoid designs characterization. Transient stability results though are reported for a SULTAN sample assembled from a spare cable of the inner layer of the Central Solenoid Model Coil. However, the sample suffered from serious current imbalance produced by a non-optimal joint assembly, that heavily affected the stability results [109]. Therefore, the transient stability data from the so-called Secret-A conductor [153] are presented here as a reference for quench behaviour in pulsed magnetic field conditions. In Table 4.5 the main characteristics of the conductor are listed. Comparing with the Central Solenoid cable data in Table 4.2, it can be noted that although it is a sub-size conductor, the Secret-A cable is similar to a last stage sub-cable of the Central Solenoid conductor.

Table 4.5: Summary of the main parameters of the Secret-A conductor.

	SecretA
Cable pattern	3x3x4x4
N. of SC strands	144
Cu:nonCu ratio	1.5
$L_{p,1}$ [mm]	51
$L_{p,2}$ [mm]	76
$L_{p,3}$ [mm]	136
$L_{p,4}$ [mm]	167
Void fraction [%]	36.8

In order to obtain the quench energy density of the Secret-A conductor in convenient units that can be compared with the power generation computed for the four Central Solenoid design variants during a 15 MA plasma scenario, the transient stability test of the Secret-A sample is simulated with JackPot-ACDC. In the simulation, a conductor section of about 320 mm long is exposed to a single full-wave sinusoidal magnetic field pulse of period $T_{pulse} = 65$ ms. The amplitude of the pulse is set equal to the value necessary to quench the sample in the experiment. The cable carries a current of 12 kA and is placed in a 9.71 T background magnetic field. Simulations are performed for the temperature margin of the conductor varying in the 0.4 to 1.6 K range, with a He mass flow rate of 3.5 g/s.

Figure 4.29 shows the computed quench energy density (normalized to superconductor volume) of the Secret-A conductor for various simulated temperature margins (empty squares). The energy is given by the sum of the dissipation along the superconducting strands and in the inter-strand contacts. Inter-filament coupling losses following Eq.2.10 ($n\tau = 1.45$ ms) are also included as they were observed to represent a relevant fraction of the Secret-A conductor dissipation during AC loss test [109]. For comparison, the energy dissipated in the four Central Solenoid conductors, both before (full triangles) and after (empty triangles) cycling, between 0<t<2 s during a 15 MA plasma scenario is included as well.

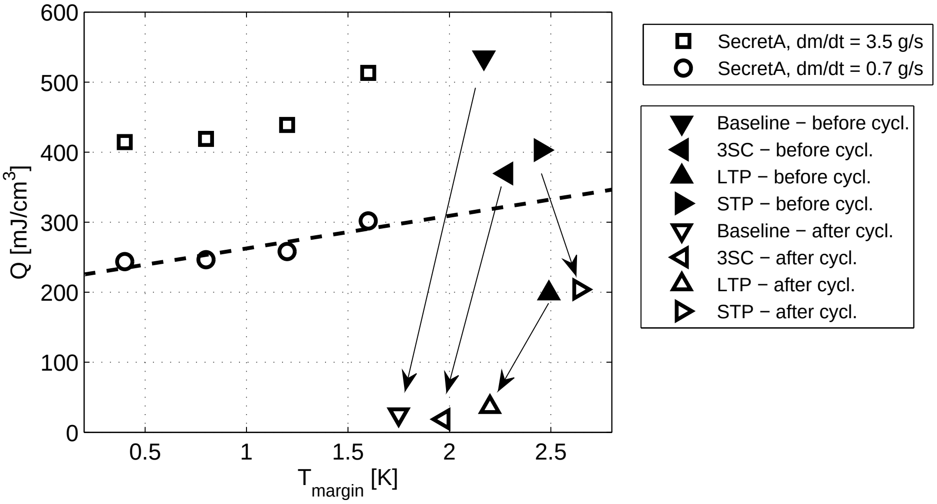

Figure 4.29: Quench energy density versus temperature margin from the simulation of the transient stability tests on the Secret-A conductor with a helium mass flow rate of 3.5 g/s, and scaled down to 0.7 g/s. For comparison the predicted energy dissipation density for 0<t<2 s during a 15 MA plasma scenario for the four Central Solenoid designs before and after cycling is also reported.

Figure 4.29 shows that the energy density required to quench the Secret-A sample in the transient stability tests is relatively larger than the energy dissipated at the Start of Discharge in any of the Central Solenoid conductors after cycling. However, in order to correctly compare the data, the different He mass flow rate in the Secret-A tests (3.5 g/s) and in the Central Solenoid operation (0.7 g/s per petal) should be taken into account.

The correction of the computed quench energy density of the Secret-A conductor for the lower mass flow rate in the Central Solenoid is carried out according to the results of a second series of experimental tests performed at a constant temperature margin of 1 K and for convenience reported in Figure 4.30 [153]. The transient stability of the conductor in Figure 4.30 is expressed in terms of the time integral of the squared magnetic field change rate, which is proportional to the energy loss caused by the magnetic field pulse, and hence to the quench energy of the sample [153]. In the case of the Secret-A conductor, the tests reveal a progressive improvement of the transient stability with the mass flow: the energy necessary to quench the sample increases up to a factor 2 as the He mass flow rate is varied by a factor 4.

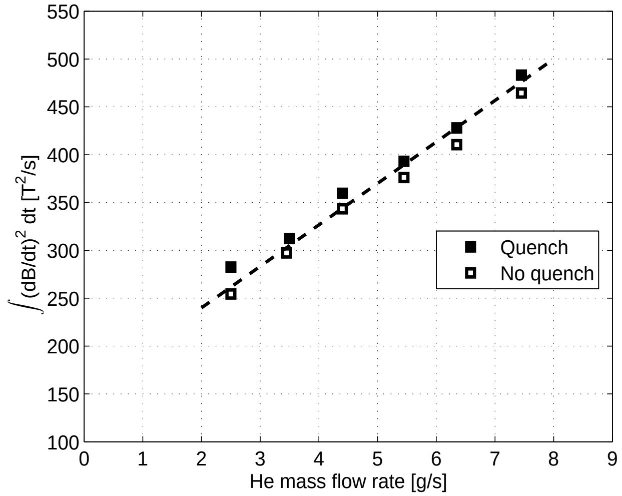

Figure 4.30: Transient stability quench energy, expressed through the time integral of the squared magnetic field change rate, versus He mass flow rate at constant temperature margin (1 K) for the Secret-A conductor. Data courtesy of P. Bruzzone.

Based on the trend in Figure 4.30 a reduction of the quench energy by a factor 1.7 can be expected for a reduction of the mass flow rate from 3.5 g/s to 0.7 g/s. The quench energy density corrected for the He mass flow rate is also reported in Figure 4.29 (empty circles); a line extrapolating the trend to the temperature margin range of the Central Solenoid samples is included as well.

After the mass flow correction, a large and thus safe stability margin exists between the reference Secret-A transient quench energy density scaled to 0.7 g/s and the plasma scenario dissipation of the Baseline, 3SC and LTP conductors. This margin appears to be instead smaller for the STP conductor, although retaining a minimum safe value of 140 mJ/cm^3.

It should be noted that the stability margin computed above is affected by a number of uncertainties that could cause a reduction compared to the present estimation. Although very hard to quantify, these issues could possibly lead to a loss of stability especially in the case of the STP conductor since it features the lowest margin of the four design variants in Figure 4.30:

- based on the difference between quench - no quench energy data in [153], an average error of 5% on the experimental assessment of the quench energy can be assumed;
- the computed energy dissipation during the plasma scenario is underestimated since the analysis is based on inter-strand resistivity values obtained without electro-magnetic load;
- the disturbance duration and shape used in the transient stability test do not match exactly the magnetic field change variation occurring at the Start of Discharge during a plasma scenario. Indeed, the initial phase of the plasma scenario featuring rapid magnetic field variations is relatively long (∼1.5 s) compared to the 65 ms pulse used in the transient stability test. On top of this, the Start of Discharge is characterized by a more constant excitation, whereas in a sinusoidal pulse the magnetic field change rate is variable. As demonstrated in [155] for step-like and $cos^2\theta$-type heat pulses, this can lead to non-negligible variations of the heat transfer coefficient, which may be significantly larger in the latter case especially at the end of the heat pulse, when recovery takes place. It follows that the actual plasma scenario quench conditions lie between the boundaries represented by the transient stability and steady-state quench conditions analysed in this section.

An interesting observation is that in accordance with Figure 4.29, during the first load cycles of the magnet only the LTP design shows convincingly stable operation during a 15 MA plasma scenario. The occurrence of premature quenches cannot be excluded during the first cycles for the other conductor designs, although at present it is not possible to establish up to which cycle number. From this point of view, the most positive scenario consists in a fast increase of the inter-strand resistance during the first several hundreds of load cycles. Considering that functioning of the ITER tokamak with the 15 MA scenario is only foreseen at a later experimental stage this may allow in the other threes designs a reduction of the loss in pulsed mode sufficient for safe operation of the magnet.

A relatively simple and probably feasible way to improve the stability of the Central Solenoid conductor during operation is to increase the He mass flow rate. Indeed, a strong improvement of the transient stability with helium mass flow is observed in Figure 4.30 for the Secret-A conductor due to the enhanced heat transfer coefficient, which increases with the coolant speed [153]. However, whether the same performance gain can be achieved in the Central Solenoid coils is questionable, since tests carried out on the Central Solenoid Insert Coil (CSIC) revealed only a weak dependence of the stability on the mass flow rate [156].

4.6 Conclusion

For the first time, the relation between coupling loss and twist pitch sequence in multi-stage ITER-type CIC conductors is investigated numerically and baselined by conductor tests. The analysis reveals that, apart from the absolute twist pitch length, the ratio between twist pitch lengths of successive cabling stages plays a major role in the final pulsed magnetic field loss of such a complex cable pattern. Notably, coupling loss can be reduced by choosing a ratio close to 1 between the twist pitches of the successive stages, the last one with high resistive wraps excluded.

This strategy opens new possibilities for the optimization of the coupling loss in multi-stage CIC conductors. In particular, the code JackPot-ACDC predicts the option to successfully combine low coupling loss with long twist pitches. In the last decade long twist pitch values have proven to limit the Nb_3Sn conductor degradation with number of load cycles within the ITER relevant range.

The model baselined the proposed twist patterns for the ITER Central Solenoid conductor. Though relying anti-intuitively on a first stage twist pitch twice to five times longer than those of the other proposed designs, AC loss measurements performed at two different laboratories on such conductors confirm the low coupling loss prediction of the model.

The four different conductor designs for the ITER Central Solenoid are qualified numerically under operating conditions, i.e. during a 15 MA plasma scenario. Given the available cycled conditions, the experimental data and simulation show the so-called STP design, featuring very short twist pitches and adopted by ITER for the Central Solenoid, to be characterized by the highest coupling loss and conductor temperature increase.

Based on petal-averaged properties, a safe temperature margin seems to be retained for all four designs both before and after cycling, although further evolution of the current sharing temperature for a larger number of load cycles, up to 60000, must be anticipated. However, after significant load cycling, the computed average electric field along the superconducting strands in the plasma scenario exceeds the safe value for the electric field as measured during steady-state current sharing temperature test for the STP design. This implies that the current sharing temperature in combination with the related temperature margin may not be a sufficient criterion to secure electro-magnetic stability.

When quench conditions from transient stability tests are assumed as reference (unfortunately only available for an equivalent sub-cable test), the energy dissipation during the initial fast transient of the plasma scenario is below the quench level for all four cable designs.

In reality, operating plasma conditions are in between the steady-state (infinitely long pulse) and transient stability (very short pulse) extremes used in the analysis to assess the stability of the four conductor designs. As such, caution is needed when confirming a stable operation on the basis of the comparison with the transient stability quench energy. Though hard to quantify, some reduction of the assessed energy margin can be expected due to the different duration and spatial distribution of the heating power during a plasma scenario.

Taking all issues into account, the short twist pitch conductor design, in its present implementation, constitutes potentially a more risky cabling pattern since even after a large number of cycles it features the lowest stability margin of the four analysed conductor options under the worst operating conditions.

Chapter 5

Performance of lap-type joints

Joints between conductors constitute a critical point of superconducting coils, due to the opposing requirements needed to achieve minimal dissipation during steady-state (low resistance) and pulsed (high resistance) operations. Optimal current sharing among the sub-cables should also be ensured to avoid severe performance loss caused by unequal strand current distribution. The severity of the requirements that have to be satisfied is strongly related to the joint operating conditions and its position in the magnet system.

This chapter deals with the analysis of lap-type joints, the most common design when using CIC conductors. The performance of the ITER Torodial Field and Poloidal Field coil joints is studied and the main issues related to lap-type joint operation identified and discussed.

Due to the relatively high cost involved in full-size joint assembly and test as well as the complexity of the system to model, only few experimental and modelling studies exist in spite of the high relevance of joints for proper magnet functioning. As such, the present analysis is one of the first numerical approaches to lap-type joint performance assessment and optimization.

5.1 Introduction

Considerable lengths of conductor are needed to wind the ITER magnets. As an example, the Toroidal Field coils require strands with a total length of 80,000 kilometres. Specific requirements may also exist, as for the Poloidal Field coils that are designed as a stack of independent modules. This ensures repair options in the case of failure, without major disassembly of the tokamak. Hence, the ITER coils comprise several conductor unit lengths connected by joints, ranging from 382 m for the PF1 coil to 910 m for the Central Solenoid modules. Joints are also needed to connect the end-turns to the feeder conductors that link them to the power supplies.

As mentioned in section 1.3.3 several joint designs exist for CIC conductors. In ITER, the Toroidal Field, Poloidal Field and Correction Coils rely on lap-type joints for their proven performance and ease of connection [157, 158]. The sintered butt-joint is used in the Central Solenoid because of space limitations [18].

Like all joints between superconductors, ITER joints have to satisfy simultaneously opposing requirements. On the one hand, the conductors need to be electrically connected with a low resistance, in order to avoid excessive ohmic heat generation under steady-state operation. The objectives are to reduce the heat load on the cryogenic system and, more importantly, to prevent quenches. On the other hand, the fact that conductors and joints are exposed to a time-varying magnetic field impose a certain minimum resistance value in order to limit the coupling currents in and between the superconducting cables. Moreover, the joint design should also guarantee sufficient stability margin and ensure efficient current sharing among petals and strands.

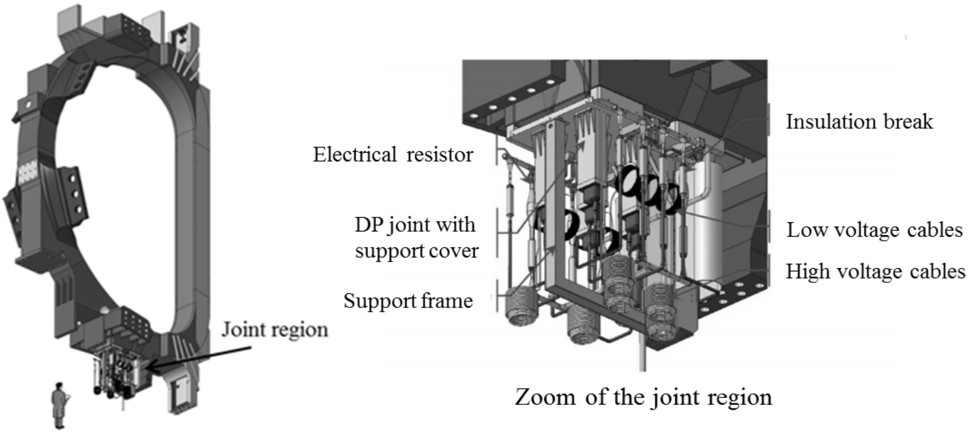

Figure 5.1: (Left) In the Toroidal Field coils, the joints are positioned just below the winding pack outside the torus. (Right) Zoomed view of the Toroidal Field coil joint region.

To improve the stability, the position of the joints is chosen away from the high field region of the magnet, as far as it is compatible with the assembly constraints. Therefore, joints are positioned just underneath the winding pack in the Toroidal Field coils and at the outer radius in the Poloidal Field coils, as shown in Figures 5.1 and 5.2.

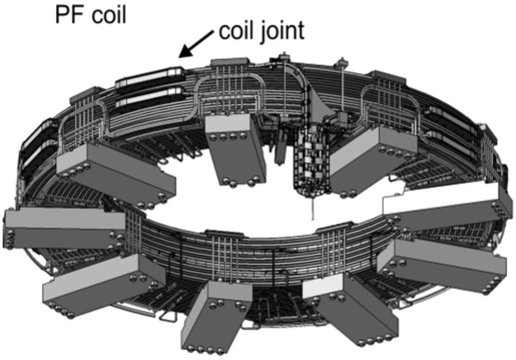

Figure 5.2: In the Poloidal Field coils, the joints are placed at the outer radius in minimum magnetic field to maximize the temperature margin.

In lap-type joints, stability against magnetic field transients is influenced by the relative joint to magnetic field orientation, as defined in Figure 2.24. In this respect the Edge On configuration appears more favourable, avoiding the formation of large coupling loops that embrace the two conductors.

Beside its position in the magnet system, the joint performance is primarily related to its resistance and geometry. In lap-type joints, the resistance is determined by the inter-strand and the strand-to-sole resistances in combination with the electrical contact between the two sole halves. Since the main challenge is achieving a good electrical contact between strands and copper sole, petal wraps are usually removed and special coatings or solder added. The influence of the joint geometry instead is tightly related to the cable configuration and twist sequence.

This chapter deals with the numerical simulation and assessment of the stability of ITER lap-type joints using JackPot-ACDC. The focus is on the Toroidal Field and Poloidal Field coil joints, since they are the largest lap-type joints in the ITER magnet system, carrying the highest steady-state current and experiencing the fastest magnetic field transients, respectively.

5.2 Performance analysis of the ITER Toroidal Field coil joints

The ITER Toroidal Field system comprises eighteen D-shaped coils arranged as a torus that will provide a static magnetic field of 5.3 T at the plasma axis, with a peak magnetic field of almost 12 T on the inner leg, as shown in Figure

1.3. A detailed description of the Toroidal Field magnet system can be found in [159, 160, 161]. Each coil is composed of seven double pancakes (DP) each formed by a double layer of conductor.

Six double pancake interconnecting joints with praying hands configuration and two terminal joints with shaking hands configuration (see Figure 1.14) interconnect the double pancakes of a winding pack and to the feeder bus bars. More details about the joint design can be found in [162]. Figure 5.3 illustrates the joint naming convention adopted here.

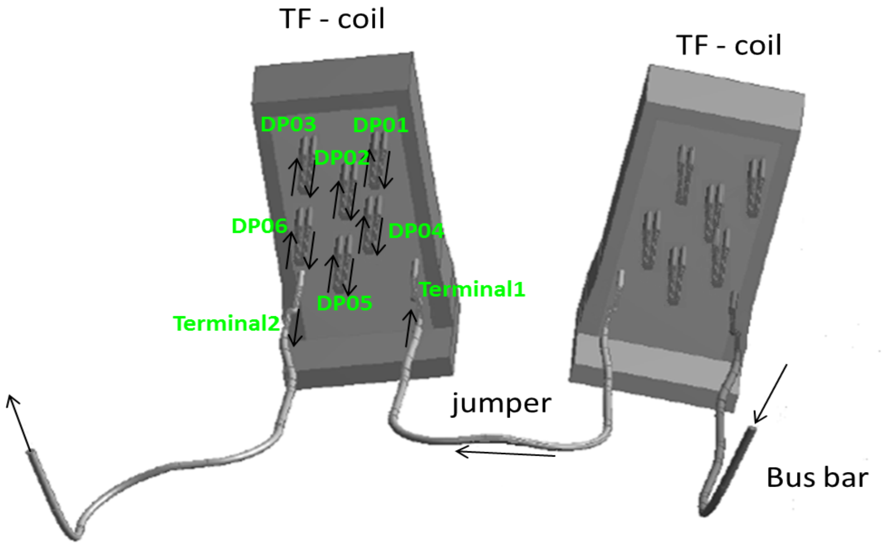

Figure 5.3: Bottom view of the Toroidal Field coil joint region showing the current path and the names used to identify the joints in the analysis.

As mentioned before, the joints are located in the low magnetic field region under the torus. The Toroidal Field coil joint stability has to allow a large DC current (68 kA), while maintaining the joint resistances as low as 1 nΩ to limit the dissipation within the 5 W design limit. The favourable Edge On configuration cannot be implemented for the interconnecting joints, due to restrictions arising from the geometry and stacking of the double pancakes in the winding pack.

Therefore, an assessment of the temperature and critical current margins expected with the present design of interconnecting and terminal joints is necessary to guarantee the required repetition rates of plasma cycles. In the next sections, the results of the performance analysis of the interconnecting and terminal joints of the ITER Toroidal Filed coils during the 15 MA and 17 MA plasma scenarios are presented. The study is completed by an assessment of various proposals for design optimisation and of the coupling loss time constants for different joint resistance values. The results presented here refer to joints DP01 and Terminal2. Although all the joints of the same type show practically identical power dissipation, these particular joints are characterized by the lowest current margin due to their distance from the closest Poloidal Field coils (PF5 and PF6).

5.2.1 Simulation conditions

The characteristics of the Toroidal Field and feeder conductors are summarized in Tables 1.4 and 1.6. Table 5.1 reports the main parameters of the joints that are relevant for the analysis. The meaning of the entries is clarified in Figure 5.4 for an interconnecting joint.

Table 5.1: Interconnecting and terminal joint specifications for the simulation model.

	Interconnecting	**Terminal TF side**	**Terminal Feeder side**
Material	Nb_3Sn	Nb_3Sn	NbTi
Width [mm]	71	71	64
Height [mm]	15	16.5	16.5
Cable offset [mm]	47.4	47.4	47.4
Joint length [mm]	450	478	478
Cable outside joint [mm]	300	272	272

Due to the large system of equations resulting from the modelling of lap-type joints with strand level detail, the simulated cable length outside the joint box is limited to about 0.3 m to keep the size of the model manageable. A uniform current distribution among the superconducting strands is imposed at the boundaries. As demonstrated in [163], the analysis of the boundary conditions reveals little effect of the imposed uniformity on the current distribution inside the joint. As a consequence, the applied condition is expected to have a minor impact on the overall joint performance.

To further reduce the CPU computation time, the non-linear V-I relationship of the superconducting strands is also neglected. Instead, strands are assumed to be always perfectly superconducting. This can be regarded as a conservative approach, since not limited by saturation, the strand currents can reach values higher than the critical current, resulting in a larger reduction of the current margin. The possibility that the omission of saturation could give rise to excessive power dissipation is unlikely given the high current margin of the strands, as will follow from the analysis presented in section 5.2.2.

Finally, although included in the initial cabling process to obtain the desired strand distribution in the cross-section of the cable, the Cu strands are later removed from the simulation. This simplification is justified by preliminary simulations (not presented here) showing that Cu strands carry negligible small currents during the entire plasma scenario. Moreover, with the superconducting strands far from saturation, as shown in section 5.2.2, the Cu strands do not contribute significantly to the stability. However, due to the significant heat capacity of copper, the mass of the Cu strands is taken into account in the calculation of the temperature of the petals.

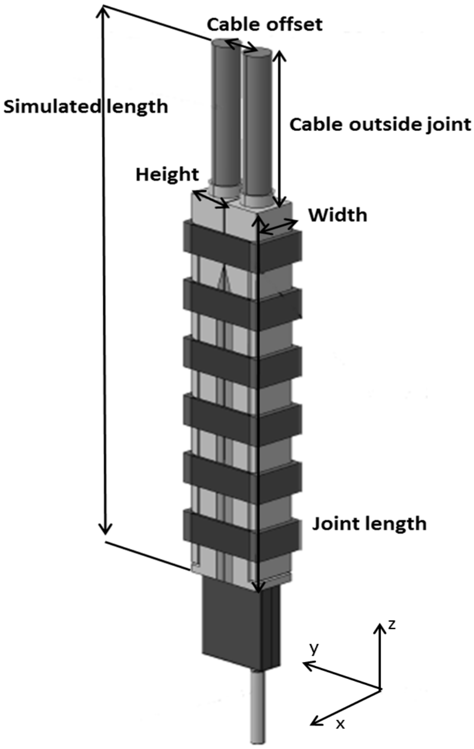

Figure 5.4: Interconnecting joint with praying hand configuration illustrating the meaning of the parameters of Table 5.1 and the orientation of the system of reference used in the analysis.

Magnetic field

The model described in section 2.5.6 is used to compute the magnetic field generated by Central Solenoid, Poloidal Field coils and plasma and its rate of change during the simulated scenario. The magnetic field error over the Toroidal Field coil joint region caused by the current centre line approximation used in the analysis compared to a 2D representation of the coils is shown in Figure 5.5 for points located in the middle plane of an interconnecting joint. The current centre line model underestimates the magnetic field due to Central Solenoid and Poloidal Field coils by 7% at most. As discussed later, this is partially compensated by an overestimation of the self-field of the joints.

The average magnetic field produced by the Central Solenoid in combination with Poloidal Field and Toroidal Field coils (excluding the plasma and joint self-magnetic field contributions) during a 15 MA plasma scenario varies from about 0.7 T at the Start of Discharge to more than 2 T at the end of the burning plasma phase, i.e. at t ~500 s in Figure 1.4. The Poloidal Field coils and Central Solenoids produce a relevant magnetic field term which is parallel to the axis of the joints.

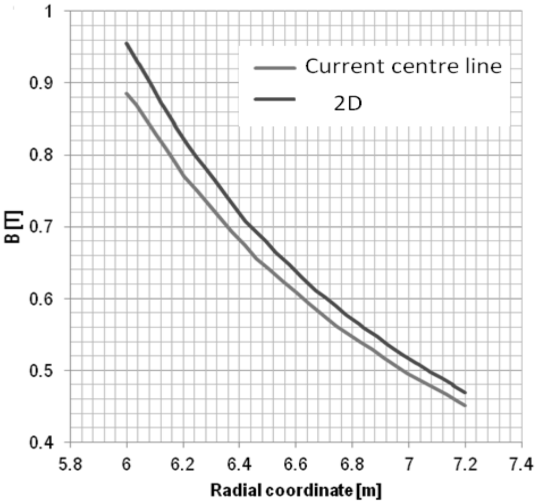

Figure 5.5: Magnetic field versus radial position over the Toroidal Field coil joint region as computed with the current centre line model and a 2D approximation of Central Solenoid and Poloidal Field coils.

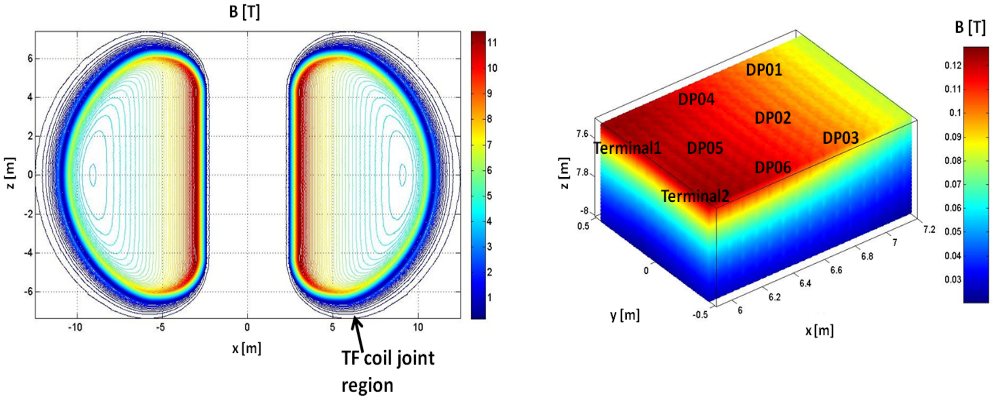

Figure 5.6: (Left) Planar view of the Toroidal Field magnet system showing the joint region below a Toroidal Field coil. The colour map shows the magnetic field of Central Solenoid, Poloidal Field and Toroidal Field coils at the Start of Discharge of the 15 MA scenario. Image courtesy of J. van Nugteren. (Right) Zoom of the Toroidal Field joint region showing the location of the 6 interconnecting and 2 terminal joints. The colour map shows the magnetic field due to the Toroidal Field coils only at the Start of Discharge phase of the 15 MA scenario.

Although not relevant from a coupling loss point of view, the steady-state magnetic field produced by the Toroidal Field coils is also taken into account in the calculation of the strand critical currents [164]. As illustrated in Figure 5.6, the maximum static magnetic field generated by the Toroidal Field coils over the joint region amounts to about 0.12 T.

Finally, both the self-magnetic field of the analysed joint and surrounding joints are also included in the critical current computation. The latter is estimated from a simplified 2D model where the conductors in the joints are represented by a constant current of ± 68 kA along the entire conductor length. This approach is likely to overestimate the magnetic field, since in reality the current gradually transfers to the other cable.

Temperature boundary conditions and coefficients

The thermal model described in section 2.5.10 is used to compute the temperature evolution of the strands, helium and copper sole during the plasma scenario. Table 5.2 summarizes the values of the main parameters of the thermal model [71, 72, 70, 165].

Table 5.2: Thermal model parameters for the Toroidal Field and feeder conductors.

Parameter	**Unit**	**TF CICC**	**Feeder CICC**
Total He mass flow	g/s	8.0	10.5
Inlet temperature	K	5.7 (intercon. joint) 5.3 (terminal joint)	4.4
Sole-Sole heat transf. coeff.	$W/(m^2 \cdot K)$	$60 \cdot 10^3$	$60 \cdot 10^3$
Sole-He heat transf. coeff.	$W/(m^2 \cdot K)$	500	500
Petal-sole heat transf. coeff.	$W/(m^2 \cdot K)$	500	500
Petal-He heat transf. coeff.	$W/(m^2 \cdot K)$	1000	600
Petal-Petal heat transf. coeff.	$W/(m^2 \cdot K)$	314	439

The temperature boundary conditions of both interconnecting and terminal joints are displayed in Figure 5.7.

Inter-strand and strand-to-sole resistance

Four sets of contact resistivity parameters are used in the analysis for the Nb_3Sn Toroidal Field conductor in the joints, which are listed in Table 5.3. The four resistivity sets correspond to joints with various overall resistance as a consequence of the exposure of the conductors to a different number of electro-magnetic load cycles or the use of solder at the strand-sole interface. As such, they allow to study the impact of load cycling and the adopted assembly technique on the joint performance under operating conditions. For the NbTi feeder conductor, inter-strand and strand-to-sole resistivities are generally set to $30 \cdot 10^{-6}$ $\mu\Omega \cdot$ m^2 and $3.9 \cdot 10^{-6}$ $\mu\Omega \cdot$ m^2, using the estimates from [48].

In the simulation, the same inter-strand resistivity is assumed within the joint section as well as in the portion of conductor outside the joint. The reason for this is that the length of conductor squeezed inside the joint box is longer than the effective sole-conductor contact length, and as such it covers most of the extra portion of cable simulated outside the joint.

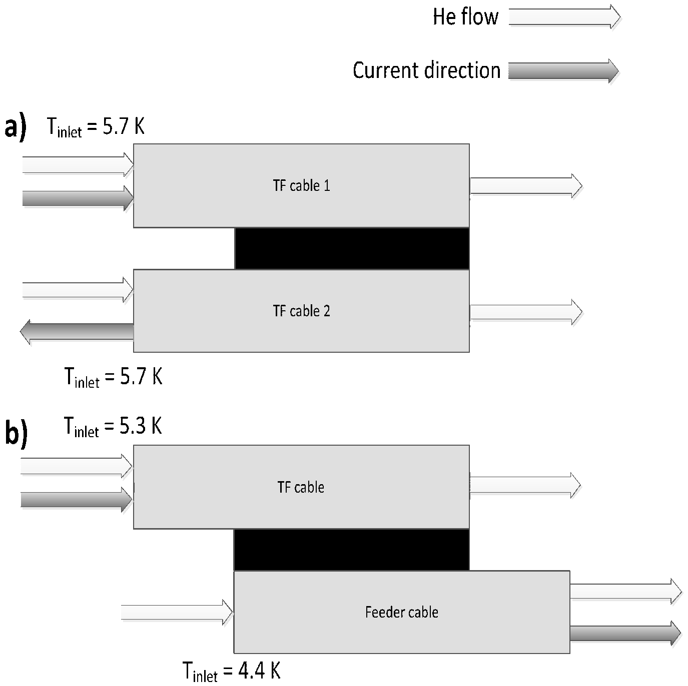

Figure 5.7: Boundary conditions for current and temperature of interconnecting (top) and terminal (bottom) joints. The inlet temperatures of the conductors are also reported.

Table 5.3: The four resistivity parameter sets used in the analysis for the Nb_3Sn Toroidal Field conductor in the joint.

Set number	**Parameter**	**Unit**	**Value**
I	Inter-strand	$\mu\Omega{\cdot}m^2$	$4.8 \cdot 10^{-6}$
	Strand-to-sole		$27 \cdot 10^{-6}$
II	Inter-strand	$\mu\Omega{\cdot}m^2$	$1.2 \cdot 10^{-7}$
	Strand-to-sole		$27 \cdot 10^{-6}$
III	Inter-strand	$\mu\Omega{\cdot}m^2$	$1.0 \cdot 10^{-6}$
	Strand-to-sole		$4.0 \cdot 10^{-6}$
	Solder thickness	mm	2.75
IV	Inter-strand	$\mu\Omega{\cdot}m^2$	$1.2 \cdot 10^{-6}$
	Strand-to-sole		$4.0 \cdot 10^{-6}$

The resistivity values of set I in Table 5.3 are obtained from inter-strand resistance measurements performed on the bottom joint of the TFJA-3 SULTAN sample [166]. This joint is selected since it is the only one for which resistance measurements exist under the same conditions as those envisaged for the final Toroidal Field joints, i.e. no solder is used and the chromium layer is removed from the strands at the cable surface.

Given the layout of SULTAN samples [53], the bottom joint is located relatively close to the high magnetic field region of the facility. Therefore, it is possible that the cyclic application of an electro-magnetic load to the conductor results in higher 'post-mortem' inter-strand resistance values also in the joint. However, the position of the Toroidal Field coil joints in the ITER machine is such that they experience a relatively low electro-magnetic load, so that hardly any inter-strand resistance variation with cycling is expected. In order to assess the impact of a lower inter-strand resistance on the performance of the joints, a second calculation is carried out with an inter-strand resistance corresponding to the initial value in [144], see set II in Table 5.3. In this simulation, a lower inter-strand resistivity ($1.0 \cdot 10^{-6} \mu\Omega{\cdot}\mathrm{m}^2$) is used for the feeder conductor as well, corresponding to the minimum value measured in [75] after several thousands of cycles.

The effect of the addition of solder between the Toroidal Field conductor and the sole is explored with the resistivity set III. The parameters used in this analysis are the average of the two terminations of the TFPRO-2 sample in [166].

Finally, resistivity set IV in Table 5.3 is not derived from measurements but is chosen to give a 1 nΩ resistance in an interconnecting joint. As emerges from the analysis, the resistivity sets I and II result in a joint resistance higher than the 1 nΩ design goal, which could help preventing significant coupling currents. Although not supported by experimental values, this last simulation aims at assessing the magnitude of the coupling loss in an 'ideal' joint, where the design resistance can be achieved without addition of solder or other changes in the assembly procedure.

5.2.2 Simulation results

The analysis covers the envisaged normal operating conditions, i.e. the 15 MA and 17 MA plasma scenarios. While the Toroidal Field coil current is constant at 68 kA, the Central Solenoid and Poloidal Field coils are operated in pulsed mode. The current variation in the Central Solenoid and Poloidal Field coils during the first 1500 s of a 15 MA and 17 MA pulse is shown in Figures 1.4 and 1.5.

Calibration runs

Calibration runs are performed for an interconnecting joint without transport current and subjected to magnetic field ramps of 50 mT/s from 0 up to 1 T along the x, y and z directions, as defined in Figure 5.4. The power dissipated in the sole, two cables and at the cable-sole interface in the three cases is illustrated in Figure 5.8. The overall height of the stacked areas correspond to the total power generated in the joint. The highest loss is found for a magnetic field ramp along the x-direction, corresponding to the Face On joint configuration, which allows large coupling currents to build up between cable and sole. Eddy current loss in the copper sole is maximum for magnetic field ramps along the y-direction, i.e. Edge On joint configuration.

Figure 5.9 shows the induced currents in the strands of Cable1 at the centre of the joint for magnetic field ramps along the three directions. Also here it is clear that significantly higher coupling currents are induced for a magnetic field

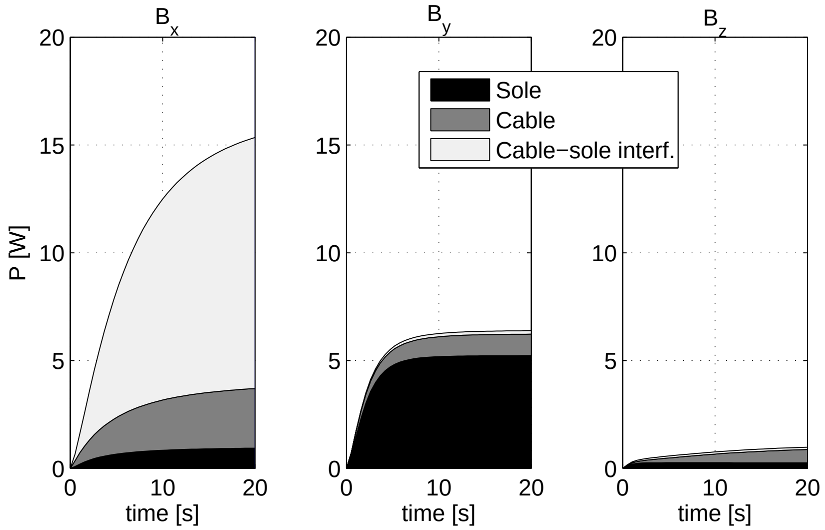

Figure 5.8: Power dissipation in the sole, two cables and cable-sole interface versus time for 50 mT/s magnetic field ramps up to 1 T along the x (left), y (centre) and z (right) directions.

ramp along the x-direction. The induced currents in the strands of Cable1 feature symmetric distributions around 0 A for magnetic field ramps along the y and z directions; however, the current distribution produced by magnetic field variations along the x direction is asymmetric. This is because the coupling currents induced

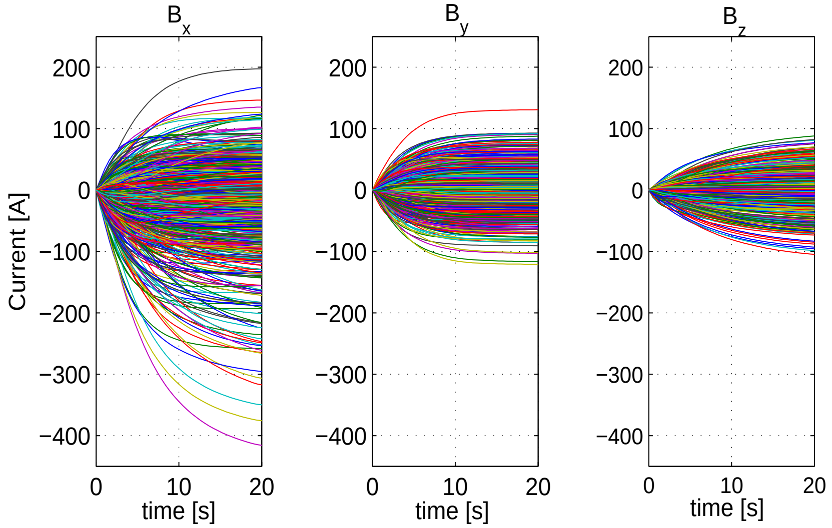

Figure 5.9: Induced strand currents versus time at the centre of the joint for Cable1 during a 50 mT/s magnetic field ramp up to 1 T along the x (left), y (centre) and z (right) directions.

in each cable by a time-varying magnetic field oriented along the y or z axis of the joint close within the cable itself or, partially, through the portion of copper sole in its immediate surroundings. Therefore, the induced current loops are confined to one of the two halves of the joint. On the other hand, coupling loops embracing the two cables on both sides of the joint are formed for magnetic field transients along the x direction.

Joint performance with resistivity set I

Figure 5.10 illustrates the contributions to the overall power dissipation during a 15 MA plasma scenario due to the copper sole, the two cables and the cable-to-sole contacts in a joint featuring the resistivity parameter set I in Table 5.3. In such a joint, i.e. in a joint with the same inter-strand and strand-to-sole resistivity parameters of the TFJA-3 bottom joint and thus sharing its assembly procedure, the main dissipation takes place at the strand-to-sole interface. The lower dissipation of the terminal joints is a consequence of the lower strand-to-sole contact resistance on the feeder side.

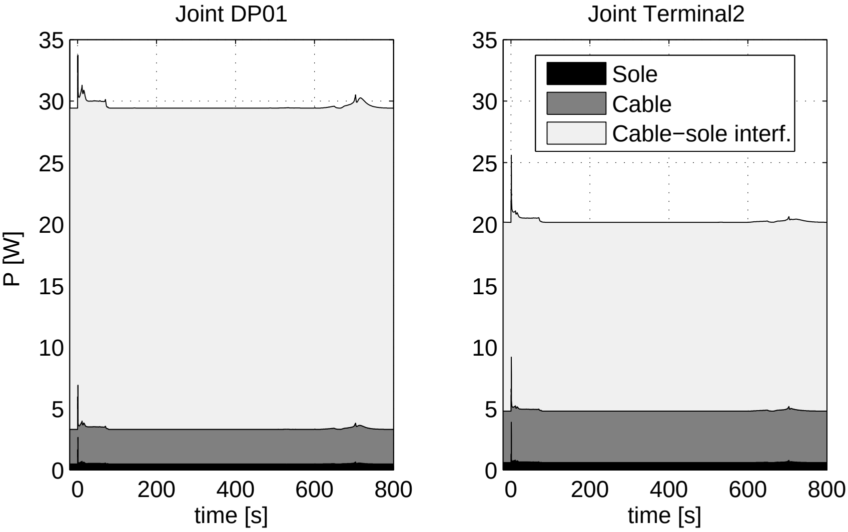

Figure 5.10: Power dissipation in the sole, two cables and cable-sole interface versus time in a Toroidal Filed coil interconnecting (left) and terminal joint (right) up to t = 800 s during a 15 MA plasma scenario.

The time-varying currents of the Central Solenoid and Poloidal Field coils produce noticeable variations of the magnetic field over the Toroidal Field coil joint region over limited time intervals during a 15 MA plasma scenario, i.e. at t ∼0 s (Start of Discharge) and t ∼700 s when the burning plasma plasma is ended, see the power peaks in Figure 5.10. During the remaining part of the scenario, the magnetic field change rate experienced by the Toroidal Field coil joints is negligible and, thus, the power generation in the joint is constant, following the 68 kA DC transport current in the windings. Figure 5.10 shows that in a Toroidal Field coil joint with the same resistivity parameters as the TFJA-3 joint, the pulsed magnetic field losses are considerably lower than the steady-state power. A maximum pulsed loss of 5 W is reached for only a fraction of a second at the Start of Discharge. With a total value of about 30 W and 20 W, respectively, the steady-state dissipation in both interconnecting and terminal joints is high and far above the 5 W design level set by the cryogenic system. Using the computed power, the resistances of the joints are estimated at 6.4 and 4.4 nΩ for the interconnecting and terminal joints, respectively.

Although not shown here, the contribution of the hysteresis loss to the total dissipation is determined as well. Hysteresis loss is marginal, with a short peak at the Start of Discharge of 3.5 and 2.0 W in the interconnecting and terminal joints, respectively.

The relatively low pulsed loss is due to the small eddy and coupling currents. This is a direct consequence of the distance between the joints and the closest sources of a changing magnetic field, i.e. the PF5 and PF6 coils, as well as to their orientation with respect to the changing magnetic field, with a significant component parallel to the strands. Figure 5.11 shows the current in the strands, sum of the transport and induced currents, in the centre of Cable1 of joint DP01 up to t = 100 s (left) during a 15 MA plasma scenario together with the total current along the joint (right) immediately after the start of the discharge.

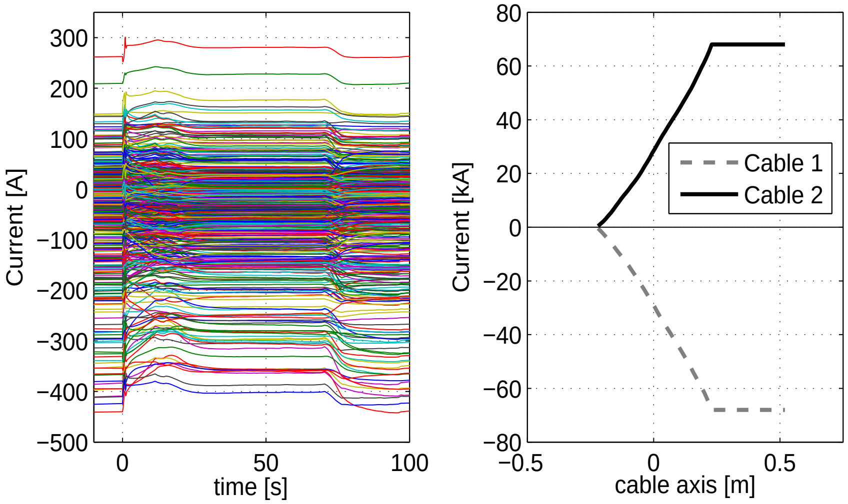

Figure 5.11: (Left) Strand current distribution, sum of the transport and induced currents, versus time at the center of the joint in Cable1 of joint DP01 up to t = 100 s during a 15 MA plasma scenario. (Right) Total current along the joint in the two cables at t = 0.5 s.

The average strand current in a Toroidal Field conductor is 75 A, with the sign of the current related to the flow direction along the vertical z-axis. Since the two cable sections in interconnecting joints carry current in opposite directions, the total current is positive in one conductor and negative in the other. As can been seen from the right part of Figure 5.11, the conductor section outside the joint extends between 0.225 and 0.525 m along the cable axis. Here the two conductors have a current of +68 kA and -68 kA, respectively. Proceeding along the simulated length from the top (+0.225 m) to the bottom (-0.225 m) of the joint, the current in each cable is progressively transferred to the other cable, so that it reduces from 68 kA to zero. The current transfer is found to be almost linear, as it would be at constant transport current in the absence of coupling currents.

In the left part of Figure 5.11 the relatively small coupling currents in the single strands can be observed: only modest variations take place at the Start of discharge when the magnetic field change rate is maximum.

As a consequence, the temperature of the petals is mainly determined by the steady-state power, causing a maximum increase of 0.50 K above the helium inlet temperature at the centre of the joint. Always in the centre of the joint, the additional pulsed power produces an additional 0.10 K temperature peak at the Start of Discharge, leading to a maximum overall temperature increase of 0.60 K. Figure 5.12 shows the temperature margin of both Nb_3Sn cables in joint DP01 and of the Nb_3Sn and NbTi cables in joint Terminal2 up to t = 100 s during a 15 MA plasma scenario. At every time step, the temperature margin is calculated as the difference between the current sharing temperature, computed based on the average strand current and magnetic field, and the peak petal temperature.

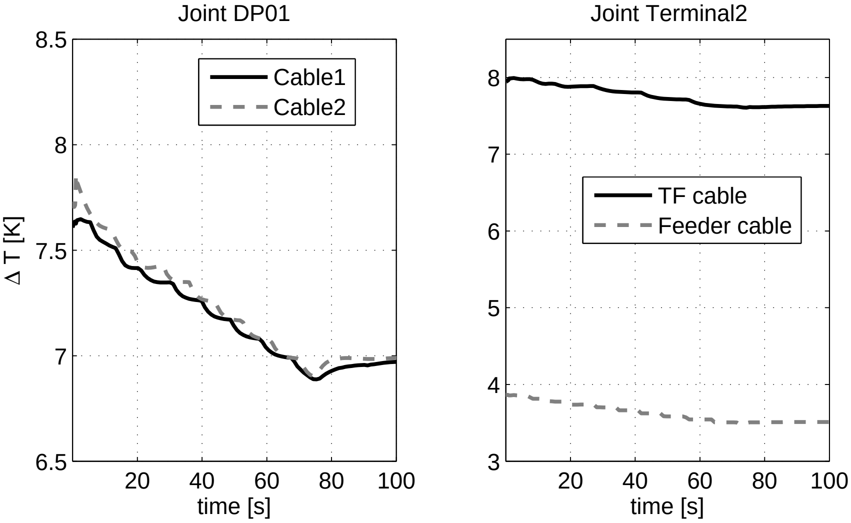

Figure 5.12: Temperature margin versus time for the two cables in joints DP01 (left) and Terminal2 (right) for 0<t<100 s during a 15 MA plasma scenario.

Since the power generated by the coupling loss at the Start of Discharge is such as to result in only a modest increase of the temperature of the strands, the change observed in the temperature margin must be related to variations of the current sharing temperature. Indeed, during the considered time span in

Figure 5.12, relatively large variations of the current sharing temperature occur due to the increase of the magnetic field over the Toroidal Field coil region. As an example between 0<t<100 s of the 15 MA plasma scenario, the T_{cs} of the two Nb$_3$Sn cables in joint DP01 is found to decrease from about 14 K to about 13.3 K. In spite of the reduction in T_{cs}, all cables in the joints feature a large temperature margin, with a minimum value exceeding 3 K in the case of the NbTi conductor in joint Terminal2.

Using the computed temperatures and magnetic field, the critical current of the strands is calculated to predict the current margin of the cables. The margin is found by subtracting the calculated strand currents from their critical current. Figure 5.13 shows the minimum current margin of a strand during the 15 MA scenario for joints DP01 and Terminal2. A value higher than zero means that the strand current does not exceed the critical current. Results below zero would imply that the current is actually higher than the critical current, i.e. that the strand is saturated. A minimum current margin per strand of several hundreds of amperes is retained during the entire scenario, meaning stable operation.

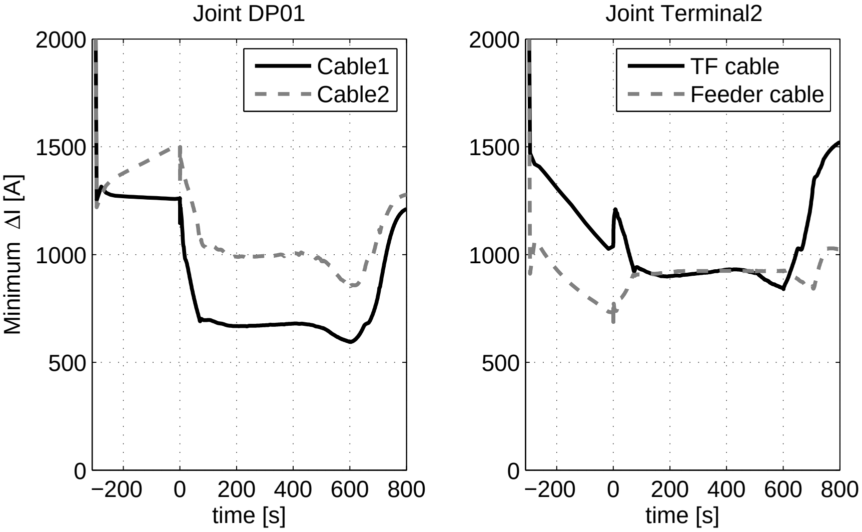

Figure 5.13: Minimum strand current margin versus time in the joint up to t = 800 s during a 15 MA plasma scenario for joints DP01 (left) and Terminal2 (right).

Although such large current margins may seem excessive, they are based on critical current values estimated with the best available data in terms of strain, temperature, magnetic field and strand-magnetic field angle dependence. Even though not critical for Toroidal Field coil joint operation, a more extensive database for the critical current at relatively low magnetic field (0-3 T) and for a wide range of strand-magnetic field angles would be advantageous for future analysis, especially for NbTi strands.

Joint performance with resistivity set II

A second set of simulations is carried out assuming a lower inter-strand resistance (as specified in Table 5.3) to verify that the safe pulsed operation concluded on the basis of the resistivity set I is not dominated by a possible resistance increase due to the electro-magnetic cycling of the sample.

The results presented in this section refer to the DP01 joint during the 15 MA and 17 MA plasma scenarios shown in Figure 1.5. Generally, the two scenarios do not differ much in terms of Central Solenoid and Poloidal Field coil currents. However, during the 17 MA scenario slightly higher currents occur in coils PF5 and PF6 about 100 s after the Start of Discharge, resulting in a stronger magnetic field over the Toroidal Field coil joint region.

Since the main contribution to the power dissipation is related to the strand-to-sole contacts, lowering the inter-strand resistances has a relatively modest impact on the overall dissipation, although it does practically reduce to zero the steady-state power in the cables. However, higher coupling currents now flow between the strands, which cause a reduction of the minimum strand current margin compared to the previous simulation, as illustrated by comparing Figures 5.13 and 5.14.

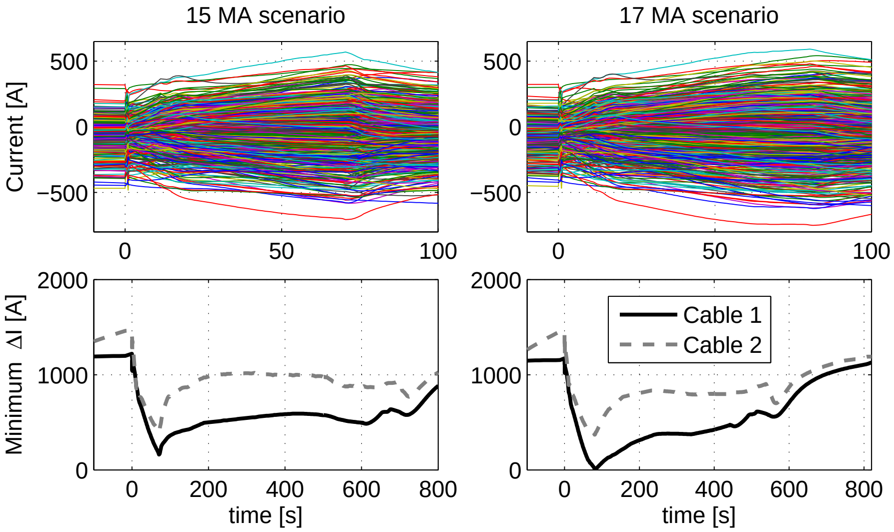

Figure 5.14: (Top) Strand currents versus time at the center of Cable1 of joint DP01 up to t = 100 s during a 15 MA (left) and 17 MA (right) plasma scenario. (Bottom) Minimum strand current margin versus time during the 15 MA (left) and 17 MA (right) plasma scenarios.

A significant decrease of the current margin occurs around t ~80 s, when it drops to 200 A and about 10 A in the 15 MA and 17 MA plasma scenarios, respectively. The large reduction observed especially in the 17 MA plasma scenario is caused by a different current distribution due to the lower inter-strand resistance and a higher current (and therefore magnetic field) in the PF5 coil compared to the 15 MA scenario. A similar decrease is also observed in the terminal joints.

Although Figure 5.14 reveals the 17 MA plasma scenario as potentially more critical, Figure 5.15 shows that the minimum margin in every position along the cable axis is for nearly all strands higher than 500 A. Only one single strand at a specific location, just outside the joint, has a margin of few A. This small minimum current margin corresponds to the particularly large current carried by this strand. The reason for the high value is not related to double contacts between the strand and the sole. However, the specific trajectory of the strand inside the conductor is such that it results in a relatively extended contact with the sole close to the centre of the joint where the spread in strand currents is highest. Note that the simulated strand trajectories do not necessarily correspond to the precise path of the strands inside the real conductors due to the unknown offset angle of bundles and cable, twist pitch variations during cabling or random displacements during compaction in the joint. Moreover, the present analysis does not take into account the voltage drop along the superconducting strands. This would certainly limit the current accumulated by a given strand and force redistribution to the surrounding strands that still have sufficient current carrying capability. Therefore, the occurrence of a single strand with low margin should not be regarded as relevant in the present simulation.

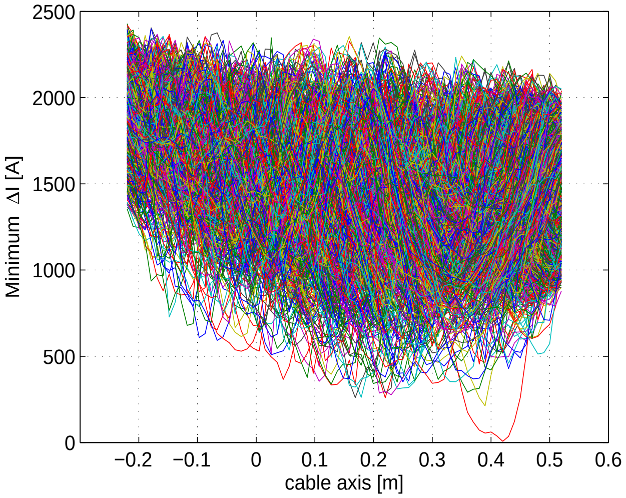

Figure 5.15: Minimum strand current margin distribution along the joint for the cable with lowest margin in the 17 MA plasma scenario.

Joint performance with resistivity set III

The analysis performed using the resistivity sets I and II in Table 5.3 both result in overall joint resistance values that significantly exceed the 1 nΩ design limit. This section deals with the simulated performance of a joint featuring the desired 1 nΩ resistance. This might result from an improved assembly procedure aimed at reducing in particular the strand-to-sole contact resistance, without the addition of solder. The aim is to verify whether a joint meeting the design criteria can still properly operate with margin during a plasma scenario.

Since no experimental inter-strand contact resistance data exist for such a Toroidal Field joint, the resistivity parameters required for the analysis are chosen such as to give a 1 nΩ DC resistance in an interconnecting joint (Table 5.3). The same values are also applied to the Toroidal Field cable in a terminal joint, which results in a steady-state joint resistance of about 2 nΩ (default parameters for feeder side). Joint resistance values slightly above 1 nΩ and some of them up to almost 3 nΩ were measured in the Central Solenoid Model Coil during three test campaigns between 2000-2002 with magnetic field on the joints ranging from 1.3 to 2.5 T [167]. Additional development work later on has shown that 1 nΩ is a realistic design target [168].

Figure 5.16 shows the power dissipation in the sole, the two cables and the cable-sole interface during the 15 MA plasma scenario for joints DP01 and Terminal2. The cable-to-sole contacts are still the main source of steady-state power, however, the steady-state power level is significantly lower than in Figure 5.10. Pulsed losses increase due to the lower joint resistance, but they still remain limited to a few watts, with short peaks of 9 W and 14 W a the Start of Discharge in the interconnecting and terminal joints, respectively.

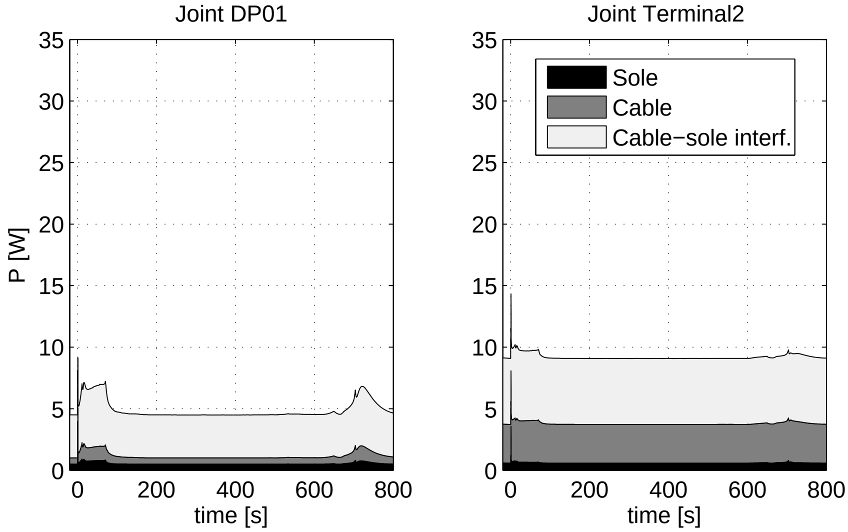

Figure 5.16: Power dissipation in the sole, two cables and cable-sole interface versus time up to t = 800 s during a 15 MA plasma scenario in joints DP01 and Terminal2 with 1 and 2 nΩ resistance, respectively.

The increase in spread of the coupling currents appears to be at most 50 A. Due to the lower steady-state dissipation, the maximum petal temperature increase compared to the helium inlet temperature is about 0.10 K. In the terminal joint, the temperature at the centre of the Toroidal Field conductor is even slightly lower than the inlet value of 5.3 K. This is caused by the contact with the feeder conductor that has a much lower temperature (inlet at 4.4 K) in combination with the reduced power dissipation caused by the lower joint resistance. The transient temperature increase produced by pulsed loss at the Start of Discharge is about 0.10 K.

Since only limited variations are observed in the strand currents and temperatures compared to the analysis with resistivity set I, the strand current margin does not undergo large changes.

Joint performance with modified design

A number of design variants are explored to test their impact on the joint performance aiming at a further optimization. The following cases are considered:

- Increase of the RRR of the Cu sole;
- Addition of a thin layer of solder inside the joint between the Toroidal Field cable and the sole;
- 90^o rotation of a terminal joint with respect to the original orientation, see Figure 5.4.

The increase of the RRR of the copper sole from 100 to 300 causes a reduction of the steady-state power generated in the sole. However, since this is the smallest contribution to the overall dissipation (see Figures 5.10 and 5.16), the change has only a marginal effect on the overall dissipation. Moreover, the pulsed loss is not noticeable affected by the variation of RRR. Therefore, increasing the RRR of the sole alone is not an effective way to reduce the excessive steady-state power dissipation of the Toroidal Field coil joints.

A more efficient way to reduce the joint dissipation towards the 5 W target is to introduce a layer of solder in order to improve the strand-to-sole contact resistance. The results in Figure 5.17 are obtained when using the solder resistivity parameter set IV of Table 5.3. For simplicity, the solder covers the entire perimeter (360^o) of the cable in the joint. With the addition of the solder, the average steady-state dissipation is reduced to about 3.2 W and peaks up to maximum 8 W for only a few seconds at the Start of Discharge. Other smaller, although longer, peaks above 5 W are observed up to t = 100 s and at the end of plasma. In spite of the presence of solder, the height of the peak at the start of the scenario does not increase much compared to the simulation with the resistivity parameter set I, shown in Figure 5.10. Presumably, this is caused by the relatively short interval over which the magnetic field change rate is high, which does not allow significant coupling currents to develop. Moreover, the increase of coupling currents is partially compensated by a reduction of the resistance thereby limiting the power dissipation.

The maximum petal temperature increase in the centre of the joint is 0.18 K above the He inlet temperature, while the strand current margin remains high, with a minimum value just below 600 A.

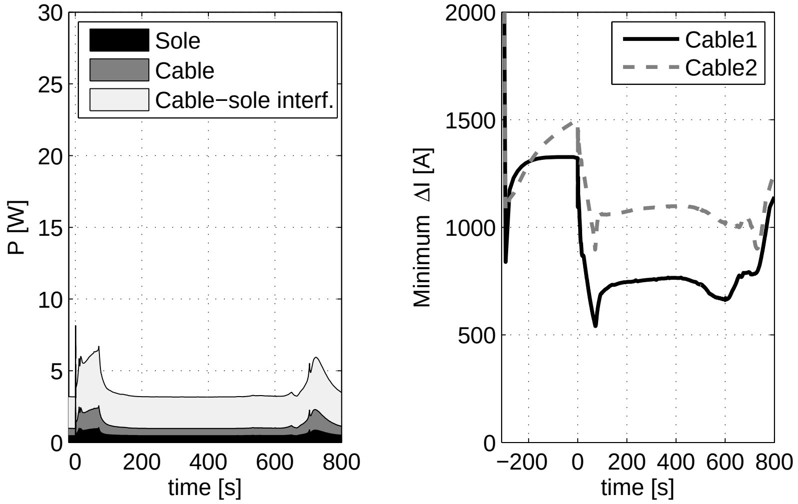

Figure 5.17: (Left) Power dissipation in the sole, two cables and cable-sole interface versus time and (right) minimum strand current margin along the entire joint versus time up to t = 800 s during a 15 MA plasma scenario for joint DP01.

The use of a layer of solder and a higher RRR of the copper sole would result in an additional reduction of the joint power dissipation, which may help to stay below the 5 W target also during the pulsed peaks.

When the results of the simulations without and with solder are compared, it appears that the presence of solder can reduce the strand minimum current margin by 200 A. Therefore, the addition of a layer of solder may cause some strands to exceed their critical current during a 17 MA scenario in the case of low inter-strand resistance, since the minimum margin under these conditions is only a few tens of ampere. To verify this, a simulation is run for joint DP01 featuring a combination of the conditions that have emerged as the most critical ones, i.e. low inter-strand resistance with solder during a 17 MA scenario.

The resulting power dissipation is shown in Figure 5.18. The average steady-state dissipation is 3 W and the total power increases to a maximum of 8 W just after the Start of Discharge.

The minimum current margin per strand is about 75 A, which is higher than the value obtained without solder. The increased margin is likely to result from the more homogeneous current distribution produced by the presence of solder. This affects also the self-magnetic field of the strands and could produce locally an alleviation of the conditions of the most critical strand. Therefore, though the 17 MA scenario appears potentially more critical, computations performed with the 'worst' available combination of parameters (from a pulsed operation point of view) still predict feasible operation with some margin of the Toroidal Field coil joints.

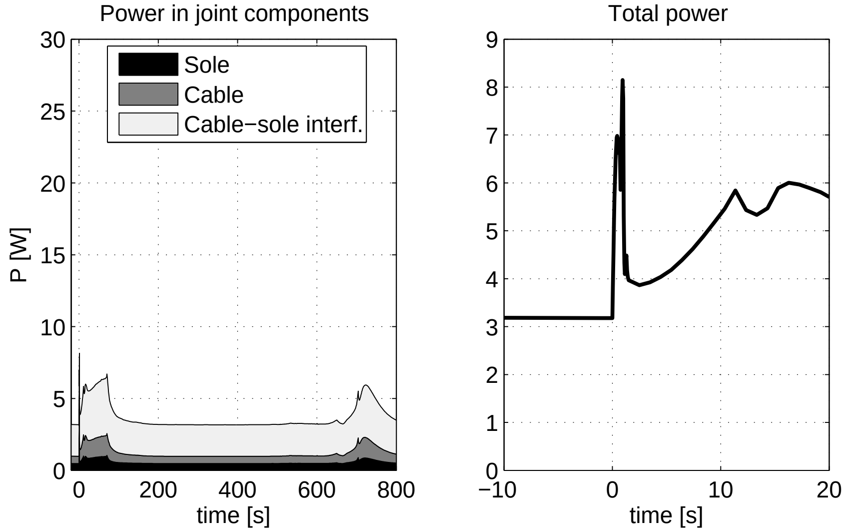

Figure 5.18: Power dissipation per element up to t = 800 s during a 17 MA plasma scenario (left) and in the whole joint immediately after the SOD (right) versus time for a DP joint with solder and low inter-strand resistance.

Finally, the effect of a 90^o rotation with respect to the original configuration of a terminal joint is considered. In the present design, all joints are oriented in the so-called Face On configuration with respect to the Poloidal Field coils field, which corresponds to the worst case from a pulsed loss point of view. Although this is not possible for the interconnecting joints, due to limitations imposed by the geometry of the windings, the orientation of the terminal joints can be rotated by 90^o. This would position the joints in the Edge On configuration with respect to the changing magnetic field, which may reduce the pulsed loss.

Compared to the original design, the rotation of $+90^o$ of joint Terminal2 slightly reduces the overall dissipation; while the peak pulsed loss at the Start of Discharge shows surprisingly a small increase for both rotations of $+90^o$ and -90^o. This is caused by the significant growth of the loss in the copper sole in the Edge On configuration, due to the larger area enclosed by the current loops. The effect appears to be larger than the expected reduction of the induced current loss within the cable section. Since the variations in the power dissipation are only limited, the minimum current margin of the strands is found not to differ significantly from the results with the default design for both cables and senses of rotation. Considering that a large minimum current margin per strand is already retained with the original design, the rotation of 90^o of the terminal joints does not yield relevant improvements.

Coupling loss time constant

The characterization of the Toroidal Field coil joints is completed by the estimation of the coupling loss time constant ($n\tau$). For this purpose, both an interconnecting and a terminal joint are subjected to a harmonic magnetic field with amplitude 0.4 T in the frequency range 10 to 200 mHz in a 0 T background magnetic field. The joints are exposed to magnetic field variations both in the Face On and Edge On configurations. The calculation includes the copper strands, and assumes no transport current and full penetration of the filaments.

The coupling loss time constant is evaluated for the resistivity parameter sets I, II and IV of Table 5.3. The case with simultaneous low inter-strand resistance and solder, here indicate as set V, is also explored. The loss is the result of the sum of coupling and eddy current losses in the two cables, strand-to-sole contacts and sole. The loss is normalized to the sum of sole and strand (i.e. both superconducting and Cu) volumes. The coupling loss time constant is found by fitting the simulated loss versus frequency curve up to 20 mHz with a third order polynomial and determining the slope of the low frequency limit.

The coupling loss density versus frequency and the coupling loss time constant values for interconnecting and terminal joints are shown in Figures 5.19 and 5.20.

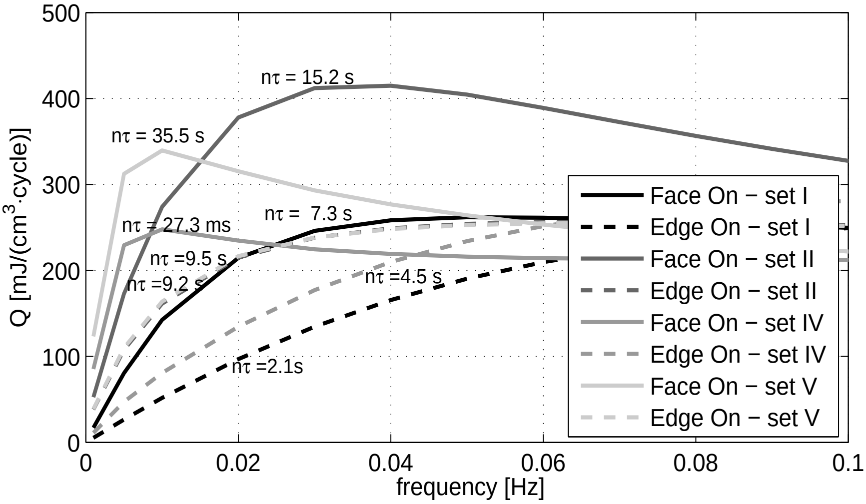

Figure 5.19: Coupling loss density per cycle versus frequency for an interconnecting joint up to 100 mHz and for different joint resistance values. The $n\tau$ loss time constant is determined from the initial slope at low frequency.

Comparing the magnitude of the coupling loss in interconnecting and terminal joints, the latter are found to be smaller due to the lower value of the strand-to-sole contact resistance of the feeder cable. For an interconnecting joint, the Face On coupling loss time constant lies between 7 and 15 s depending on the inter-strand resistance in the case without solder. If a layer of solder is added, the

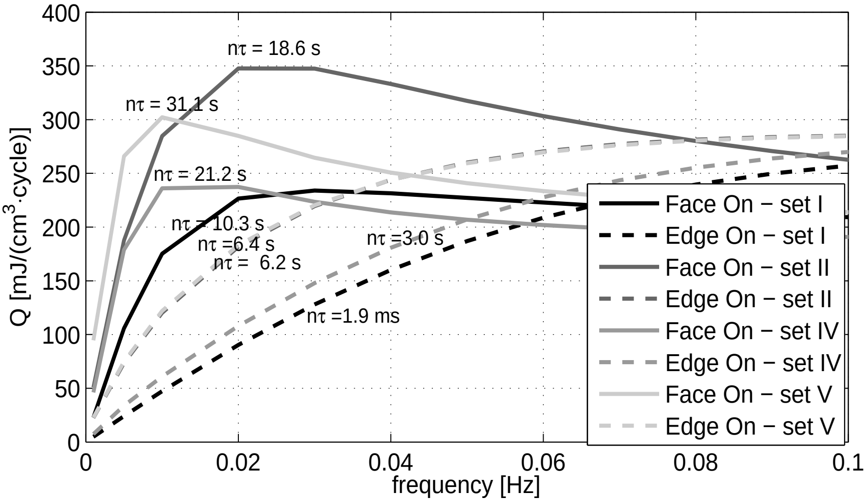

Figure 5.20: Coupling loss density per cycle versus frequency for a terminal joint up to 100 mHz and for different joint resistance values. The $n\tau$ loss time constant is determined from the initial slope at low frequency

value of $n\tau$ increases to about 30 s. For a terminal joint, the Face On $n\tau$ varies between 10 and 31 s, with a peak value for the case of low inter-strand resistance and solder. For Edge On magnetic field, the coupling loss time constant is in the range of 2 to 10 s for both joints.

5.3 Performance analysis of the ITER Poloidal Field coil joints

The Poloidal Field coil system of ITER comprises six co-axial solenoidal coils positioned around the toroidal magnet [6]. As detailed in Tables 1.2 and 1.5, the coils are designed with NbTi CIC conductors wound in double pancakes which are connected in series with shaking hands type of lap-type joints. This configuration is selected since it allows the so-called 'natural' orientation, which means that the joint axis is positioned along the prolongation of the axis of the cable, and hence the current is transferred and proceeds to flow in the same direction. This orientation requires a minimum conductor deformation for joint assembly.

The location of the joints at the coil periphery (at the top and bottom edges and in the centre of the windings, see Figure 5.2) is such as to maximize their temperature margin, since the magnetic field decreases from the inner to the outer radius of the coils. Moreover, in combination with a He cooling circuit with inlets at the inner radius and outlets at the outer radius of the coil, it allows to protect the high field region of the magnet against the heat load of the joints.

The Poloidal Field coil joints have to transfer currents up to 55 kA and are subjected to fast-varying magnetic fields along both radial and axial directions, up to 0.5 and 0.8 T/s in absolute value, respectively. Given the potential stability risk implied by such conditions during plasma operation, the pulsed performance of the Poloidal Field joints has been subject of investigations before [38, 163, 169]. While in [38] an analytic macroscopic (petal-level detail) approach is used, a numerical analysis at strand-level is carried out in [163, 169]. Both studies converge in identifying the PF2 coil joints as most critical, since they experience the largest current and magnetic field ramp rates during a 15 MA plasma scenario.

In spite of using the same code as here (i.e. JackPot-ACDC) and hence featuring strand-level detail, the results reported in [163, 169] are affected by a number of inaccuracies. Firstly, the voltage drop along the superconducting strands is omitted in order to simplify the solution of the system of equations. While acceptable in the case of the Toroidal Field coil joints, where strands are far from saturation, this approximation is not applicable for the Poloidal Field coil joints where strands exceeding their current carrying capability are present. Secondly, the length of the cable-to-sole contact is overestimated and taken as 500 mm instead of 450 mm. Although the parametric analysis in section 3.8 shows negligible effect on steady-state performance of joints longer than the cable final stage twist pitch, the excessive contact length can have relevant consequences for pulsed operation. In particular, it can cause large low-resistive current loops involving strands in contact with the copper sole at both joint ends.

Therefore, to correctly assess the pulsed performance of the Poloidal Field coil joints, the response of a PF2 joint in its envisaged ITER layout and including strand saturation is studied under current and magnetic field sweeps closely resembling the conditions expected during a 15 MA plasma scenario. A parametric analysis is also carried out to study the effect of the cable orientation within the joint and of possible design variants for joint optimization.

5.3.1 Simulation conditions

The main characteristics of the Poloidal Field coil joints are summarized in Table 5.4, while the details of the PF2 conductor can be found in Table 1.5. The meaning of the entries is as already illustrated for the Toroidal Field coil joints in Figure 5.4.

Table 5.4: Poloidal Field coil joint specification for the simulation model.

	PF coil joint
Width [mm]	64
Height [mm]	17.5
Cable offset [mm]	52.8
Joint length [mm]	450
Cable outside joint [mm]	300

Just like for the Toroidal Field coil joints, the simulated cable length outside the joint is 0.3 m to limit the size of the system to be solved. Uniform current distribution is assumed at the boundaries of the conductors. For the same reason, the Cu strands are not included in the computation, although they are taken into account during the initial creation of the cable and in the evaluation of the petal temperature increase.

Unlike the Toroidal Field coil joint analysis however, the non-linear voltage drop along the superconducting strands is included in the simulations in order to limit coupling currents and thus the current margin reduction of the conductor. The two-pinning components scaling law, see section 2.5.8, is used to represent the V-I characteristic of the NbTi strands, since it adequately fist the experimental critical current behaviour also at low magnetic field values.

In the analysis, two different conductor orientations with respect to the copper sole are considered (Figures 5.21 and 5.22), which are identified as the 0^o and the 30^o configurations, respectively. Figure 5.21 shows how in the 0^o cable orientation two petals touch the copper sole at each joint extremity. Due to the twist of the cables, in the top cable petal 1 has a larger contact area with the sole at the joint end. On the contrary, petal 2 has an extended contact at the joint start. Similarly, in the bottom cable, petals 5 and 6 have large contact areas with the sole at the joint end and start, respectively.

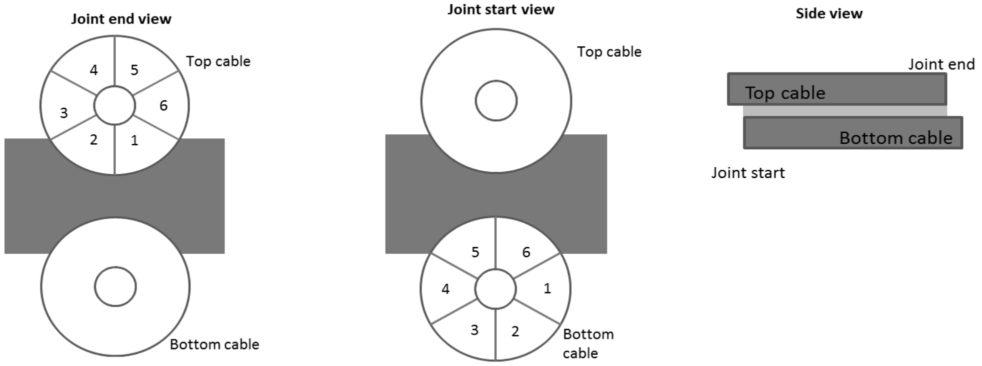

Figure 5.21: Poloidal Field coil joint 0^o orientation.

In the 30^o configuration, three petals make contact with the copper sole at the joint extremities. At the joint end, petal 5 in the top cable and petal 2 in the bottom cable have extended contact areas with the sole. Petal 1 in the top cable and petal 4 in the bottom cable instead have a larger connection area at the joint start. Finally, petal 6 in the top cable and petal 3 in the bottom cable have similar contact areas with the sole at both joint extremities.

Current and magnetic field profiles

The current and magnetic field pulses shown in Figures 5.23 and 5.24 are applied in the analysis.

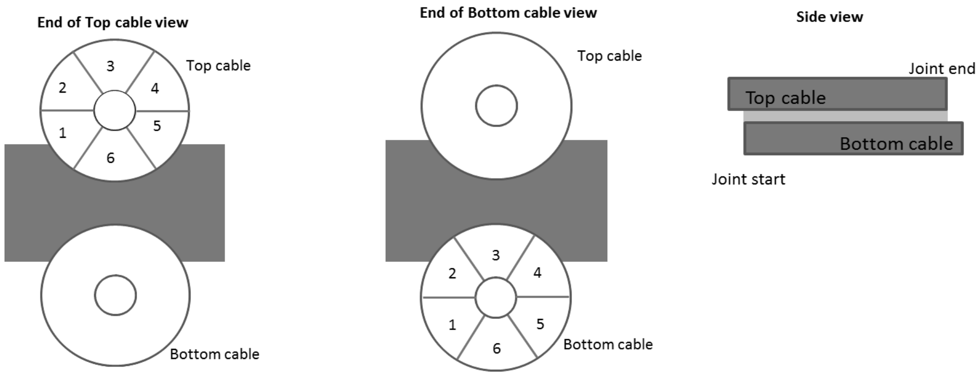

Figure 5.22: Poloidal Field coil joint 30^o orientation.

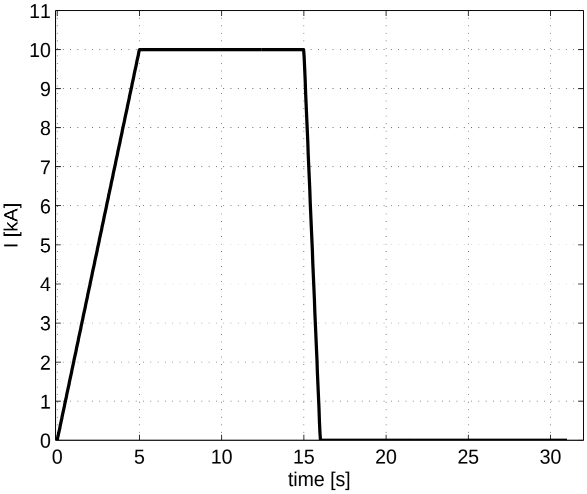

Figure 5.23: Current cycle applied in the Poloidal Field coil joint performance assessment.

The current sweep is carried out in a radially oriented background magnetic field of 2 T, i.e. parallel to the joint plane. The initial current ramp up is characterized by a constant dI/dt of 2 kA/s, while in the discharge phase a peak dI/dt value of 10 kA/s is reached. During a 15 MA plasma scenario the maximum current in a Poloidal Field coil at the Start of Discharge is 45 kA, while the coil energization takes 300 s. Therefore, the initial ramp rate is much lower than the conditions used for test. During the successive plasma pulse, current ramp rates as high as 12 kA/s at 2 T and 20 kA/s at 0.2 T will be present in the PF1 and PF2 joints, respectively.

Magnetic field ramp 1 (dB/dt = 0.5 T/s for 1 s) corresponds to the maximum radial magnetic field rate experienced by the PF1 and PF2 top joints during the 15 MA plasma scenario. In the axial direction, i.e. perpendicular to the joint plane, ramp rates as high as 0.65 T/s and -0.78 T/s can be reached in the PF1

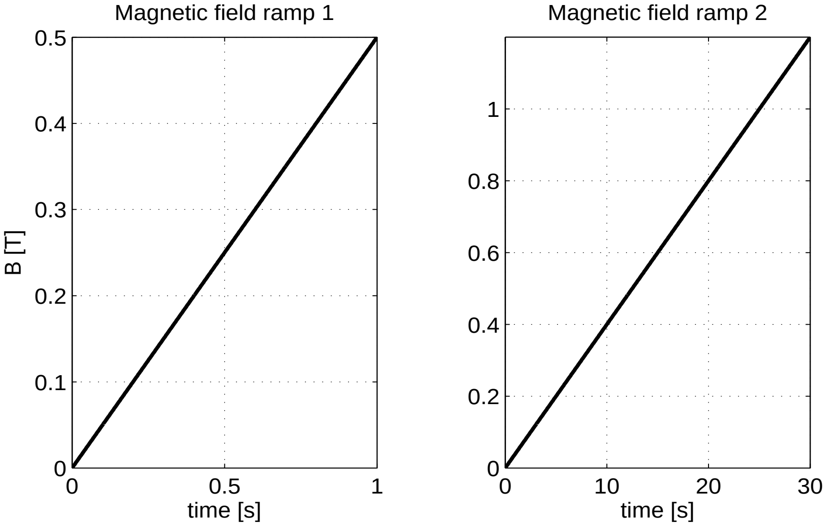

Figure 5.24: Magnetic field sweeps applied in the Poloidal Field coil joint performance assessment.

and PF2 centre joints. However, radial magnetic fields corresponding to the Face On configuration of Figure 2.24 are potentially more critical for the joint stability, enabling the formation of current loops that embrace the two conductors on both sides of the joint.

Finally, magnetic field ramp 2, with 40 mT/s, is representative for the slow magnetic field variation seen at the joints during most of the 15 MA plasma scenario.

Temperature boundary conditions and coefficients

Table 5.5 and Figure 5.25 give a summary of the values of the parameters of the thermal model presented in section 2.5.10 [71, 72, 70, 165].

Table 5.5: Thermal model parameters for the Poloidal Field coil joint analysis.

Parameter	**Unit**	**RRR$_{sole}$ = 100**	**RRR$_{sole}$ = 6**
Total He mass flow	g/s	9.7	
Inlet temperature	K	5	
Sole-Sole heat transf. coeff.	W/(m^2·K)	55·10^3	2.8·10^3
Sole-He heat transf. coeff.	W/(m^2·K)	500	
Petal-sole heat transf. coeff.	W/(m^2·K)	500	
Petal-He heat transf. coeff.	W/(m^2·K)	600	
Petal-Petal heat transf. coeff.	W/(m^2·K)	400	

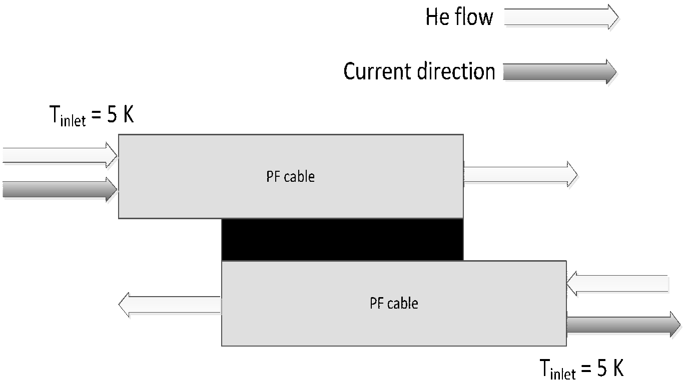

Figure 5.25: Boundary conditions for current and temperature of the Poloidal Field coil joints.

Resistance

For the Poloidal Field coil joint assembly, the steel jacket is removed from the conductors over a length slightly longer than the cable twist pitch; cable wraps are also removed. The sub-cable wraps are cut and removed only at the outer surface facing the sole in order to maintain sufficient inter-petal resistance to counteract coupling currents in pulsed operation. The cable is then compressed in the joint box to a void fraction of about 25%.

Featuring the same level of compaction, the same inter-strand resistivity parameter as the one estimated in section 2.5.11 for the NbTi strands of the Correction Coils joint is used in the Poloidal Field coil joint analysis. However, the inter-petal resistivity is taken a factor four higher, which is still significantly lower than the value reported in Table 4.4 for Central Solenoid conductors. This takes into account both the lower wrap coverage (50%) in the Poloidal Field conductor and their reduced void fraction in the joints. The resulting resistance between two neighbouring petals is about 50 nΩ·m. The strand-to-sole resistivity is then adjusted to achieve an overall joint resistance of 1 nΩ, in accordance with the design goal.

For optimization purpose, the effect of so-called petal masks is explored in some simulations. Petal masks are steel foils, similar to the petal wraps, that can be inserted locally at selected petal-to-sole interfaces during joint assembly. The aim is to increase the strand-to-sole resistance significantly at one of the joint extremities for those petals that feature double contacts with the sole. This has to prevent the formation of large coupling current loops for magnetic field pulses in the Face On configuration. The masking is to be applied to the shortest of the double petal-to-sole contacts to avoid poorly connected petals and hence an increase of the current imbalance. In the 30^o configuration, one petal per cable has identical contacts with the sole at both joint extremities and the masking is applied where the conductor enters the joint. In absence of experimental data, the value of the strand-to-sole resistivity at the mask locations is set to 400 times the intra-petal resistivity parameter. This causes an increase of the the resistance at the interface to about 1000 nΩ·m, corresponding to the average value reported in [75] for inter-petal contacts under load after several thousands of loading cycles in an ITER Poloidal Field prototype conductor with high wrap coverage (80%).

5.3.2 Simulation results

The analysis aims at comparing the performance of the following joint design variants:

- Case I: 0^o cable orientation, $RRR_{sole} = 100$ and no petal masks;
- Case II: 0^o cable orientation, $RRR_{sole} = 100$ and petal masks;
- Case III: 0^o cable orientation, $RRR_{sole} = 6$ and no petal masks;
- Case IV: 30^o cable orientation, $RRR_{sole} = 100$ and no petal masks.

Current ramp

The joint resistance R_{joint} value is determined from the power dissipation following the current profile in Figure 5.23, and specifically during the top current plateau, see Figure 5.26, after the decay of the coupling currents induced by the ramp. Table 5.6 summarizes the values for the cases analysed. The time constants following an exponential fit of the power decay after the initial slow ramp up (τ_1) and after the successive fast ramp down (τ_2) are reported as well.

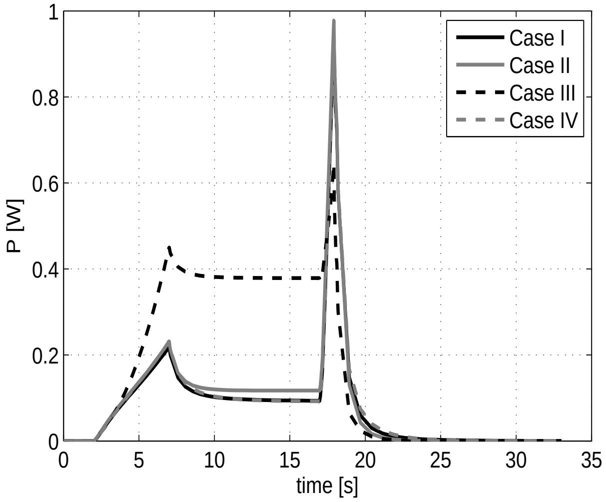

Figure 5.26: Overall joint power dissipation versus time for the four design variants.

The joint resistance is not affected by the selected cable orientation. However, the use of petal masks rises the value of R_{joint} in the 0^o configuration by 25% up to just above the 1 nΩ design goal. The effect is relatively small since the masking

Table 5.6: Joint resistance and coupling currents decay time constant of the four Poloidal Field coil joint variants.

Case	**R$_{joint}$ [nΩ]**	**ΔR$_{joint}$ [%]**	**τ_1 [s]**	**τ_2 [s]**
I	0.95	5	0.76	1.00
II	1.2	2	0.59	1.01
III	3.8	1	0.68	0.98
IV	0.95	5	0.91	1.00

is applied only to two petals and along their shortest contact with the sole. On the contrary, increasing the RRR of the copper sole leads to a factor 4 increase of the joint resistance.

The coupling current decay times show negligible differences among the four tested cases for fast current ramps, when the dominating coupling takes place within each cable or even petal. Larger variations are observed following a slow current ramp. The 30^o configuration shows a longer decay time constant compared to the 0^o one, due to the presence of three petals in contact with the sole at the extremities of the joint. Acting directly on the petals with double contacts, masks allow a faster decay time than a lower Cu RRR.

Figure 5.27 displays the current in the six petals of the top cable along the axis of the joint (with the copper sole located between -0.225 m and +0.225 m) at the end of the current plateau. The effect of the petal masks can be clearly observed in Case II, where petals 1 and 2 are forced to transfer their currents at the end and start of the sole, respectively, due to the increased strand-to-sole resistance at the mask locations. As a result, the power dissipation at the extremities of the

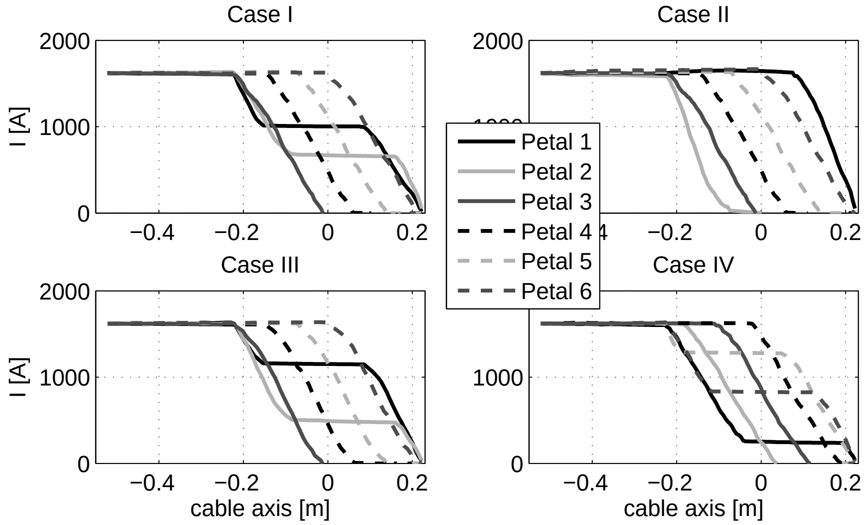

Figure 5.27: Petal currents the top cable along the joint axis at t = 15 s for the four design variants. Copper sole extends between ±0.225 m.

joint is significantly reduced in the presence of petals masks, see Figure 5.28.

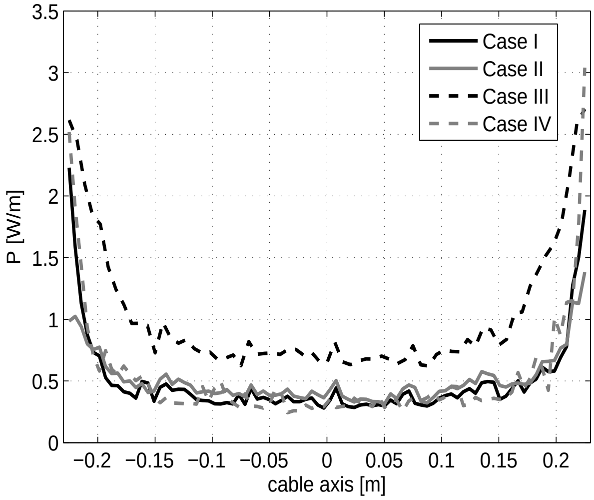

Figure 5.28: Power per meter along the joint axis at t = 5 s of the four design variants.

Fast magnetic field ramp in Face On direction

The effect of the variations in the designs on the coupling currents can be observed in Figure 5.29 showing the petal currents along the top cable at the end of magnetic field ramp 1 (see Figure 5.24). The peak coupling currents originate as expected in the petals with double contacts with the sole. Comparing the 0^o (Case I) and 30^o (Case IV) configurations, the latter is characterized by slightly lower peak coupling currents per petal. However, since more petals form a double contact with the sole, the overall coupling currents in the cables are larger as shown in Figure 5.30. In the case of fast magnetic field ramps, the use of a copper sole with low RRR does not have a relevant effect on the coupling currents.

Petal masks, however, cause a reduction of the coupling currents in the cables of some 20%. Although, as shown in Figure 5.29, the use of masks allows a decrease of about 25% of the peak coupling currents in the petals with double contacts with the copper sole, the coupling currents in the unmasked petals are found to increase, especially in the ones adjacent to the masked petals. This can be observed in Figure 5.31, comparing the strand current distributions in petals with double and single contacts in Cases I and II. Impeded by the petals masks, the coupling currents form alternative loops closing through the surrounding petals. As shown in Figure 5.29, these current loops can also extend to the sections of the conductor outside the sole region, where they cause a significant increase of the petal current.

Therefore, depending on the specific trajectories of the strands, some of the masked petals can be characterized by a relatively larger dissipation, which results

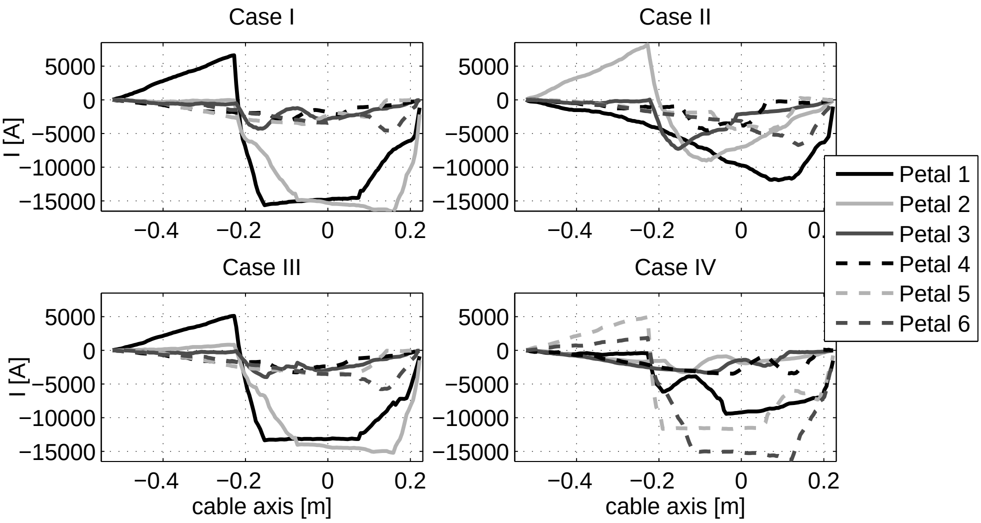

Figure 5.29: Petal currents in the top cable along the joint axis at the end of magnetic field ramp 1 for the four tested design variants. Copper sole extends between ±0.225 m.

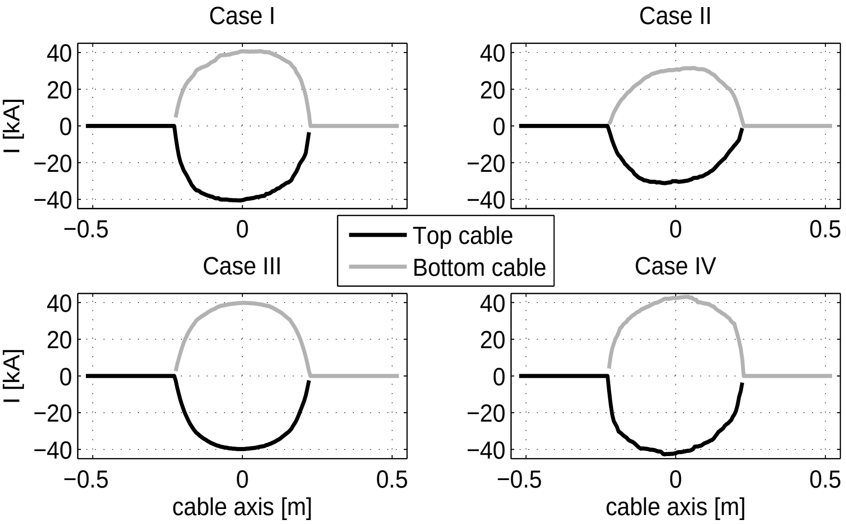

Figure 5.30: Cable currents along the joint axis at the end of magnetic field ramp 1 in the four design variants. Copper sole extends between ±0.225 m.

in a higher temperature increase, as shown in the case of petal 1 of the top cable in Figure 5.32. The higher dissipation within the cables in the presence of masks can also be noticed in Figure 5.33, which shows the contributions of coupling currents in the cables, cable-to-sole interface and sole to the overall dissipation. The dissipation in the cable-to-sole contact layer is minimized by the presence of petals masks. As expected, this term is the highest in the 30^o configuration because of the three petals that are contacting the sole.

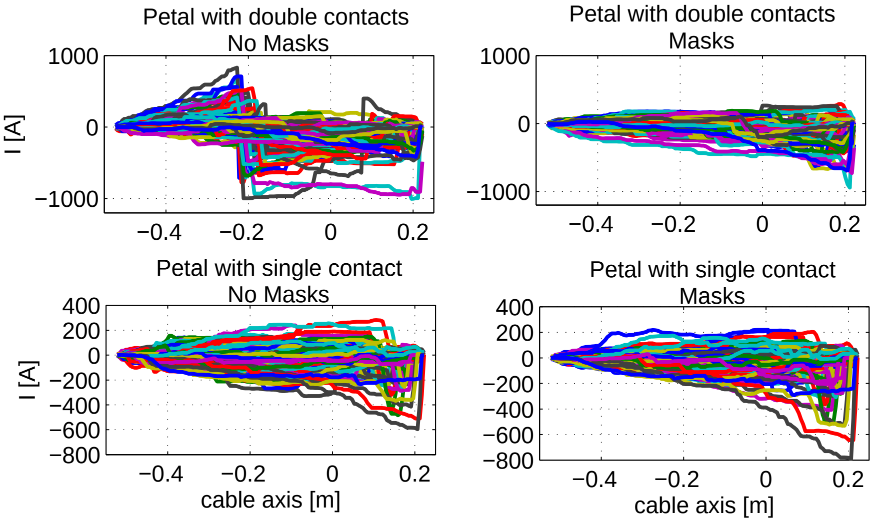

Figure 5.31: Strand currents along the joint axis in petals 1 (double contacts) and 6 (single contact) of the top cable with and without petal masks at the end of magnetic field ramp 1 in the four design variants. Copper sole extends between ±0.225 m.

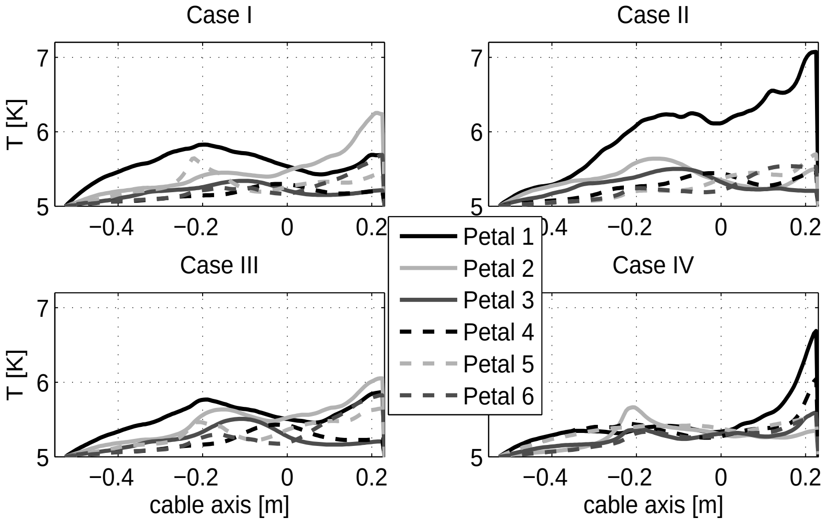

Figure 5.32: Petal temperature in the top cable along the joint axis at the end of magnetic field ramp 1 in the four design variants. Copper sole extends between ±0.225 m.

In Figure 5.33, it can be observed as well that masks even cause an increase of the dissipation and hence of the temperature of the copper sole ($T_{max} = 7.6$ K). However, this temperature rise is lower than the one in the sole with low RRR, where a peak temperature of 8.8 K is achieved.

Finally, in all cases strands exceed their critical current at the end of the magnetic field ramp; although their number as well as the moment at which the

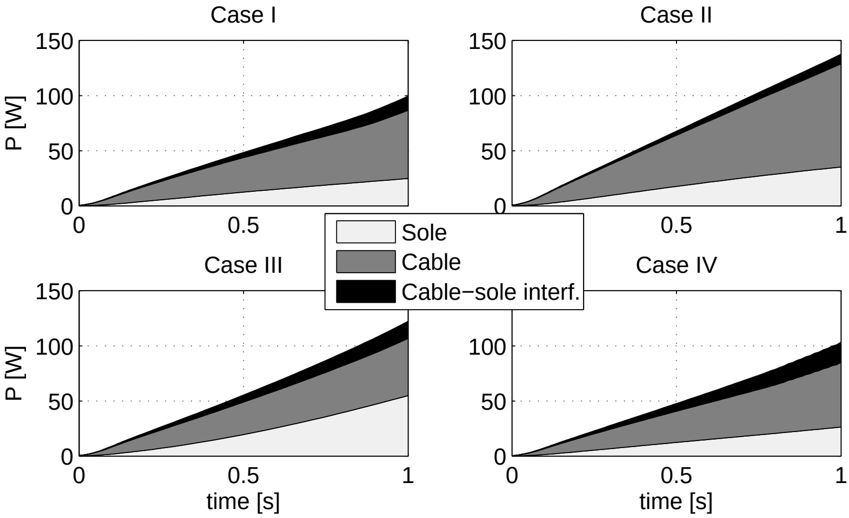

Figure 5.33: Power dissipation in the sole, two cables and cable-sole interface versus time in the four design variants.

current margin becomes negative depend on the specific joint design. Figure 5.34 shows the number of strands with current higher than their critical current at different instants of the ramp for the four tested cases. Significantly all strands with negative current margin feature a double contact with the copper sole. At worst (Case I at the end of the fast magnetic field ramp), 2% of the strands in a cable are found to exceed their critical currents. Considering the current carrying capacity available in the surrounding strands and the limitations of the present thermal routine discussed in chapter 4, it is at present not possible to conclude whether this would result in a quench. However, for sure the use of petal masks can help to reduce the probability of a quench by diminishing the number of critical strands.

Slow magnetic field ramp in Face On direction

Figure 5.35 shows the coupling currents in the petals of the top cable at the end of the slower magnetic field ramp 2 (see Figure 5.24). Whereas for fast magnetic field ramps the 0^o and 30^o orientations are characterized by similar coupling currents, much higher values are found for the 30^o orientation during slow magnetic field variations. In both configurations, higher coupling current values are reached at the end of the ramp when compared to the fast magnetic field sweep.

For slow magnetic field sweeps, petal masks prove to be quite effective in limiting the coupling currents, allowing a 70% reduction of the peak currents in the petals. Using a sole with low RRR value causes a similar effect. Although the currents are then limited to 60% of the peak value in Case I, the higher sole resistivity prevents the increase of the currents in the sub-cables with a single contact with

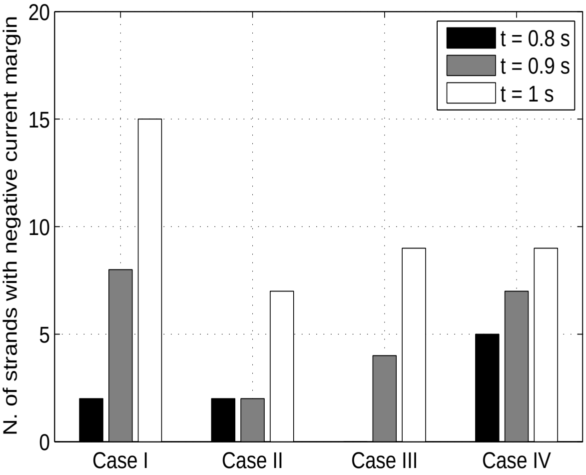

Figure 5.34: Number of strands exceeding their current carrying capacity I_c in the top cable for the four design variants at three moment during magnetic field ramp 1.

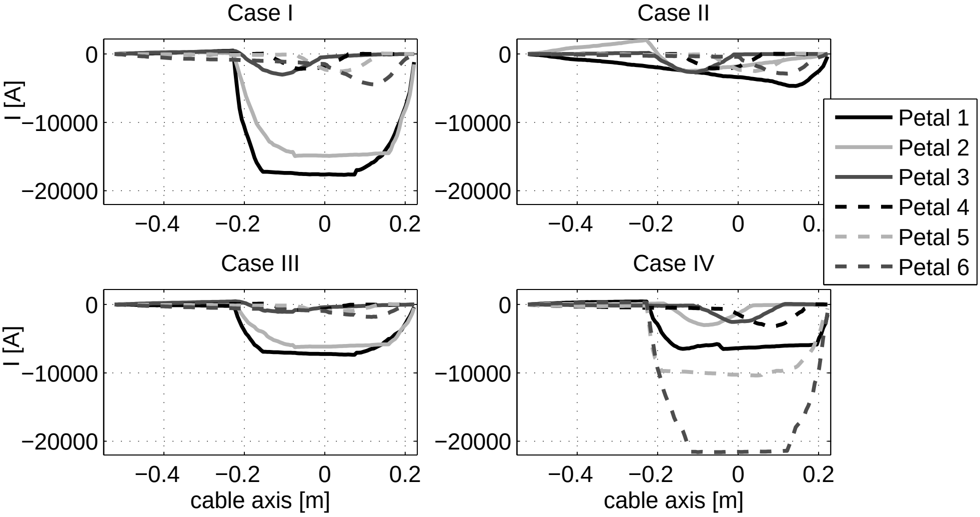

Figure 5.35: Petal currents in the top cable along the joint axis at the end of magnetic field ramp 2 for the four design variants. Copper sole extends between ±0.225 m.

the sole, which is observed in the other unmasked petals. However, as illustrated in Figure 5.36, a more efficient reduction of the overall cable coupling currents is obtained with the adoption of petals masks. Indeed, while the maximum current in the cables at the end of magnetic field ramp 2 is 10 kA in Case II with petals masks, a peak value of 16 kA is obtained in Case III with low copper sole RRR.

The use of both petals mask and a low sole RRR result in an earlier saturation of the coupling currents with time. While the currents in the petals that are in

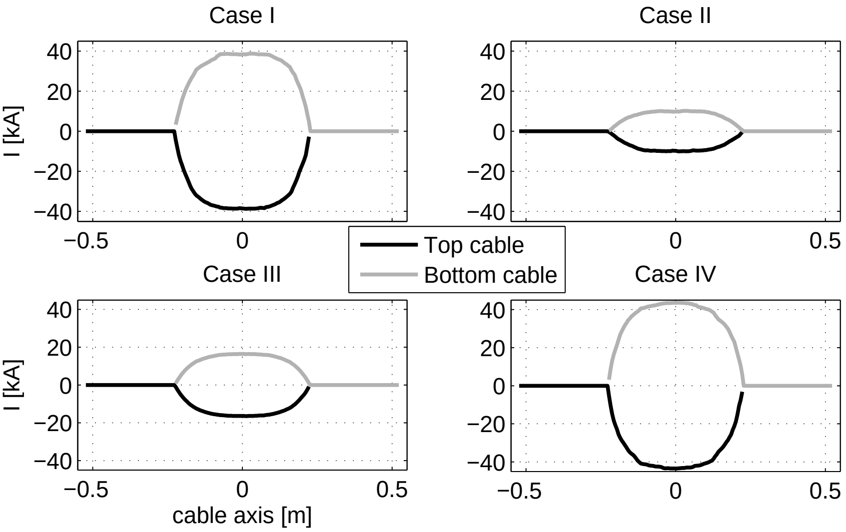

Figure 5.36: Cable currents along the joint axis at the end of magnetic field ramp 2 in the four design variants. Copper sole extends between ±0.225 m.

double contact with the sole continuously increase till the end of the ramp in Cases I and IV, no extra variation takes place in Cases II and III after 15 s. This can be observed in the power dissipation evolution with time shown in Figure 5.37, which reaches a plateau before the end of the magnetic field ramp in Cases II and III. The power generated during slow magnetic field sweeps is significantly lower (about 1/3) than in the analysed fast ramp and, in contrast to the fast ramp scenario, is further reduced by the use of petal masks and low copper RRR.

Finally, the coupling current limitation exerted by petals masks and low sole RRR is sufficient to avoid strands exceeding their critical current during the analysed slow magnetic field ramp, as demonstrated in Figure 5.38. Vice versa, when compared to the fast ramp a higher number of strands with negative current margin is observed at the end of the transient in Cases I and IV.

Fast magnetic field ramp in Edge On direction

The Edge On configuration is far less critical for the joint stability, as demonstrated by the significantly lower coupling currents during fast magnetic field transients as compared to the Face On orientation, see Figure 5.39. Similar petal current values are obtained in Cases I, II and IV. Compared to these three cases, the use of a low RRR copper in the sole causes an increase of the coupling within the cables in the joint. However, both the spread in current in the the cable sections outside the sole as well as the overall cable coupling currents shown in Figure 5.40 are smaller.

In all cases, no strands exceed their critical current, contrary to what happening

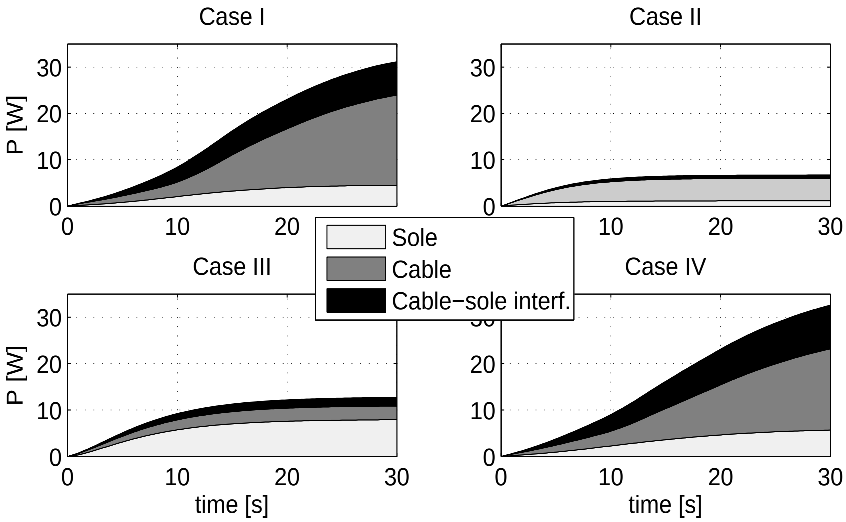

Figure 5.37: Power dissipation in the sole, two cables and cable-sole interface versus time in the four design variants.

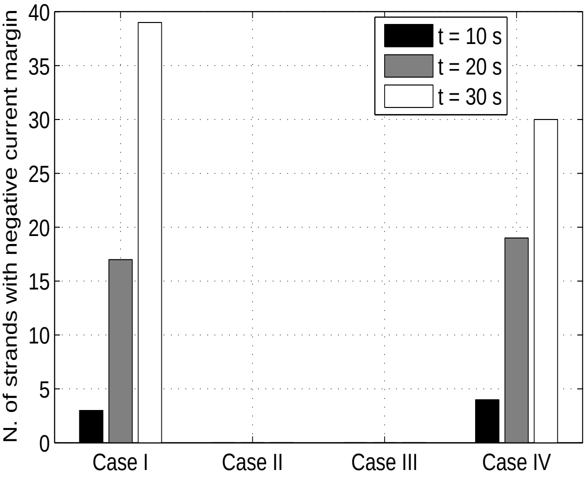

Figure 5.38: Number of strands exceeding their current carrying capacity I_c in the top cable for the four design variants at different times during magnetic field ramp 2.

during radial (i.e. Face On) magnetic field sweeps. Nevertheless, severe reduction of stability can be caused by the highly increased dissipation in the sole in the Edge On orientation, as shown in Figure 5.41. A peak temperature of the sole at the end of the run of more than 11 K is present in Cases I, II and IV. Although not predictable by the present thermal model, which features only petal-level accuracy, a noticeable temperature increase of the strands in touch with the sole can be expected, causing a reduction of their critical current to a level where no

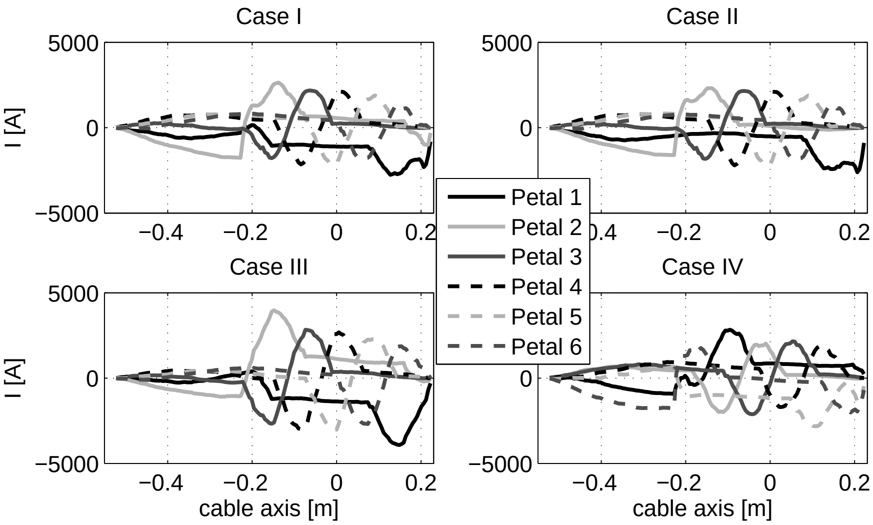

Figure 5.39: Petal currents in the top cable along the joint axis at the end of magnetic field ramp 1 for the four design variants. Copper sole extends between ±0.225 m.

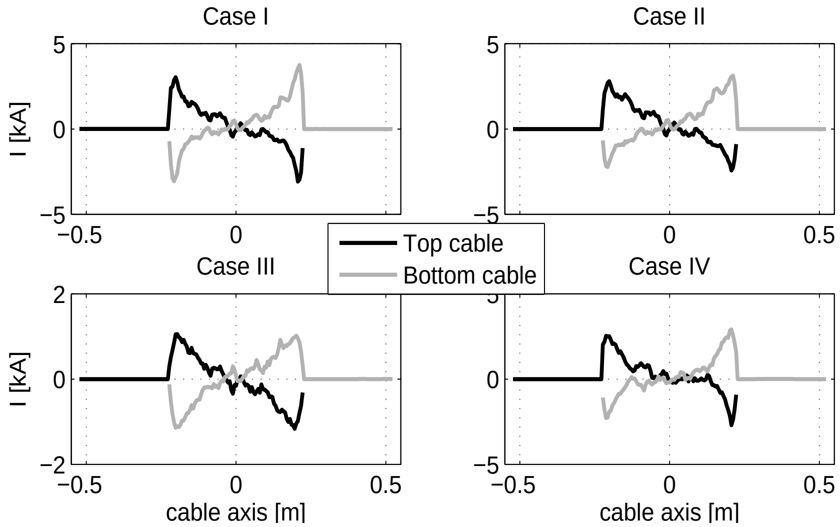

Figure 5.40: Cable currents along the axis of the joint at the end of magnetic field ramp 1 for the four design variants. The contact with the copper sole extends between -0.225 m and + 0.225 m.

stability margin remains .

To reduce this risk, high-resistivity copper may be used for the sole, which significantly limits the power dissipation in this component as illustrated in Figure 5.41. The use of a RRR value of 6, as in the presently tested Case III would lower the temperature reached by the sole at the end of the considered ramp down to a much safer value of 7.1 K.

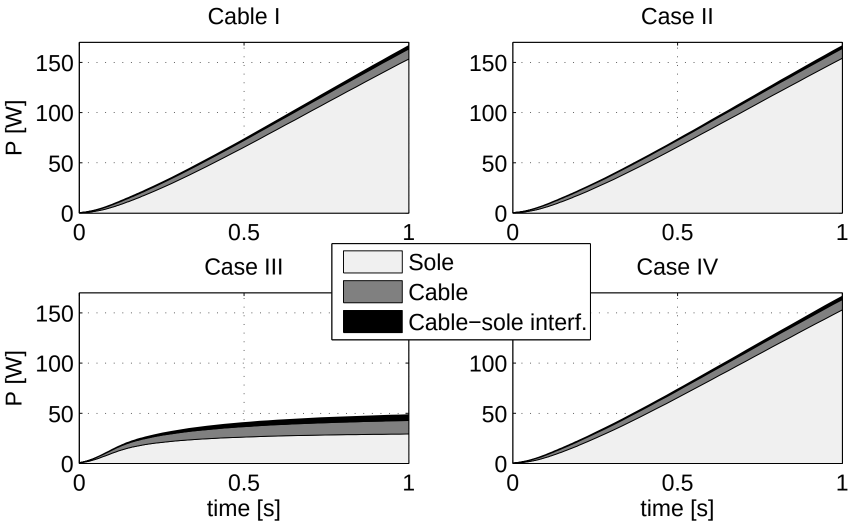

Figure 5.41: Power dissipation in the sole, two cables and cable-sole interface versus time in the four design variants.

Slow magnetic field ramp in Edge On direction

Slow magnetic field ramps in the Edge On direction are characterized by the lowest coupling currents and power dissipation of all the analysed cases. Figures 5.42 and 5.43 show the currents in the petals of the top cable and in the two cables at the end of the transient.

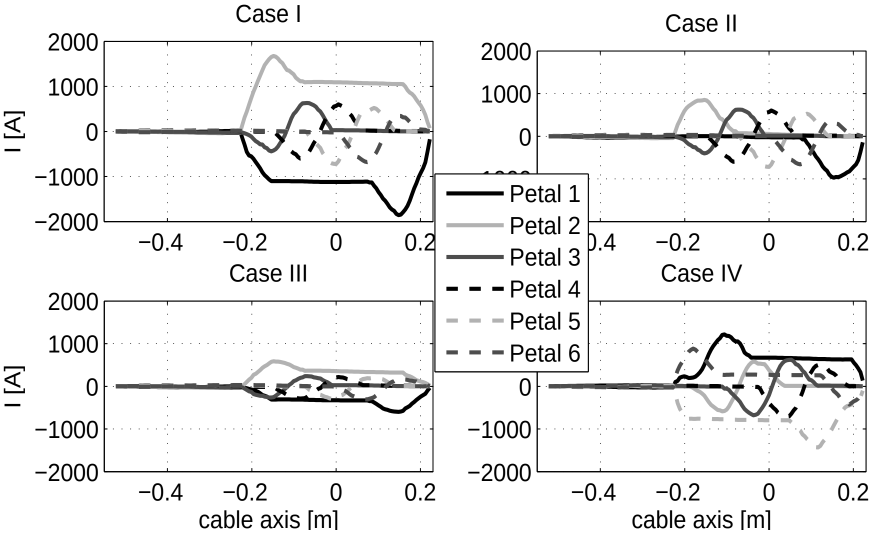

Figure 5.42: Petal currents in the top cable along the joint axis at the end of magnetic field ramp 2 in the four design variants. Copper sole extends between ±0.225 m.

Unlike rapid magnetic field variations but in accordance with slow sweeps in

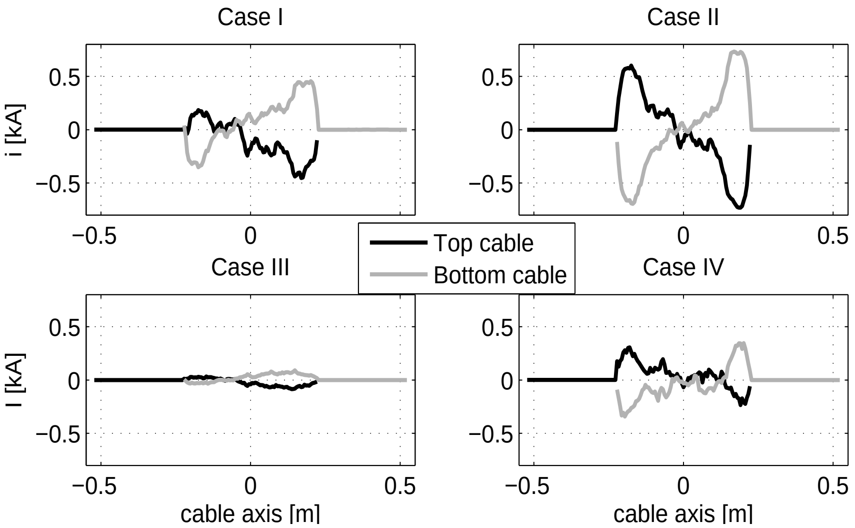

Figure 5.43: Cable currents along the joint axis at the end of magnetic field ramp 2 in the four design variants. Copper sole extends between ±0.225 m.

the radial (Face On) direction, the presence of petal mask limits the peak coupling currents in the petals. However, the overall cable currents are found to be somewhat higher in this case. Interestingly, the 30^o configuration features slightly lower currents than the 0^o one, which is likely related to the lower average contact angle of the petals with the sole at the extremes of the joint.

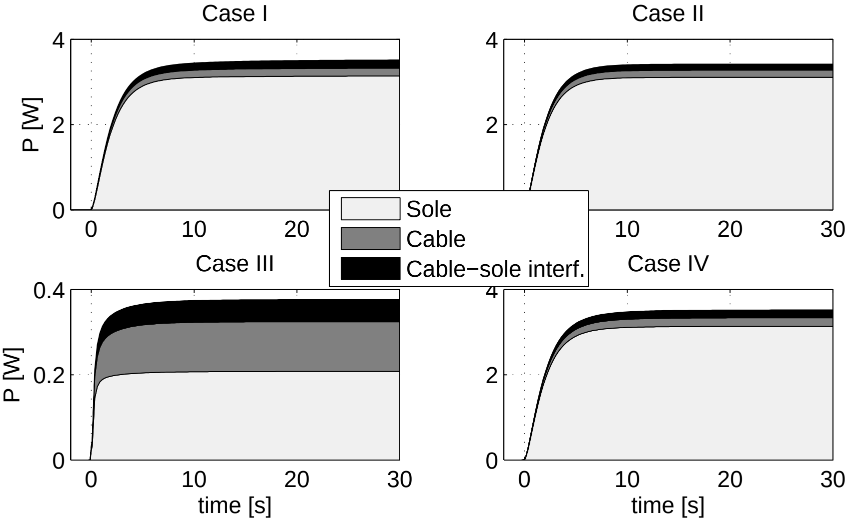

Figure 5.44: Power dissipation in the sole, two cables and cable-sole interface versus time in the four design variants.

As for the fast transients, the best performance is achieved by reducing the

RRR of the sole, which minimizes the eddy currents in the copper that represent the main dissipation source for magnetic field ramps in the axial direction. As can be observed in Figure 5.44, the induced power generation is quite low in all joint design variants, leading to a negligible temperature increase in both cables and sole.

Coupling loss time constant

To complete the characterization of the four Poloidal Field coil joint design variants, their coupling loss time constants $n\tau$ are computed for an harmonic magnetic field of amplitude with 0.2 T (no static background magnetic field present) and frequencies in the range 1 to 100 mHz, see Figures 5.45 and 5.46. The joints are exposed to magnetic field variations both in the Face On and Edge On configurations. The calculation assumes no transport current and full penetration of the filaments. The loss is the sum of coupling and eddy current losses in the two cables, strand-to-sole contacts and sole. It is normalized to the sum of sole and strand volumes. The coupling loss time constant is found by fitting the loss up to 20 mHz with a second or third order polynomial and taking the slope at the low frequency limit. Table 5.7 summarizes the computed $n\tau$ values.

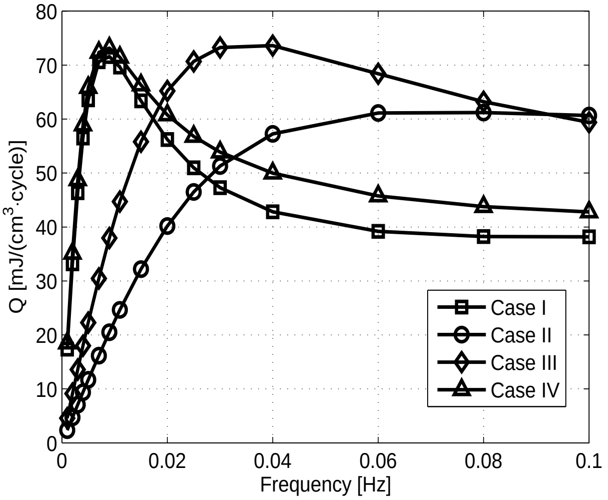

Figure 5.45: Coupling loss density per cycle versus frequency for a PF2 joint exposed to Face On magnetic field variations up to 100 mHz for the four design variants.

As already emerged from the previous analysis, in the Face On configuration Case I and IV have similar loss, with the latter design showing slightly higher values due to the presence of three petals with double contacts with the sole. The highest loss reduction is obtained by blocking the formation of large current loops between the two cables through the use of petal masks. A noticeable decrease of $n\tau$ is also achieved through the use of a resistive sole, although the peak value of

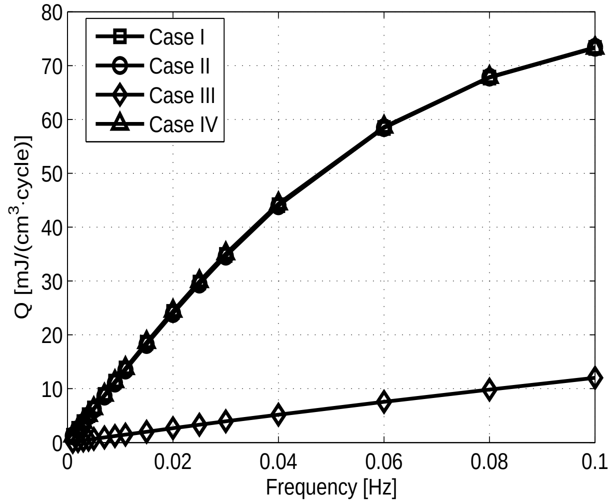

Figure 5.46: Coupling loss density per cycle versus frequency for a PF2 joint exposed to Edge On magnetic field variations up to 100 mHz for the four design variants.

Table 5.7: Coupling loss time constant for Face On and Edge On magnetic field changes for the four design variants.

Case	$n\tau_{FaceOn}$ [s]	$n\tau_{EdgeOn}$ [s]
I	31	2.1
II	3.8	2.0
III	7.7	0.2
IV	31	2.1

the loss is unchanged, but only shifted in frequency.

For Edge On magnetic field, the main contribution to the loss originates from the eddy currents in the sole and coupling currents within each cable. Accordingly, Cases I, II and IV result in practically the same loss performance, while a low RRR sole minimizes the dissipation in this configuration. Although the loss increase with frequency in the Edge On direction is much slower than in the Face On one, the peak loss in the considered frequency range can reach the same absolute value.

5.4 Conclusion

The JackPot-ACDC joint model is applied to assess the performance of the lap-type joints for the ITER Toroidal Field and Poloidal Field coils. The analysis is carried out using either plasma scenario conditions or specific magnetic field and current sweeps representative for the operating environment.

In the Toroidal Field coil joint analysis, different joint resistance values based on experimentally measured inter-strand resistance distributions are used to verify the proper behaviour of the joints under all cyclic conditions. The study reveals that pulsed losses are not critical for Toroidal Field coil joints due to their position and orientation within the ITER magnet system. However, the joint assembly procedure should be carefully controlled to achieve a 1 nΩ joint resistance following the steady-state dissipation target of 5 W, in accordance with the available cooling power of the cryogenic system. An effective way to reduce the large steady-state power dissipation is the addition of solder on the outer cable surface to reduce the strand-to-sole contact resistance. Further reduction of the steady-state power can be achieved by increasing the RRR value of the copper sole.

The conclusions for the Poloidal Field coil joints are qualitatively different. Transients, and especially fast magnetic field variations in the Face On direction, are potentially critical for some of the envisaged 1 nΩ joints, depending on their location within the magnet system. In this configuration, the presence of petals contacting twice the copper sole at both joint extremities enables the formation of large coupling loops. Although they allow a significant reduction (up to 70%) of the peak coupling currents for slow magnetic field ramps, petal masks show only limited effect in the case of fast magnetic field variations, failing to contain the currents in the doubly connected petals to the level of the singly-connected ones. Similarly, lowering the RRR of the copper sole is also an ineffective measure against fast radial magnetic field transients. However, a highly resistive sole allows to curtail the dissipation due to Edge On ramps significantly, which also improves the joint stability by limiting the temperature rise at the cable-sole interface. The downside is, of course, a relatively large increase of the joint resistance.

Finally, the coupling loss time constants for both Toroidal Field (interconnecting and terminal joints) and Poloidal Field coil joints are evaluated for Face On and Edge On magnetic field changes and for all joint resistance values and design variants considered in the previous analysis. $n\tau$ is found to vary between 0.2 and 35 s, depending on inter-strand and sole resistances and on the presence of solder.

Chapter 6

Conclusion

The focus of this thesis has been on the understanding and optimization of the performance of Cable-In-Conduit conductors and lap-type joints for nuclear fusion type of magnets, with specific reference to the ITER project.

6.1 Modelling the performance of CIC conductors and lap-type joints

Modelling the performance of CIC conductors and their interconnecting and terminal joints is an essential part of the R&D effort for the construction of fusion magnets. It allows to test multiple design variants in a fast and inexpensive way. Simulation based on a high-level model including strand-level details enables to gain a deeper understanding of the various phenomena involved.

Numerical modelling of CIC conductors comprising several hundreds of strands cabled in multiple stages, such as the conductors for the ITER tokamak magnet system, is a challenging task due to the considerable number of unknowns to be assessed, requiring significant computing resources and time. *The new electromagnetic code JackPot-ACDC, especially developed for this purpose, is a state-of-the-art model that allows to simulate the performance of full-size ITER-type CIC conductors up to lengths of several tens of meters with strand-level details included.* In addition, lap-type joints between the CIC conductors and their influence on the performance can be simulated as well.

By using the Multi-Level Fast Multiple Method, the mutual- and self-inductances of all strand sections are incorporated in the model, enabling time-dependent analysis following any shape of magnetic field sweep. In steady-state conditions, the effect of the joint layout on the non-uniformity of the strand current can be studied as well when coupling the cable network to a Finite Element model of the joint.

Among the key strengths of JackPot-ACDC is its ability to compute the complex trajectories of all strands inside a conductor, which are then used to define all network variables. Remarkably, *the only required input are resistivity parameters* that, properly scaled with the contact area, defines the inter-strand and strand-to-sole resistances. The resistivity parameters can be derived either from direct inter-strand resistance or AC loss measurements. With the exception of the strain state of Nb_3Sn strands, no free parameters exist in the model that can be tuned to match the experimental results. The model results are truly a-priori predictions.

Since inter-strand and strand-to-sole resistances determine to a high degree the performance of conductors and lap-type joints, *the knowledge of the resistivity parameters turns out to be the key factor when quantitative predictions are required.* At present a significant amount of inter-strand resistance data exist especially on cable sections, which were mostly measured at the University of Twente. However, some data sets feature inter-strand resistances measured between bundles of strands or sub-cables, which makes the derivation of the resistivity parameters required by JackPot-ACDC impractical. To improve the analysis even further, the measurement of a higher variety of couples of strands both within the same petal and in different petals would be beneficial for a better quantitative mapping of the network of resistances. Moreover, the assessment of the influence of twist pitch, wraps coverage and void fraction on the value of the resistivity parameters beyond the available data on ITER-type CIC conductors and joints would allow a more quantitative performance analysis of modified or new conductor designs.

More challenging is the determination of the axial strain state of the Nb_3Sn strands. Although an average strain value can be deduced from the experimental V-T characteristics of the cable, the local strain state is unknown. In recent years, considerable effort has been spent on the development of a numerical model of the mechanical behaviour of the strands for computing strain maps of the conductors incorporating both the thermal stress after cool-down and Lorentz force [170]. However, *up to now these attempts of combined electro-magnetic and mechanical modelling of CIC conductors do not yet converge conclusively with the measurements* and hence such maps have not been adopted in the analysis presented in this thesis.

Upgrading the thermal routine is recommended if the stability of the cable is to be unequivocally predicted. As emerged in chapter 4, the present thermal model only computes the average petal temperature increase and this is not sufficient to distinguish between quench and recovery of conductors in the case of saturated strands. Such prediction would require a similar strand-level thermal refinement as the one adopted in the electro-magnetic part of the code. A further development is the implementation of a complete thermal-hydraulic routine to describe the compressible helium flow (i.e. featuring continuity, momentum and energy conservation laws completed with the transverse mass, momentum and energy transfer terms to take into account the coupling with different flows and solid materials), which can ideally be fully coupled to the electro-magnetic model. The main difficulty of such an extension lies in the assessment of the constants involved, like heat transfer coefficients, friction factors, that can heavily affect the reliability of the stability evaluation.

6.2 CIC conductor optimization in steady-state operation

An uneven current distribution among the strands is the main source of thermal instability in large current carrying NbTi-type CIC conductors under (quasi) steady-state conditions, because of the sharp dependence of their critical current on the magnetic field. The unbalance originating at the joints may be such that the most overloaded strands become saturated when they enter the high field region of the magnet.

In chapter 3 the current non-uniformity and the power dissipation distribution are computed for the first time with strand-level detail included.

Current non-uniformity is particularly critical in short conductor samples where current re-distribution cannot take place due to the short distance between the joint and the high-magnetic field region. The model simulations reveal how in ITER Poloidal Field short conductor samples an imbalance by a factor 2 is qualitatively associated with a transition from the cable to the single strand quench regime, and hence with the appearance of sudden quenches. The same joint layout results in a significantly lower current non-uniformity ($\sim$1.5) in a long sample and no quench regime transition is observed. Nevertheless, *current distribution related instabilities can also affect the performance of coils, when joints are located in relatively high-magnetic fields without adequate cooling.*

As a rule of thumb based on the cases analysed, the maximum current imbalance allowed in ITER-type Poloidal Field conductors in operating conditions is 1.5. The expected cable power dissipation at quench is then typically in the range of 0.15-0.20 $\mathrm{mW/cm^3}$, whereas the strand peak power varies, depending on the strand characteristics and cable configuration, between 65 and 250 $\mathrm{mW/cm^3}$. Once the allowable peak power and the acceptable level of current non-uniformity are known in relation to the magnetic field and temperature profile in the conductor, the electric resistance of the joint components can be optimized for minimal heat load determined by AC losses and steady-state resistance.

Separating the petals within the cable terminal area and individual connection of the petals to the copper sole (joint combo box design) is an effective solution to decrease current non-uniformity. Although not-practical for implementation in fusion magnets, this joint design can be used to avoid termination effects during short sample conductor qualification tests.

Alternatively, *the addition of solder at the strand-to-sole interface during joint assembly can help to achieve an equivalent result.* However, the usefulness of soldered joints in real magnets should be carefully assessed taking into consideration the specific joint location and coil operating conditions to avoid a reduction of stability during pulsed operation.

While *reduction of the joint length below the final stage twist pitch length has to be avoided to prevent sharp performance degradation in short conductor samples*; negligible improvements are within reach by making the joint longer. Little influence is also observed for an increase of the cable-to-sole contact angle up to 180^o, although this results can be influenced by the presence of a sleeve between the two components in the analysed design.

Finally, *only relatively small improvements are visible in short conductor samples by removing the petal wraps* when the cable is affected by a relatively high current imbalance. Under these conditions, the short available length for re-distribution may not be sufficient to avoid the transition to the strand quench regime even when the re-distribution capability is facilitated by removing the wraps.

6.3 CIC conductor optimization in pulsed operation

Parametric variation has been used to analyse the relation between twist pitch sequence and coupling loss in multi-stage CIC conductors. In chapter 4, this issue is investigated for the first time in conductors of similar complexity as those envisaged for the ITER magnets. The numerical study shows that *the coupling loss during pulsed operation is determined essentially by two factors:*

- *the absolute value of the twist pitches;*
- *the ratio between the pitch lengths of successive cabling stages (the last one with resistive wraps excluded).*

As generally recognized, coupling losses can be limited by applying short twist pitches. However, as convincingly demonstrated here, *a significant reduction can also be achieved by using a ratio between the pitches of the successive stages that is close to one*, i.e. successive twist pitches of similar length. The reduction is a consequence of flux linkage minimization in the narrow current loops between the strands.

This newly found correlation allows to combine long twist pitches with low coupling loss. The relevance of the result lies in the proven potential of long twist pitches *to mitigate the degradation of the current sharing temperature with electro-magnetic and thermal cycling in* Nb_3Sn *strands*, one of the major issues faced in the development of the conductors for the ITER Toroidal Field coils and Central Solenoid.

Following a proposal from the University of Twente, this strategy was incorporated in the Long Twist Pitch (LTP) prototype design for the ITER Central Solenoid CIC conductor. Also three other solutions were included in an experimental test campaign. The so-called Baseline and Short Twist Pitch (STP) conductors share the same overall LTP cabling layout, but with different twist schemes, namely the ITER original and significantly shorter ones. The 3SC conductor instead relies on the same twist scheme as the Baseline design, but with a higher number of superconducting strands featuring a larger overall Cu content and no pure Cu strands.

Despite a first stage twist pitch that is twice to five times longer than those of the other designs, the measured AC loss for the LTP conductor sample up to 0.4 Hz is two to three times lower, confirming the prediction of the code. However, the current sharing temperature of the LTP design seems to degrade faster than expected and especially at a higher rate than the STP one, which is characterized even by a slight increase of the current sharing temperature with cycling.

AC loss characterization of the ITER samples is performed by exposing the conductors to a purely sinusoidal magnetic field in the absence of transport current. These conditions are not fully representative for the operating plasma scenarios, when both external magnetic field and transport current vary in a much more complex way. Since it is well known that the stability of strands and the entire conductor depends on the shape and time duration of the applied excitation, *an appropriate stability performance assessment has to incorporate operating plasma conditions or pulsed conditions closely resembling those.*

At present, plasma-scenario like conditions cannot be reproduced in any of the existing conductor test facilities, implying that numerical simulation is the only viable tool for such parametric studies. In chapter 4 the performance of the four prototype conductors proposed for the ITER Central Solenoid is compared when exposed to the 15 MA plasma scenario, both before and after the application of load cycling.

The simulations show that after several thousands of load cycles, *the STP design is characterized by a significantly higher coupling loss compared to the other three conductor variants.* This is a consequence of the stiff structure of the cable following the short pitches, which on the other hand also ensures the excellent mechanical performance. Due to the higher coupling loss *in the STP conductor, the advantage of a higher current sharing temperature is largely compensated by the higher temperature increase of the strands during real plasma operating conditions.*

If the effective temperature margin ΔT, defined as the difference between steady-state current sharing temperature and plasma scenario peak temperature in a petal, is used as safety criteria, a quench-free operation is predicted for all the proposed design variants ($\Delta T >1$ K before cycling and $\Delta T >1.5$ K after cycling). However, the effect of high coupling loss on the current distribution, which can lead to local strand saturation, also has to be taken into account.

The analysis of the strand current margin indeed reveals that *in all the four simulated conductor variants, even after cycling, a number of strands exceeds their current carrying capacity at the Start of Discharge.* This negative current margin may seem in contradiction with the positive temperature margin, but it has to be noted that:

- the temperature margin ΔT is deduced from the average petal temperature increase, whereas the local temperature in single strands at the saturated spots can very well rise to higher values. As such, the previously defined temperature margin is likely overestimated;
- pulsed and steady-state quench conditions can differ significantly, depending

on the pulse shape and duration. *Therefore, characterization of conductor performance in terms of a steady-state current sharing temperature alone may not be sufficient to ensure stability.*

Predicting whether or not the saturated spots evolve into a quench is beyond the capability of the present thermal routine. Therefore, the probability of quench or recovery is evaluated by comparing the simulation output with relevant experimental data on quench behaviour, i.e. the quench electric field obtained from the steady-state conductor characterization and the quench energy recorded during transient stability tests. The major difficulty, however, lies in the fact that plasma quench conditions are situated between these two boundaries and the effect of different dissipation profiles on quench energy and electric field cannot be estimated based on the available data.

The comparison with steady-state quench conditions shows that *after cycling, quench-free operation can be expected for the Baseline, 3SC and LTP designs.* On the other hand, the simulated average electric field along the STP superconducting strands at the Start of Discharge features peaks exceeding the steady-state quench electric field. The energy dissipation in the four conductor variants during the first 2 s of the plasma scenario is below the transient stability quench energy of a sub-size conductor. However, while a large and safe margin seems to exist for the Baseline, 3SC and LTP variants, the same cannot be stated convincingly for the STP variant when the experimental and simulation uncertainties that may reduce the about 140 mJ/cm^3 margin are considered.

Based on the above considerations, *the use of short twist pitches in their actual implementation appears as potentially more risky from a pulsed stability point of view than the other variants explored*, if no changes are expected of the present plasma scenarios. The possibility of a significant improvement of the stability margin by acting on the helium mass flow rate is questionable in light of the results obtained in past model coils and would require a higher pumping power. *The addition of a resistive strand coating would easily allow a decrease of the coupling loss in the STP conductor design.* However, this solution is not applicable for ITER magnets, since it requires a new qualification round incompatible with its present construction schedule.

Given its interesting loss performance, further investigation of the influence of void fraction and cabling pattern on the mechanical behaviour of the LTP design is advisable, in order to understand its higher than expected degradation as measured.

Since transient loss characterization and loss limitation should be a priority in the design of pulsed fusion magnets (and given the present impossibility of experimental test under plasma-scenario like conditions), *transient stability measurements could be routinely included in the conductor characterization program* *to better assess their stability performance.*

6.4 Lap-type joint optimization

The optimization of lap-type joints in terms of design and resistance of the components for both improved steady-state and pulsed operation strongly depends on the position of the joint relative to the coils generating the magnetic field. Therefore, the expected operational conditions (transport current, external magnetic field, etc...) have to be taken into account in studies, since they can lead to a significant relaxation of some constraints.

The analysis carried out in chapter 5 shows how *pulsed operation is not critical for the stability of the joints in the ITER Toroidal Field coils.* Despite the disadvantage of the Face On orientation with regard to the changing magnetic field, their position within the magnet system prohibits excessive coupling currents for a wide range of joint resistance values.

Pulsed operation should be carefully optimized for some of the Poloidal Field coil joints, especially with regard to radial magnetic field sweeps that can cause large current loops which embrace both cables on the either sides of the joint. Such loops involve sub-cables with double contacts to the sole, which originate from the requirement that the joint length must be at least equal to the last stage twist pitch length in order to reduce current imbalance within the conductors.

To inhibit the induction of high coupling currents, the effect of petal masks inserted locally at selected cable-to-sole interfaces is explored. This solution is found effective in the case of slow transients, since it prevents strands from exceeding their current margin. However, its efficiency during fast magnetic field sweeps is limited and insufficient for reducing the coupling currents in the double connected sub-cables all the way to the level of the other petals. The outcome is not significantly different when increasing the mask resistance, since the current loops close through alternative paths within the cable or petals, sometimes even outside the joint region. Considering the limited performance gain for fast pulses and also the fact that the following increase of assembly complexity of this solution has not yet been experimentally qualified, *the whortwhileness of implementing masks in the final Poloidal Field coil joints should be carefully considered.*

Alternatively, to reduce the coupling between the conductors the resistance of the sole can also be increased. Although it yields a more limited improvement of the joint performance compared to the use of petal masks, this solution offers the advantage that it is easily applicable. Moreover, it drastically reduces the eddy current dissipation and temperature rise in the sole during axial magnetic field pulses. This reduced temperature in turn results in a higher stability of the strands in contact with the sole.

Nonetheless, the analysis shows that *for fast Face On transients either petal mask nor low sole RRR are able to avoid strands that exceed their critical currents*, although both reduce their number. Considering the limitations of the thermal simulation routine and the finding that even in the most demanding conditions tested 2% of the superconducting strands are in a potentially critical state, it is not really possible to predict whether or not the joint will quench. To eliminate all doubt, *the most promising design option is a reduction of the length of the sole such as to avoid double contacts*, as already suggested before [163, 169]. The optimal sole length is related to the cable orientation within the joint, which cannot be controlled a-priori. The risk of a sharp loss of performance, as found in short conductor samples presented in chapter 3, has to be assessed as well. The degradation in a large coil is likely to be less severe and strongly linked to the precise magnetic field profile on the cable outside the joint. Therefore, the feasibility of this solution requires more analysis and, possibly, the simulation of a full conductor length in the final Poloidal Field coil configuration.

A major drawback associated with the decrease of the RRR of the sole in lap-type joints is the resulting increase of the resistance in steady-state. The issue is particularly relevant for joints carrying large steady-state currents, like in the ITER Toroidal Field coils. When pulsed operation is not critical, *a good solution is the addition of a layer of solder to reduce the strand-to-sole contact resistance.* However, the increased complexity of joint assembly, and specifically the compatibility of the solder melting temperature with the heat treatment required for the Nb_3Sn strands, should be taken into consideration. Alternatively, a solder-free construction needs to be qualified that consistently allows to achieve the required 1 nΩ joint resistance.

A few last words:

This thesis provides an overview of the new high level of understanding of the performance of CIC conductors and joints that has been made available in recent years by progress in their numerical modelling. Nevertheless, several issues still remain open that require additional refinement of the existing models.

Although at present the question how to build the perfect CIC conductor and lap-type joint for fusion magnets cannot be answered conclusively, I sincerely hope that the knowledge acquired in this thesis is a significant contribution to the success of future nuclear fusion machines.

Appendix A

This appendix deals with the direct calculation of the current normalized vector potential $\vec{A_{ij}}$ introduced in Eq. 2.29 to compute the mutual inductances between strands.

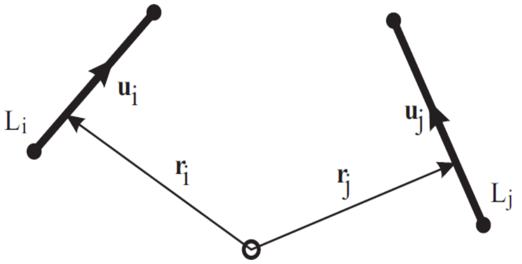

Figure 1: Configuration for the calculation of the mutual inductances between current carrying elements $\vec{L_i}$ and $\vec{L_j}$.

In the configuration above, a variable t is introduced in the interval $-\frac{1}{2} \leqslant t \leqslant \frac{1}{2}$ to parametrize the segment $\vec{L_j}$ extending from $\vec{x_2}$ to $\vec{x_1}$, leading to

$$|\vec{r_{ij}}| = |\vec{x_i} - \frac{\vec{x_2} + \vec{x_1}}{2} - (\vec{x_2} - \vec{x_1})t| \quad [\mathrm{m}] \tag{1}$$

and

$$d\vec{L}_j = \frac{\vec{x_2} - \vec{x_1}}{|\vec{x_2} - \vec{x_1}|} dt \quad [\mathrm{m}]. \tag{2}$$

After some elaboration the vector potential can be written as

$$\vec{A'_{ij}} = \frac{\mu_0}{4\pi} \frac{\vec{x_2} - \vec{x_1}}{|\vec{x_2} - \vec{x_1}|} \int_{-\frac{1}{2}}^{\frac{1}{2}} (at^2 + bt + c)^{-\frac{1}{2}} dt \quad [\mathrm{V} \cdot \mathrm{s} \ /(\mathrm{A} \ \cdot \mathrm{m})] \tag{3}$$

with

$$a = |\vec{x_2} - \vec{x_1}|^2 \quad [\mathrm{m}^2] \tag{4}$$

$$b = 2(\vec{x_2} - \vec{x_1}) \cdot (\frac{\vec{x_2} + \vec{x_1}}{2} - \vec{x_i}) \quad [\mathrm{m}^2] \tag{5}$$

$$c = |\frac{\vec{x_2} + \vec{x_1}}{2} - \vec{x_i}|^2 \quad [\mathrm{m}^2]. \tag{6}$$

Eq. 3 can be integrated analytically and gives

$$\vec{A'_{ij}} = \frac{\mu_0}{4\pi} \frac{\vec{x_2} - \vec{x_1}}{|\vec{x_2} - \vec{x_1}|} \ln(\frac{k_1}{k_2}) \quad [\mathrm{V} \cdot \mathrm{s} \ /(\mathrm{A} \ \cdot \mathrm{m})] \tag{7}$$

with

$$k_1 = \frac{b + a}{2\sqrt{a}} + \sqrt{\frac{a}{4} + \frac{b}{2} + c} \quad [\mathrm{m}^2] \tag{8}$$

and

$$k_2 = \frac{b - a}{2\sqrt{a}} + \sqrt{\frac{a}{4} - \frac{b}{2} + c} \quad [\mathrm{m}^2]. \tag{9}$$

The current-normalized vector potential is not defined for $b < 0$. However, since the system is defined to be symmetric around the mid point of the source line, the problem can be solved by taking the absolute value of b.

Bibliography

[1] F. Romanelli et al. A roadmap to the realisation of fusion energy. *EFDA scientific publication*, 2012.

[2] H. S. Bosch et al. Wendelstein 7-X a technology step towards Demo. *Paper in Plasma and Fusion Research*, 5:S1002, 2009.

[3] International Atomic Energy Agency. Summary of the ITER final design report. *IAEA report*, IAEA-ITER-EDA-DS-22, 2001.

[4] J. Knaster et al. ITER non-axisymmetric error fields induced by its magnet system. *Paper in Fusion Engineering and Design*, 86(6-8):1053–1056, 2011.

[5] J. H. Schultz et al. The ITER Central Solenoid. *Proceedings 21st IEEE/NPS Symposium on Fusion Engineering*, 1-4, 2005.

[6] B. Lim et al. Design of the ITER PF coils. *Paper in IEEE Transactions on Applied Superconductivity*, 21(3):1918–1921, 2011.

[7] N. Mitchell. Scenarios for coil, power supply and cryoplant analysis. *ITER report*, 2FTVKV v1.10, 2009.

[8] National High Magnetic Field Laboratory - Applied Superconductivity Centre, Tallahassee, FL, USA. *Materials database available on website.* http://www.magnet.fsu.edu/magnettechnology/research/asc/plots.html.

[9] F. van Howell. Design estimates for a medium-sized SMES system based on different superconducting materials. *Master of Science graduation report, University of Twente*, 2008.

[10] L. Bottura. A practical fit for the critical surface of NbTi. *Paper in IEEE Transactions on Applied Superconductivity*, 10(1):1054–1057, 2000.

[11] A. Godeke et al. Scaling of the critical current in ITER-type niobium-tin superconductors in relation to the applied field, temperature and uni-axial applied strain. *Paper in IEEE Transactions on Applied Superconductivity*, 9(2):161–164, 1999.

[12] Y. Iwasa. Case studies in superconducting magnets. *Book published by Springer, New York*, 2010.

[13] M. N. Wilson. Superconducting magnets. *Book published by Clarendon Press, Oxford*, 1983.

[14] I. Pong et al. Current sharing temperature of NbTi SULTAN samples compared to prediction using a single pinning mechanism parametrization for

NbTi strand. *Paper in Superconductor Science and Technology*, 25:054011, 2012.

[15] N. Mitchell. Design Description Document 11-7: Conductors. *ITER report*, 2NBKXY v1.2, 2009.

[16] P. J. Lee. ITER TF strand characterization at FSU. *Presentation at Design Reconciliation Workshop (Aix en Provence)*, 65AJYA v1.0, 2011.

[17] A. Nijhuis et al. Optimization of ITER Nb_3Sn CICC for coupling loss, transverse electromagnetic load and axial thermal contraction. *Paper in Superconductor Science and Technology*, 25:015007, 2012.

[18] N. N. Martovetsky. Development of the butt joint for the ITER Central Solenoid. *Paper in IEEE Transactions on Applied Superconductivity*, 17(2):1358–1360, 2007.

[19] A. Di Zenobio et al. Joint design for the EDIPO. *Paper in IEEE Transactions on Applied Superconductivity*, 18(2):192–195, 2008.

[20] N. N. Martovetsky et al. Qualification of the joints for the ITER Central Solenoid. *Paper in IEEE Transactions on Applied Superconductivity*, 22(3):4804004, 2012.

[21] J. L. Duchateau et al. Development of high-current high-field conductors in Europe for fusion application. *Paper in Superconductor Science and Technology*, 15:R17–R29, 2002.

[22] T. Schild et al. Effect of actual cabling pattern on the critical current of a multi-stage CICC. *Paper in Advances in Cryogenic Engineering B*, 46:1051–1058, 2000.

[23] P. Bruzzone et al. Upgrade of operating range for SULTAN test facility. *Paper in IEEE Transactions on Applied Superconductivity*, 12(1):520–523, 2002.

[24] D. Ciazynski et al. DC performances of ITER NbTi conductors: models vs. measurements. *Paper in IEEE Transactions on Applied Superconductivity*, 15(2):1355–1358, 2005.

[25] D. Bessette. DC performance analysis of NbTi and Nb_3Sn ITER relevant Cable-In-Conduit Conductors. *Paper in IEEE Transactions on Applied Superconductivity*, 15(2):1403–1406, 2005.

[26] E. Zapretilina. Analysis of anomalous behaviour of V-I characteristic with bumps. *CRPP report*, 2004.

[27] L. Zani. PFIS DC test analysis. *Presentation at 5th PFIS Test Group Meeting (Villigen)*, 27XQ2A v1.0, 2004.

[28] N. N. Martovetsky. Trying to predict NbTi PFIS in SULTAN. *Presentation at PFIS Test Group Meeting (Cadarache)*, 2004.

[29] R. Wesche et al. DC performance of subsize NbTi Cable-In-Conduit Conductors. *Paper in IEEE Transactions on Applied Superconductivity*, 14(2):1499–1502, 2005.

[30] R. Zanino et al. A two-fluid code for the thermohydraulic transient analysis of CICC superconducting magnets. *Paper in Journal of Fusion Energy*, 14(1):25–40, 1995.

[31] B. Seeber. Handbook of applied superconductivity: Volume I. *Book published by IOP, Bristol*, 1998.

[32] W. J. Carr Jr. AC loss in a twisted filamentary superconducting wire. *Paper in Journal of Applied Physics*, 45(2):929–934, 1974.

[33] W. J. Carr Jr. et al. Alternating field losses in a multifilamentary superconducting wire for weak AC fields superimposed on a constant bias. *Paper in Journal of Applied Physics*, 46(9):4048–4052, 1975.

[34] G. H. Morgan. Theoretical behavior of twisted multi-core superconducting wire in a time varying uniform magnetic field. *Paper in Cryogenics*, 41:3673–3679, 1970.

[35] G. H. Morgan. Eddy currents in flat metal-filled superconducting braids. *Paper in Cryogenics*, 44:3319–3322, 1973.

[36] A. M. Campbell. A general treatment of losses in multifilamentary superconductors. *Paper in Cryogenics*, 22(1):3–16, 1982.

[37] G. Ries. AC losses in multifilamentary superconductors at thecnical frequencies. *Paper in IEEE Transactions on Magnetics*, MAG-13(1):524–526, 1977.

[38] D. Ciazynski et al. Electrical and thermal designs and analyses of joints for the ITER PF coils. *Paper in IEEE Transactions on Applied Superconductivity*, 12(1):538–542, 2002.

[39] A. Nijhuis et al. Effect of self-field and current non-uniformity on the voltage-temperature characteristic of the ITER Central Solenoid insert coil by numerical calculations. *Paper in Cryogenics*, 42:469–483, 2002.

[40] A. P. Verweij. Electrodynamics of superconducting cables in accelerator magnets. *PhD Thesis, University of Twente*, 1995.

[41] F. Bellina et al. Modeling a multistrand SC cable with an electrical DC lumped network. *Paper in IEEE Transactions on Applied Superconductivity*, 12(1):1408–1412, 2002.

[42] M. Ciotti et al. THELMA code electromagnetic model of ITER superconducting cables and application to the ENEA stability experiment. *Paper in Superconductor Science and Technology*, 19:987–997, 2006.

[43] M. Breschi et al. Electromagnetic modeling of the jacket in Cable-In-Conduit Conductors. *Paper in IEEE Transactions on Applied Superconductivity*, 18(1):18–28, 2008.

[44] F. Bellina et al. The THELMA model of the joint resistance distribution test with JORDI. *Paper in IEEE Transactions on Applied Superconductivity*, 18(2):1092–1096, 2008.

[45] E. P. A van Lanen et al. JackPot: a novel model to study the influence of

current non-uniformity and cabling patterns in Cable-In-Conduit Conductors. *Paper in Cryogenics*, 50:139–148, 2010.

[46] E. P. A. van Lanen et al. Simulation of interstrand coupling loss in Cable-In-Conduit Conductors with JackPot-AC. *Paper in IEEE Transactions on Applied Superconductivity*, 21(3):1926–1929, 2011.

[47] E. P. A. van Lanen et al. Full-scale calculation of the coupling losses in ITER size Cable-In-Conduit Conductors. *Paper in Superconductor Science and Technology*, 25:025012, 2012.

[48] E. P. A. van Lanen et al. Validation of a strand-level CICC-joint coupling loss model. *Paper in Superconductor Science and Technology*, 25:025013, 2012.

[49] MathWorks, Natick, MA, USA. *Software code available on website.* http://www.mathworks.com.

[50] Y. J. Chen et al. A method for modeling the winding pattern of a large scale superconducting cable. *Paper in IEEE Transactions on Magnetics*, 32(5):5145–5147, 1996.

[51] COMSOL, Stockholm, Sweden. *Software code available on website.* http://www.comsol.com.

[52] G. Rolando et al. Minimum quench power dissipation and current non-uniformity in International Thermonuclear Experimental Reactor type NbTi Cable-In-Conduit Conductor samples under direct current conditions. *Paper in Journal of Applied Physics*, 111:093904, 2012.

[53] P. Bruzzone et al. Test results of the ITER PF Insert conductor short Sample in SULTAN. *Paper in IEEE Transactions on Applied Superconductivity*, 15(2):1351–1354, 2005.

[54] B. Liu et al. Test results and analyses of conductor short samples for China first PF conductor. *Paper in Cryogenics*, 51:90–94, 2011.

[55] J. Ekman. Electromagnetic modeling using the partial element equivalent circuit method. *PhD thesis, Lulea University of Technology*, 2003.

[56] W. Abbas et al. A fully automatic press for mechanical and electrical testing of full-size ITER conductors under transverse cyclic load. *Paper in Advances in Cryogenic Engineering*, 50:51–58, 2004.

[57] G. Rolando et al. Minimizing coupling loss by selection of twist pitch lengths in multi-stage Cable-In-Conduit Conductors. *Paper submitted to Superconductor Science and Technology*, 2013.

[58] G. Rolando et al. Temperature and current margin of ITER Central Solenoid conductor designs during a 15 MA plasma scenario. *Paper submitted to Superconductor Science and Technology*, 2013.

[59] B. Stepanov et al. SULTAN test facility: summary of recent results. *Paper in Fusion Engineering and Design*, 88:282–285, 2013.

[60] F. W. Grover. Inductance calculations: working formulas and tables. *Book*

published by Dover Publication, Inc., New York, 1946.

[61] F. Bellina et al. Computation of the magnetostatic field by means of a mixed analytica-numerical procedure. *Paper in IEEE Transactions on Magnetics*, 40(2):834–837, 2004.

[62] L. F. Greengard. The rapid evaluation of potential fields in particle systems. *Book published by MIT Press, Cambridge, MA*, 1988.

[63] N. A. Gumerov. Fast multipole methods for the helmholtz equation in three dimensions. *Book published by Elsevier, Oxford*, 2005.

[64] B. van de Wiele et al. Application of the fast multipole method for the evaluation of magnetostatic fields in micromagnetic computations. *Paper in Journal of Computational Physics*, 227:9913–9932, 2008.

[65] Lawrence Livermore National Laboratory Center for Applied Scientific Computing. Livermore, CA, USA. *Equation solver available on website*, <http://computation.llnl.gov/casc/sundials/main.html>.

[66] L. Muzzi et al. Test result of a NbTi wire for the ITER poloidal field magnets: a validation of the 2-pinning components model. *Paper in IEEE Transactions on Applied Superconductivity*, 21(3):3132–3137, 2011.

[67] T. Schild et al. Magnetic field orientation dependence of critical current in industrial Nb_3Sn strands. *Paper in Cryogenics*, 38:1251–1257, 1998.

[68] S. Takacs et al. Critical currents of NbTi tapes with differently oriented anisotropic defects. *Paper in Cryogenics*, 23(3):153–159, 1983.

[69] E. P. A. van Lanen et al. Impact of cabling pattern, magnet field profile and joint properties on short sample qualiĄcation tests of ITER conductors. *Paper in IEEE Transactions on Applied Superconductivity*, 19(3):1444–1447, 2009.

[70] W. Offringa. Thermo-hydraulic joint model with typical PF joint parameters as exemplary input (TeST-Joint). *ITER report*, 4BZB5N v1.4, 2011.

[71] L. Bottura et al. Analysis of transverse heat transfer coefficient in CICCs with central cooling channel. *Paper in Cryogenics*, 46:597–605, 2006.

[72] C. Marinucci et al. Analysis of the transverse heat transfer coefficient in a dual channel ITER-type Cable-In-Conduit Conductor. *Paper in Cryogenics*, 47:563–576, 2007.

[73] Cryocomp v3.01, Cryodata Inc, Eckels engineering, Florence, SC, USA. *Materials database available on website.* http://www.eckelsengineering.com.

[74] National Institute of Standards and Technology. Gaithersburg, MD, USA. *Materials database available on website*, <http://webbook.nist.gov/chemistry/fluid>.

[75] Y. Ilyin et al. Effect of cyclic loading and conductor layout on contact resistance of full-size ITER PFCI conductors. *Paper in IEEE Transactions on Applied Superconductivity*, 15(2):1359–1362, 2005.

[76] F. Cau et al. Inter-strand resistance and current redistribution in a Cable-

In-Conduit Conductor (CICC) termination. *Paper in IEEE Transactions on Applied Superconductivity*, 19(3):1452–1456, 2009.

[77] Y. Miyoshi et al. AC loss, inter-strand resistance and mechanical properties of an option-II ITER CICC up to 30,000 cycles in the press. *Paper in IEEE Transactions on Applied Superconductivity*, 21(3):1944–1947, 2011.

[78] Y. Miyoshi et al. AC loss measurements with transversal load cycles in Twente press on Hitachi-81JNC002-S4T1. *University of Twente report*, 2011.

[79] A. Foussat. Functional specification for the Correction Coil terminal joint DC resistance and AC losses. *ITER report*, 33338E v1.0, 2010.

[80] A. Foussat. ITER magnet system side Correction Coils: SCC terminal joint details. *ITER technical drawing*, 006493, 2010.

[81] A. Nijhuis et al. ITER NbTi CC joint AC loss tests. *University of Twente report*, 82331, 2012.

[82] D. Shuangsong. The result of ITER CC conductor joint DC test. *ASIPP report*, 2011.

[83] K. V. Namjoshi et al. Low-frequency eddy-current loss estimation in long conductors by using the moment of inertia of cross sections. *Paper in IEEE Transactions on Magnetics*, 24(5):2181–2185, 1988.

[84] A. K. Ghosh et al. V-I transition and n-value of multifilamentary LTS and HTS wires and cables. *Paper in Physica C*, 401(1):15–21, 2004.

[85] N. Amemiya et al. Experimental study on current re-distribution and stability of multi-strand superconducting cables. *Paper in IEEE Transactions on Applied Superconductivity*, 7(2):942–945, 1997.

[86] N. Amemiya. Overview of current distribution and re-distribution in superconducting cables and their influence on stability. *Paper in Cryogenics*, 38:545–550, 1998.

[87] N. Amemiya et al. Influence of current re-distribution on minimum quench energy of superconducting triplex cable against local disturbance. *Paper in Cryogenics*, 38:559–568, 1998.

[88] N. Amemiya et al. Normal zone propagation process accompanied by current re-distribution in superconducting triplex cables. *Paper in Cryogenics*, 40:655–662, 2000.

[89] N. Amemiya et al. Current re-distribution and stability of superconducting triplex cable without electrical insulation carrying non-uniform current. *Paper in Cryogenics*, 43:249–254, 2003.

[90] G. Bansal et al. Quench characteristic of a NbTi CICC with non-uniform current distribution. *Paper in IEEE Transactions on Applied Superconductivity*, 18(2):1245–1248, 2008.

[91] R. Wesche et al. DC performance, AC loss and transient field stability of five medium size NbTi Cable-In-Conduit Conductors with parametric

variations. *Paper in Cryogenics*, 43:249–254, 2003.

[92] V. S. Vysotsky et al. Current distribution in multi-strand superconducting cables - experimental methods and results. *Paper in Physica C*, 310:351–357, 1998.

[93] Y. A. Ilyin et al. Case studies in reconstruction efficiency of current distribution in CICC's by self-field measurements. *Paper in IEEE Transactions on Applied Superconductivity*, 13(2):1748–1751, 2003.

[94] Y. Ilyin et al. Reconstruction of the current unbalance in full-size ITER NbTi CICC by self field measurements. *Paper in IEEE Transactions on Applied Superconductivity*, 15(2):1391–1394, 2005.

[95] Y. Ilyin et al. Interpretation of conduit voltage measurements on the Poloidal Field Insert Sample using the CUDI-CICC numerical code. *Paper in Cryogenics*, 46:517–529, 2006.

[96] A. Nijhuis et al. The effect of inter-bundle resistive barriers on the coupling loss and current distribution in ITER NbTi Cable-In-Conduit Conductors. *Paper in IEEE Transactions on Applied Superconductivity*, 16(2):868–871, 2006.

[97] R. Wesche et al. Comparison of the DC performance of full- and sub size NbTi Cable-In-Conduit Conductors. *Paper in IEEE Transactions on Applied Superconductivity*, 16(2):819–822, 2006.

[98] R. Zanino et al. EU contribution to the test and analysis of the ITER poloidal field conductor insert and the central solenoid model coil. *Paper in Superconductor Science and Technology*, 22:085006, 2009.

[99] F. H. Hurd et al. Design and manufacture of a Full Size Joint Sample (FSJS) for the qualiĄcation of the Poloidal Field (PF) Insert Coil. *Paper in IEEE Transactions on Applied Superconductivity*, 15(2):1379–1382, 2005.

[100] F. H. Hurd et al. Status of investigations on PF Conductor Insert (PFCI) joints. *Presentation at 5th PFIS Test Group Meeting (Villigen)*, 2FV4HL v1.0, 2004.

[101] C. Sborchia et al. Design and manufacture of the Poloidal Field Conductor Insert coil. *Paper in Fusion Engineering and Design*, 66-68:1081–1086, 2003.

[102] W. Baker et al. Manufacture of the Poloidal Field Conductor Insert coil (PFCI). *Paper in Fusion Engineering and Design*, 82(5-14):1567–1573, 2007.

[103] H. Rajainmaki. *Private email communication*, 2010.

[104] L. Reccia. Report on ITER contract CT/09/4300000048. *ENEA report*, 2010.

[105] R. Zanino et al. Predictive analysis of the ITER Poloidal Field Conductor Insert (PFCI) test program. *Paper in IEEE Transactions on Applied Superconductivity*, 17(2):1353–1357, 2007.

[106] R. Zanino et al. Analysis of sudden quench of an ITER superconducting

NbTi full-size short sample using the THELMA code. *Paper in Superconductor Science and Technology*, 24:105001, 2011.

[107] G. P. Willering. Stability of superconducting rutherford cables. *PhD Thesis, University of Twente*, 2009.

[108] R. Wesche et al. Analysis and implications of V-I characteristic of PF insert conductor sample. *Paper in Fusion Engineering and Design*, 75-79:229–233, 2005.

[109] P. Bruzzone et al. Test results for the high field conductor of the ITER Central Solemoid Model Coil. *Paper in Advances in Cryogenic Engineering*, 45:729–736, 2000.

[110] N. Mitchell. Design Description Document 11-7: Conductors. *ITER report*, 2NPLKM v1.8, 2009.

[111] T. Ando et al. Effect of chrome coating on coupling losses in a Nb_3Sn Cable-In-Conduit Conductor. *Paper in Cryogenic Engineering*, 22:362–367, 1987.

[112] P. Bruzzone et al. Effect of Cr plating on the coupling current loss in Cable-In-Conduit-Conductors. *Proceedings of the 16th International Cryogenic Engineering Conference-International Cryogenic Materials Conference*, 2:1243–1248, 1996.

[113] A. Nijhuis et al. Inter-stand contact resistance and AC loss of a 48-strands Nb_3Sn CIC Conductor with a Cr/Cr-oxide coating. *Paper in IEEE Transactions on Applied Superconductivity*, 10(1):1090–1093, 2000.

[114] A. Nijhuis et al. The influence of Lorentz force on the AC loss in sub-size Cable-In-Conduit Conductors for ITER. *Paper in IEEE Transactions on Applied Superconductivity*, 7(2):262–264, 1997.

[115] N. N. Martovetsky et al. Test of the ITER Central Solenoid Model Coil and CS Insert. *Paper in IEEE Transactions on Applied Superconductivity*, 12(1):600–605, 2002.

[116] P. Bruzzone et al. Test results of ITER conductors in the SULTAN facility. *Proceedings of the 24th IAEA Fusion Energy Conference*, pages 1–8, 2012.

[117] N. Mitchell. Summary, assessment and implications of the ITER model coil test results. *Paper in Fusion Engineering and Design*, 66-68:971–993, 2003.

[118] T. Hemmi et al. Test results and investigation of T_{cs} degradation in japanese ITER CS conductor samples. *Paper in IEEE Transactions on Applied Superconductivity*, 22(3):4803305, 2012.

[119] A. Nijhuis. A solution for transverse load degradation in ITER Nb_3Sn CICCs: verification of cabling effect on Lorentz force response. *Paper in Superconductor Science and Technology*, 21:054011, 2008.

[120] A. M. Campbell. AC losses in cables of twisted multifilment superconductors. *Paper in Cryogenics*, 20(11):651–654, 1980.

[121] K. Kwasnitza et al. Experimental evidence for an interaction effect in the

coupling losses of cabled superconductors. *Paper in Cryogenics*, 23(11):9–14, 1983.

[122] S. Kawabata et al. Inter-strand coupling effect on losses and current distributions in superconducting cable conductors. *Paper in Cryogenics*, 34(4):293–301, 1994.

[123] T. Schild et al. A model for calculating AC losses in multi-stage superconducting cables. *Paper in Cryogenics*, 36(12):1039–1049, 1996.

[124] M. Ciotti et al. Loss calculations in a CICC solenoid exposed to rapidly changing magnetic fields. *Paper in Physica C: Superconductivity*, 372-376(3):1750–1753, 2002.

[125] S. A. Lelekhov. A physical model and numerical method for losses investigation in superconducting Cable-In-Conduit Conductors (CICC). *Paper in Cryogenics*, 46:1–8, 2006.

[126] L. Bottura et al. Computations of AC loss in the ITER magnets during fast field transients. *Paper in IEEE Transactions on Applied Superconductivity*, 17(2):2438–2441, 2007.

[127] T. Yagai et al. Flux linkage areas of coupling current loops for different shape Cable-In-Conduit Conductor. *Paper in Cryogenics*, 50(3):200–203, 2010.

[128] B. Turck et al. A macroscopic model for coupling current losses in cables made of multi-stages of superconducting strands and its experimental validation. *Paper in Cryogenics*, 50(8):443–449, 2010.

[129] Y. Miyoshi et al. Inter-strand Rc, AC loss, and mechanical properties of EUTF3-EAS up to 30,000 load cycles in the Twente press. *University of Twente report*, 2010.

[130] J. W. Ekin. Effect of stress on the critical current of Nb_3Sn multifilamentary composite wire. *Paper in Applied Physics Letters*, 29(3):216–219, 1976.

[131] N. N. Martovetsky. ITER Model Coil tests overview: Nb_3Sn strand properties in Cable-In-Conduit Conductors. *Paper in Physica C*, 401(1):22–27, 2004.

[132] N. Mitchell. Operating strain effects in Nb_3Sn Cable-In-Conduit Conductors. *Paper in Superconductor Science and Technology*, 18:S396–S404, 2005.

[133] N. N. Martovetsky et al. Effect of conduit material on CICC performance under high cycling loads. *Paper in IEEE Transactions on Applied Superconductivity*, 15(2):1367–1370, 2005.

[134] A. Nijhuis et al. Transverse load optimization in Nb_3Sn CICC design; inĆuence of cabling, void fraction and strand stiffness. *Paper in Superconductor Science and Technology*, 19:945–962, 2006.

[135] A. Nijhuis et al. Effect of periodic cyclic deformation on the voltage current transition of Nb_3Sn strands tested in the novel TARSISŹ setup. *Paper in IEEE Transactions on Applied Superconductivity*, 14(2):1464–1467, 2004.

[136] N. Mitchell. Assessment of conductor degradation in the ITER CS insert coil and implications for the ITER conductors. *Paper in Superconductor Science and Technology*, 20:25–34, 2005.

[137] P. Bruzzone et al. Test results of two European ITER TF conductor samples in SULTAN. *Paper in IEEE Transactions on Applied Superconductivity*, 18(2):1088–1091, 2008.

[138] D. Ciazynski et al. InĆuence of cable layout on the performance of ITER-type Nb_3 Sn conductors. *Paper in Journal of Physics: Conference Series*, 97:012027, 2008.

[139] P. Bruzzone et al. Test results of a Nb_3Sn Cable-In-Conduit Conductor with variable pitch sequence. *Paper in IEEE Transactions on Applied Superconductivity*, 19(3):1448–1451, 2009.

[140] N. N. Martovetsky et al. Test results of the first US ITER TF conductor in SULTAN. *Paper in IEEE Transactions on Applied Superconductivity*, 19(3):1478–1482, 2009.

[141] C. Gung et al. Fabrication of the first US ITER TF conductor sample for qualification in SULTAN facility. *Paper in IEEE Transactions on Applied Superconductivity*, 19(3):1474–1477, 2009.

[142] A. Devred et al. Status of conductor qualification for the ITER Central Solenoid. *Paper in IEEE Transactions on Applied Superconductivity*, 23(3):6001208, 2013.

[143] A. Nijhuis et al. Optimization of inter-strand coupling loss and transverse load degradation in ITER Nb_3Sn CICCs. *Paper in IEEE Transactions on Applied Superconductivity*, 23(3):4201206, 2013.

[144] A. Nijhuis et al. Impact of void fraction on mechanical properties and the evolution of coupling loss in ITER Nb_3Sn conductors under cyclic transverse loading. *Paper in IEEE Transactions on Applied Superconductivity*, 15(2):1633–1636, 2005.

[145] A. Nijhuis et al. Change of inter-strand contact resistance and coupling loss in various prototype ITER NbTi conductors with transverse loading in the Twente Cryogenic Cable Press up to 40,000 cycles. *Paper in Cryogenics*, 44:319–339, 2004.

[146] P. Libeyre et al. Detailed design of the ITER Central Solenoid. *Paper in Fusion Engineering and Design*, 84(7-11):1188–1191, 2009.

[147] A. Nijhuis et al. Performance of an ITER CS1 Model Coil conductor under transverse cyclic loading up to 40,000 cycles. *Paper in IEEE Transactions on Applied Superconductivity*, 14(2):1489–1494, 2004.

[148] J. L. Duchateu et al. Stability of a Cable-In-Conduit-Conductor under fast magnetic field variations. *Paper in IEEE Transactions on Applied Superconductivity*, 22(3):4803205, 2012.

[149] L. Bottura. Cable stability. *Proceedings of CERN Accelerator School*, 2013.

[150] L. Dresner. Parametric study on the stability margin of Cable-In-Conduit superconductors: theory. *Paper in IEEE Transactions on Magnetics*, 17(1):753–756, 1981.

[151] M. O. Honig. Internally cooled cabled superconductors part I. *Paper in Cryogenics*, 20:373–389, 1980.

[152] L. Dresner. Heating induced flows in Cable-In-Conduit Conductors. *Paper in Cryogenics*, 19:653–658, 1979.

[153] P. Bruzzone et al. Test results of SeCRETS, a stability experiment about segragated copper in CICC. *Paper in IEEE Transactions on Applied Superconductivity*, 11(1):2018–2021, 2001.

[154] P. Bruzzone et al. Transient stability results for Nb_3Sn Cable-In-Conduit Conductors. *Paper in IEEE Transactions on Applied Superconductivity*, 12(1):512–515, 2002.

[155] C. Marinucci et al. Transient stability analysis of the SeCRETS experiment in SULTAN. *Paper in IEEE Transactions on Applied Superconductivity*, 12(1):1524–1527, 2002.

[156] R. Zanino et al. Inductively driven transients in the CS Insert Coil (I): heater calibration and conductor stability test and analysis. *Paper in Advances in Cryogenic Engineering: Proceedings of the Cryogenic Engineering Conference - CEC*, 415-422, 2001.

[157] D. Ciazynski et al. Large superconductors and joints for fusion magnets: from conceptual design to testing at full scale. *Paper in Nuclear fusion*, 41(2):223–226, 2001.

[158] D. Ciazynski et al. Test result on the first 50 kA NbTi full size sample for the International Thermonuclear Experimental Reactor. *Paper in Superconductor Science and Technology*, 17:155–160, 2004.

[159] F. Savary et al. Status report on the Toroidal Field coils for the ITER project. *Paper in IEEE Transactions on Applied Superconductivity*, 20(3):381–384, 2010.

[160] F. Savary et al. The Toroidal Field coils for the ITER project. *Paper in IEEE Transactions on Applied Superconductivity*, 22(3):4200904, 2010.

[161] C. Sborchia et al. Design and specifications of the ITER TF coils. *Paper in IEEE Transactions on Applied Superconductivity*, 18(2):463–466, 2008.

[162] C. Sborchia et al. Progress on R&D and design work for the ITER Toroidal Field coils. *Proceedings of Fusion Engineering 20th IEEE/NPSS Symposium*, pages 432–435, 2003.

[163] E. P. A van Lanen et al. Performance analysis of ITER PF coil joints. *ITER report*, 67JFBM v2.1, 2011.

[164] J. van Nugteren. Software development for the science and design behind superconducting magnet systems. *University of Twente report*, 2011.

[165] N. Mitchell. Magnet superconducting and electrical design criteria. *ITER*

report, 22GRQH v1.2, 2009.

[166] E. P. A. van Lanen et al. Numerical analysis of the DC performance of ITER TF samples with different cabling pattern based on resistance measurements on terminations. *Paper in Superconductor Science and Technology*, 24:085010, 2011.

[167] Y. Takahashi et al. Performance of joints in the CS model coil and application to the full size ITER coils. *Paper in IEEE Transactions on Applied Superconductivity*, 14(2):1410–1413, 2004.

[168] X. Huang et al. Design and test results of joints for ITER TF feeder current leads and superconducting busbars. *Paper in IEEE Transactions on Applied Superconductivity*, 20(3):1722–1724, 2010.

[169] G. Rolando et al. Analysis of heat load, current margin and current nonuniformityin ITER PF Coil joints. *Paper in IEEE Transactions on Applied Superconductivity*, 23(3):4201405, 2013.

[170] H. Bajas. Numerical simulation of the mechanical behavior of the ITER Cable-In-Conduit Conductors. *PhD thesis, Ecole Centrale de Paris*, 2011.

Summary

Thermonuclear fusion is one of the most promising energy source candidates for the post peak oil era. For the fusion reaction to occur, an extremely dense plasma is required, having a temperature exceeding 100 million degrees. In ITER, a tokamak-type fusion machine currently under construction at the Cadarache site in southern France, the control and shaping of the hot plasma is obtained through a high magnetic field generated by a superconducting magnet system. In order to ensure specified repetition rates of plasma cycles, the superconducting magnets need to be built with a well-proven stability margin to avoid a quench, i.e. the undesired transition from the superconducting to the normal resistive state, which would interrupt the fusion process.

Due to the high cost involved in sample assembly and tests, the assessment of the stability of the Cable-In-Conduit conductors and lap-type joints between the conductors used in the ITER magnets based on experiments only is not attractive. As a consequence, numerical simulations are required for studying and optimizing the performance of conductors and joints. Since the stability against current imbalance and inter-strand coupling loss are tightly related to the specific paths of the strands within the conductors, strand-level detail simulation models are needed to correctly address the phenomena. In practice, the simulation task is complicated by the complex networks of contacts resulting from the assembly of around thousand strands in multiple cabling stages and by the short bending wavelength of the strands.

Under quasi steady-state conditions, a major treat for conductor stability is represented by current imbalance among strands originated from the uneven contact distribution between strands and the internal parts of the joints. If the resulting local strand current exceeds the critical current determined by the local magnetic field and temperature, a transition to the normal state occurs. The evolution of the initial normal zone eventually into a quench or into recovery depends on the possibility for the saturated strand to expel excess current into the surrounding strands. Instead, inter-strand coupling loss is the main power dissipation mechanism in highly compacted high current-carrying CIC conductors exposed to time-varying magnetic field. Coupling loss not only result in ohmic heating as the induced current cross the resistive parts within strands and cable, but may also rise the strand total current above its critical value. Stability issues are even more critical in the joints due to the necessity to simultaneously satisfy opposing requirements. On the one hand low-resistive joints allow reduction of ohmic heating and, possibly, improved current uniformity by facilitating current sharing among strands. On the other hand, highly resistive barriers around strands and petals are required to limit eddy, inter-strand and inter-cable coupling currents for pulsed operation.

In this thesis the results are laid down of a four year study on the stability of the CIC conductors and lap-type joints envisaged for the ITER magnets under both quasi steady-state and pulsed operating conditions performed with the numerical code JackPot-ACDC. With the exception of the strain state of Nb_3Sn strands, no free parameters exist in the model, though of course still certain assumptions have to be made. All the information required to define the electric and thermal networks of cable and joint part are obtained either from the computed trajectories of the strands or from experimental data.

CIC conductors under steady-state conditions

Current imbalance is particularly critical for the quasi steady-state performance of CIC conductors with NbTi strands due to the large n-values and steep J_c dependence on magnetic field of this material. As the self-magnetic field gradient over the cross-section of the conductor increases with the cable diameter and transport current, the maximum allowable current non-uniformity in the ITER Poloidal Field conductors needs to be defined to avoid the occurrence of premature quenches. The issue is studied on full-size short conductor samples as tested in the SULTAN facility at CRPP (Switzerland) as well as on a model coil.

For the first time the heating power and current non-uniformity are quantified and visualized at the strand level. According to the model, a quench in large NbTi CIC conductors is initiated in the form of local hot spots, often composed of single wires, of length <10 mm and located on the high-field side of the cable. At operating conditions, a maximum current imbalance of 1.5 is allowed in the ITER Poloidal Field conductors to avoid the transition from the cable to the strand quench regime, i.e to prevent the risk of sudden quenches. Under the same conditions, the expected cable heating power at quench is in the range 0.15 to 0.20 mW/cm^3, while the strand peak heating power varies between 65 and 250 mW/cm^3. Although the constantly increasing current imbalance can be qualitatively associated to the occurrence of premature quenches, a quantitative correlation with the quench regime transition cannot be clearly established based on the available data.

The current imbalance is studied in relation to the joint layout and the sample configuration. A parametric analysis of the effect of joint length, last stage twist pitch and cable-sole contact angle is performed on a full-size short conductor sample. Current non-uniformity can be reduced by the removal of the petal wraps or by allowing sufficient re-distribution length between the joint and the high field region of the sample. In the case of short samples, the current imbalance can be effectively suppressed through the use of solder locally in the joint or using alternative joint layouts like the so-called combo box joint.

CIC conductors under pulsed conditions

Containment of the loss when exposed to a time-varying magnetic field is a relevant design criteria for the ITER conductors, given the pulsed operation of the machine. The area of the current loops in bundle of strands linked to the changing magnetic field and the twist pitch sequence of the successive cabling stages highly influence the inter-strand coupling loss. The numerical investigation of their relation reveals that, apart from the absolute twist pitch length, also the ratio between twist pitch lengths of successive cabling stages plays an important role on the loss under pulsed conditions. Notably, inter-strand coupling loss can be significantly reduced with a ratio close to 1 between the twist pitches of the successive stages, the last one with high resistive wraps excluded. This newly found correlation allows combining long twist pitches with low coupling loss. The relevance of the result lies in the proven potential of long twist pitches to mitigate the degradation of the current sharing temperature with electro-magnetic and thermal cycling in Nb_3Sn strands, main issue faced in the development of the conductors for the ITER Toroidal Field coils and Central Solenoid.

The ratio 1 strategy is applied in the Long Twist Pitch (LTP) design for the ITER Central Solenoid conductor. Three other solutions are considered for test as well. The Baseline and Short Twist Pitch (STP) conductors share the same LTP cabling layout, but with different twist schemes, namely the ITER original and significantly shorter ones. The 3SC conductor instead relies on the same twist scheme as the Baseline design, but with a higher number of superconducting strands featuring a larger Cu content. Despite a first stage twist pitch twice to five times longer than those of the other designs, the measured AC loss for the LTP conductor up to 0.4 Hz is two to three times lower, confirming the prediction of the simulation code. However, the current sharing temperature of the LTP design degrades faster than expected and especially at a higher rate than the STP one.

The four conductors are further qualified with the simulation code for a so-called 15 MA plasma scenario. Given the limited available experimental data, the simulation shows the STP design to be characterized by the highest coupling loss and temperature increase. Based on petal-averaged properties a safe temperature margin seems to be retained by the four designs in all cyclic conditions. However, after cycling, the computed average electric field along the superconducting strands in the plasma scenario exceeds the quench electric field measured during steady-state test for the STP design. This implies that current sharing temperature and the related temperature margin may not be a sufficient criterion to secure electro-magnetic stability.

When quench conditions from transient stability tests are assumed as reference, the energy dissipation during the initial fast transient of the plasma scenario is below the quench level for all four cable designs. In reality, operating plasma conditions lie in between the steady-state and transient stability boundaries. As such, though hard to quantify, some reduction of the calculated energy margin can be expected due to the different duration and spatial distribution of the heating power during a plasma scenario.

Lap-type joints

Lap-type joint optimization under steady-state and pulsed operations is strongly related to the experienced conditions, for example transport current and local external magnetic field, its magnitude and direction. Depending on the precise location in the magnet system, this can lead to relaxation of some constraints.

While not critical for the stability of the ITER Toroidal Field coils joints (despite their disadvantageous Face On orientation with regard to the changing magnetic field), pulsed operation should be carefully optimized for some of the Poloidal Field coil joints. The main issue is the presence of petals contacting twice the copper sole at both joint extremities, which enables the formation of large coupling loops. To inhibit high coupling currents, petals masks can be inserted at selected cable-to-sole interfaces. Although allowing a reduction up to 70% of the peak coupling currents for slow magnetic field ramps, petal masks show only limited effect in the case of fast magnetic field variations. Alternatively, to reduce the inter-cable coupling the resistance of the sole can be increased. Although it yields a more limited improvement compared to petal masks, this solution drastically reduces the eddy current dissipation and temperature rise in the sole during axial magnetic field pulses. This in turn results in a higher stability of the strands in contact with the sole.

The main disadvantage of a relatively highly of a resistive sole is the increase of steady-state power dissipation. This is particularly relevant for joints carrying large steady-state currents, like the Toroidal Field coils where joint resistance as low as 1 nΩ are required to limit the dissipation within 5 W, in accordance with the available cooling power of the cryogenic system. When pulsed operation is not critical, an effective way to reduce the large steady-state power dissipation is the addition of solder on the outer cable surface to reduce the strand-to-sole contact resistance.

Samenvatting (summary in Dutch)

Thermonucleaire fusie als bron van energie is één van de meest veelbelovende kandidaten voor het komende tijdperk van afnemende olievoorraden. Voor het fusieproces is een plasma nodig met een extreme dichtheid bij een temperatuur van meer dan 100 miljoen graden. In ITER een fusiemachine van het zogenaamde tokamak type en momenteel in aanbouw is Cadarache in Zuid Frankrijk, de controle en afstemmen van het hete plasma worden bereikt door een sterk magneetveld dat wordt opgewekt met een systeem van supergeleidende magneten. Om de gespecificeerde herhalingsfrequentie van plasma cycli te garanderen moeten de supergeleidende magneten geconstrueerd worden met een bewezen stabiliteitsmarge om een zogenaamde quench, de ongewenste overgang van de supergeleidende naar de normaal geleidende toestand die het fusieproces onderbreekt, te voorkomen. Ten gevolge van de hoge kosten van het maken van proefstukken en tests is een beoordeling van de stabiliteit van de te gebruiken Cable-in-Conduit geleiders en overlapverbindingen tussen deze geleiders op basis van alleen experimenten niet aantrekkelijk. De consequentie hiervan is dat numerieke simulaties nodig zijn om het gedrag van geleiders en verbindingen te bestuderen en te optimaliseren. Omdat de stabiliteit tegen niet gebalanceerde stromen en koppelingsverliezen tussen de draden in de kabel in hoge mate bepaald wordt door de specifieke paden die de draden volgen in de kabels, zijn simulatiemodellen nodig die details tot op draadniveau in de kabels laten zien om op een correcte wijze de verschijnselen zichtbaar te maken. In de praktijk wordt de simulatie lastig door de aanwezigheid van complexe netwerken van contacten als gevolg van de ongeveer duizend draden die in meerdere verkabelingsstappen zijn gebundeld en door de korte buigingsgolflengtes van de draden.

Onder quasi stationaire omstandigheden is de belangrijkste bedreiging voor de geleiderstabiliteit de niet uniforme stroomverdeling in de draden in de kabel ten gevolge van de niet homogene verdeling van de contactweerstanden tussen de draden en de onderdelen in de verbindingen. Als ten gevolge hiervan de lokale stroom in draad de kritieke stroom overstijgt, dan zal een overgang naar de normaal geleidende toestand optreden. De overgang van het initiële normale gebied naar eventueel een *quench* of herstel, hangt af van de mogelijkheden die de verzadigde draad heeft om zijn overstroom kwijt te raken aan naburige draden. Anderzijds zijn koppelingsverlies tussen de draden in de kabel het belangrijkste mechanisme voor vermogensverliezen in deze hoog gecompacteerde hoge stroom CIC kabels die bloot staan aan in de tijd variërende magneetvelden. Koppelingsverliezen veroorzaken niet alleen ohmse verliezen wanneer de geïnduceerde stroom door de delen van de draden en de kabel met weerstand loopt, maar kunnen er ook voor zorgen dat de totale stroom in de draden boven de kritieke waarde stijgt. De stabiliteitsargumenten zijn zelfs nog kritieker in de verbindingen omdat daar tegelijkertijd voldaan moet worden aan tegen elkaar in werkende voorwaarden. Aan de ene kant kan een verbinding met lage weerstand de weerstandsverliezen beperken en mogelijkerwijs de stroomuniformiteit verbeteren door een betere stroomverdeling tussen draden te bewerkstelligen. Anderzijds zijn hoge weerstandbarrières om draden en dradenbundels nodig om de geïnduceerde verliezen in metalen, tussen draden en tussen kabels bij gepulst bedrijf te beperken. In dit proefschrift zijn de resultaten neergelegd van een vierjarige studie van de stabiliteit van CIC geleiders en overlapverbindingen zoals voorzien voor de ITER magneten waarvoor het numerieke simulatieprogramma JackPot-ACDC is ontwikkeld en gebruikt voor quasi stationaire en gepulste omstandigheden. Met uitzondering van de rektoestand van de Nb_3Sn draden, heeft het model geen vrije parameters, hoewel uiteraard bepaalde aannames nodig zijn. Alle noodzakelijke informatie om de elektrische en thermische netwerken van de kabel en de verbinding te definiëren zijn verkregen door berekening van de paden van de draden in de kabel of van experimentele waarden.

CIC geleiders onder stationaire omstandigheden

Ongelijkheden in stroom zijn vooral kritiek voor de quasi stationaire prestaties van CIC geleiders met NbTi draden vanwege de hoge n-factoren en de steile Jc afhankelijkheid als functie van magneetveld van dit materiaal. Omdat de gradiënt van het eigenveld over de doorsnede van de geleider toeneemt met de diameter van de kabel en met de transportstroom, moet de maximaal te tolereren stroom inhomogeniteit in de geleiders voor de ITER Poloïdale Spoel geleiders bepaald worden om het optreden van vroegtijdige quenches te voorkomen. Het onderwerp is bestudeerd aan de hand van testen in korte maar volledige proefstukken van geleiders in de SULTAN faciliteit bij CRPP (Switzerland) en ook met een modelspoel. Voor de eerste keer zijn het warmteopwekkende vermogen en de stroominhomogeniteit cijfermatig bepaald en zichtbaar gemaakt op het niveau van de draden in de kabels. Volgens het model begint een quench in grote CIC geleiders met NbTi draden in de vorm van lokale hete plekken, vaak bestaande uit enkele draden, met een lengte van minder dan 10 mm en bevinden zich aan de hoogveldkant van de geleider. Onder bedrijfsomstandigheden is een stroomonbalans tussen de draden van maximaal 1.5 te tolereren in de geleiders voor de ITER poloïdale veldspoel om een overgang van het quench regime van kabel naar draad te voorkomen, dus om het risico van plotselinge quenches te vermijden. Onder dezelfde omstandigheden ligt het te verwachten verwarmingsvermogens in de kabel tussen de 0.15 en 0.20 mW/cm^3 terwijl de topwaardes van het verwarmingsvermogen in de draad liggen tussen de 65 en 250 mW/cm^3. Hoewel de continu toenemende stroomonbalans kwalitatief geassocieerd kan worden met het optreden van vroegtijdige quenches, kan op basis van de beschikbare gegevens een kwantitatieve korrelatie niet duidelijk worden bepaald. De stroomonbalans is bestudeerd in relatie tot de uitvoering van de verbinding en de configuratie van het proefstuk. Een parametrische analyse is uitgevoerd van een kort geleider proefstuk met ware doorsnede om het effect van de lengte van de verbinding, de twisthoek van de laatste kabelslag, en de contacthoek tussen kabel en de stroom opnemende geleider te bestuderen. De stroominhomogeniteit kan worden gereduceerd door de zogenaamde *petal-wraps*, of kabelomslagband, een dunne stalen band die om de één na laatste kabelslag is gewikkeld om koppelingsverliezen tegen te gaan, lokaal in de verbinding te verwijderen; of door te zorgen voor voldoende herverdeling van de stroom tussen de verbinding en de plek met hoog veld in de spoel door voldoende afstand hiervoor te reserveren. In het geval van korte proefstukken kan de stroomonbalans effectief worden onderdrukt door het gebruik van soldeer lokaal in de verbinding of een alternatief ontwerp van een verbinding te gebruiken (de zogenaamde combo box joint).

CIC geleiders onder gepulste omstandigheden

De beheersing van de verliezen onder invloed van een wisselend magneetveld is een relevant ontwerp criterium voor de ITER geleiders gegeven het gepulst bedrijven van de machine. The oppervlaktes van de stroomlussen in de bundel van draden die het wisselende magneetveld zien en de serie van twistlengtes van de opeenvolgende verkabelingsstappen bepalen in hoge mate het koppelingsverlies. Het numeriek onderzoek van de onderlinge relatie heeft aan het licht gebracht dat naast de absolute waardes van de verschillende twistlengtes, ook de verhouding tussen de twistlengtes van opeenvolgende verkabelingsstappen een belangrijke rol spelen in de hoogte van het verlies onder gepulste omstandigheden. Vooral het koppelingsverlies tussen de draden kan significant worden gereduceerd met een twistlengteverhouding dicht bij 1 tussen de twistlengtes van opeenvolgende stappen, echter met uitzondering van de laatste verkabelingsstap waarbij een kabelomslagband wordt gebruikt. Deze nieuwe correlatie die gevonden is maakt het mogelijk om lange twistlengtes te combineren met lage koppelingsverliezen. Dit resultaat is belangrijk omdat het bewezen is dat lange twistlengtes ook de degradatie van de stroomherverdelingstemperatuur in Nb_3Sn draden onder invloed van elektromagnetische en thermische cycli helpen te voorkomen, een belangrijk aspect in de ontwikkeling van de geleiders voor de ITER toroïdale veldspoelen en de centrale solenoïde.

De verhouding-1 strategie is toegepast in het zogenaamde lange-twistlengte (LTP) ontwerp in de geleider voor de ITER centrale solenoïde. Drie andere oplossingen zijn eveneens getest. De referentie en de korte-twistlengtes (STP) geleiders hebben dezelfde verkabelingsstappen alleen dan met andere twistlengtes, namelijk de eerste met de originele ITER en de tweede met veel kortere twistlengtes. De laatste, de 3SC geleider is verkabeld net als de referentiegeleider, echter nu met meer supergeleidende draden en met een hoger gehalte aan koper. Ondanks een eerste twistlengte die twee tot vijf keer langer is dan in de andere ontwerpen, is het gemeten wisselstroomverlies tot 0.4 Hz aan de LTP geleider twee tot drie keer lager, wat de voorspelling van het simulatieprogramma bevestigt. Echter, de stroomherverdelingstemperatuur in het LTP ontwerp degradeert sneller dan verwacht, en vooral sneller dan in het STP ontwerp.

De vier geleiders zijn verder gekwalificeerd met simulaties voor het zogenaamde 15 MA plasma scenario. Gegeven de beperkte hoeveelheid meetresultaten, laat de simulatie zien dat het STP ontwerp kan worden gekarakteriseerd met het hoogste koppelingsverlies en temperatuurtoename. Ondanks dat de temperatuur wordt berekend als een gemiddelde in de laatste verkabelingsstap, kan toch worden gezegd dat een veilige temperatuurmarge aanwezig is in de vier ontwerpen onder alle cyclische omstandigheden. Echter, na cyclisch belasting, is het gemiddelde elektrische veld langs de supergeleidende draden tijdens het plasma scenario hoger dan het elektrische veld waarbij een quench optreedt zoals gemeten onder stationaire omstandigheden. Dit impliceert dat de stroomherverdelingstemperatuur en de daaraan gekoppelde temperatuurmarge wellicht een onvoldoende scherp criterium is om elektromagnetische stabiliteit te waarborgen. Wanneer quench-omstandigheden zoals gemeten in stabiliteitstests in gepulst bedrijf als referentie worden genomen, dan blijkt de vrijkomende energie tijdens de initiële snelle stijging in het plasma scenario te liggen beneden het quench-niveau in alle vier geleiderontwerpen. In werkelijkheid liggen de plasmabedrijfs-omstandigheden tussen de stationaire en de gepulste stabiliteitsgrenzen. Op deze wijze, maar moeilijk te kwantificeren kan enige reductie in de berekende energiemarge worden verwacht vanwege de verschillende tijdsduur en ruimtelijke verdeling van de warmteontwikkeling tijdens een plasma scenario.

Overlapverbindingen

De optimalisatie van overlapverbindingen voor stationaire en gepulste omstandigheden is sterk afhankelijk van de bedrijfsomstandigheden, bijvoorbeeld de transportstroom en het lokale magnetische veld in hoogte en richting. Afhankelijk van de precieze positie in het magneetsysteem kan dit leiden tot een afzwakking van sommige eisen. Hoewel ze niet kritiek zijn voor de stabiliteit van de ITER toroïdale veldspoelen en ondanks de nadelige face-on oriëntatie met betrekking tot het veranderende magneetveld, voor gepulst bedrijf moeten sommige verbindingen in de poloïdale veldspoelen met zorg worden geoptimaliseerd. Het belangrijkste aspect is de laatste verkabelingsbundel die twee keer contact kan maken met het koperen stroomopnemende deel bij de beide uiteinden van de verbinding wat het mogelijk maakt dat lussen ontstaan waarin grote koppelingsstromen gaan lopen. Om deze hoge koppelingsstromen te voorkomen kan men weerstandsbarrieres in de vorm van folies inbrengen op bepaalde plekken op het grensvlak tussen de kabel en de koperen stroomgeleider. Ondanks dat een afname met 70% van de maximale koppelingsstroom bereikt kan worden in geval van langzame veldveranderingen is het effect te beperkt in geval van snelle magneetveranderingen. Als alternatief kan de weerstand van de gehele stroomopnemer worden verhoogd. Hoewel deze oplossing een beperkte verbetering laat zien in vergelijking met kabelweerstandsbarrières, vermindert deze oplossing wel drastisch de geïnduceerde verliezen door eddy stromen evenals de temperatuur verhoging in de stroomopnemer onder invloed van axiaal gerichte magneetveldpulsen. En dit zorgt voor een hogere stabiliteit van de draden die in contact zijn met de stroomopnemer. Het belangrijkste nadeel van een stroomopnemer met een relatief hoge soortelijke weerstand is de toename van het stationaire vermogensverlies. Dit is vooral relevant voor verbindingen met een grote stroom zoals in de toroïdale veldspoelen waarin de verbindingsweerstanden kleiner moeten zijn dan 1 nΩ om de warmteontwikkeling beneden de 5 W te houden in overeenstemming met het beschikbare koelvermogen van het cryogene systeem. Als gepulst bedrijf niet kritiek is, dan is het toevoegen van een laag soldeer tussen de kabel en de stroomopnemer een goede oplossing om de contactweerstanden te verlagen.

Acknowledgements

This thesis is the conclusion of a 4 years work that I have had the pleasured to carry out in the Energy, Materials & Systems group of the University of Twente. I am very grateful for having had the opportunity to join this group and to have a part in such a challenging project as ITER. Here I would like to acknowledge the people who have contributed to the successful outcome of my PhD research.

In the first place I would like to thank my supervisor Arend Nijhuis for his help and guidance during the course of my PhD. His extensive knowledge of strands, Cable-In-Conduit conductors and fusion magnets have been of great value.

This work would have also not been possible without Ezra van Lanen. I have really appreciated the availability for discussing the code JackPot-ACDC even when miles away from Twente.

Although I haven't spent much time in the laboratory, I would like to thank Sander, Erik and Rutger for their technical support in the AC loss measurements. About Sander, I have also appreciated the rapidity in solving all the computer hardware issues faced in the course of my simulation work.

I would like to extend my sincere gratitude to Herman ten Kate and Marc Dhallé for their general support and Yuri Ilin for many useful discussions.

I would also like to thank Bram, Cris, Gonzalo, Haishan, Harrie, Marcel, Roger, Ruben, Sergi, Srini, Tim and Wilco for the many coffee breaks I have enjoyed with you.

My special thanks go to my family for their interest and encouragement.

Nie ma wystarczających słów aby oddać to jak bardzo jestem wdzięczna mojemu mężowi Sebastianowi. Dziękuję za bezwarunkowe wsparcie podczas wzlotów i upadków w pracy nad doktoratem. Dziękuję za podróże do Enschede, tam i z powrotem, aby być przy moim boku. Dziękuję za cierpliwość i zrozumienie.